

N O T I C E

THIS DOCUMENT HAS BEEN REPRODUCED FROM
MICROFICHE. ALTHOUGH IT IS RECOGNIZED THAT
CERTAIN PORTIONS ARE ILLEGIBLE, IT IS BEING RELEASED
IN THE INTEREST OF MAKING AVAILABLE AS MUCH
INFORMATION AS POSSIBLE

JOINT INSTITUTE FOR AERONAUTICS AND ACOUSTICS



National Aeronautics and
Space Administration

Ames Research Center



Stanford University

JIAA TR - 39

SOME OBSERVATIONS OF SURFACE PRESSURES AND THE NEAR WAKE OF A BLUNT TRAILING EDGE AIRFOIL



R.V. Digumarthi, S.P. Koutsoyannis, and K. Karamcheti

(NASA-CR-168563) SOME OBSERVATIONS OF
SURFACE PRESSURES AND THE NEAR WAKE OF A
BLUNT TRAILING EDGE AIRFOIL (Stanford Univ.)
189 p HC A09/MF A01

CSCL 01A

N82-19174

Unclass

G3/02 13889

STANFORD UNIVERSITY
Department of Aeronautics and Astronautics
Stanford, California 94305

JUNE 1981

JIAA TR - 39

SOME OBSERVATIONS OF SURFACE PRESSURES AND
THE NEAR WAKE OF A BLUNT TRAILING EDGE AIRFOIL

R. V. Digumarthi, S. P. Koutsoyannis, and
K. Karamcheti

The work here presented has been supported by the
National Aeronautics and Space Administration under
Contract NASA NSG 2007 and NASA NSG 2233

JUNE 1981

ACKNOWLEDGEMENTS

Present investigations were carried out as part of the research program of the Joint Institute for Aeronautics and Acoustics, Department of Aeronautics and Astronautics, of Stanford University and was sponsored by NASA Ames Research Center under Grant NSG 2007 and NSG 2233.

The authors appreciate the help and advice given by Dr. Sanford Davis of NASA Ames Research Center during the progress of the work.

This report is based on the work of R. Digumarthi, for Doctor of philosophy degree at Stanford University.

ABSTRACT

The structure of the flow past a blunt trailing edge airfoil is of considerable interest, both from the point of view of practical application and fundamental understanding. The boundary layer on such an airfoil separates at the blunt trailing edge and generates a well organized structure in the wake. This facilitates a convenient experimental study. An experimental investigation is thus undertaken to study some features of such flow. This report presents the experiments undertaken, the results obtained and discusses their implications.

Experiments with a truncated and untruncated airfoils of profiles NACA 640A10, are carried out in subsonic wind tunnels in a velocity range of 19m/s to 54m/s corresponding to Reynolds numbers of 2.0×10^5 to 4.68×10^5 based on the chord. Airfoil spanned the test section to achieve two-dimensionality of the model. Velocity measurements both mean and fluctuating, pressure measurements, both static and fluctuating and vortex shedding in the wake are measured using a hotwire and pressure transducers.

The measured chordwise static pressure distribution on the smooth trailing edge airfoil along the midspan plane, agreed with the theoretical results calculated on the basis of the potential flow for that airfoil. Boundary layer profiles measured in the midspan plane, behind the maximum thickness of the airfoil showed no separation of the flow. Spanwise distribution of the measured static pressure on the upper surface of the airfoil showed uniformity for both configurations with and without the boundary layer trip. This uniformity of pressure distribution and separation indicates that the flow on the airfoil was uniform and two-

dimensional in character.

Chordwise static pressure distribution of the blunt trailing edge airfoil agreed with that for a smooth trailing edge airfoil except at the vicinity of the trailing edge. The boundary layer profiles in the mid-span plane showed no separation as in the case of the smooth trailing edge airfoil. The spanwise distribution of the static pressure with tripped boundary layer, was found to be uniform on the upper surface of the airfoil. But the spanwise distribution of the static pressure for an untripped boundary layer configuration was found to be nonuniform as the trailing edge was approached. The base pressure distribution was not uniform in the spanwise direction for either of the configurations (tripped or untripped) of the airfoil.

No discrete frequency fluctuations are observed in the wake of the smooth trailing edge airfoil. Vortex shedding occurs behind blunt trailing edge airfoils. The characteristic vortex shedding frequency varied linearly with velocity. The values of the shedding frequency in the case of the tripped boundary layer were lower than those in the case of the untripped boundary layer. The shedding frequency of a circular cylinder, of diameter equal to the thickness of the airfoil trailing edge, was found to lie between the frequencies measured in the cases of the tripped and untripped boundary layer configurations. Although the intensity (RMS) of the base fluctuating pressure showed negligible variation in the spanwise direction, cross-correlations indicate spanwise phase variation in the base pressure.

TABLE OF CONTENTS

ACKNOWLEDGEMENTS	iv
ABSTRACT	vi
TABLE OF CONTENTS	viii
LIST OF FIGURES	x
LIST OF TABLES	xv
NOMENCLATURE	xvi
I INTRODUCTION	1
II NATURE AND BACKGROUND OF THE PROBLEM	3
II.1 Features and Parameters of the Problem	3
II.2 Review of Work on the Flow Past A Blunt Based Two-dimensional Body	5
III INITIAL INVESTIGATION OF A BLUNT TRAILING EDGE AIRFOIL	10
III.1 Airfoil Model and Experimental Setup	10
III.2 Analysis of the Measurements	13
III.3 Cross-Correlations of the Fluctuating Pressure	18
IV EXPERIMENTAL SETUP FOR SUBSEQUENT INVESTIGATIONS	25
IV.1 The Subsonic Wind Tunnel	25
IV.2 Models and the Experimental Setup	27
IV.3 Instrumentation	31
IV.3.1 Manometer Board and Thermocouple	32
IV.3.2 Hotwire Anemometer System	34
IV.3.3 Measurements of Correlation and Spectra	36
IV.3.4 Microphone Measurements	37
IV.4 Calibration of the 45.7 x 45.7 cm Wind Tunnel	37
IV.4.1 Calibration of the Tunnel With an Empty Test Section	38
IV.4.1.1 Velocity Profiles	38
IV.4.1.2 Acoustic Features	39
IV.4.1.3 Temperature Variation	41
IV.4.2 Calibration with Side Plates in the Test Section	43
IV.4.2.1 Velocity Profiles	43
IV.4.2.2 Acoustic Features	44

V	NEAR FLOW FIELD MEASUREMENTS AND RESULTS	45
V.1	Smooth Trailing Edge Airfoil Model	45
V.1.1	Measurements of Static Pressure	46
V.1.2	Boundary Layer and Wake Velocity Profiles	50
V.2	Blunt Trailing Edge Airfoil Model	51
V.2.1	Static Pressure Measurements	53
V.2.2	Velocity Profiles of the Boundary Layer and the Near Wake	56
V.2.3	Characteristic Vortex Shedding Frequency of the Airfoil	58
V.3	Same Measurements of Flow Past a Circular Cylinder	61
V.4	Acoustic Features of the Blunt Trailing Edge Airfoil	63
VI	CONCLUDING REMARKS	67
	FIGURES	71
	TABLES	160
	BIBLIOGRAPHY	165

LIST OF FIGURES

II.1	Strouhal Number of 2-dimensional Body with Blunt Trailing Edge	71
III.1	Blunt Trailing Edge Airfoil with Transducers (Airfoil I)	72
III.2	Data Reduction System for Experiments	73
III.3	Real Time Signals of Hotwire in the Wake at 0.6cm. Downstream of the Blunt Trailing Edge of the Airfoil I.	74
III.4	Real Time Signals of the Pressure Transducers on the Surface of the Blunt Trailing Edge Airfoil I.	75
III.5	Auto-Correlation Function of the Signal from the Hotwire in the Wake	77
III.6	Auto Power Spectral Density of the Hotwire Signal in the Mid Wake Position and at 0.6cm. Downstream of the Blunt Trailing Edge	78
III.7	Auto Power Spectral Density of the Hotwire Signal at 0.6cm. Downstream of the Upper Separation Point of the Blunt Trailing Edge	79
III.8	Auto Power Spectral Density of the Signal from the Transducer Near the Blunt Trailing Edge	80
III.9	Auto Power Spectral Density of the Signal from the Transducer in the Blunt Trailing Edge	83
III.10	Auto Power Spectral Density of the Signal from the Transducer Near the Leading Edge	85
III.11	Variation of Shedding Frequency of Airfoil I with Velocity	87
III.12	Variation of the Strouhal Number of the Airfoil I with Velocity	88
III.13	Variation of the Base Pressure of the Truncated Airfoil with Transducers (Airfoil I) with Velocity	89
III.14	Comparison of the Strouhal Number	90
III.15	Near Wake Profile of the RMS Value of the Fluctuating Velocity Measured at 0.6cm. Downstream of the Blunt Trailing Edge	91

III.16	Cross-Correlation of the Filtered Pressure Signal from Transducers #11 and #12, in the Blunt Trailing Edge	92
IV.1	Plan View of the 45.7 x 45.7cm Subsonic Wind Tunnel	93
IV.2	Planform of the Airfoil with the Smooth Trailing Edge, (Airfoil III) Showing the Layout of the Pressure Taps	94
IV.3	Blunt Trailing Edge Airfoil with Static Pressure Taps (Airfoil II)	95
IV.4	Airfoil Model Held Between the End Plates and in the Tunnel	96
IV.5	Profiles of the Mean Velocity and RMS of the Fluctuating Velocity in Mid Vertical Plane for Empty Test Section	97
IV.6	Mean Velocity and RMS of the Fluctuating Velocity in the Mid Horizontal Plane with Empty Test Section	99
IV.7	Power Spectral Density of Fluctuating Velocity Component	101
IV.8	Measured 1/3 Octave Band Acoustic Spectrum at the Center of the Empty Test Section	103
IV.9	Time Variation of Static Temperature in Test Section Flow	105
IV.10	Profiles of Mean Velocity and RMS of Fluctuating Velocity in the Vertical Plane, with End Plates in the Test Section	106
IV.11	Profiles of Mean Velocity and RMS of Fluctuating Velocity in a Horizontal Plane, with End Plates in Test Section	107
IV.12	Measured 1/3 Octave Band Acoustic Spectrum at the Center of the Test Section, with End Plates and at a Velocity of 24m/s	108
V.1	Airfoil Model in the 45.7 x 45.7cm Tunnel	109
V.2	Velocity Profiles Measured at 6cm Upstream of the Leading Edge of the Airfoil Model at a Velocity of 26m/s	110
V.3	Chordwise Distribution of Static Pressure of Smooth Trailing Edge Airfoil (Airfoil III) Along the Midspan	111

V.4	Comparison of Corrected Static Pressure Distribution of the Smooth Trailing Edge Airfoil Along the Mid Span Plane with the Theoretical Distribution	113
V.5	Spanwise Distribution of the Static Pressure of the Smooth Trailing Edge Airfoil	115
V.6	Boundary Layer Profiles on the Smooth Trailing Edge Airfoil Along the Mid Span at Velocity of 45m/s	117
V.7	Comparison of the Boundary Layer Profiles at $x/c = 0.82$	119
V.8	Measured Wake Profiles Behind the Airfoil with Smooth Trailing Edge Along the Mid Span at velocity of 45m/s	120
V.9	Chordwise Static Pressure Distribution for Blunt Trailing Edge Airfoil with Pressure Taps in the Mid Span	122
V.10	Comparison of the Chordwise Distribution of Static Pressure in the Mid Span and at Velocity of 24m/s	123
V.11	Spanwise Static Pressure Distribution for the Blunt Trailing Edge Airfoil with Pressure Taps, with Boundary Layer Trip	124
V.12	Spanwise Static Pressure Distribution for the Blunt Trailing Edge Airfoil with Pressure Taps, Without Boundary Layer Trip	125
V.13	Base Pressure Distribution for the Airfoil with Transducers	126
V.14	Comparison of the Base Pressure with the Velocity	127
V.15	Variation of Base Pressure in the Spanwise Direction for the Blunt Trailing Edge Airfoil with Pressure Taps, Without the Boundary Layer Trip	128
V.16	Variation of Base Pressure in the Spanwise Direction for the Blunt Trailing Edge Airfoil with Pressure Taps, With the Boundary Layer Trip	129
V.17	Boundary Layer Profiles of the Truncated Airfoil with Pressure Taps at a Velocity of 24m/s	130
V.18	Boundary Layer Profiles of the Truncated Airfoil with Pressure Taps at a Velocity of 34m/s	132
V.19	Boundary Layer Profiles Along the Mid Span on the Truncated Airfoil with Transducers	134

V.20	Comparison of the Boundary Layer Profiles of Blunt Trailing Edge Airfoils at x/c of 0.99 and Velocity of 24m/s	135
V.21	Comparison of the Boundary Layer Profiles for the Airfoils with Pressure Taps, at a Velocity of 45m/s	136
V.22	Wake Profiles Behind the Truncated Airfoil with Transducers at a Velocity of 26m/s and at x/d of 3.3	137
V.23	Wake Profiles of the Truncated Airfoil with Pressure Taps Along the Mid Span and a Velocity of 24m/s	138
V.24	Wake Profiles of the Truncated Airfoil with Pressure Taps Along the Mid Span and at a Velocity of 34m/s	139
V.25	Wake Profiles of the Airfoil with Pressure Taps at Different Spanwise Positions at x/d of 2.0 and at Velocity of 24m/s	140
V.26	Wake Profiles of the Airfoil with Pressure Taps at Different Spanwise Positions at x/d of 2.0 and at Velocity of 34m/s	141
V.27	Characteristic Vortex Shedding Frequency of the Truncated Airfoil with Transducers at Different Velocities	142
V.28	Comparison of the Shedding Frequency Between the Truncated Airfoil with Transducers and a Circular Cylinder	143
V.29	Variation of the Vortex Shedding Frequency with Velocity	144
V.30	Comparison of the Strouhal Number	145
V.31	Variation of Shedding Frequency in the Spanwise Direction of the Truncated Airfoil with Transducers, at a Velocity of 26m/s	146
V.32	Variation of Shedding Frequency in the Spanwise Direction of the Truncated Airfoil with Pressure Taps, at $x/d = 2.0$ for Various Velocities	147
V.33	Characteristic Vortex Shedding Frequency of a Circular Cylinder at Different Velocities	148
V.34	Resonance Characteristic of the Tunnel Measured with the Truncated Airfoil	149
V.35	Frequency Measurements of the Truncated Airfoil with Pressure Taps for Tripped Boundary Layer Configuration	150

V.36	Measured Power Spectral Density Measurement for Tripped Boundary Layer Configuration of the Blunt Trailing Edge Airfoil with Pressure Taps at a Velocity of 34m/s	151
V.37	Measured Power Spectral Density Measurement for Tripped Boundary Layer Configuration of the Truncated Airfoil with Pressure Taps at a Velocity of 24m/s	152
V.38	Characteristic Vortex Shedding Frequency Measurements of the Truncated Airfoil with Untripped Boundary Layer	153
V.39	Measured Power Spectral Density Measurement of Untripped Boundary Layer for the Truncated Airfoil with Pressure Taps at Velocity 34m/s	154
V.40	Measured Power Spectral Density Measurement of the Untripped Boundary Layer for the Truncated Airfoil with Pressure Taps at at Velocity of 34m/s	155
V.41	1/3 Octave Band Spectrum from Microphone outside the Tunnel for the Truncated Airfoil with Pressure Taps at Velocity 33m/s	156
V.42	Near Field Pressure Directivity Pattern for the Blunt Trailing Edge Airfoil with Pressure Taps at a Velocity of 26m/s and a distance of $R = 2.0\text{cm}$	158
V.43	Near Field Pressure Directivity Pattern for the Blunt Trailing Edge Airfoil with Pressure Taps at a Velocity of 34m/s and at a distance of $R = 2.0\text{cm}$	159

LIST OF TABLES

III.1	Intensities of the Fluctuating Pressure Signal as Measured by the Transducers	160
III.2	Phase Speeds and Angles from the Oblique Wave Model	160
IV.1	Blade Passing Frequencies of the Tunnel Drive Fan	161
IV.2	Duct Mode Frequencies for the 45.7 x 45.7cm Tunnel	161
IV.3	Static Temperature Rise in the Tunnel Flow	162
IV.4	Duct Mode Frequencies for the 25.0 x 45.7cm Tunnel	162
V.1	Shedding Frequencies of the Hotwire Support Rods	163
V.2	Shedding Frequency Variation Behind the Airfoil With Transducers in the Spanwise Direction	163
V.3	Measured Shedding Frequencies Behind A Circular Cylinder	164

NOMENCLATURE

A	Amplitude of the signal harmonic
a	Speed of sound ; Speed of the signal harmonic
B	Amplitude of the signal harmonic
b	Wake half width
C	Chord of the airfoil ; Characteristic length
Cp	Pressure Coefficient = $\frac{P - P_{\infty}}{\frac{1}{2} \rho U_{\infty}^2}$
d	Trailing edge thickness ; Diameter of the circular cylinder
f	Frequency
g	Defined by equation III.2.22
h	Side dimension of the test section
k	Wave number ; $\sqrt{1.0 - Cp_b}$
M	Mach number = U/a
p	Pressure
R	Correlation Coefficient ; Distance of the microphone from the airfoil trailing edge
Re	Reynolds Number = Uc/ν
r	Separation distance
S	Semi-span of the airfoil model
St	Strouhal number = fd/U
T	Temperature
t	Maximum thickness of the airfoil
U	Mean velocity

- u Fluctuating velocity component
 x, y, z Axial, lateral and spanwise distances
 α Angle of attack ; Oblique angle
 δ Boundary layer thickness where $U_e = 99\%$ of U_∞
 δ_1 Boundary layer displacement thickness = $\int_0^\infty \left[1.0 - \frac{U}{U_e} \right] dy$
 ϵ Blockage factor = $\Delta U/U$
 ζ Separation distance in the spanwise direction
 θ Boundary layer momentum thickness = $\int_0^\infty \frac{U}{U_e} \left[1.0 - \frac{U}{U_e} \right] dy$
 ν Kinematic viscosity
 ξ Separation distance in the axial direction
 ρ Mass density ; Normalized correlation function
 τ Time delay
 ϕ Phase angle
 ω Radian frequency = $2\pi f$

Subscripts

- B Total blockage factor
 b In the base
 c Based on the chord ; Measured at the center line
 d Based on the trailing edge thickness
 f At the vortex formation region
 m Maximum ; Harmonic number
 n Harmonic number

- s Shedding frequency ; Static value
- x,y,z In axial, lateral and spanwise directions
- δ_1 Based on the boundary layer displacement thickness
- o Fundamental frequency
- ∞ Condition at infinity

Superscript

- * Universal number

I INTRODUCTION

The structure of the flow past a blunt trailing edge airfoil is of considerable interest, both from the point of view of practical application and fundamental understanding. The boundary layer on such an airfoil separates at the blunt trailing edge and generates a well organized structure in the wake. This facilitates a convenient experimental study. An experimental investigation is thus undertaken to study some features of such flow.

The farfield radiated noise from such an airfoil has discrete structure due to vortex shedding in the wake besides broad band background due to turbulence. The flow structure in the region near the trailing edge is believed to play the central role in the generation of this noise. Investigations of such noise were based either on an analytic model of a semi-infinite rigid plate with wake, in a uniform two-dimensional flow or on an experimental model of a two-dimensional finite body with a wake in a uniform flow field.

Davis (1975) developed a model for discrete noise generated by an airfoil using a semi-infinite flat plate with discrete vortex wake in the uniform flow. Davis was able to show agreement between his theoretical far field directivity pattern and that measured for a blunt trailing edge airfoil. He also discussed the importance of knowing the precise trailing edge flow conditions.

The blunt base flat plate or an airfoil was the subject of many investigations in the past with an emphasis on reducing the base pressure drag by modifying the blunt trailing edge flow. All these experimental investigations were carried out with two-dimensional models in uniform

flow and the spanwise variations were ignored.

Experiments with a truncated and untruncated airfoils of profiles NAXA 640A10, are carried out in subsonic wind tunnel in a velocity range of 19m/s to 54m/s corresponding to Reynolds numbers of 2.0×10^5 to 4.68×10^5 based on the chord. Airfoil spanned the test section to achieve two-dimensionality of the model. Velocity measurements, both mean and fluctuating, pressure measurements, both static and fluctuating and vortex shedding in the wake are measured using a hotwire and pressure transducers.

In Chapter II, the nature of the problem and the resume of the related past studies are described. Chapter III gives the description of the experimental setup, measurement techniques and the results obtained in the initial investigation. Chapter IV describes the experimental setup for the subsequent investigations. Chapter V describes near flow field measurements and results of subsequent investigations. Chapter VI summarizes results and discusses their implications.

II NATURE AND BACKGROUND OF THE PROBLEM

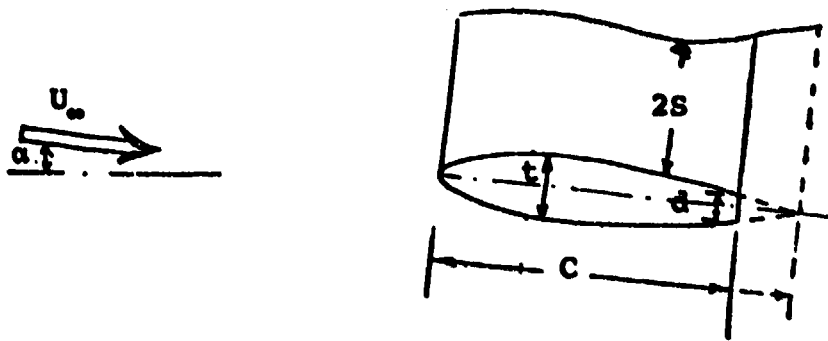
As mentioned in the introduction, understanding the near wake field of an isolated airfoil with a blunt trailing edge in uniform flow was the motivation for the present investigations. In this chapter the nature of the problem, along with the parameters and factors that govern the flow field are discussed. A brief survey of past work relating to the study is also presented.

II.1 Features and Parameters of the Problem

In the subsonic flow region, flow past a blunt trailing edge airfoil is accompanied by discrete vortex shedding and consequently the surface pressure fluctuations are characterized by discrete frequency spectra. Basic features, in particular, the characteristics of the near wake field consisting of both mean and fluctuating quantities, are of interest.

The parameters and the factors governing the flow field of a blunt trailing edge airfoil are listed below (also shown in the sketch)

- a) Geometrical Characteristic of the airfoil consisting of chord (c), maximum thickness (t), thickness of the trailing edge (d), span ($2s$) and profile of the airfoil.
- b) Geometrical parameters, such as the wind tunnel test section dimensions and the experimental set up depicting the relative disposition of the model in the tunnel.
- c) Angle of attack of the airfoil (α)



- d) Uniformity of the inflow such as the mean velocity, and the spatial uniformity of the turbulence intensity i.e.

RMS values.

- e) Reynolds number of the model, $Re = \frac{Uc}{\nu}$
- f) Mach number of the flow, $M = U/a$

Next, the features that characterize the near flow field of the blunt trailing edge airfoil are given below:

- a) Mean properties of the pressure field of the airfoil such as the surface static pressure distribution and the mean base pressure distribution are required properties. The fluctuating field is characterized by the frequency spectrum, the intensity of the fluctuations and their spatial correlations.
- b) The nature of the boundary layer on the surface of the airfoil, whether it is laminar or turbulent, and its characteristics like the displacement thickness (δ_1) and the momentum thickness (θ) at the trailing edge are needed. The measurement of the boundary layer at various spanwise locations will aid the understanding of the trailing edge flow.

c) Similarly, velocity profiles, both mean and fluctuating, in the wake of the airfoil, also characterize the near flow field. The correlations and the frequency spectra of the fluctuating velocity in the wake are essential.

If the sound field, either the far field or near field, is to be investigated, then the appropriate parameters pertaining to the acoustic field such as the acoustic directivity pattern need to be added to the above.

Before discussing the experiment and its results, a brief review of the work on the flow field of a blunt trailing edge airfoil will be discussed.

II.2 Review of work on the Flow Past a Blunt Based Two-Dimensional Body

As stated before, both mean and fluctuating quantities in the near flow field are of interest. Though the forebody of the airfoil is streamlined, the blunt trailing edge generates a wake flow which is characteristic of a bluff body. References that discuss general concepts of a bluff body flow were included in the bibliography.

Features of the flow past a streamlined two-dimensional body with a blunt trailing edge that were investigated are the base drag and some characteristics of the wake. Investigations of the base drag dealt with changing the trailing edge configuration to reduce the base drag. A selective bibliography of the work on this aspect is given at the end of the report.

Nash and his co-workers (1962, 1963, and 1964) have summarized the work done before 1963, bringing into focus the features of the base flow. In their experimental investigations of a flat plate, with a sharp leading edge, for flow Mach number above 0.2, they found uniform mean base pressure in the spanwise direction. The angle of incidence created an asymmetric base pressure distribution in the direction perpendicular to the flat plate.

Typical variations of the mean base pressure upstream of a blunt trailing edge were measured on an airfoil by Bellhouse and Lindley (1965), Maull (1966) and Lawrance and Lindley (1974) and recently on an elliptic nosed flat plate by Blake (1975). All these investigations were conducted with a tripped boundary layer for various trailing edge thicknesses. It was found that there was no noticeable variation in the mean pressure distribution in the chordwise direction at the midspan, except very close to the trailing edge.

The spanwise variation of base pressure should be accompanied by corresponding features in the spanwise structure of the near wake, and the variation is not only a function of base height but also depends on the chord and the end conditions. Bearman (1965), in his experimental investigations of an elliptic-nosed flat plate, found that the end wall effects propagated across the tunnel and he recommended the usage of end plates to reduce this influence. Nash (1963 and Blake (1975) reported uniform spanwise base pressure for a similar model. Tanner (1974) investigating various modifications of the

trailing edge profiles of an airfoil, found pronounced spanwise non-uniformities in the measured base pressure. Simmons (1975) and Prasad and Gupta (1977) reported uniform base pressure in the spanwise direction for flow past wedges and cylinders.

Blake (1975) measured uniform RMS values of the fluctuating pressures in the spanwise direction near the blunt trailing edge with his elliptic nosed flat plate model spanning the test section. Blake assumed that the uniformity of the RMS values of the fluctuating pressures over a span of 8 inches, situated about the midspan, is an indication of uniformity in the spanwise direction (i.e. two-dimensionality). Bearman (1965), measuring the vortex streamwise separation distance behind a blunt trailing edge flat plate, reported that the steadiest Lissajou figures could only be constructed when both hot wires in the wake were in the same spanwise plane. Sato and Kuriki (1961) found phase variation along the span, in the fundamental of the axial fluctuating velocity in the wake. They attributed this variation to the changes in the flat plate thickness in the spanwise direction. Ghram (1969) investigating the effect of aspect ratio based on the base height (span/base height) on the vortex street behind a thick flat plate with blunt trailing edge, found almost constant spanwise spatial correlation of the fluctuating axial velocity in the wake for the aspect ratio of 4 or less, which is similar to the work of Keefe (1961) for a circular cylinder.

Another feature of the blunt based body in the subsonic flow is the vortex shedding frequency. The vortex shedding frequency was usually reported as a Strouhal number defined as

$$St = ft/U \quad (II.2.1)$$

and the variation of the vortex shedding frequency with the Reynolds number based on the chord, for some of the investigations reported, is shown in figure II.1. Results of Bauer (1961), Nash (1963), Parker (1966), Bearman (1967), Ghram (1969) and Blake (1975) with an elliptic nose flat plate with different trailing edge thickness are shown in figure II.1. Measurements of Davis (1975) with a NACA-64A006 airfoil, Lawrance and Lindley (1974) with a "C4" airfoil, were also shown in the figure. Both airfoils were truncated at 80% of the true chord. The Strouhal number for these experimental investigations varied between 0.18 to 0.26 corresponding to a range of the Reynolds number from 1×10^5 to 1×10^6 .

Using the axial separation distance (d_f) between the two vortices at the vortex formation region as the characteristic length and using the separation velocity (U_s) as defined by Roshko (1954) as the characteristic velocity, Bearman (1961) defined a new Strouhal number as

$$St_B = \frac{fd_f}{U_s} \quad (II.2.2)$$

where $U_s = \sqrt{1 - C_{p_b}}$ $U_\infty = kU_\infty$

$$C_{p_b} = \frac{P_b - P_\infty}{\frac{1}{2} \rho U_\infty^2}$$

Bearman was able to achieve a constant Strouhal number (St_B) of 0.181 for various models, when plotted against the measured base pressure coefficient (Cp_B). Simmon (1975) supported the usage of the Strouhal number defined by Bearman but showed that the base pressures have to be corrected for the blockage effect of the wind tunnel.

Hanson (1970) and Blake (1975) found that the wake momentum thickness to be a better characteristic length than vortex separation distance for their experimental investigations.

Blake (1975) found that the correlation between fluctuating pressures measured at two points separated by a spanwise distance of r_z near the blunt trailing edge, behaved like a cosine function i.e. $A \cos (\omega_s \tau + \phi)$ where the ω_s is the radian shedding frequency. The amplitude "A" and the phase angle " ϕ " were slowly varying functions of time and the maximum correlation was produced for a time delay of $\tau = \phi / \omega_s$. Blake also showed that the phase angle could be related to the angle α of the vortex filament with the trailing edge, similar to the angle of oblique vortex shedding behind the cylinder in the low Reynolds number region. The relationship between the two angles, i.e. ϕ and α , is given as

$$\phi = (\omega_s r_z \tan \alpha / U_\infty) \quad (II.2.3)$$

Blake deduced that for a velocity (U_∞) of 100 ft/sec, with his flat plate model the angle α varied up to 17° .

From the above mentioned investigations it could be deduced that a possibility for three-dimensionality in the near wake flow of the blunt trailing edge body exists. Irregularities in both body and flow conditions may contribute to the three-dimensionality of the flow.

III INITIAL INVESTIGATIONS OF A BLUNT TRAILING EDGE AIRFOIL

The farfield acoustic directivity pattern of a blunt trailing edge airfoil with a discrete vortex wake was investigated by Davis (1975). To compliment the investigation of Davis and to extend the understanding of the trailing edge flow region, a preliminary experimental investigation of the near field of a symmetric airfoil with a blunt trailing edge was undertaken. The measurement of the near wake velocity profiles and the fluctuating surface pressures and the analysis of these near field properties formed the essential part of this investigation. Correlations of the fluctuating pressures along the chord wise direction and along the spanwise direction provide information regarding the characteristics of the fluctuating pressure field of the airfoil. The preliminary experiment data was recorded by Koutsoyannis and Davis in the NASA-Ames 25 x 35cm quiet wind tunnel. The reproducibility of the preliminary experimental data was established in the initial investigations. In the following subsections, the experimental setup and the results of the initial investigation are presented.

III.1 Airfoil Model and Experimental Setup

A symmetric airfoil, NACA 640A010, was used as the experimental model. The airfoil was constructed out of aluminum with a chord of 15.2cm, which was later truncated at 85% of the chord. The chord (c) of the truncated airfoil was 13cm, and the truncated trailing edge thickness (d) was measured to be 0.45cm. The airfoil boundary layer separated at the blunt trailing edge and generated a regular, well definable vortex street behind the airfoil.

Kulite transducers, with a sensing area of 0.33cm diameter, were chosen for the measurement of the fluctuating surface pressures. The transducers were imbedded in the upper surface of the airfoil and in the truncated trailing edge as shown in figure III.1. Transducers on the upper surface were mounted along the midspan of the airfoil. Three transducers were mounted near the leading edge of the airfoil along the midspan. The leading transducer was mounted 2cm from the leading edge of the airfoil and the other two transducers were mounted 0.4cm and 0.8cm, respectively, behind the leading transducer. A group of six transducers were imbedded about the midspan plane and 0.50cm upstream of the trailing edge as shown in the figure. To measure the fluctuating pressures in the base, five transducers were situated along the centerline of the blunt trailing edge and symmetric about the midspan with 1.24cm separation distance. A static pressure hole was situated next to the transducer, to utilize the local static pressure as the reference pressure for the measurement. All transducers with the reference static taps, were mounted such that there was negligible protrusions into the boundary layer. All transducers had linear calibration with some differences in the calibration curve slope which only affected the magnitude of the response and no changes were found in the calibration.

The initial experiment was conducted at NASA-Ames Research Center utilizing the indraft-type Acoustic Wind Tunnel (Davis 1975). The tunnel had a background noise, with a fairly flat spectrum, with a magnitude of 92dB per 1/3 octave band beyond 500 Hz, when measured at the

centerline of the tunnel test section. The flow had a variation of $\pm 0.25\%$ in the mean velocity across the test section. The RMS value of the turbulence is 0.083% of the mean velocity, measured at a velocity of 58m/s .

The output from the pressure transducers along with the velocity measurements with a single DISA-CTA hot wire were recorded on tape as shown in the data reduction system (Figure III.2). The output from the transducers was fed into NEFF amplifiers and the signal was amplified by a factor of 1000. It was found that even at this amplification, the signal was not strong enough to be recorded on the Ampex 1300A tape recorder. A 7A1A Textronix Scope Amplifier with a band-pass filter (band-width of 1 kHz to 30 kHz) was used to further amplify the signal to the level required for the tape recorder. In light of the available instrumentation, only nine pressure transducers were used in the experiment. Two data channels were further amplified per measurement position. The nine transducers utilized in the experiment were shown in Figure III.1 as solid circles.

A DISA-CTA (M-system) hotwire system with 5m cable compensator, was used to measure the near wake profile of the airfoil. The non-linear output of the hot wire was amplified by the NEFF amplifier, before being recorded on the tape. The hot wire traverse of the near wake was made at 0.6cm downstream of the trailing edge across the shear layer from the upper surface of the airfoil. The hot wire traverse consisted of five steps, of 0.136cm each, in the midspan of the model. Each wake traverse was made in one direction, and next to the lowest measuring step was the centerline of the wake.

The airfoil was mounted in the test section at geometrical zero angle of attack and spanned the tunnel cross-section along the mid plane to achieve two-dimensionality of the model. The span (2S) of the airfoil was 25cm and the aspect ratio of the airfoil based on the chord and the trailing edge thickness were 1.92 and 55.6, respectively.

The experiment was conducted at a tunnel velocity of 54m/s corresponding to the Reynolds numbers of 4.68×10^5 and 1.62×10^4 , based on the chord and the trailing edge thickness of the airfoil, respectively.

III.2 Analysis of the Measurements

The data recorded on the Ampex 1300A recorder was reproduced and fed into a SAICOR model 43A correlator. The generated correlation function was then fed into a HP9830A calculator through a digital interface. The digitized correlation curve was then scaled, plotted, and recorded on a cassette for future use. The correlation from the SIACOR 43A was fed into a SAICOR 470 Fourier Transform Analyzer to generate the frequency spectrum of the signal. The produced spectrum was then plotted on a XY-plotter.

The hot wire signals in the wake (Figure III.3) were periodic and the signal corresponding to the mid wake showed twice the frequency when compared to the signal from the upper shear layer. Signals from the leading edge pressure transducers and the transducers near the trailing edge also showed a periodic structure (Figure III.4). Both base transducer signals showed a double frequency character similar to the hot wire signal from the mid-wake. From these traces,

the vortex shedding frequency of the airfoil was deduced to be 2540 Hz and was confirmed through the correlation measurements. Thus, the vortex shedding frequency could be identified by two independent measuring techniques i.e., surface pressure transducer and the hot wire in the wake.

Fluctuating signals are usually expressed in terms of the time correlation function, defined as

$$R(\tau) = \lim_{T \rightarrow \infty} \frac{1}{T} \int_{-T/2}^{+T/2} p(t) p(t + \tau) dt \quad (\text{III.2.1})$$

and in terms of the power spectral density, defined by the following relationships,

$$\phi(\omega) = \int_{-\infty}^{\infty} R(\tau) e^{-i\omega\tau} d\tau \quad (\text{III.2.2})$$

and

$$R(\tau) = \frac{1}{2\pi} \int_{-\infty}^{\infty} \phi(\omega) e^{i\omega\tau} d\omega$$

Autocorrelations (i.e. time correlations) of the hot wire (Figure III.5) showed that the signal was a narrow band signal centered around the vortex shedding frequency or its harmonics. The autocorrelations of the base transducers and transducers near the trailing edge also have shown narrow band characteristics.

The power spectral densities of these signals were evaluated from the correlation function by the SIACOR 470 Fourier Transform Analyzer. In evaluating these spectra, the attenuation, and amplification factors

of SAICOR 470 were different for each spectrum. These factors would only affect the amplitude of the spectrum. Thus, the power spectral densities were presented to an arbitrary scale and were shown to present the spectral content only.

The hot wire signal spectrum showed narrow band signals centered on the fundamental or second harmonic of the shedding frequency depending on the hot wire position in the wake (Figure III.6 and III.7). The spectrum of the transducers near the trailing edge have the signal centered around the fundamental frequency only (Figure III.8). The base transducer spectrum showed both the fundamental and the second harmonic of the characteristic shedding frequency (Figure III.9). Transducer signals from the leading edge region (Figure III.10) showed narrow band frequency signals (i.e. 400 and 3000 Hz) that were different from the shedding frequency or its harmonics along with the harmonics of the shedding frequency. At present it can only be assumed that these different frequencies could be due to the acoustic characteristics of the tunnel.

The variation of the characteristic shedding frequency with the tunnel velocity was shown in Figure III.11. The variation was nearly linear. The Strouhal number ($St = fd/U_\infty$) variation with these velocities and Re was shown in Figure III.12. The results shown agree with the data shown in Figure III.1.

Next, correlation of the measured frequency data with different Strouhal numbers was tried. The Strouhal number defined by Bauer (1961) with the displacement thickness (δ_1) of the boundary layer,

as the characteristic length, is given as

$$St^* = \frac{fd_b}{U_s} \quad (III.2.3)$$

with

$$d_b = d + 2\delta_1$$

$$U_s = (1 - C_{p_b})^{1/4} U_\infty$$

$$C_{p_b} = \frac{P_b - P_\infty}{\frac{1}{2} \rho U_\infty^2}$$

The Reynolds number of the experiment, based on the airfoil chord at a velocity of 54m/s was

$$Re_c = \frac{Uc}{\nu} = 4.68 \times 10^5 \quad (III.2.4)$$

and the Reynolds number based on the trailing edge thickness was

$$Re_d = 1.62 \times 10^4$$

At this Reynolds number (Re_c), the displacement thickness (δ_1) of the boundary layer for laminar flow, based on the flat plate approximation is

$$\delta_1 = 1.721(Re_c)^{-1/2} c = 0.0327\text{cm} \quad (III.2.5)$$

which was about 7% of the trailing edge thickness.

With the assumption of the base pressure equal to zero, the Strouhal number leads to

$$St_{\delta_1} = \frac{fd_b}{U_\infty} \quad (III.2.6)$$

and the Strouhal number was evaluated to be,

$$St_{\delta_1} = 0.233 \quad (\text{III.2.7})$$

The mean base pressure of the above model was measured for a velocity range of 19m/s to 60m/s. The spanwise static pressure variation measured at the centerline of the base with the reference static pressure taps showed considerable variation with speed (Figure III.13). It could be seen from the figure, that the base pressure was not uniform or symmetric across the span and that the base pressure decreased with increasing tunnel velocity. This non-uniformity of the base pressure was an indicator of the three-dimensionality of the base flow.

With the measured base pressure coefficient in the midspan plane, of $C_{p_b} = -0.2$, the corresponding Strouhal number was evaluated (Eg. III.2.3) to be,

$$St^* = 0.213$$

Present data correlated well with data of Davis (1975) and of Bauer (1961) as shown in Figure III.14.

The rms values of the surface fluctuating pressure signal were of low magnitude and were listed in Table III.1. The rms values of the fluctuating pressure measured by the base transducers were within one-half dB of each other. The relative rms values of hot wire signals at various hotwire positions (hwp) compared to hwp 2 i.e., at the center line of the wake, are plotted in Figure III.15 showing the near wake profile of the fluctuating velocity.

III.3 Cross-Correlations of the Fluctuating Pressure

The fluctuating pressure signal from the base transducers had narrow band signals (Figure III.9) centered around the fundamental and the second harmonic of the shedding frequency. The rms values of these fluctuating pressures were within 1/2 dB of each other as shown in Table III.1. Although there is some data on the measured mean base pressure in the blunt trailing edge, no reported literature as to the measurement of fluctuating pressure in the blunt trailing edge, exists.

An interesting feature of the fluctuating base pressure was found in the time cross-correlation of the fluctuating pressure signal, defined at

$$R_{1,2}(\tau) = \lim_{T \rightarrow \infty} \frac{1}{T} \int_{-T/2}^{T/2} p_1(\vec{x}_1, t) p_2(\vec{x}_2, t + \tau) dt \quad (\text{III.3.1})$$

where p_1 and p_2 are the pressure signals measured at locations given by \vec{x}_1 and \vec{x}_2 respectively.

Pressure fluctuations measured by the base transducer were filtered around the fundamental vortex shedding frequency before the cross-correlation function was evaluated. From the normalized measured cross correlation function (Figure III.16) and from the characteristic of the correlation of two sinusoidal functions, the value of correlation at zero time lag ($\tau=0$) could be used to evaluate the phase difference between signals from two measuring points. Thus from Figure III.16 it could be deduced that the signals from the base transducers have a phase difference of 106° . This phase difference could be an indication

of non-uniformity or 3-dimensionality. This phase variation could have resulted from the possible waviness of the vortex sheet emanating from the trailing edge. Another possibility is oblique vortex shedding from the trailing edge similar to the oblique shedding from a cylinder at the low Reynolds number.

Utilizing arguments of Blake (1975) in evaluating the oblique vortex shedding (Sec. II.2), it was deduced, from the initial investigation data at a velocity of 54m/s, that the oblique angle was 13.3°. This angle was in fair agreement with the angle of 17°, given by Blake.

Next, the evaluation of the speed of the surface pressure fluctuations, based on the narrowness of the signal band width, could be idealized as the sum of propagating monochromatic waves, with the frequencies being harmonics of a fundamental given by

$$p(x, y, z, t) = \sum_{n=1}^{\infty} A_n \cos(\vec{k}_n \cdot \vec{r} - \omega_n t) \quad (\text{III.3.2})$$

where

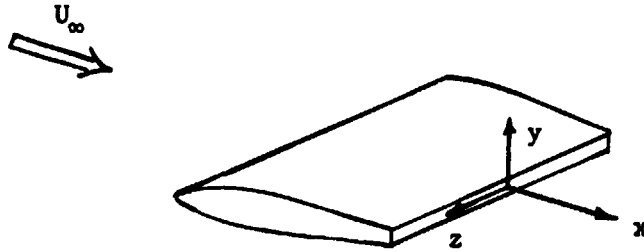
ω = fundamental radian frequency = $2\pi f$

ω_n = $n\omega$

$|k_n|$ = ω_n/a_n

a_n = phase speed of n^{th} harmonic

A_n = amplitude of n^{th} harmonic



Sketch #2

Assuming a two-dimensional wave pattern in the XZ-plane, i.e. the disturbance is constant in the Y-direction (the coordinate system was shown in the above sketch) and wave traveling obliquely in the XZ-plane has the wave number vector

$$\vec{k}_n = (k_{x,n}, 0, k_{z,n}) \quad (\text{III.3.3})$$

Let the angle between the wave number vector and the Z-axis (measured positive in the counterclockwise direction) be θ , then

$$p(x, z, t) = \sum_{n=1}^{\infty} A_n \cos\{k_{x,n} x + k_{z,n} z - n\omega_1 t\} \quad (\text{III.3.4})$$

where

$$k_{x,n} = k_n \sin\theta$$

$$|k_{z,n}| = k_n \cos\theta$$

$$|k_n| = n\omega_1 / a_n$$

with

$$\phi_n = k_{x,n} x + k_{z,n} z \quad (\text{III.3.5})$$

The first harmonic felt by a transducer was

$$p_{1,1} = A_1 \cos(\omega_1 t - \phi_{1,1}) \quad (\text{III.3.6})$$

where the second subscript '1' represents a transducer number.

Similarly the response of transducer 2 was given by

$$p_{1,2} = B_1 \cos(\omega_1 t - \phi_{1,2}) \quad (\text{III.3.7})$$

and the phase angle by

$$\phi_{1,1} = k_{x,1} x_1 + k_{z,1} z_1$$

$$\phi_{1,2} = k_{x,1} x_2 + k_{z,1} z_2 \quad (\text{III.3.8})$$

The space-time correlation function between transducer 1 and 2 is given by

$$R_{21}(\tau) = \frac{A_1 B_1}{2} \cos(\omega_1 \tau + (\phi_{1,2} - \phi_{1,1})) \quad (\text{III.3.9})$$

where subscript 2 1 on R means that the signal at the transducer 1 was delayed with respect to the signal at transducer 2 in the evaluation

of the correlation. Now normalizing the equation (III.2.17) with rms values of $p_{1,1}$ and $p_{2,2}$ given by

$$\frac{A_1 B_1}{2} = [R_{11}(0) R_{22}(0)]^{\frac{1}{2}} \quad (\text{III.3.10})$$

yields

$$\begin{aligned} \rho_{2,1}(\tau) &= \frac{R_{21}(\tau)}{[R_{11}(0) R_{22}(0)]^{\frac{1}{2}}} \\ &= \cos[\omega_1 \tau + (\phi_{1,2} - \phi_{1,1})] \end{aligned} \quad (\text{III.3.11})$$

Now with $\tau = 0$

$$\begin{aligned} \phi_{1,2} - \phi_{1,1} &= k_{x,1}(x_2 - x_1) + k_{z,1}(z_2 - z_1) \\ &= \cos^{-1}[\rho_{2,1}(0)] \end{aligned} \quad (\text{III.3.12})$$

using equation III.2.13, yields

$$\begin{aligned} \phi_{1,2} - \phi_{1,1} &= \left(\frac{\omega_1}{a}\right) \cos[\theta(x_2 - x_1)] \\ &\quad - \left(\frac{\omega_1}{a}\right) \sin[\theta(z_2 - z_1)] \end{aligned} \quad (\text{III.3.13})$$

Using space-time cross-correlations between any three transducers, the values of the phase speed and oblique angle could be solved. As an

example, using transducers 4, 5, and 8 (Figure III.1) the correlations yield,

$$\rho_{5,4}(0) = 0.943458 \rightarrow \cos^{-1}[\rho_{5,4}(0)] = 0.33899 \text{ Rad}$$

$$\rho_{8,4}(0) = 0.923081 \rightarrow \cos^{-1}[\rho_{8,4}(0)] = 0.3948 \text{ Rad}$$

and let

$$g = \frac{\cos^{-1}[\rho_{5,4}(0)]}{\cos^{-1}[\rho_{8,4}(0)]} \quad (\text{III.3.14})$$

with

$$\xi_2 = x_8 - x_4 \quad \zeta_2 = z_8 - z_4$$

$$\xi_1 = x_5 - x_4 \quad \zeta_1 = z_5 - z_4$$

then,

$$\theta_{4,5,8} = \tan^{-1} \left[\frac{g\xi_2 - \xi_1}{\zeta_1 - g\zeta_2} \right] = 10.418 \text{ deg} \quad (\text{III.3.15})$$

and phase speed was

$$a_{4,5,8} = -257 \text{ m/s} \quad (\text{III.3.16})$$

Using surface transducers near the trailing edge, Table III.2 was constructed. There was no correlation of the phase angles and phase speed of the fluctuations, except that it could be concluded that the waves were traveling upstream towards the leading edge. It could only be assumed that the simple representation of the oblique plane wave was not an adequate representation.

IV EXPERIMENTAL SETUP FOR SUBSEQUENT INVESTIGATIONS

With the results of the initial investigations in view, and to achieve further understanding of the base flow of the blunt trailing edge airfoil, experiments were conducted in a 45.7 x 45.7cm subsonic wind tunnel. In this section, the wind tunnel characteristics, the models used in experimentation along with the experimental setup and the instrumentation, are discussed.

IV.1 The 45.7 x 45.7cm Subsonic Wind Tunnel

The low speed wind tunnel of the Aeronautics and Astronautics Department, Stanford University, is a closed circuit wind tunnel. The closed test section that is vented to the atmosphere just downstream of the test section. A plan view of the tunnel is shown in Figure IV.1. Basic characteristics were investigated by Smith, Varzally and Baganoff, and were discussed in an unpublished report. Some of the general characteristics could be found in Smith and Karamcheti (1978) and Varzally and Karamcheti (1978). Some features of the wind tunnel are described below.

The wind tunnel is powered by a constant rpm variable pitch fan. The 16 bladed fan, 114cm diameter, is driven by 20hp motor and generates a nominal flow rate of 8.495×10^5 liter/minute at 1150 rpm. The speed of the airflow in the tunnel is controlled through the variation of the pitch of the fan blade. The pitch of the blades is varied through a linkage mechanism that is activated remotely by the control system located on the side wall of the room.

The air from the fan passes through two sets of right angle corner vanes and the flow is expanded slightly through an upstream diffuser before reaching the contraction section. There are four wire mesh screens in the settling chamber just upstream of the contraction section, and there are two more screens in the diffuser section to reduce the non-uniformity of the incoming flow.

The test section has a cross section of 45.72 x 45.72cm and is 90.12cm long. The test section consists of top and bottom walls made of 1.24cm thick aluminum plates and side walls made of 2.54 cm thick plexiglass. Side walls are used as viewing areas and special windows can be mounted within the side wall boundaries to facilitate flow visualization experiments. The model could be attached to any of the four walls. The test section has a slot [64.7cm long, 1.11cm wide] in the top wall of the tunnel along the mid-plane of the test section, starting 21cm from the beginning of the test section. This slot provides access to the tunnel test section for a measuring probe along the mid-plane. There are two cut-outs in the bottom of the test section that can be fitted with a slotted plate. The cut-outs are 12.7cm x 38cm in size and start at 39.7cm and 62.8cm measured from the beginning of the test section. These cut-outs fitted with the slotted plate provide access into the tunnel for cross plane measurements. The velocity of the inflow to the test section was measured by a reference pitot tube situated 10.2cm from the beginning of the test section, 7.6cm from the top of the test section, and 16cm from the front side wall.

A ventilation window (gap), consisting of 1cm gap between the end of the test section and downstream diffuser, provides for the recovery of pressure and causes the static pressure in the test section to be maintained close to the atmospheric pressure. The air then passes through the downstream diffuser and two sets of right angle corner vanes.

Calibration and flow characteristics of the wind tunnel will be given later.

IV.2 Models and the Experimental Setup

As mentioned before, a NACA 64A010 symmetric airfoil profile was chosen for the experimental investigations. The airfoil profile and its flow characteristics were described by Abbott et. al. (1959). The airfoil was made from an aluminum block with a chord (c) of 15.2cm and span (2S) of 25cm. As described before, the airfoil was truncated at 85% of the chord resulting in a truncated trailing edge airfoil of chord equal to 13cm and the thickness (d) of the blunted trailing edge equal to 0.45cm.

The construction of the airfoil with pressure transducers (Airfoil I) was described in Section III.2. To investigate the static pressure variation in both chordwise and spanwise directions, another blunt trailing edge airfoil was manufactured and was instrumented with static pressure taps. This blunt trailing edge airfoil will be referred to as AIRFOIL II, in the rest of the report.

Before investigating the blunt trailing edge airfoil, it is necessary to measure the flow field of a corresponding smooth trailing edge

airfoil. For this purpose, the trailing edge (i.e. the trailing edge piece that was cut off) was reattached to the airfoil. This recombined or reattached airfoil with a smooth trailing edge and a chord of 15.2cm will be referred to as AIRFOIL III, for the rest of the report.

To measure the static pressure variation over the airfoil surface, the airfoil was instrumented with static pressure taps on the upper surface in a matrix consisting of 7 rows and 13 columns used to position these static holes. The position of these holes were shown in Figure IV.2. As shown, row 1 was 1.27cm downstream from the leading edge, and row 2 was 1.0cm downstream of row 2. There were five columns placed at 1cm apart, and symmetric about the midspan. The placement of other columns was shown in Figure I.3a. These holes were numbered by a combination of row numbers and column numbers with the midspan column being numbered zero.

The static pressure taps were fabricated in the following way. A hole of 0.025cm diameter was drilled into the wall of a 0.076cm I.D., drawn (Type 327) steel tube. The hole was situated about 0.1cm from the end of the tube, and the tube end was blocked with RTV plastic glue to avoid any seepage of epoxy into the tube when imbedded into the surface. Grooves, to hold the tube, were milled into the surface. The tube was held in the position with the static hole perpendicular to the local surface and epoxy bonding material was used to cement the tubes into the surface of the airfoil. The open end of the tube was fed through the side of the airfoil. When the epoxy hardened, the static holes were honed and blown clean of surface dirt.

Airfoil III was examined for the smoothness of surface and variation from the basic NACA 64A010 airfoil profile. It was found that the airfoil surface was smooth and the profile was within acceptable error.

To measure the static pressure variation in the base of the blunted trailing edge airfoil, 17 static pressure taps were distributed along the midplane of the base (Figure IV.3b). All holes were in midplane. Only one of the seventeen holes could not be used as the tube was broken close to the surface and could not be repaired. The airfoil surface was cleaned and all the static holes were found to be clean and free of any blockage.

Experiments were conducted with untripped and tripped boundary layers over the airfoil. For the latter case, boundary layer trips were employed on both sides of the airfoil. The boundary layer trip was made of a drill rod of 0.076cm in diameter, and was centered in a groove of 0.03cm diameter on the surface of the airfoil. The trip was situated at 3.4cm downstream of the leading edge of the airfoil (see Figure IV.2). These positions correspond to x/c of 0.225 and 0.22 for the blunt trailing edge airfoil (Airfoil II) and for the smooth edge airfoil (Airfoil III) respectively when referred to their respective chords.

To compare the vortex shedding frequency of the airfoil, with the vortex shedding frequency of a bluff body, a stainless steel (drill rod) circular cylinder, with a diameter (0.45 cm) equal to the thickness of the blunt trailing edge of the airfoil, was used. As the cylinder diameter was small, the cylinder was not instrumented with static pressure taps to measure the base pressure.

As the tunnel at Stanford University has a square cross section with a side of 45.7cm, a pair of side (end) plates were used to mount the airfoil model that was constructed for the Ames 25 x 35cm quiet wind tunnel. The end plates were designed to achieve two-dimensionality of the model, such that the flow exterior to the end plates did not influence the flow between the plates and that there was no flow separation on the end plates.

A pair of end plates 45 x 53cm and 0.95cm thick were made out of plexiglass and the positioning of these end plates in the tunnel was shown in Figure V.1. The leading edge of the plate was made to be the cross section of a wedge with an apex angle of 20° and a height of 4cm. The sharp leading edge was rounded to avoid any leading edge separation. The end plates were chamfered on the exterior side of the plate at the trailing to generate a sharp trailing edge. The end plates were attached to a hollow circular cylinder of 14.6cm diameter, 9.4cm long with 1.27cm thick walls. These cylinder supports were then attached to the side walls. Four small solid plexiglass cylinder stiffeners of 1.9cm diameter were used to dampen the vibrations of the end plate at high speeds.

A slot was cut in the end plates at the mid plane to facilitate passing of the static pressure tubes of the airfoil model. The leading edge of the end plates was 20cm (or 1.5 chords) upstream of the leading edge of the airfoil. The end plate trailing edge must be at least 2 diameter or 29cm measured from the

center of the support cylinders to eliminate the contamination due to the shedding from these cylinders, as recommended by Cowdrey (1926). This was easily achieved because the cylinder diameter was almost equal to the chord of the airfoil. Also, the trailing edge of the end plate was designed to be at 30cm (2.4 chords) downstream of the maximum thickness of the airfoil, which coincided with the center of the support cylinder. A preliminary test for flow separation on the end walls was conducted with the help of tufts. These tests showed that there was no flow separation over either of the end plates was independent of the flow exterior to the end plates.

As the model and its support create blockage to the through flow, its effect in terms of a blockage factor need to be investigated. A list of references on a closed test section blockage factor is included in the bibliography. The effect, if any, of the breather gap on the blockage factor was not considered. In the calibration of velocity profiles, the profiles were normalized with centerline velocity, thus in presenting these profiles, the blockage factor was not used.

The instrumentation used in the experimentation with the data acquisition and the reduction system (also see Figure III.2) will now be described.

IV.3 Instrumentation

In this section a brief description of the instrumentation used along with accuracy estimation of the data will be given.

Measuring probes, the hotwire and the microphone are traversed in the test section with the help of appropriate mechanisms located at

the top and at the bottom of the test section. The traversing mechanism at the top was constrained to travel along the midplane in the axial direction with a travel of 45cm, and had a free travel of 30cm in the vertical direction. The traverse of the probe from the top, was restricted to 7.7cm from the top and 7.2cm from the bottom of the test section. The traversing mechanism at the bottom was free to travel in 3 directions i.e. axial, vertical and horizontal. Due to the geometry of the slots in the bottom plate, the horizontal plane (i.e. crossplane) movement was constrained to 6cm from either of the sidewalls and the axial movement could only be made in steps of 1cm each with the vertical traverse limited to 16cm. It was felt that these traverses provided sufficient freedom of travel for present investigations. All traversing mechanisms consisted of a sliding block for long and coarse movements and a vernier for short and fine movements when the sliding block was locked. With the probe moving only in one direction for each traverse to minimize the backlash error and with the vernier traverse, the probe movements could be repeated with an accuracy of $\pm 0.01\text{mm}$.

IV. 3.1 Manometer Board and Thermocouple

Static pressure measurements in the tunnel and on the model were achieved with the help of a bank of manometers, using red gauge oil ($\text{sp} = 0.834$) as the manometer fluid. All the manometer readings were made with atmospheric pressure as the reference pressure. A graduated graph sheet scaled in centimeter divisions was used to measure the pressure rise or fall in the bank. Due to the length of tubing connecting the manometer bank and the pressure taps in the model, the bank of monometers had a large integration time to achieve an equilibrium position.

As described in Sec IV.1, the dynamic head $\frac{1}{2} \rho U^2$ of the tunnel was measured using a 0.32cm pitot-static tube. As the local pressure in the test section is close to atmospheric pressure, the density was calculated by the relation

$$\rho [\text{kg/m}^3] = \frac{P_a [\text{mm.Hg}]}{2.158619(T_s^\circ [\text{C}] + 273.15^\circ)} \quad (\text{IV.3.1})$$

where

P_a = atmospheric pressure measured by a barometer in mm Hg.

T_s = local static temperature (as deduced by Eq. IV.3.4)

with the use of Bernoulli's equation, the reference velocity measured by the Pitot tube with the bank of manometers ($sp = .834$) was evaluated by

$$V [\text{m/s}] = 18.781456 \left[\frac{(T_s^\circ [\text{C}] + 273.15) (\Delta p [\text{cm.oil}])}{P_a [\text{mm.Hg}]} \right]^{\frac{1}{2}} \quad (\text{IV.3.2})$$

and the Mach number was calculated by

$$M = 0.9269669 \left[\frac{\Delta p [\text{cm.oil}]}{P_a [\text{mm.Hg}]} \right]^{\frac{1}{2}} \quad (\text{IV.3.3})$$

An iron-constantin thermocouple imbedded in the tip of the pitot tube was used to measure the stagnation temperature of the tunnel air

stream. Using a recovery factor of 0.86 for parallel flow past the temperature measuring probe, the static temperature of the air flow could be evaluated by,

$$\left\{ \frac{T_t^{\circ} [c] - 41.16724 \Delta p [cmo11]}{\rho_{\infty} [mmHg]} \right\} \quad (IV.3.4)$$

$$T_s^{\circ} [c] = \frac{\left\{ 1 + 0.150713 \frac{\Delta p [cmo11]}{\rho_{\infty} [mmHg]} \right\}}{\left\{ 1 + 0.150713 \frac{\Delta p [cmo11]}{\rho_{\infty} [mmHg]} \right\}}$$

The variation of the stagnation temperature was measured with a voltmeter and was noted down with each reading.

With the reference pitot tube aligned carefully with flow direction, error in measuring the dynamic head was about $\pm 1\%$. Evaluation of static temperature may involve an error of $\pm 1\%$. Thus it was estimated that the reference velocity measured was within $\pm 1\%$ of error. The readings of model static pressure were estimated to be within $\pm 2\%$.

IV.3.2 Hotwire Anemometer System

The velocity measurements, both mean and fluctuating, were made with DISA-CTA (M-system) hotwire anemometer. Two single hotwire channels each with a 5m compensation circuit and a linearizer, were used. All measurements were made with a single hotwire probe, consisting of a regular and a boundary layer type probe.

In all measurements, the hot wire measuring element was held parallel to the trailing edge of the model and in the horizontal plane. The hot wire measured the instantaneous magnitude of the velocity vector in a plane perpendicular to the hot wire axis. The time averaged value of the magnitude will be referred to as the mean velocity. The variation of the instantaneous magnitude from the measured mean value will be referred to as the fluctuating quantity or fluctuating velocity. Velocities in other directions could only be satisfactorily resolved with a cross wire, and were not measured in the present investigations.

Even though the static temperature variation (which will be described later) in the tunnel affects the hot wire anemometer measurements, no temperature compensating circuits were used because these circuits were not available with these channels. Analytic temperature corrections to the hot wire data were described by Kristenson (1974) and Bearman (1969), and it was found that the corrections given by Kristensen were easy to apply and were utilized. The linearized output was fed to a D. C. voltmeter for measurement of the mean value and to a RMS meter for the measurement of the intensity of fluctuation of velocity.

Both the hot wire anemometers were calibrated in the tunnel flow with reference velocity measured by the pitot tube. The calibration and the setup of the linearizer were periodically checked and found not to change during the course of the experiment.

As the hot wire anemometer was calibrated with reference to the Pitot tubes measurement error was estimated to be within 2%. As velocity measurements were normalized with measurements in uniform flow velocity, the velocity profiles were not significantly affected by any error. In the measurement of fluctuating velocities, the source of error was implicit in the hot wire velocity measuring technique and depended on the ratio of the rms of the velocity fluctuations to the measured mean velocity value.

IV.3.3 Measurements of Correlation and Spectra

The fluctuating and periodic flow quantities were best represented in the form of correlations and frequency spectra. To achieve this, a ASICOR 43A correlator and the coupled instrument SAICOR 470 Fourier Transform Analyzer were used. SAICOR 43A correlator generated a 400 point analysis with time delays from 2 μ sec to 1 sec. In present investigations, a time delay of 0.2msec was used. The output of the correlator could be plotted on a XY-plotter so that it could be further studied at a later time.

The output from the correlator was fed into a Fourier transform analyzer for generating a spectrum. Corresponding to a 0.2 msec time delay on the correlator, the frequency range of the spectrum was 0-5kHz. A marker generated by the analyzer, displayed on a scope, was used to read the frequency measurement corresponding to any point on the spectrum. The marker measurement displayed on the analyzer had a \pm 5Hz error corresponding to the time

delay of 0.2m sec. Amplitudes corresponding to the frequency displayed by the marker, were read on a voltmeter. The frequency spectra was displayed to an arbitrary scale with a value of one or zero at maximum magnitude corresponding to a linear or log scale, respectively.

IV.3.4 Microphone Measurements

A 1.25cm microphone, situated outside the tunnel test section, near the ventilation gap, was used to measure the far field radiated acoustic pressure. A 0.635cm microphone with nose cone attached, was utilized to measure the directivity pattern of the pressure field near the trailing edge. Similarly a 0.32cm microphone with nose cone was used for the acoustic calibration of the tunnel. Both the 635cm and 0.32 cm microphones were mounted in the top traversing mechanism and were restricted to measurements in the midplane. All microphone measurements were made with a B&K Audio Spectrum (1/3 octave) Analyzer and strip chart recorder. The cross-correlations between the microphone and hot wire were made using the SAICOR instruments and when the cross-correlation were evaluated, the microphone data was fed from the B&K spectrum analyzer set at linear output. All microphones were calibrated with a piston phone before and after the measurements and the calibrations were found to remain unchanged.

IV.4 Calibration of the 45.7 x 45.7cm Wind Tunnel

Calibrations presented in this section supplement the work presented in the report of Smith et. al. The features investigated

were the velocity profiles, acoustics of the tunnel, and finally the temperature variation in the test section.

IV.4.1 Calibration of the Tunnel with an Empty Test Section

The dynamic head of the tunnel as mentioned was measured using the reference Pitot tube. The atmospheric pressure and the tunnel room temperature was measured with a barometer and thermometer respectively.

IV.4.1.1 Velocity Profiles

The velocity range of the tunnel with an empty test section is 19m/s to 64m/s corresponding to a Mach number range of 0.055 to 0.188, and thus the flow may be regarded as incompressible.

The calibration of the tunnel was made at flow speeds of 19, 32, 47.6 and 64.14m/s. Velocity profiles at two representative velocities of 32m/s and 48m/s and at axial distances of 16.2, 36.2, and 46.0cm from the start of the test section were shown in Figures IV.5 and IV.6 corresponding to vertical and horizontal planes respectively. The mean velocity profiles were normalized with velocity measured at the center of the vertical traverse. The profiles of RMS values of the fluctuating velocity (turbulence intensity) were normalized with the local mean velocity. Vertical axis in both profiles were normalized with tunnel half-width.

The mean velocity profile could be seen to have uniformity in both the vertical and horizontal plane. The fluctuating velocity level was below 0.7% of the local mean velocity. The turbulence level could be seen to be fairly uniform across the cross-section. Typical turbulence spectra measured by the hot wire at two different

mean velocities of 32 and 48m/s are shown in Figure IV.7. Both spectra, plotted on a log-linear scale, show band-limited white noise between 0 to 50kHz. The turbulence intensity increased with increasing speed. The spectra did not exhibit any peaks that could mask measurements at any particular frequency.

Characteristics of the wall boundary layer at 38cm from the start of the test section at 20 and 60m/s were measured by Smith et. al.. They showed that the shape of the boundary layer profiles indicated a fully developed turbulent flow.

When the calibration for the maximum possible velocity of 64.2m/s was attempted, the measured dynamic head varied about 8% of the measured maximum dynamic head, showing that the maximum possible velocity could not be maintained for any reasonable period of time. This variation could have been caused due to flow separation in the fan flow or due to the constant rise in the tunnel temperature. The calibration at 60m/s showed a variation of 2% of the maximum measured dynamic head at this speed. Finally, the maximum velocity with no apparent dynamic head variation was found to be 55m/s and this should be considered as the maximum practical velocity of the tunnel.

IV.4.1.2 Acoustic Features

Acoustic characteristics of the empty wind tunnel are important as background information. The acoustic measurements were made with a 0.32cm (1/8") microphone with a preamplifier and nose cone at the center of the test section. A B&K audio (1/3 octave) frequency

analyzer with a recorder was used to record the level of the spectra in terms of dB referred to $20 \times 10^{-5} \text{ N/m}^2$ and frequency in Hz.

The tunnel room could, at best, be described as semi-reverberant from an acoustical point of view. When the tunnel was running, the metal structure of the wind tunnel generated low frequency "rumble". The outside acoustic level in the tunnel room varied during the day due to external noise.

A dominant frequency that might occur in the background noise would be the blade passing frequency of the fan. With 16 blades at a constant speed of 1150 rpm, the blade passing frequency of the fan was 307Hz. Depending upon the speed of the tunnel flow, higher harmonics of the blade passing frequency could become predominant. A list of the first ten harmonics were given in Table IV.

Typical 1/3 octave band spectra measured in the test section, with no flow and at a velocity of 24m/s were shown in Figure IV. The background noise in the tunnel with no flow was considerably lower than the level with flow. The blade passing frequencies could not be easily identified as the noise level was averaged over a third of the octave band.

The resonance frequencies of the wind tunnel could play a role in aeroacoustic measurements in the tunnel due to possible coupling between these natural frequencies and acoustic phenomena under investigation. These natural frequencies could be described in terms of acoustic pressure wave patterns (duct modes). The wave patterns could be viewed as standing waves in the cross-sectional

plane and the wave patterns could be traveling in the axial direction. As a first approximation, viewing the tunnel as a long duct of rectangular cross-section, the duct mode pattern was given by

$$p_{m,n} = \psi_{m,n}(Y,Z) \exp\{i(k_x x - \omega t)\} \quad (\text{IV.4.1})$$

with

m,n - mode number in the YZ-plane

$$\left(\frac{\omega}{a_o}\right)^2 = k_x^2 + k_y^2 + k_z^2, \text{ with } a_o \text{ being ambient speed of sound.}$$

The frequency of the wave pattern in the cross-sectional plane of the tunnel could be evaluated by

$$f_{m,n} = \frac{a_o}{2} \left[\frac{m^2 \pi^2}{L_y^2} + \frac{n^2 \pi^2}{L_z^2} \right]^{1/2} \quad (\text{IV.4.2})$$

The duct modes for the empty test section were shown in Table IV.2. The tunnel modes were calculated for no-flow condition, and the effect of the through flow could be introduced through a multiplying factor $(1 - M_\infty^2)^{1/2}$.

IV.4.1.3 Temperature Variation

In a closed circuit wind tunnel, some of the energy supplied by the fan blades to airflow, emerged as an increase of heat energy and resulted in the increase of static temperature of the air stream. Because no cooling mechanism was available with this tunnel, and because the tunnel room was small, there was not sufficient heat transfer to balance the heat increase, therefore the airstream temperature continued to rise.

To measure and document the rise in tunnel temperature, a Chromell-Alumell thermocouple with a shroud that was designed to reduce the viscosity correction to the thermocouple reading to a value below 0.1°C , was used. The thermocouple in the shroud was mounted 10.0cm from the beginning of the test section, 6cm from the side wall, and 2.3cm from the bottom of the test section. Typical variations of the static temperature with time during the calibration process were reproduced in Figure IV. 9. The typical initial temperature varied from 20°C to 30°C during these tunnel runs of 45 to 90 minutes.

At the minimum tunnel speed (i.e. 19m/s), the temperature rise was negligible. But at higher speeds the temperature rise was considerable and during the complete calibration process, an equilibrium temperature could never be achieved. A list of typical static temperatures in the tunnel are given in Table IV.3.

It was found that opening the tunnel room doors dampened the rise in tunnel temperature. Thus it was recommended to keep the tunnel room doors open when the tunnel was running. It was also discovered that running the tunnel intermittently, i.e. with run-time of an hour coupled with a rest time of 1/2 hour, would also keep the rise in the tunnel temperature within a reasonable level.

As the temperature variation is a problem with the present setup of the tunnel, it was recommended that hotwire measurements should be corrected for the temperature rise or a temperature compensating circuit be used. In the results of the present investigation, as temperature

compensation circuits were not available, (see Section IV. 3.2) analytic corrections to the hotwire data were applied.

The next section describes the calibration of the tunnel with side plates that were used to mount the model.

IV. 4.2 Calibration with End Plates in the Test Section

As described in Section IV. 2, a pair of end plates were utilized to achieve two-dimensionality of the model. With the experimental set-up shown in Figure IV. 4, the two-dimensionality of the incoming flow needs to be confirmed.

IV. 4.2.1 Velocity Profiles

As described in Section IV. 2, there was no separation on the end plates and the boundary layer measurements on the end plates confirmed that there was no separation of the flow.

To measure the two-dimensionality of the flow between the side plates, hotwire traverses in both vertical and horizontal plane were made. Two representative locations of 3cm and 45cm from the leading edge of the end plate were used for vertical traverses. Due to the limited accessibility into the tunnel, axial distances of 24cm and 48cm from the leading edge of the end plate were used for horizontal traverses. These traverses were normalized by the local centerline velocity and were presented in Figures IV.10 and IV.11 for two different speeds of 24m/s and 48m/s. The arrow marks on the vertical scale of Figure IV.11 mark the position of side plates. As it can be seen from these figures, the mean velocity profile was uniform across

the test area and the turbulence intensities were also fairly uniform across the test area. These confirm the uniformity of the incoming velocity field. It should also be noted that these turbulence intensities were lower than comparable intensities in the test section with no end plates.

IV.4.2.2 Acoustic Features

As the end plates reduce the cross-sectional area of the test section, different cross modes could dominate the acoustic field of the tunnel. These modes in the cross sectional area of 25 x 45cm were shown in Table IV.4. As before, these modes need to be corrected for the through flow effect.

The spectral output measured by a 0.32cm microphone, in the test section with end plates was shown in Figure IV.12 for a representative velocity of 24m/s. This 1/3 octave band spectra, of the microphone, does not show any difference from the spectra without end plates, (Figure IV.8(b)).

Temperature variation in the tunnel was similar with or without the side plates in the test section.

V RESULTS OF THE SUBSEQUENT INVESTIGATIONS

The initial experimental investigations as described previously of the flow around a blunt trailing edge airfoil, indicated the possibility of three-dimensionality in the near wake. To achieve further understanding of the near flow field, subsequent experimental investigations of a symmetric airfoil (NACA 64A010) with a smooth trailing edge and with a blunt trailing edge were undertaken. These experimental investigations were conducted in the Stanford 45.7 x 45.7cm wind tunnel. A smooth trailing edge airfoil with static pressure taps (Airfoil III Sec. IV.2), a blunt trailing edge airfoil also with static pressure taps (Airfoil II, Sec. IV.2) and a blunt trailing edge airfoil with unsteady pressure transducers (Airfoil I, Sec. III.1), were utilized as experimental models. In this chapter, the results of these experimental investigations will be discussed.

V.1 Smooth Trailing Edge Airfoil Model

The construction of the airfoil with 15.2cm chord and 25cm span was described in Sec. IV.2. All static pressure taps in the upper surface were found to be free of any blockage. Measurements with the smooth trailing edge airfoil (Airfoil III) were first made without the boundary layer trip and were later repeated with the boundary layer trip on both surfaces.

Airfoil III was mounted between two end plates (Figure V.1) at a geometrical zero angle of attack as shown schematically in Figure IV.4. The positioning of the airfoil in the tunnel with the end plates and the coordinates system were shown in Figure IV.4.

Measurements with the smooth trailing edge airfoil were conducted at a speed of 24m/s corresponding to a Reynolds number based on the chord (Re_c) of 2.6×10^5 and were repeated at a speed of 45m/s corresponding to Re_c of 4.8×10^5 .

To establish the two-dimensionality of the incoming flow, with the model in place, velocity measurement at 6cm upstream of the airfoil leading edge, were conducted. The position corresponds to axial distance of 32.6cm from the beginning of the test section. The typical velocity profiles in both the vertical and spanwise directions are shown in Figure V.2 at a representative velocity of 26m/s. As it could be seen from the figure, the mean velocity profile was uniform in both vertical and spanwise directions, except very close to the side plates. Similarly, the rms values of the fluctuating velocity were also uniform in both directions. These measurements are in fair agreement with measurements of flow with end plates only. This confirmed the two dimensional character of the incoming flow.

V.1.1 Measurements of the Static Pressure

Static pressure distributions on the surface of Airfoil III were measured at two different speeds with and without a boundary layer trip. Figure V.3 shows the chordwise variation of the static pressure for both configurations at speeds of 24 and 45m/s. The static pressure p_s is shown in terms of the pressure coefficient defined by

$$C_p = \frac{p_s - p_\infty}{\frac{1}{2} \rho_\infty U_\infty^2}$$

where p_s = local static pressure

and $\rho_\infty U_\infty$ and p_∞ refer to free stream conditions

The crosses correspond to the data for the configuration without the boundary layer trip and the circled crosses correspond to the data for the configuration with the boundary layer trip. Only measurements behind the maximum thickness of the airfoil were shown with the boundary layer trip configuration because the boundary layer trip was situated at $x/c = 0.22$. In both figures, the variation of static pressure coefficient and the magnitudes were in agreement. Before comparing this data with the theoretical data based on the source-sink representation of the airfoil in a uniform and unbounded fluid, the measured data needs to be corrected for the tunnel blockage.

The presence of the model and its supporting system produces blockage to the through flow. The blockage factor is usually defined as the ratio of the increased velocity felt by the model to the reference flow velocity. The blockage factor relates the dynamic head (q_2) in the bounded flow of the tunnel to the dynamic head (q_1) for the unbounded flow (see sketch below).



The relationship is given by

$$q_1^2 = (1 + \epsilon_B)^2 q_2^2 \approx (1 + 2\epsilon_B) q_2^2 \quad (V.1.1)$$

where

$$q_1^2 = \frac{1}{2} \rho u_1^2$$

$$q_2^2 = \frac{1}{2} \rho u_2^2$$

$$u_1 = (1 + \epsilon_B) u_2$$

ϵ_B = blockage factor

The blockage factor was evaluated either by geometrical area considerations or by the measured static pressure variations in the uniform flow above the model. With the geometrical dimensions (Pope and Harper, 1952) of the model support structure, the blockage factor was found to be about 7%. Using the measured static pressure value, one chord distance above the airfoil model, the blockage factor could also be evaluated as

$$\epsilon_B = (1 - C_{p_L})^{\frac{1}{2}} - 1 \quad (V.1.2)$$

where C_{p_L} was the static pressure coefficient in the flow above the model.

The measured model static pressure coefficient can be corrected for the blockage factor, (Gerner et. al., 1966) as

$$C_{p_C} = C_{p_m} + \left[2 - (2 - M^2) C_{p_m} \right] \epsilon_B \quad (V.1.3)$$

where

C_{p_m} = measured static pressure coefficient

C_{p_C} = corrected static pressure coefficient

M = tunnel mach number

As the maximum Mach number in the experiments was equal to 0.113 the M^2 terms, in the above equation, can be neglected. Hence,

$$Cp_c = Cp_m + (2 - 2Cp_m)\epsilon_B \quad (V.1.4)$$

The corrected value of the static pressure for the speeds of 24 and 45m/s along with the theoretical pressure distribution (the chain line) from Abbott (1959) was shown in Figure V.4. The data shown as crosses were for the configuration without the boundary layer trip and the circled crosses were for the tripped boundary layer configuration of the airfoil. The differences could be traced to the possible errors in the measurement of the reference pressure because the reference pitot tube is only at a distance of one-half of the tunnel height from the model. As it could be seen, there was fair agreement between the theoretical distribution and measured pressure coefficient in the chordwise direction.

The uniformity of the static pressure across the span is an indicator of uniformity of the velocity along the span. The static pressure coefficient across the span is shown in Figure V.5 for speeds of 24m/s and 45m/s. The dashed lines were for the configuration without the boundary layer trip and the chain lines were for the tripped boundary layer configuration and these pressure coefficients were corrected for the blockage factor. As shown in both figures, the static pressure coefficient was fairly uniform across the span, except close to the end walls. This verifies that the flow over the airfoil was uniform except very close to the end plates.

V.1.2 Boundary Layer and Wake Velocity Profiles

Measurements of the near flow field of the airfoil consisted of the velocity profiles of the boundary layer and the wake. Since movement of the probe is restricted to the midspan plane, measurements of the boundary layer and wake were made in the ~~midspan~~ plane only.

The boundary layer velocity measurements were made behind the maximum thickness of the airfoil and at x/c of 0.55, 0.68, 0.82, 0.85 and 0.99, measured from the leading edge. The first three measuring locations correspond as described in Sec. IV.2, to 5, 6, and 7 of the static pressure tap rows and the location $x/c = 0.85$ corresponds to the location of the trailing edge when the airfoil is blunted. For both configurations of the airfoil with and without the boundary layer trip, and at a tunnel velocity of 45m/s, the boundary layer profile is shown in Figure V.6. The dash line corresponds to the untripped boundary layer configuration and the chain line corresponds to the tripped boundary layer configuration. It could be concluded from these profiles that there was no separation of flow over the surface of the airfoil.

Figure V.7 shows the comparison of the boundary layer profiles at $x/c = 0.82$ and at different speeds. The dash line was the boundary layer profile for the configuration without the boundary layer trip at a speed of 45m/s. The solid line was the boundary layer profile taken from NACA TN 2235, which was measured at 80°C and at 58m/s corresponding to a Re_c of 4.1×10^6 on a NACA 64A010 airfoil. The third profile shown was for the configuration without the boundary layer trip at a velocity of 24m/s. As it could be seen, the boundary layer profiles of these untripped boundary layer configurations show fair agreement.

The wake profiles behind the airfoil in the midspan plane, at x/c of 0.033, 0.133, and 0.266 were shown in Figure V.8, for both tripped and untripped boundary layer configurations at a tunnel speed of 45m/s. The profiles were normalized by wake deficit at the wake centerline and by the wake half width defined as the point where the magnitude of the velocity deficit reached, half of the value at the centerline. It can be seen that the velocity profiles are similar and do not show any pronounced variations. On the basis of these results, it was deduced that the flow around the smooth trailing edge airfoil was two-dimensional in character.

Because the above wake measurements showed similar behavior, no spanwise measurements were made. As no narrow band frequencies could be found in the wake fluctuating velocity spectrum, it was assumed that there was no vortex shedding from the smooth trailing edge airfoil (Airfoil III) in present investigations. As no audible acoustic noise was heard, no acoustic measurements were taken.

V.2 The Blunt Trailing Edge Airfoil Model

In the present phase of investigations, two identical blunt trailing edge airfoils 1) the airfoil with pressure transducers imbedded in the surface (Airfoil I) described in Section IV.2; 2) the airfoil with static pressure taps (Airfoil II) also described in Section IV.2 were utilized.

Due to the non-availability of the required power supplies and amplifiers for the pressure transducers and due to some broken connectors of the transducers, investigation of the fluctuating pressure field was not undertaken. It was assumed that the investigation of the velocity field

would provide sufficient information and the examination of the fluctuating pressure field was left for future investigations.

To measure the static pressure variation in the base, 17 static holes (Figure IV.3) were distributed along the mid plane of the base (see Section IV.2). Only one of seventeen holes in the base could not be used as the tube was broken close to the surface and could not be repaired. Similar to the smooth trailing edge airfoil investigations, two configurations of Airfoil II, i. e., without the boundary layer trip and with the boundary layer trip, were investigated.

All investigations with the airfoil model held at a geometrical zero angle of attack, were carried out at tunnel speeds of 24, 33 and 44m/s corresponding to Reynolds number based on the chord of 2.6×10^5 , 3.5×10^5 and 4.38×10^5 respectively.

To confirm the two-dimensionality of the incoming flow, velocity traverses in the plane parallel to the span of the model and in the plane perpendicular to the span of the model, were made at a position 6cm upstream of the model. The mean velocity and turbulence intensities were found to be uniform for both the velocity traverses confirming the two-dimensionality of the incoming flow.

In the following section, static pressure, boundary layer and wake velocity profiles and characteristic shedding frequency measurements are presented.

V.2.1 Static Pressure Measurements

The static pressure distributions on Airfoil II (i.e. airfoil with static pressure taps) with and without the tripped boundary layer were investigated. The static pressure distribution for the configuration without the boundary layer trip of the airfoil along the midspan at three speeds 24, 32, and 44m/s, was shown in Figure V.9(a) and these coefficients were not corrected for any blockage factor. It can be seen that the data agreed well for all speeds, but close to the trailing edge there were some variations with speed. Figure V.9(b) showed the mid-span chordwise distribution of the static pressure for the configuration with the boundary layer trip of the airfoil and at three speeds of 24m/s, 33m/s and 44m/s. There was better agreement of the data in this case than in the case of the untripped boundary layer configuration. The midspan distribution of the static pressure in the chordwise direction for the smooth trailing edge airfoil is compared with that for the blunt trailing edge airfoil. Data from these airfoils was plotted in Figure V.10 for a speed of 24m/s. The axial distance is normalized by the untruncated airfoil chord (15.2cm). As seen, there is agreement for the distribution, except very close to the trailing edge.

Figure V.11 depicts the spanwise distribution of the static pressure over the blunt trailing edge airfoil with the boundary layer trip. The static pressure is uniform across the span of the airfoil, except very close to the side plates, because of the sidewall boundary layer effect. Figure V.12 shows the spanwise distribution of the static pressure for the untripped boundary layer configuration. The variation of the static

pressure is more pronounced in this case than in the case with the boundary layer trip. The pressure coefficient was fairly uniform over the center portion of the airfoil and the variation became more pronounced close to the trailing edge. Due to the lack of uniformity in the static pressure distribution close to the trailing edge in the spanwise direction, two-dimensionality of the flow could not be verified in the case of the untripped boundary layer configuration. Tripping of the boundary layer leads to the uniformity of the static pressure across the span and to the two-dimensionality of the flow.

With a limited number of transducer reference static pressure taps in the base, placed 1.24cm apart and symmetric about the midspan of the airfoil, the spanwise distribution of the base static pressure for the airfoil with transducers (Airfoil I) was measured. Figure V.12(a) depicts the spanwise variation of the base pressure coefficient and Figure V.13(b) shows the variation of the pressure coefficient with tunnel velocity. As noticed in the initial investigation, the base pressure decreased with increasing velocity. The spanwise distribution of the base pressure did not show any consistency. This non-uniformity could have been caused by the side wall conditions, such as the boundary layer characteristics near the base and in turn could result in three-dimensionality of the near wake.

Figure V.14 shows the variation of the base pressure at the midspan with velocity, where the chain lines and dash lines refer respectively to the configuration with and without the boundary layer trip

configurations of Airfoil II and the solid line shows the base pressure coefficient of Airfoil I. The difference between Airfoil II and Airfoil I data could be due to the small differences in the construction of the airfoils. The base pressure coefficient decreased with increasing speed as shown in the figure and the coefficients were not corrected for blockage effect.

The spanwise distribution of the base pressure with the speed of the tunnel for the configuration without the boundary layer trip is shown in Figure V.15. Figure V.16 depicts the spanwise distribution for the configuration with the boundary layer trip. The base pressure distribution in either case of the configurations was not uniform in the spanwise direction and varies with speed. The distribution of the base pressure for the configuration with the boundary layer trip is uniform over a larger portion of the center span than for that without the boundary layer trip. This uniformity could be due to the tripped boundary layer and also could be due to interaction of the turbulent boundary layer on the airfoil and the sidewall boundary layer. It is seen that even though mean pressure, over the upper surface of the airfoil is uniform, the base pressure in the blunt trailing edge is non-uniform. With the measurements of flow characteristics of a blunt trailing edge body, the uniformity of the mean base pressure must also be examined.

V.2.2 Velocity Profiles of the Boundary Layer and the Near Wake

The boundary layer velocity profiles near the trailing edge influence the vortex shedding from the blunt trailing edge airfoil. The effect of truncation on the flow field could also be measured with the changes in the boundary layer profiles. These boundary layer and wake profiles were measured with a single hotwire with the measuring element parallel to the trailing edge.

Boundary layer profiles for Airfoil II with and without the boundary layer trip were measured behind the maximum thickness of the airfoil and in the midspan plane. The boundary layer profiles were surveyed at x/c of 0.62, 0.77, 0.92 and 0.99 and at velocities of 24, and 34m/s. The profiles were normalized with the uniform mean velocity of the tunnel.

The measured boundary layer profiles for 24 and 34m/s were shown in Figures V.17 and V.18 and the chain lines and dash lines correspond to the tripped and untripped boundary layer cases, respectively. Similarly, the boundary layer profiles for Airfoil I with pressure transducers at $x/c = 0.89$ and 0.98 at a velocity of 24 and 45m/s were shown in Figure V.19. The boundary layer profile at these speeds show that there was no flow separation along the midspan. Due to the inability of the transversing mechanism, boundary layer measurements only at midspan locations could be made.

Figure V.20 compares the boundary layer profiles at $x/c = 0.98$ and at a velocity of 24m/s. The dash lines and solid lines refer to the configurations without the boundary layer trip of Airfoil II and Airfoil I,

respectively. The chain line shown in the Figure are for the Blasius profile and it could be seen that measured boundary layer profiles were not laminar profiles. Figure V.21 compares the boundary layer profiles of Airfoil II measured at $x/c = 0.98$, with boundary layer profiles measured at $x/c = 0.85$ for a smooth trailing edge airfoil (i.e. Airfoil III). The chordwise distance was normalized with respective airfoil chords and the measuring location corresponds to the blunt trailing edge position. The lines with squares and circles were for Airfoil II, and the dash and chained lines were for Airfoil III corresponding to configurations with and without the boundary layer trip, respectively. The solid line shows turbulent boundary layer profiles, calculated by $1/7$ power law. The tripped boundary layer profile with the turbulent boundary layer profile. The untripped boundary layers showed some differences. From these figures it could be concluded that boundary layer profiles are consistent and there was no flow separation before the trailing edge along the midspan.

The near wake measurements behind the airfoil with transducers at two different streamwise locations $x/d = 3.3$ and 10.2 and at 3 spanwise locations of $z/s = 0, \pm 0.5$ were made at a speed of 26m/s and were shown in Figure V.22. The mean velocity profiles measured at off midspan locations ($z/s \pm 0.5$) agreed with each other, but there was disagreement with the midspan profile ($z/s = 0$). The wake profile in the midspan plan also showed asymmetric behavior. The fluctuating velocity intensity profiles at these three measuring locations agreed. The difference in the mean velocity profiles could be caused by three-dimensionality of the near wake flow.

Similar measurements of the wake profiles of Airfoil II (i.e. with pressure taps), for both configurations with and without the boundary layer trip, in the midspan plane, and at axial stations of 0.5, 1, 2, and 4 were measured. These profiles were shown in Figure V.23 and V.24 corresponding to 24 and 34m/s respectively. The (a) and (b) of each figure correspond to the configurations with and without the boundary layer trip respectively. These profiles are normalized by the wake center-line velocity deficit and by the wake half width.

Spanwise stations of $z/s = 0, \pm 0.33$ were chosen to compare the wake mean velocity profiles at different spanwise locations. Normalized wake profiles with untripped and tripped boundary layer configurations measured at speeds of 24 and 34m/s were shown in Figure V.25 and V.26, respectively. The profiles of the tripped boundary layer configurations have less scatter when compared with untripped configurations. The boundary layer trip seems to aid the flow in gaining uniformity in the spanwise direction. This was also seen, as mentioned before, in base pressure measurements.

V.2.3 Characteristic Vortex Shedding Frequency of the Airfoil

A major characteristic of a body with a blunt trailing edge is the vortex shedding frequency of the body. The shedding of vorticity into the wake of a bluff body was examined in literature and some three-dimensionality of the shedding was shown.

The measured shedding frequency of Airfoil I, at 2.2 and 4.4 base heights behind the airfoil (Figure V.27) increased linearly with the velocity. The velocities plotted in the Figure and used in subsequent

evaluation of the Strouhal number, were not corrected for any blockage. Past a tunnel velocity of 30m/s, a second frequency was detected, which varied linearly with further increase of the velocity. The variation of the frequency was identical at both measuring locations.

As vortex shedding from a blunt based body is usually characterized by only one frequency, a possible source for the second frequency could be probe support rods. The measured vortex shedding frequencies of the hotwire support rods were shown in Table V.1 along with calculated frequencies of these support rods with a Strouhal number of 0.2. The measured second frequencies of the airfoil did not correspond to any of these frequencies. When the amplitudes of the frequencies were taken into account, the frequencies with maximum amplitude agreed (Figure V.28) well with the data of a circular cylinder of diameter equal to the thickness of the blunt trailing edge. (See Section V.3). At present, no explanation can be presented about the second frequency.

The variation of the shedding frequency with velocity (Figure V.29) was shown as circles and crosses corresponding to Airfoil II configurations with and without the boundary layer trip, respectively. Both configurations showed linear variation of frequency with velocity. The measured frequency of the tripped boundary layer configuration was lower than measured frequency of the configuration with an untripped boundary layer. There was only one shedding frequency found in the wake of Airfoil II, and the measured data of the untripped configuration agreed with the data of the airfoil with transducers (Figure V.27 and Figure V.29).

As a comparison, shedding frequency of a circular cylinder (see Section V.3) of a diameter equal to the trailing edge thickness was shown by squares in Figure V.29. The frequency of the cylinder was found to lie between the measured values of the two boundary layer conditions.

A constant Strouhal number could be generated with linear variation of the frequency with a characteristic length. Strouhal numbers evaluated on the basis of displacement and momentum thickness, as characteristic lengths for both configurations are shown in Figure V.30. It is clear from the figure, that the scatter in the Strouhal number for both configurations was about 5%.

It can be deduced that the boundary layer characteristics at the trailing edge could affect the shedding of vortices into the wake. The generation of a constant Strouhal number for the airfoil could depend on a characteristic length of the near wake and on the base pressure.

The characteristic frequency is measured at a velocity of 26m/s along the span of Airfoil I and the upper shear layer and at streamwise locations of x/d of 0.35, 3.33 and 10.2 are shown in Figure V.31(a). It is seen that there exists a variation in the shedding frequency in the spanwise direction. This variation of the frequency is symmetric about the centerline. There seems to exist a region about the midspan where the frequency did not change. The measurement of the frequency downstream of the upper and lower separation points at the trailing edge showed similar behavior as shown in Figure V.31(b). Frequencies measured at different velocities and at three representative locations of $z/s = 0, \pm 0.5$ are given in Table V.2. The frequency variation did not show any systematic trend, but was symmetric about the midspan of the airfoil.

Similar measurements for the blunt trailing edge airfoil with pressure taps, for configurations with and without the boundary layer trip, are shown in Figure V.32. The tripped boundary layer configuration showed little or no variation of frequency in the spanwise direction, but the configuration without the boundary layer trip showed some variation similar to the data of the blunt trailing edge airfoil with transducers. The frequency variation in the spanwise direction could be influenced both by the model trailing edge and by the boundary layer on the sidewall as well as that on the surface of the airfoil.

V.3 Some Measurements of Flow Past a Circular Cylinder

As shown in previous sections, the blunt trailing edge airfoil showed characteristics of a bluff body. To achieve some comparison with a bluff body flow mounted between the side plates, a circular cylinder of diameter (0.45cm) equal to the thickness of the blunt trailing edge was used.

The circular cylinder was held between the two side plates, at the location where the blunt trailing edge of the airfoil was located. A set of circular end plates of 5cm diameter were also used, to ensure the elimination of the end plate boundary layer effect. The usage of these circular end plates did not change any measured quantities as the aspect ratio of the cylinder (span/diameter) with these end plates was about 50. As there were no provisions for changing the aspect ratio of the airfoil, measurements of the cylinder with other aspect ratios were not taken. As the cylinder was very small, no static pressure taps could be situated to measure the base pressure distribution across the span.

The leading edge of the circular cylinder was at 33.0cm measured from the leading edge of the side plates. Similar to the investigations with the airfoil, the wind tunnel velocity was varied between 19m/s and 46m/s corresponding to the Reynolds number based on the diameter of 7.1×10^3 to 1.7×10^4 . This Reynolds number region corresponds to subcritical flow regime for the cylinder. The wake flow in this regime is characterized by regular vortex shedding. The incoming flow was measured at 14.5cm upstream of the circular cylinder and it was found that the mean and turbulent intensity profiles were uniform in both the vertical and horizontal planes, confirming the uniformity of the incoming flow.

The vortex shedding frequency was measured with a hotwire situated at the location of the maximum RMS value of the fluctuating velocity in the midspan and at 1/2 diameter in y-direction from the mid-wake position. The hotwire data showed strong single frequency dominance corresponding to vortex shedding.

Variation of the characteristic frequency (i.e. vortex shedding), measured by the hotwire was shown in Figure V.33. As described in Section V.2.2, data with the boundary layer trip configuration of the truncated airfoil with pressure, and data of truncated airfoil with transducers were also shown in the figure. The measured shedding frequency of the cylinder is consistently above the measured data of Airfoil II with tripped boundary layer configuration. As the frequency varied linearly with velocity, a constant Strouhal number could represent the characteristic frequency. The Strouhal number based on

the diameter of the cylinder was evaluated by the relation

$$St = \frac{fd}{U_{\infty}} = 0.22$$

The Strouhal number was higher as velocity was not corrected for blockage. With the velocity corrected for blockage, the corrected Strouhal number becomes 0.2, which is equal to the generally used Strouhal number for a circular cylinder in the subcritical flow region.

Next, the spanwise variation of the vortex shedding with and without the small circular endplates was investigated. With or without these endplates the vortex shedding frequency at the center of the cylinder span varied within $\pm 5\text{Hz}$, which is within the tolerance of the spectrum analyzer. The measured shedding frequency in the spanwise direction, with and without the small endplates, was shown in Table V.3. These measurements were made at $x/d = 2.5$ and $y/d = 0.5$ from the center line of the wake. As could be seen, the frequency distribution in the spanwise direction with and without the small endplates was similar and the variation was symmetric for both configurations. The frequency increased towards the endplates for the configurations at a speed of 43m/s but at a lower speed, the variation was within the error of the spectrum analyzer.

V.4 Acoustic Features of the Blunt Trailing Edge Airfoil

The vortex shedding from the blunt trailing edge airfoil is accompanied by acoustic radiation. Such radiation from an airfoil in the tunnel is likely to be influenced by the resonances of the enclosure. Section III showed

the tunnel duct pressure modes calculated for both empty test section and test section with sideplates. Because of the through flow of the tunnel, different tunnel modes became important. In this section, some features of the acoustic measurement in near and farfield are discussed.

A 1.25cm B & K microphone, without a nose cone, was mounted on a tripod outside the tunnel test section at the ventilation gap at 2.0cm from the walls of the tunnel. A 0.638cm B & K microphone with a nose cone and a preamplifier was mounted on the traversing mechanism to measure the directivity of the near field in the mid-span plane in the test section. Each microphone was used with the hotwire situated at the maximum rms value of u' , i.e., in the upper shear layer, to identify the vortex shedding frequency.

No narrow band acoustic radiation from the airfoil with smooth trailing edge was found, indicating that there was no discrete vortex shedding from the airfoil which was confirmed by hotwire data (Section V.1). Thus, no acoustic measurements for smooth trailing edge airfoil will be presented. Only the acoustic data of the blunt trailing edge airfoil are discussed.

During the course of the experimental investigation, audible tones, possibly due to the tunnel resonances, could be heard. From these audible tones, the tunnel resonances could be divided into different regions as shown in Figure V.34. The shedding frequency of the airfoil with transducers is shown in the figure to depict the frequency trend.

Next, the characteristic frequency of the airfoil with tripped boundary layer measured with hotwire and microphone were shown in Figure V.35. The shedding frequency of the blunt trailing edge airfoil with pressure taps (with the boundary layer trip) measured by the microphone agreed fairly well with hotwire data, as shown in the figure. Typical hotwire and microphone narrow band frequency spectra with no audible tone, corresponding to a velocity of 34m/s were given in Figure V.36. The dash line in Figure V.36(a) was the cross-correlation spectrum between the hotwire and microphone. Though the low frequency noise was dominant, the cross-correlation spectrum showed the presence of the vortex shedding frequency. Figure V.37 showed the hotwire and microphone spectrums, when there was a strong resonance in the tunnel corresponding to a velocity of 24m/s. Both hotwire and microphone data show strong narrow band signals at the vortex shedding frequency.

The microphone measured frequency data for Airfoil II and Airfoil I without the boundary layer trip did show similar behavior as shown in Figure V.38. Some of the frequencies, as measured by the microphone, for the airfoil with untripped boundary layer did not agree with hotwire data. This is also shown in the figure. The spectral densities of the hotwire and microphone at a velocity of 24m/s with strong tunnel resonance was shown in Figure V.39. The vortex shedding frequency was evident in both spectrums.

Spectral densities at a velocity of 34m/s, where no distinct audible noise was present, are given in Figure V.40. Again the microphone

data was dominated by low frequency noise and the cross-spectral densities showed the vortex shedding frequency. Typical 1/3 octave band spectrum for both cases of the boundary layer conditions at 33m/s were shown in Figure V.41 emphasizing the low frequency noise.

The feature that needs to be emphasized was that the characteristic frequency of the airfoil could be extracted with cross-spectral density of the hotwire and microphone.

The directivity pattern of the near field acoustic pressure of the blunt trailing edge airfoil was measured downstream of the trailing edge at a radial distance (R) of 2cm. The directivity pattern at speeds of 26m/s and 34m/s of the configuration with boundary layer trip and without boundary layer trip of Airfoil II were shown, respectively, in Figures V.42 and V.43. The circles and triangles were for the configuration with the boundary layer trip and without the boundary layer trip, respectively, as shown in the figures.

The data showed strong radiation at small angles to the chord line of the airfoil with a pressure peak downstream of the trailing edge as shown in the figure. The directivity pattern showed the preference of radiation in upstream and downstream direction, as seen in the Lobe pattern.

VI CONCLUDING REMARKS

In this investigation, the main features of the structure of the flow around a blunt trailing edge airfoil fixed in an initially uniform speed are examined experimentally. Of special concern are the characteristics such as mean surface pressure distribution, nature of the boundary layer near the trailing edge, and the velocity profiles in the near wake. In addition, certain unsteady features of the flow are also investigated. Specifically, the vortex shedding and surface pressure fluctuations in the case of the blunt trailing edge airfoil are investigated. Main observations and implications are summarized in the following.

From the investigations of a smooth trailing edge airfoil in a uniform flow, the following results and features were found.

- a) The velocity field of the incoming flow onto the airfoil was found to have uniformity in both mean velocity profile and turbulence intensity profile.
- b) The measured chordwise static pressure distribution on the airfoil, along the midspan plane, agreed with the theoretical results calculated on the basis of the potential flow for that airfoil.
- c) Boundary layer profiles measured in the midspan plane, behind the maximum thickness of the airfoil showed no separation of the flow.
- d) Spanwise distribution of the measured static pressure on the upper surface of the airfoil showed uniformity for both config-

urations with and without the boundary layer trip. This uniformity of pressure distribution and separation indicates that the flow on the airfoil was uniform and two-dimensional in character.

- e) Mean and fluctuating velocity profiles in the near wake along the midspan plane exhibit well known observed features.

On the basis of the above, the flow past a smooth trailing edge airfoil can be regarded as essentially two-dimensional.

Investigations of the flow around the blunt trailing edge airfoil showed the following features of the flow field.

- a) The flow ahead of the airfoil is again uniform as in the case of a smooth trailing edge airfoil.
- b) The chordwise distribution of the static pressure is unaffected by the tripping of the boundary layer. When the chordwise distribution is compared with that for a smooth trailing edge airfoil, agreement was good, except at the vicinity of the trailing edge.
- c) The boundary layer profiles in the midspan plane showed no separation as in the case of the smooth trailing edge airfoil. Separation occurs at the trailing edge resulting in vortex shedding.
- d) The spanwise distribution of the static pressure with tripped boundary layer, was found to be uniform on the upper surface of the airfoil. But the spanwise distribution of the static pressure for an untripped boundary layer configuration was found to be nonuniform as the trailing edge was approached.

- e) The base pressure distribution was not uniform in the spanwise direction for either of the configurations (tripped or untripped) of the airfoil. The variations were more pronounced in the case of the untripped boundary layer.
- f) Although similiarity is observed for the wake profiles in the case of the tripped boundary layer, it is not apparent in the case of the untripped boundary layer.

Observations of the unsteady aspects of the flow indicate the following results.

- a) No discrete frequency fluctuations are observed in the wake of the smooth trailing edge airfoil.
- b) Vortex shedding occurs behind blunt trailing edge airfoils. This is identified from the spectra of the signals obtained both by the hotwire in the wake and by the surface pressure transducers.
- c) The characteristic vortex shedding frequency varied linearly with velocity. The values of the shedding frequency in the case of the tripped boundary layer were lower than those in the case of the untripped boundary layer. The Strouhal numbers based on the base height are 0.21 to 0.22.
- d) The shedding frequency of a circular cylinder, of diameter equal to the thickness of the airfoil trailing edge, was found to lie between the frequencies measured in the cases of the tripped and untripped boundary layer configurations.
- e) Although certain spanwise variation in the vortex shedding frequency was observed in the case of the untripped boundary layer, such variation was not discernable in the case of the

tripped boundary layer.

- f) Although the intensity (RMS) of the base fluctuating pressure showed negligible variation in the spanwise direction, cross-correlations indicate spanwise phase variation in the base pressure. This is likely to result from the waviness of the vortex sheet shed from the trailing edge or due to the oblique vortex shedding.

Present studies, although they have yielded more insight into the flow around the blunt trailing edge than is presently available, they are inadequate in furnishing a detailed picture of the flow structure. Further studies along the following lines need to be undertaken. Appropriate visualization studies of the discrete structure of the flow, both in the streamwise and spanwise directions; detailed survey of the fluctuating surface pressure field and their statistical characteristics; spanwise correlations of the fluctuating velocity in the region of the trailing edge and the near wake.

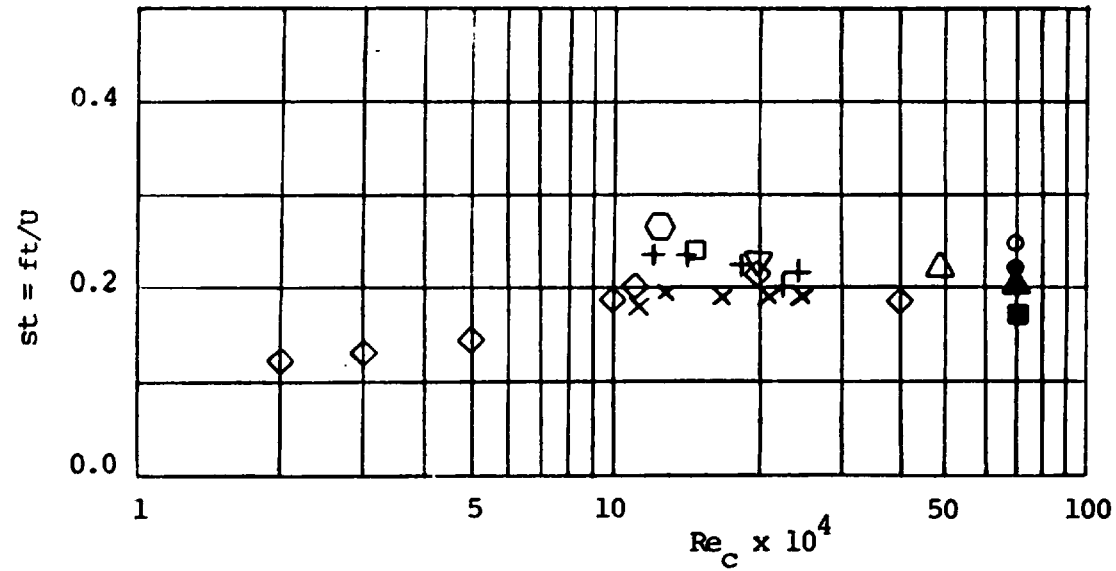


Figure II.1 Strouhal Number of 2-Dimensional Body with Blunt Trailing Edge
 (Bauer (1961) \diamond , $t/c = 0.21$; Nash (1963) \circ , $t/c = 0.1$;
 Parker (1966) x , $t/c = 0.021$; $+$, $t/c = 0.031$;
 Bearman (1967) \square , $t/c = 0.166$; Ghram (1969) \odot , $t/c = 0.667$;
 Lawrence and Lindley (1974) \bullet , $t/c = 0.039$; \blacktriangle , $t/c = 0.035$;
 and \blacksquare , $t/c = 0.027$; Davis (1975) Δ , $t/c = 0.024$)

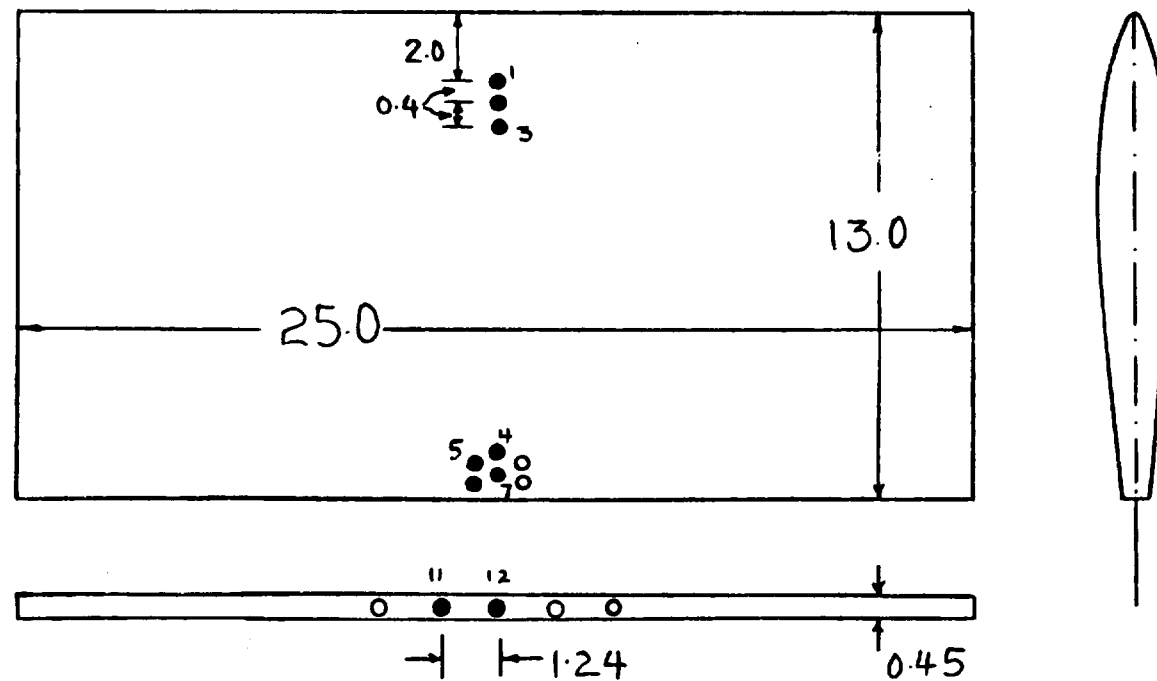


Figure III.1 Blunt Trailing Edge Airfoil with Transducers (Airfoil I)
 (NACA 64A010 profile, truncated at 85% of true chord;
 all dimensions are in cm.)

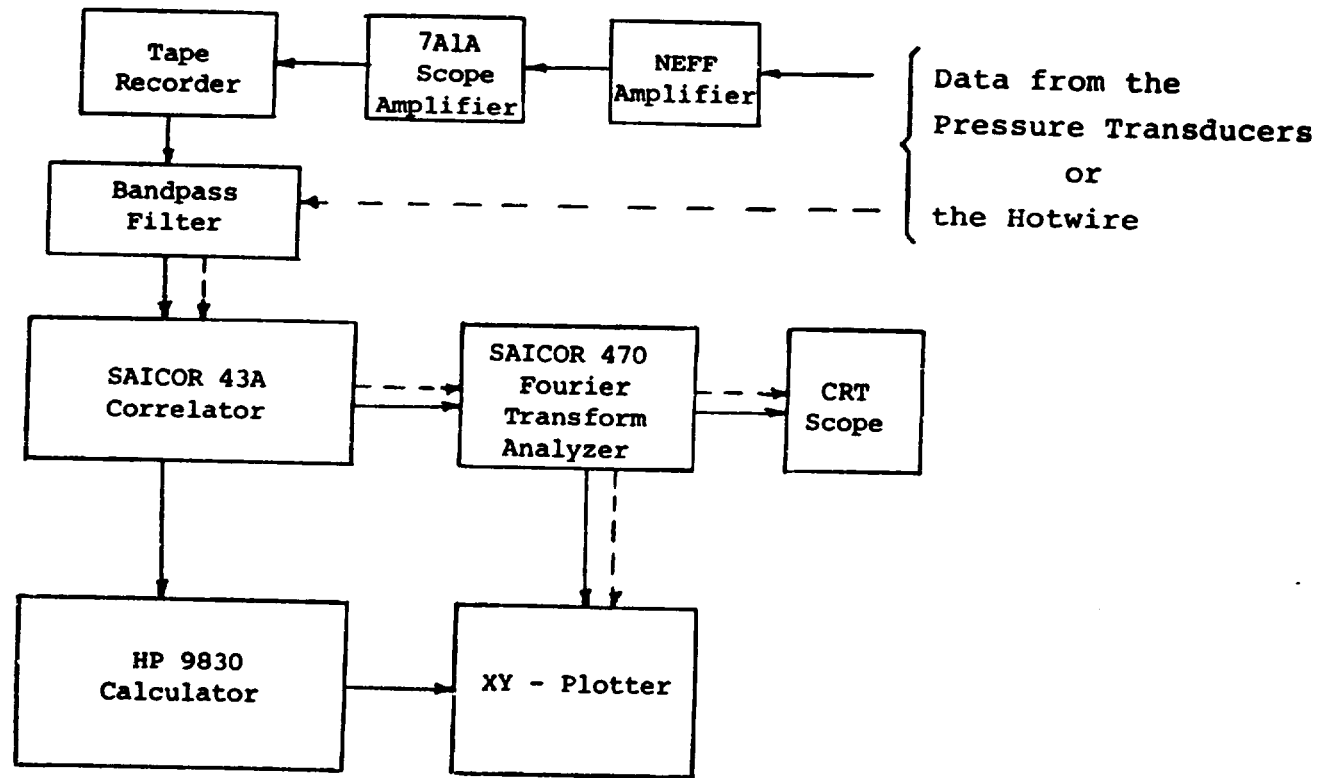
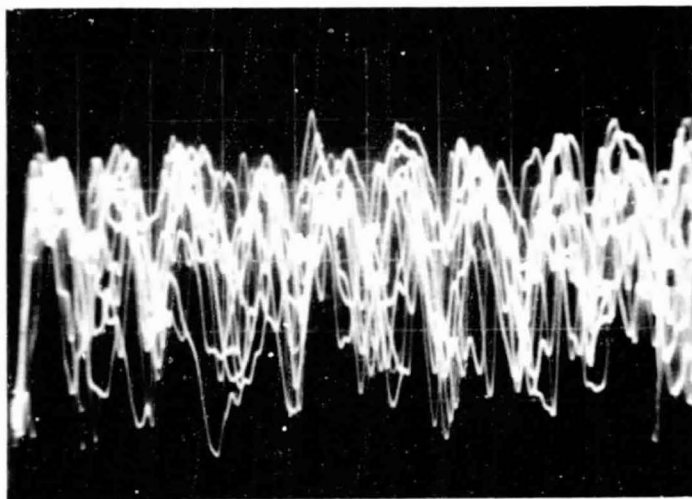
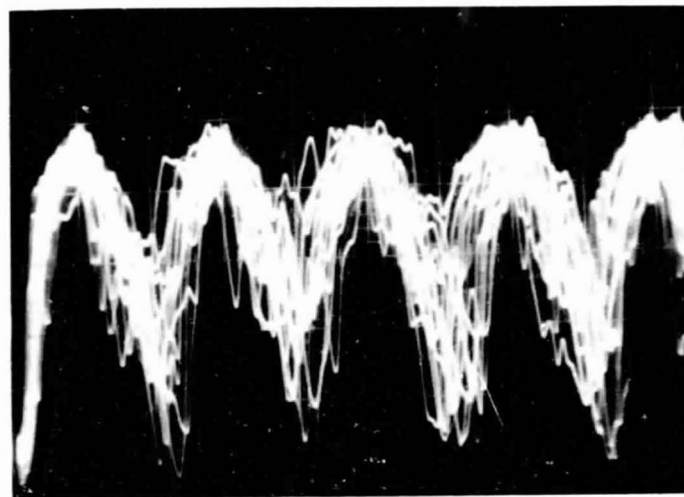


Figure III.2 Data Reduction System for the Experiments
 (data path for the initial investigations, —; data path for the subsequent investigations, ----)

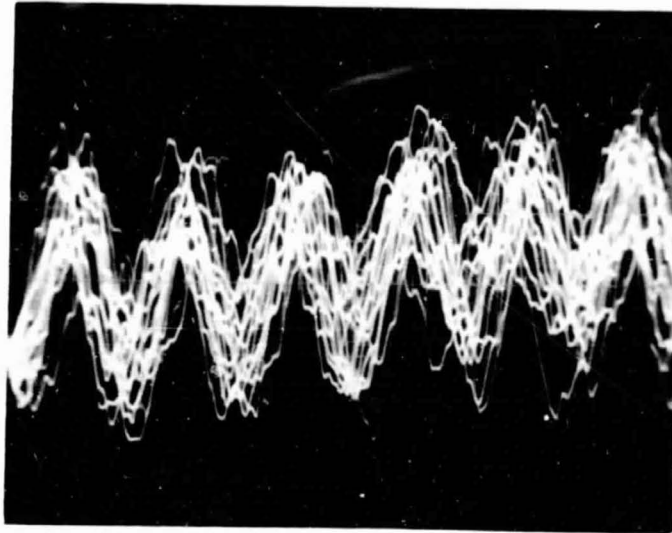


a) Mid Wake Position

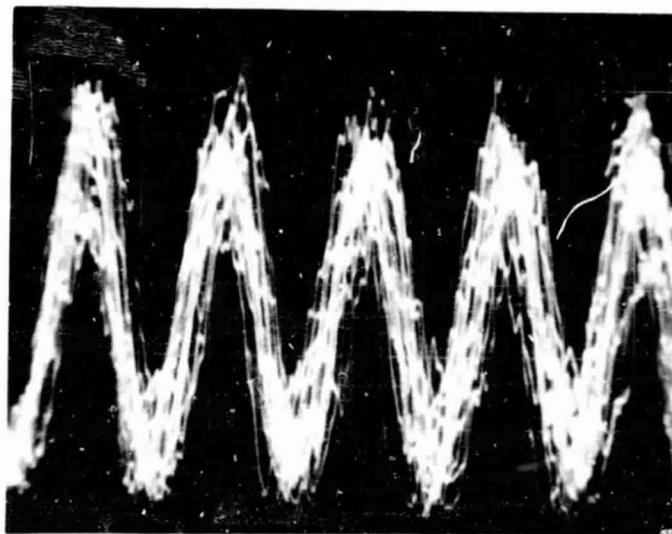


b) Behind the Upper Separation point

Figure III.3 Real Time Signals of Hotwire in the Wake at 0.6cm. Downstream of the Blunt Trailing Edge of the Airfoil I
(vertical axis 1.0V/cm; horizontal axis 0.2ms/cm.)



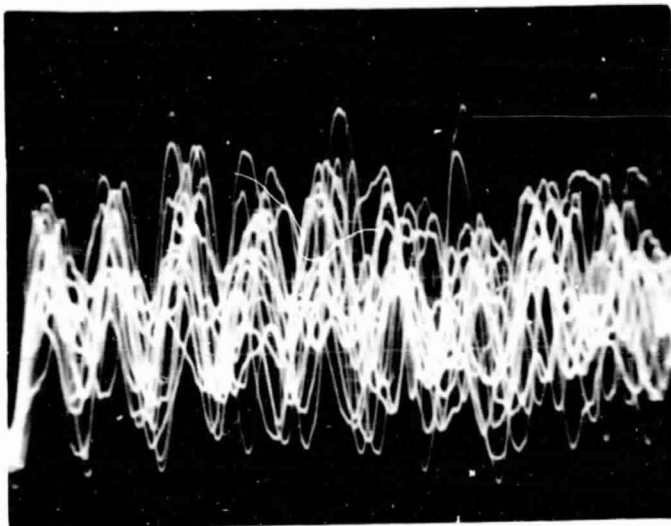
a) Transducer near the Leading Edge
(Transducer #1)



b) Transducer near the Trailing Edge
(Transducer #7)

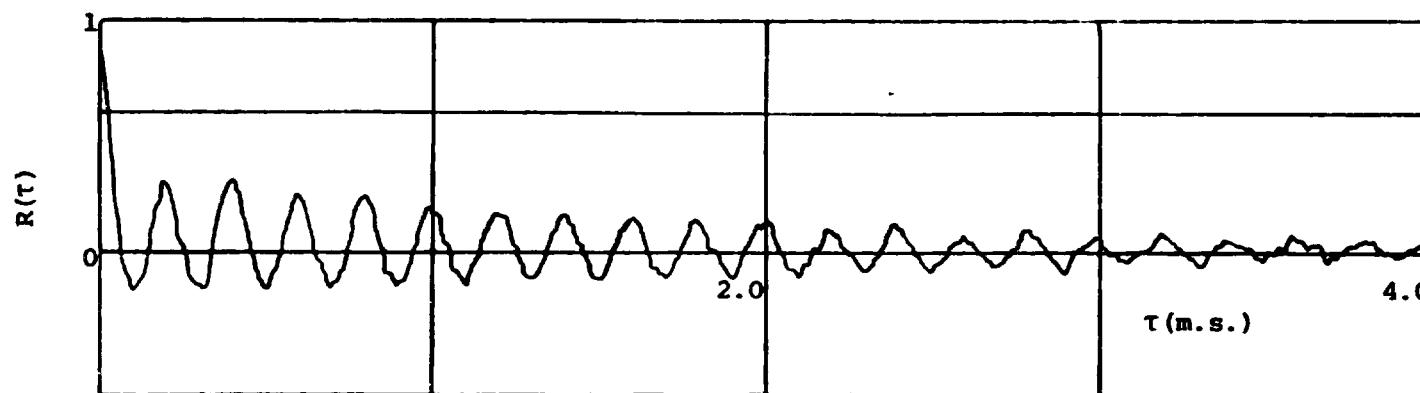
Figure III.4 Real Time Signals of the Pressure Transducers
on the Surface of the Blunt Trailing Edge
Airfoil I
(vertical axis 1.0v/cm; horizontal axis 0.2ms/cm)

ORIGINAL PAGE
BLACK AND WHITE PHOTOGRAPH

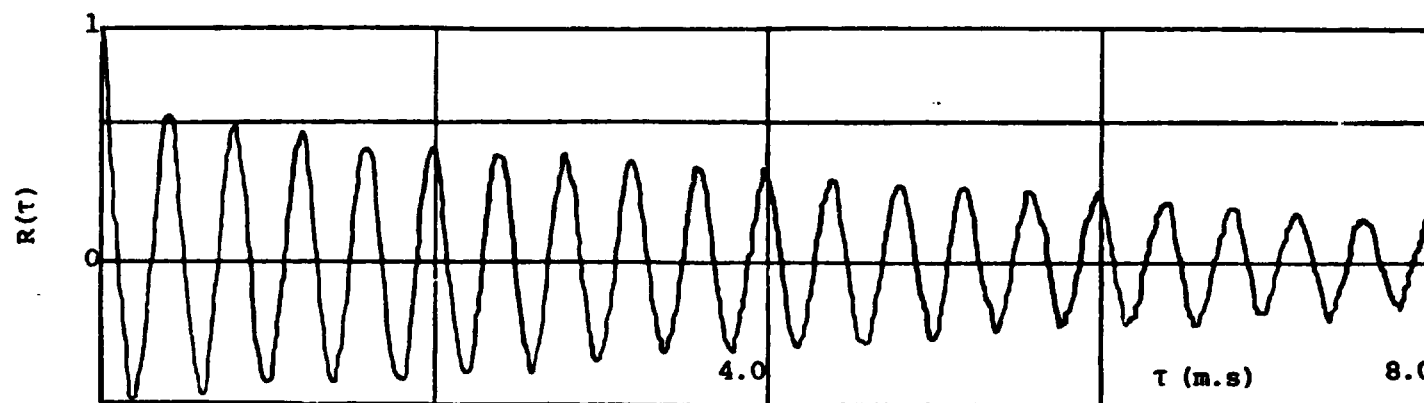


c) Transducer in the Blunt Trailing Edge
(Transducer #12)

Figure III.4 (continued)



a) The Mid Wake Position



b) Behind the Upper Separation Point

Figure III.5 Auto-Correlation Function of the Signal of the Hotwire in the Wake

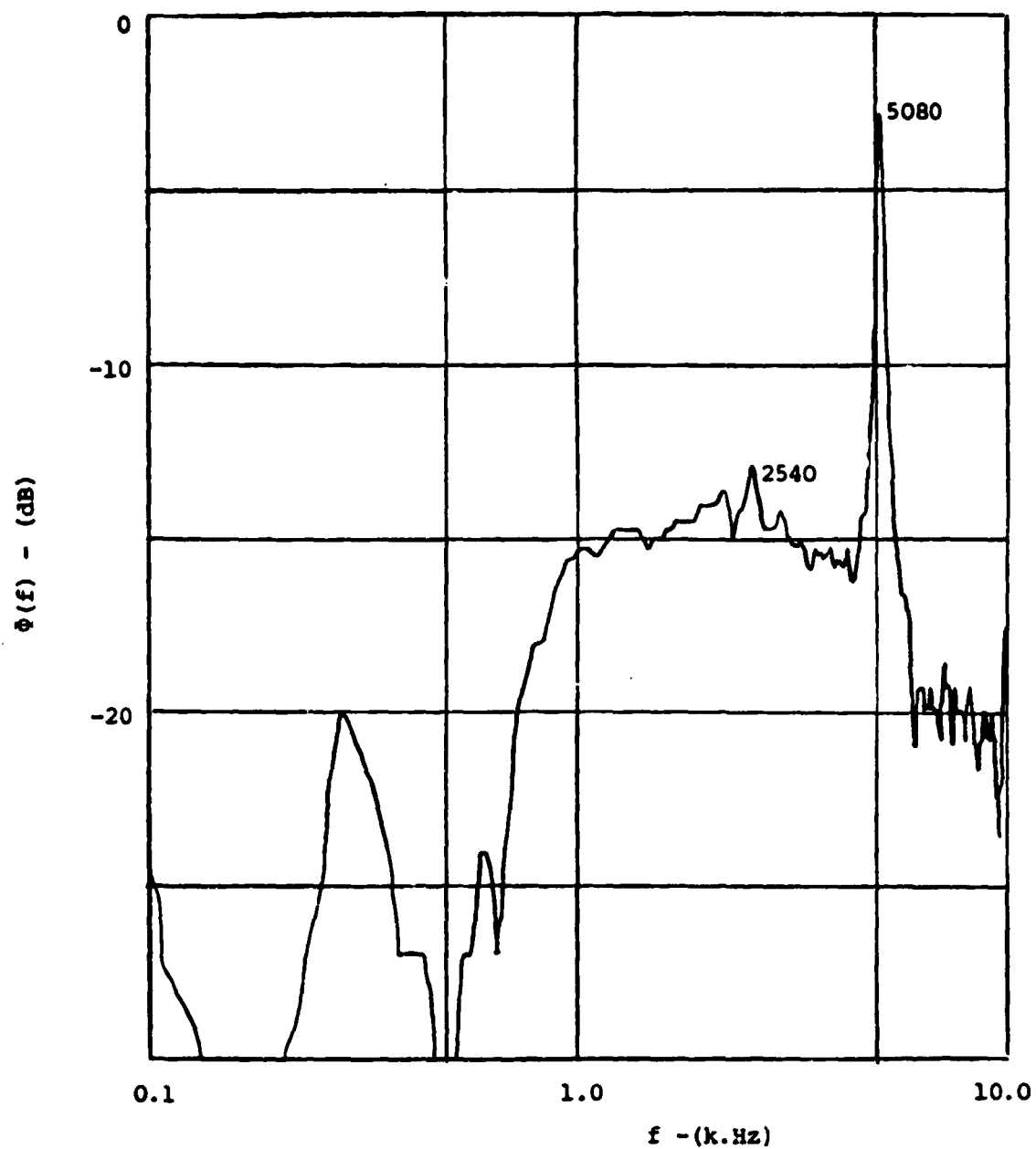


Figure III.6 Auto Power Spectral Density of the Hotwire Signal in the Mid Wake Position and at 0.6cm. Down stream of the Blunt Trailing Edge

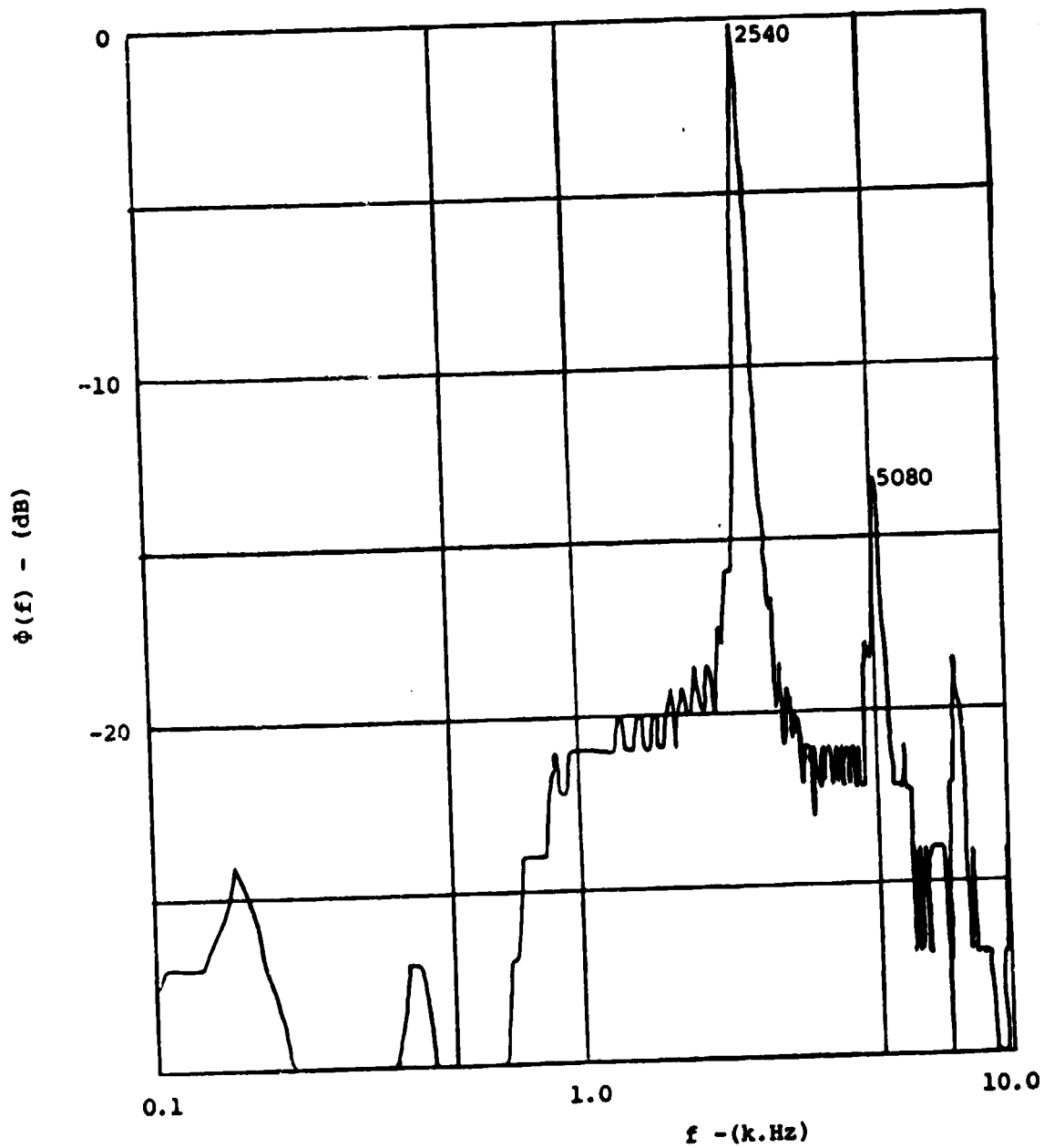
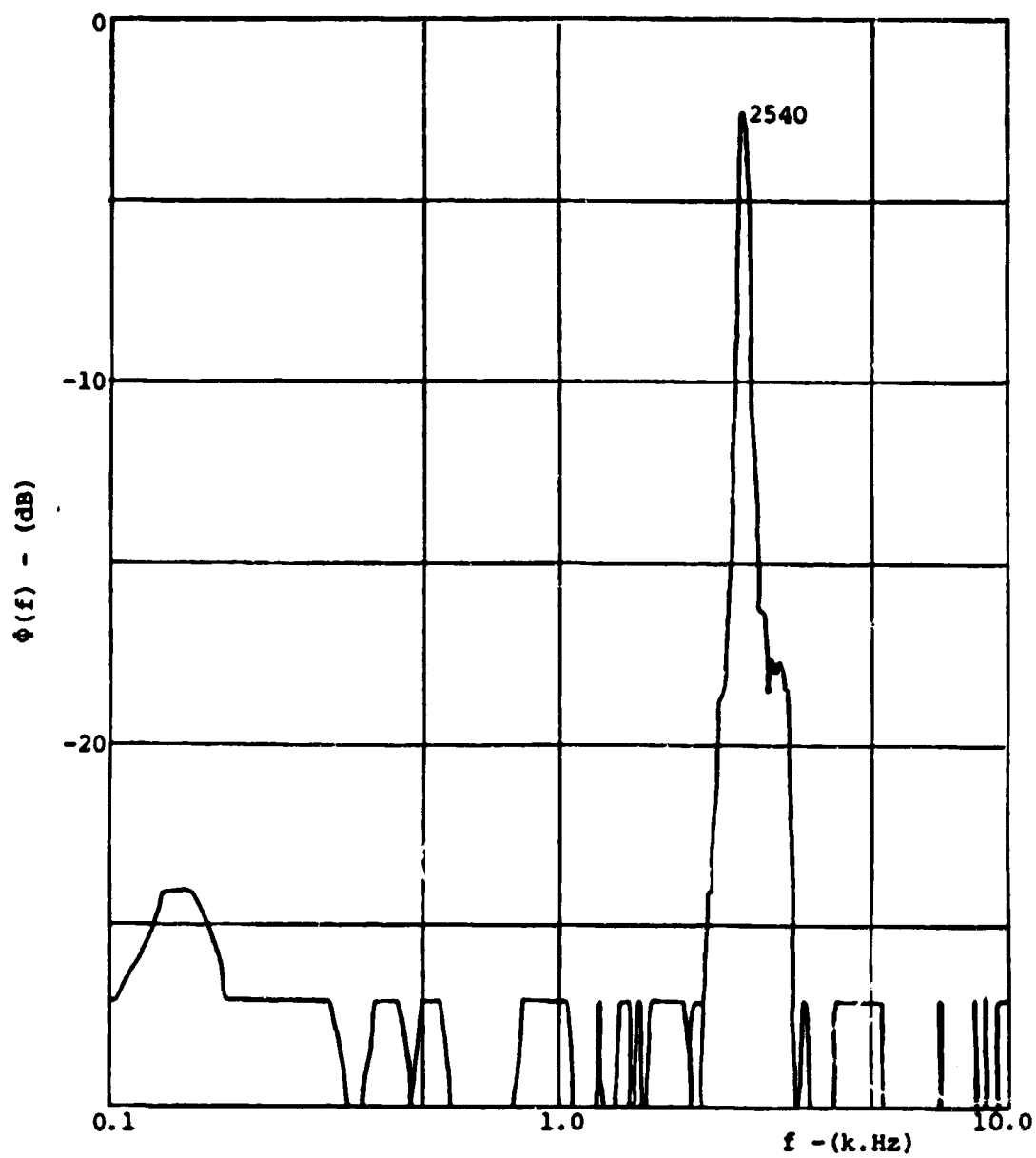
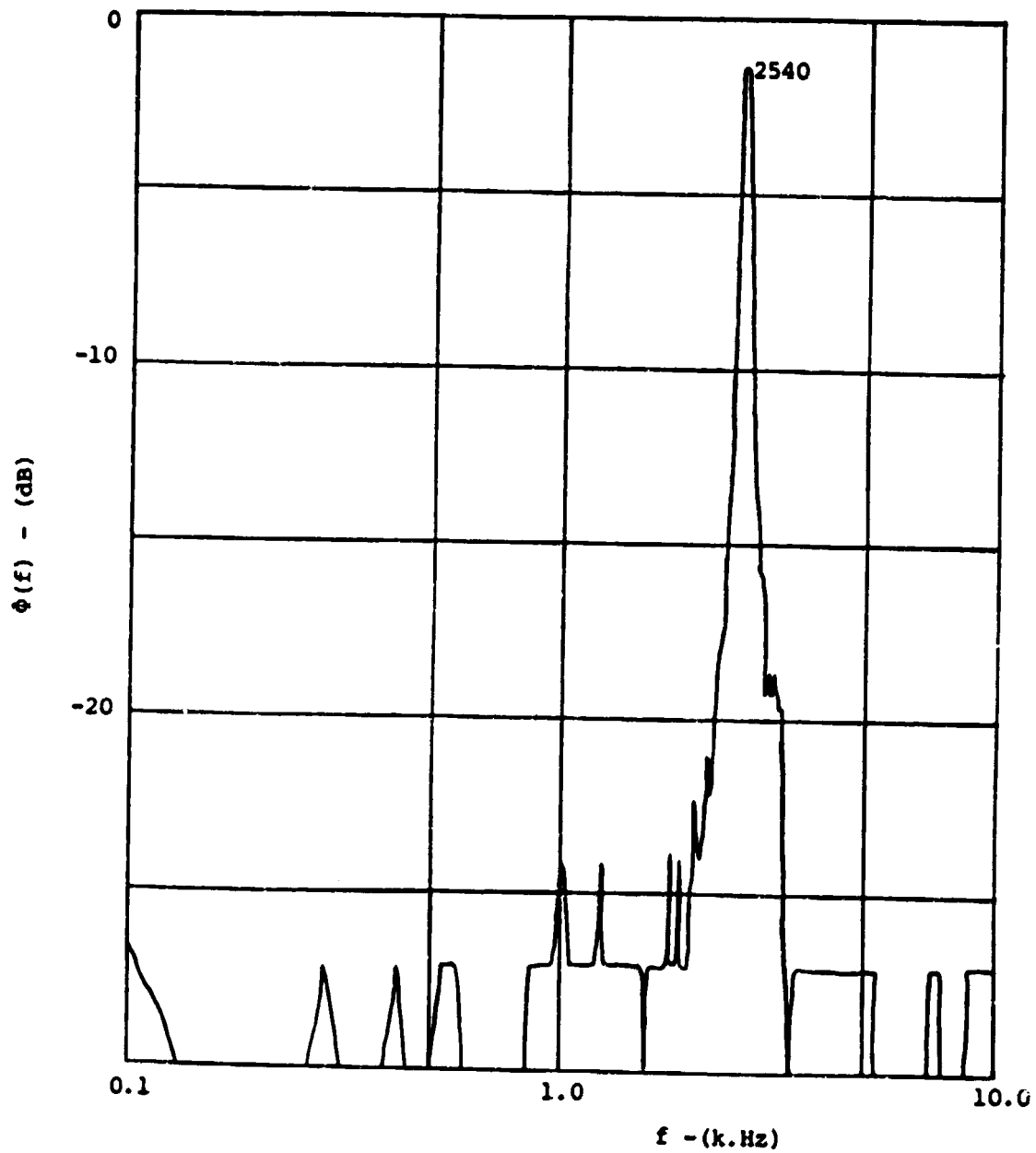


Figure III.7 Auto Power Spectral Density of the Hotwire Signal at 0.6cm. Down Stream of the Upper Separation Point of the Blunt Trailing Edge



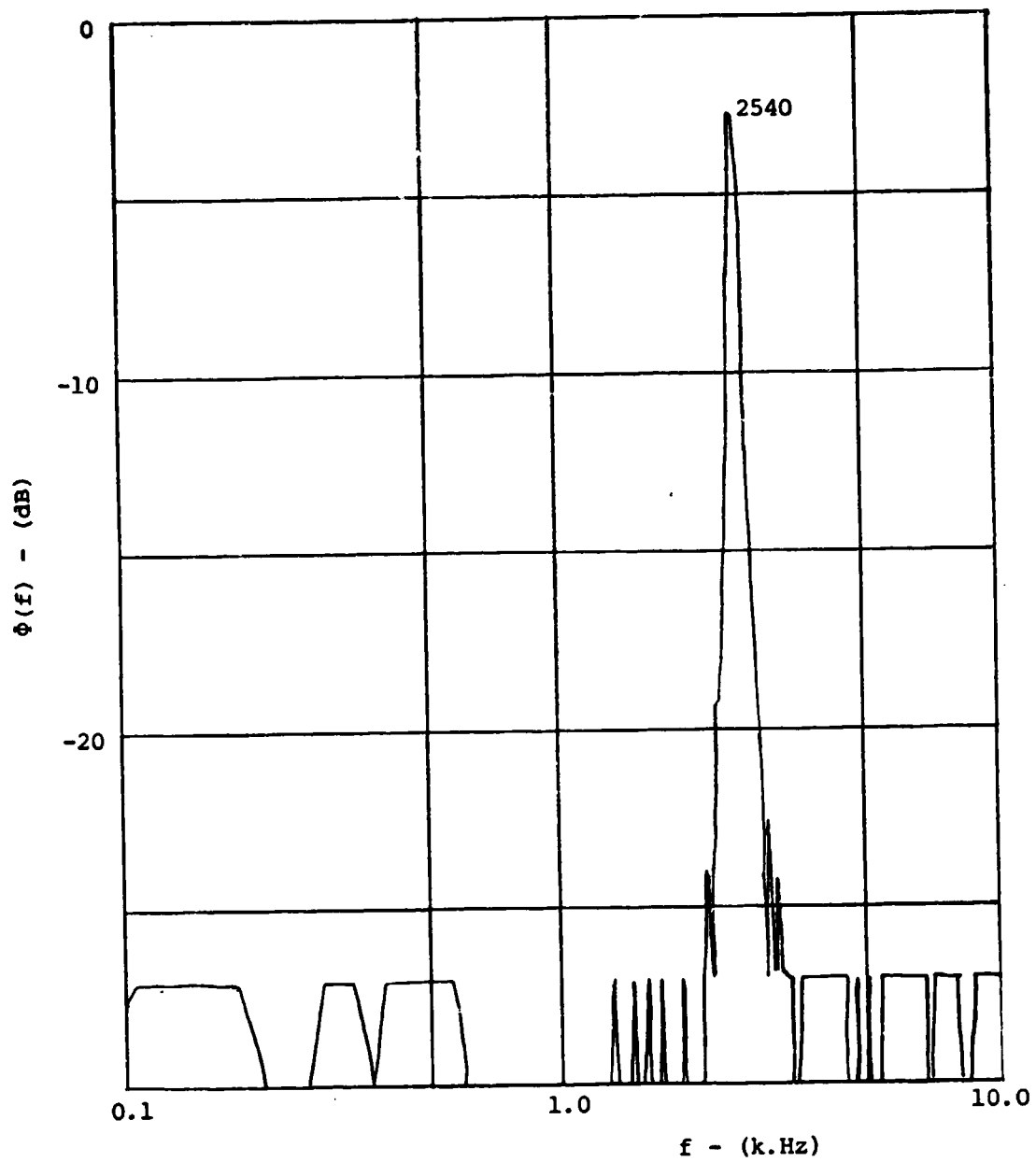
a) Transducer #4

Figure 11I.8 Auto Power Spectral Density of the Signal from the Transducer Near the Blunt Trailing Edge.



b) Transducer #5

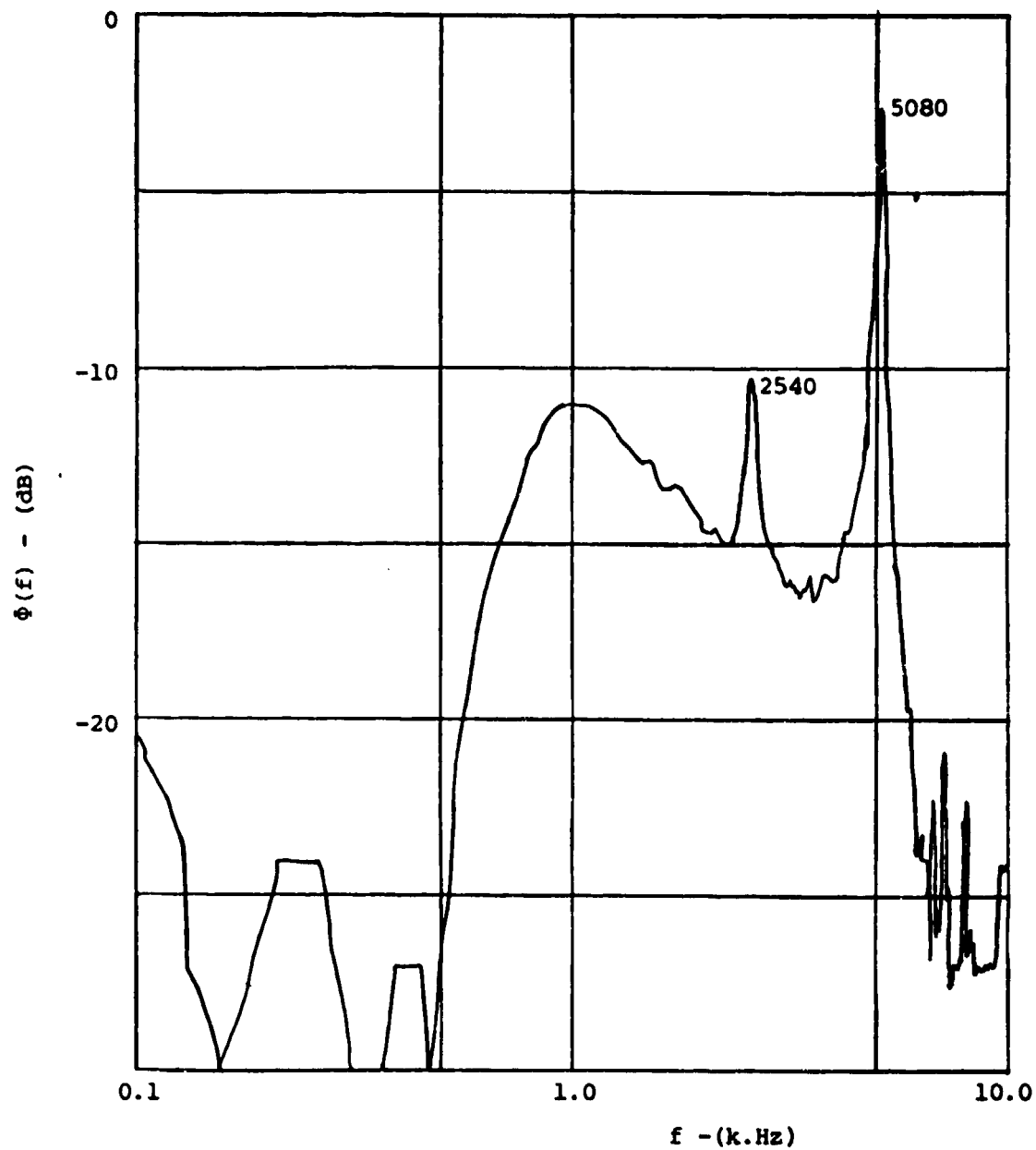
Figure III.8 (continued)



c) Transducer #7

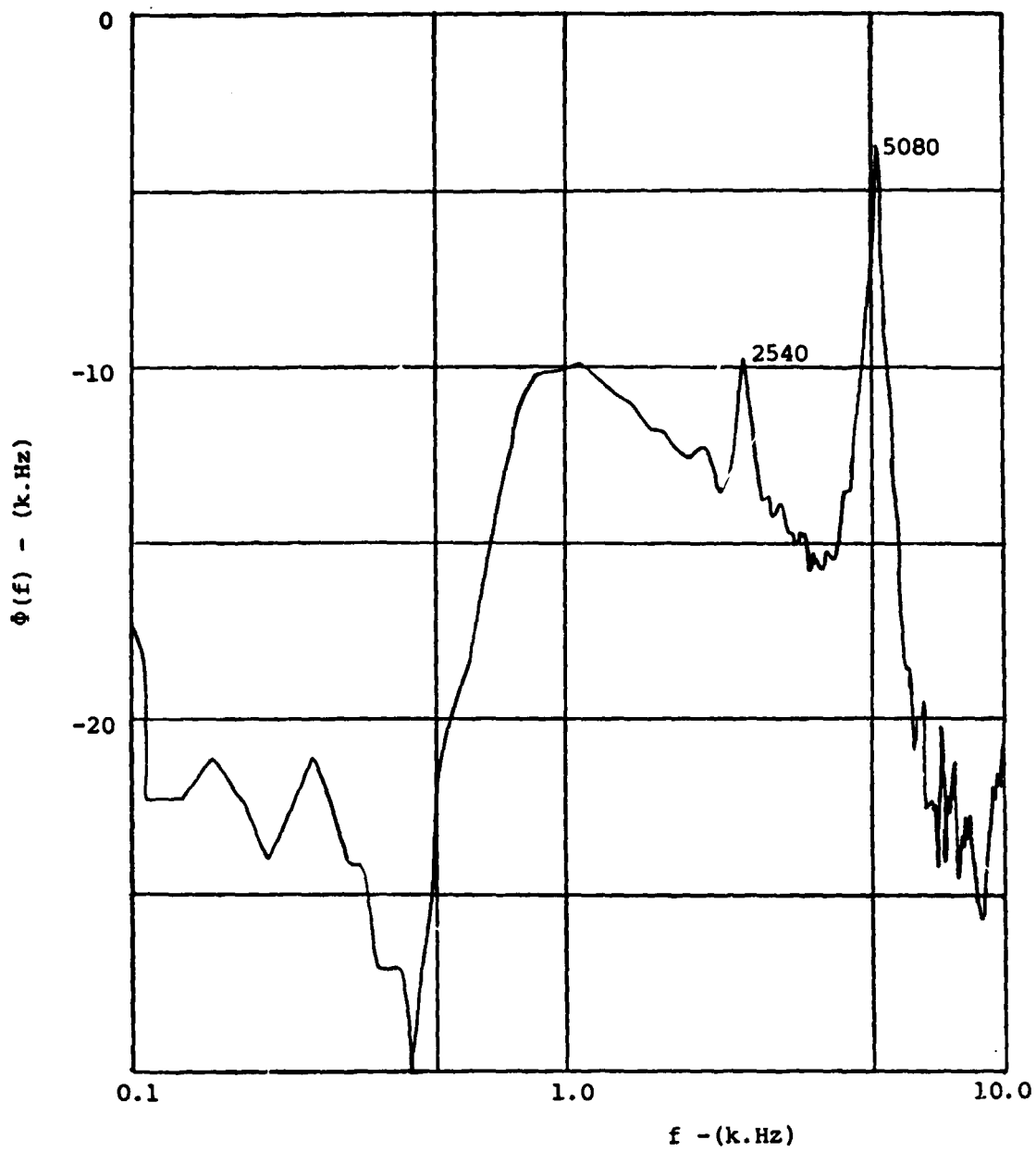
Figure III.8 (continued)

C-2



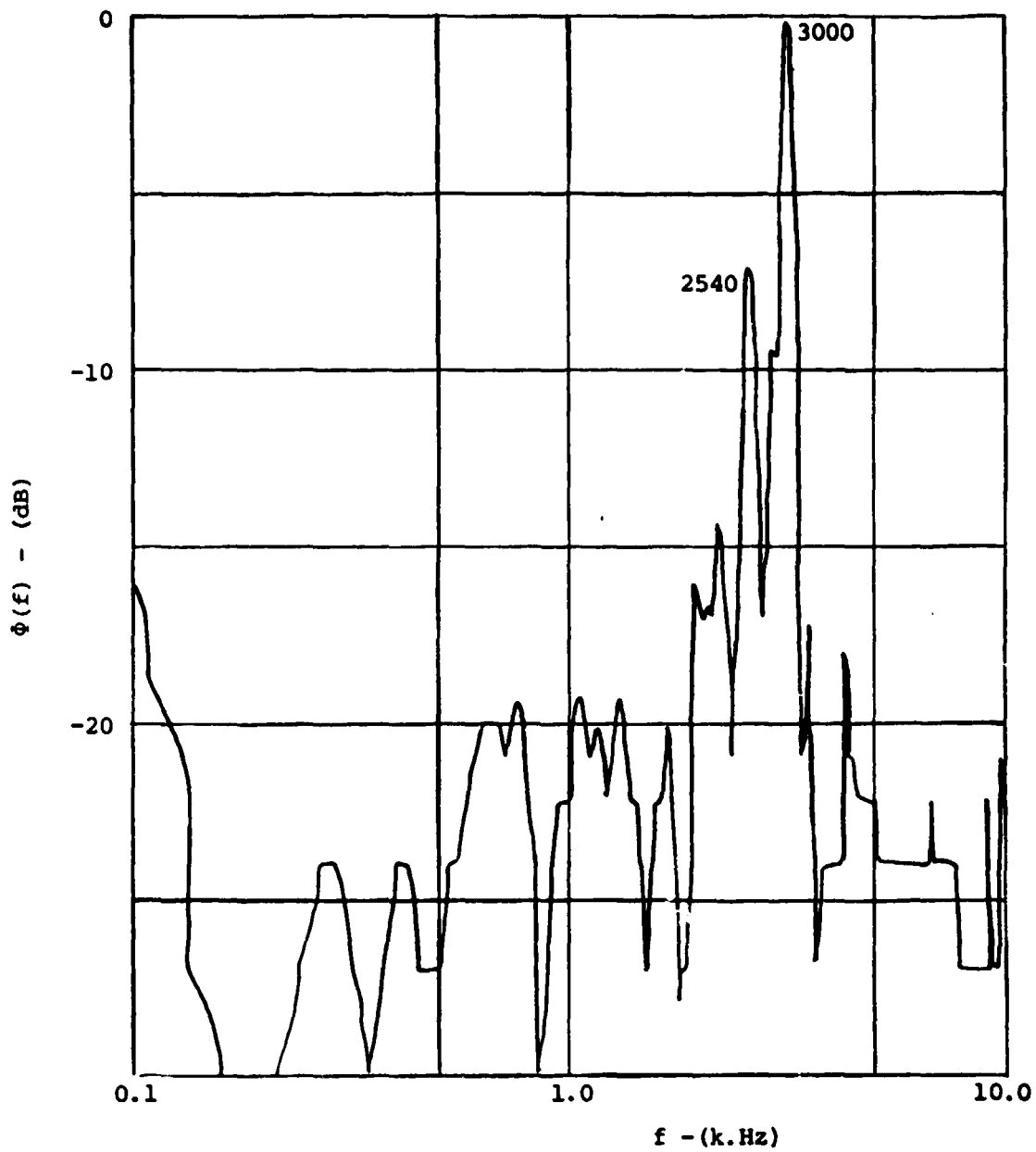
Transducer #12

Figure III.9 Auto Power Spectral Density of the Signal from the Transducer in the Blunt Trailing Edge



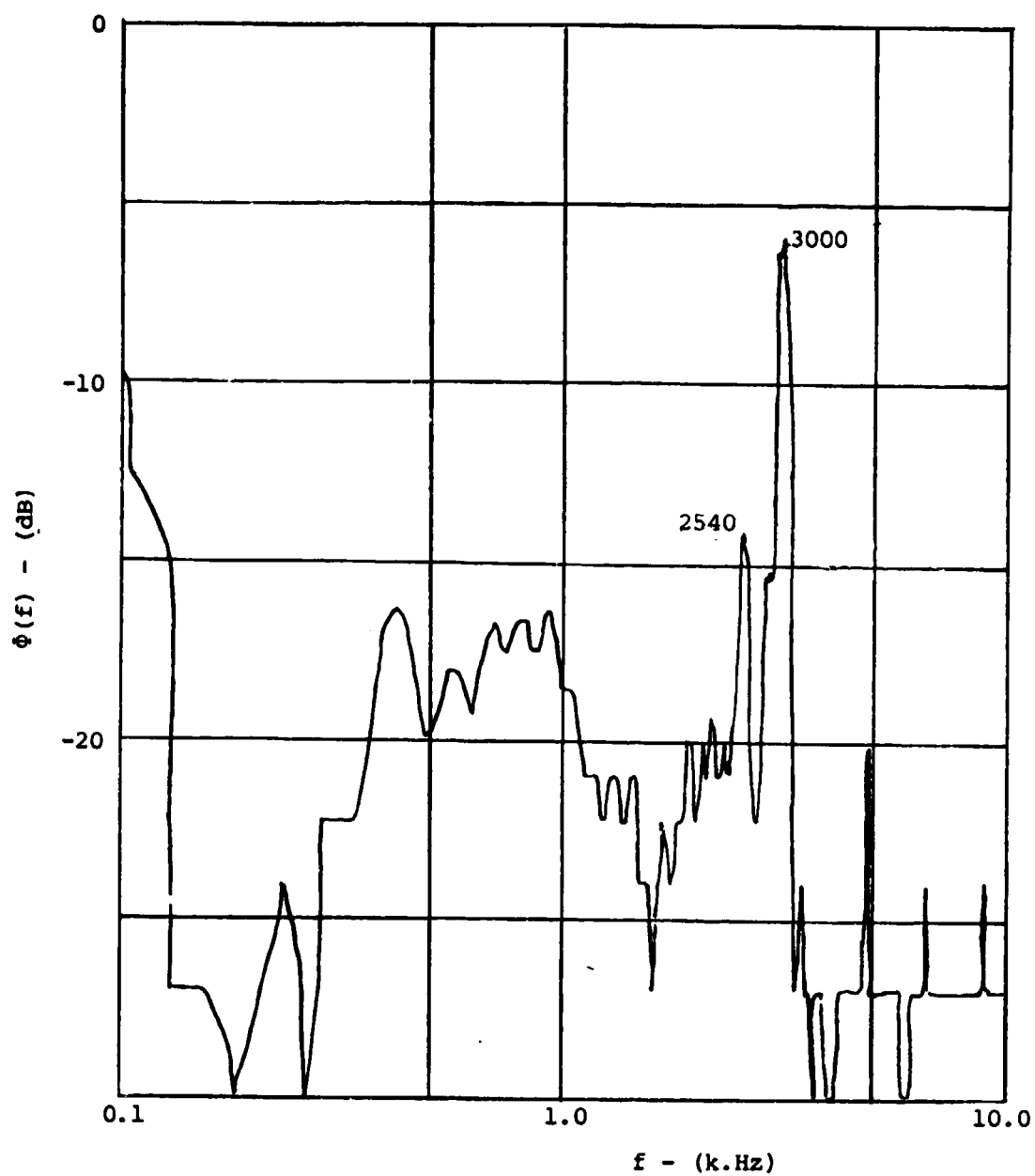
b) Transducer #11

Figure III.9 (continued)



a) Transducer #1

Figure III.10 Auto Power Spectral Density of the Signal from the Transducer Near the Leading Edge



b) Transducer #2

Figure III.10 (continued)

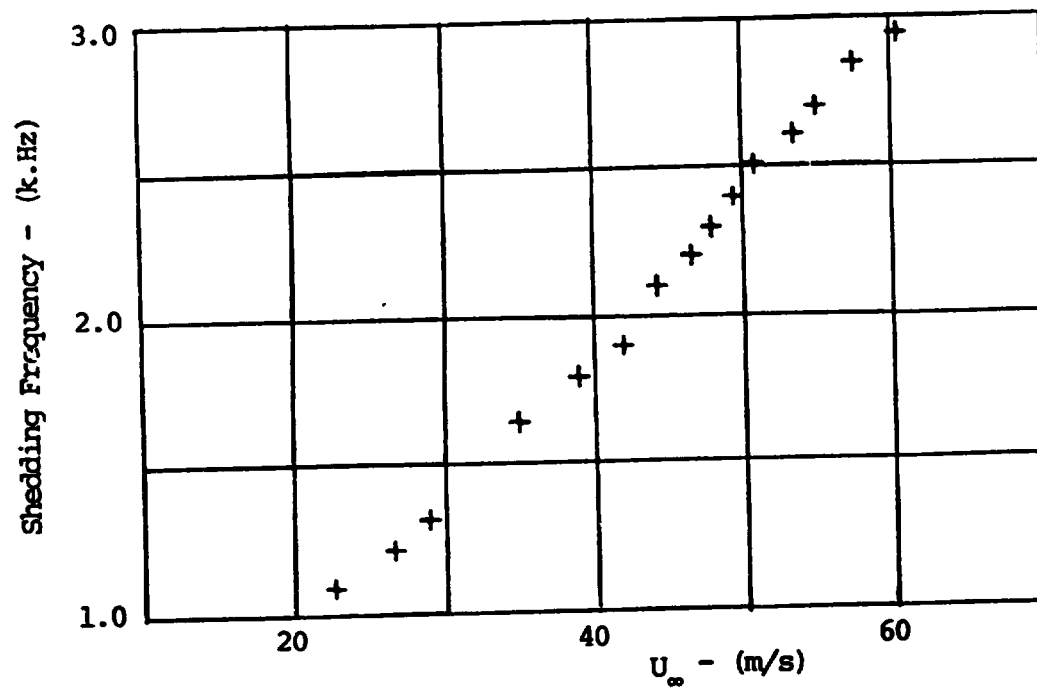


Figure III.11 Variation of the Shedding Frequency of the Airfoil I with Velocity

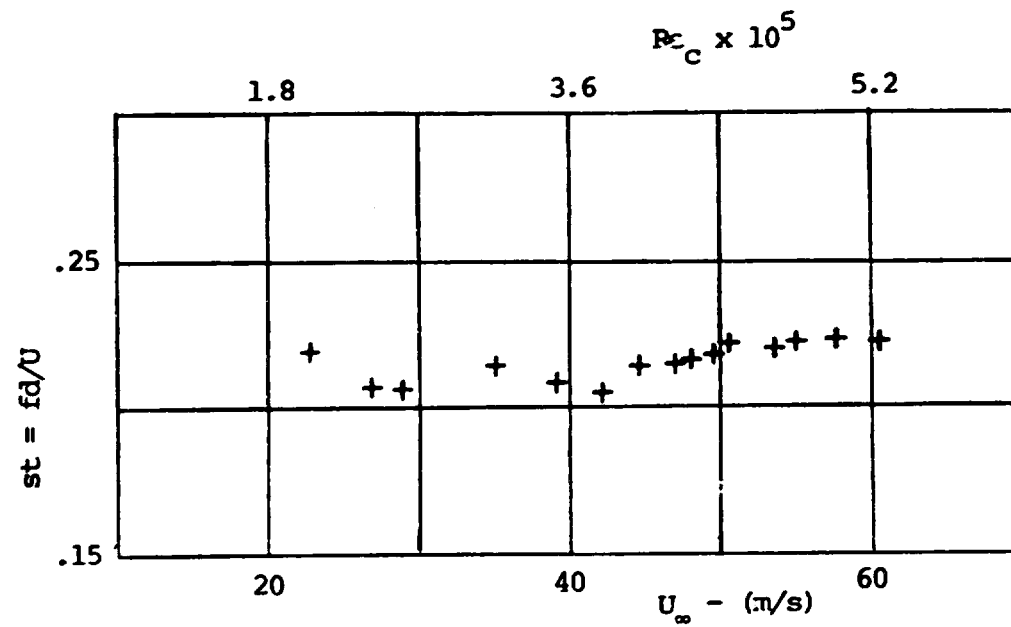


Figure III.12 Variation of Strouhal Number of Airfoil I with Velocity

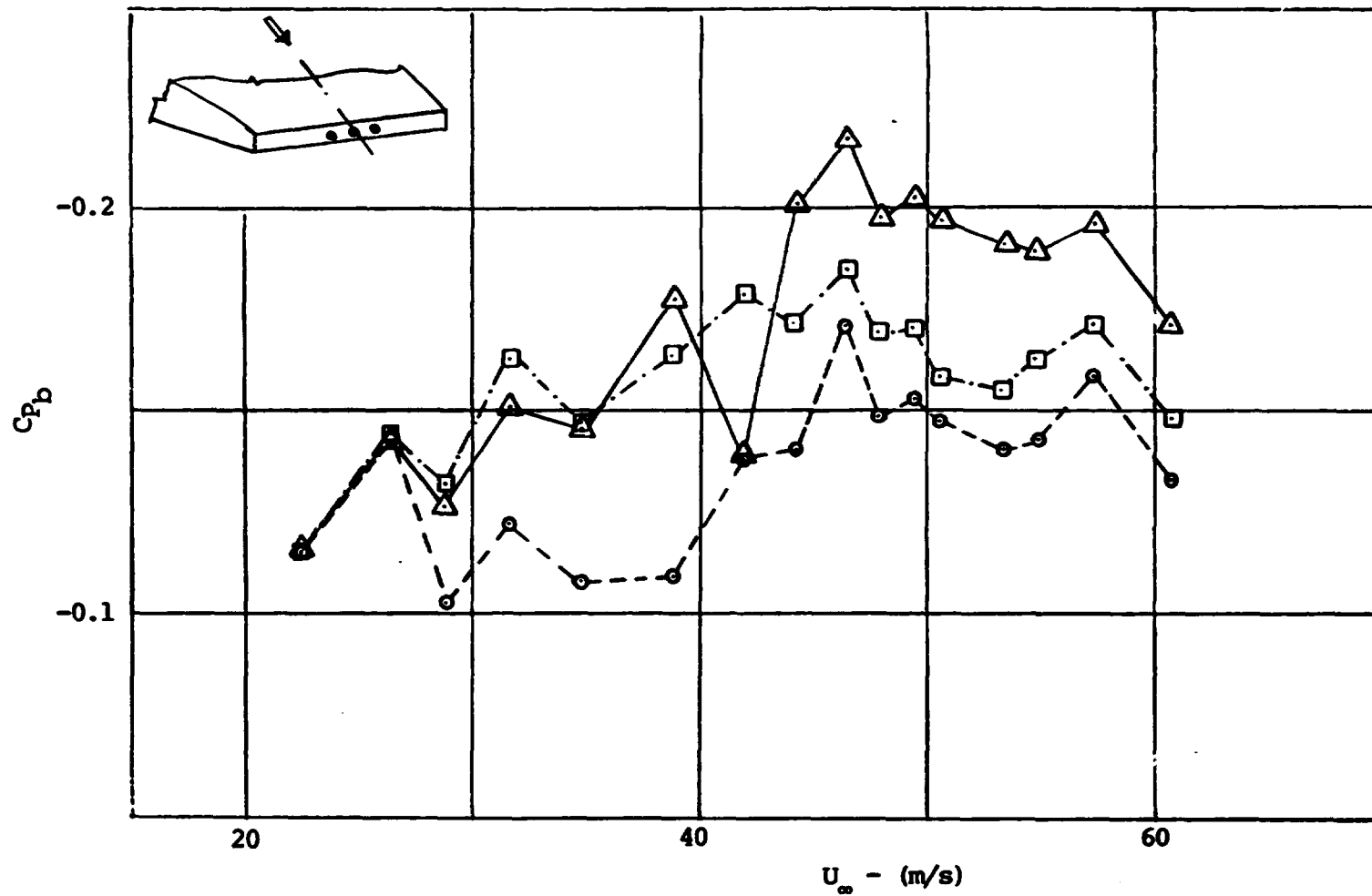


Figure III.13 Variation of the Base Pressure of the Truncated Airfoil with Transducers (Airfoil I) with Velocity
 (\circ , pressure tap #11 ; Δ , pressure tap #12 ; \square , pressure tap #13)

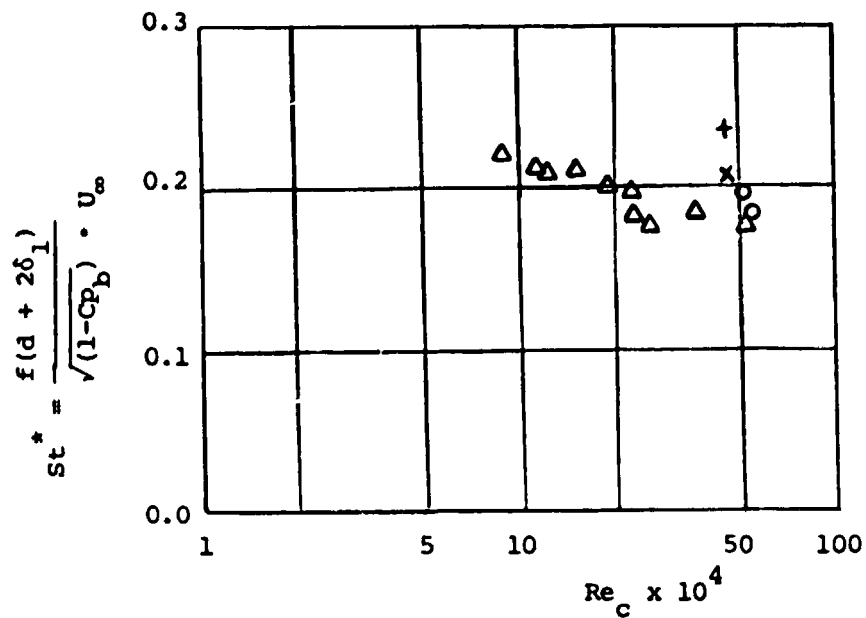


Figure III.14 Comparison of the Strouhal Number
 (Bauer (1961) Δ ; Davis (1975) O ;
 initial experimental data $\left\{ \begin{array}{l} C_{pb} = 0.0, +; \\ C_{pb} = -0.2, \times \end{array} \right.$

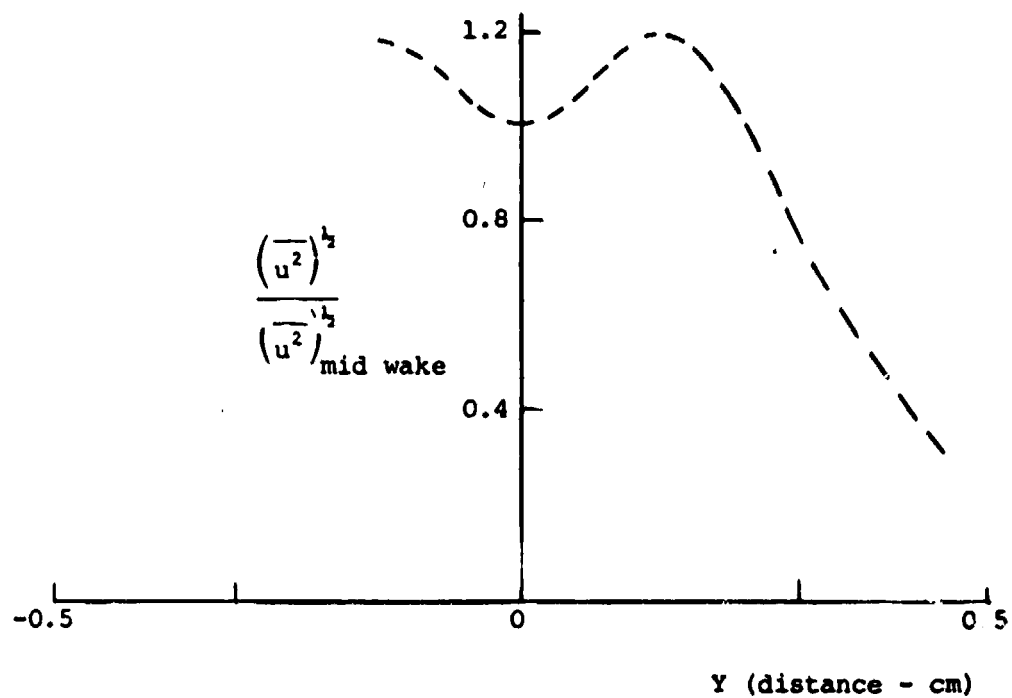


Figure III.15 Near Wake Profile of the RMS Value of the Fluctuating Velocity measured at 0.6cm. Down Stream of the Blunt Trailing Edge

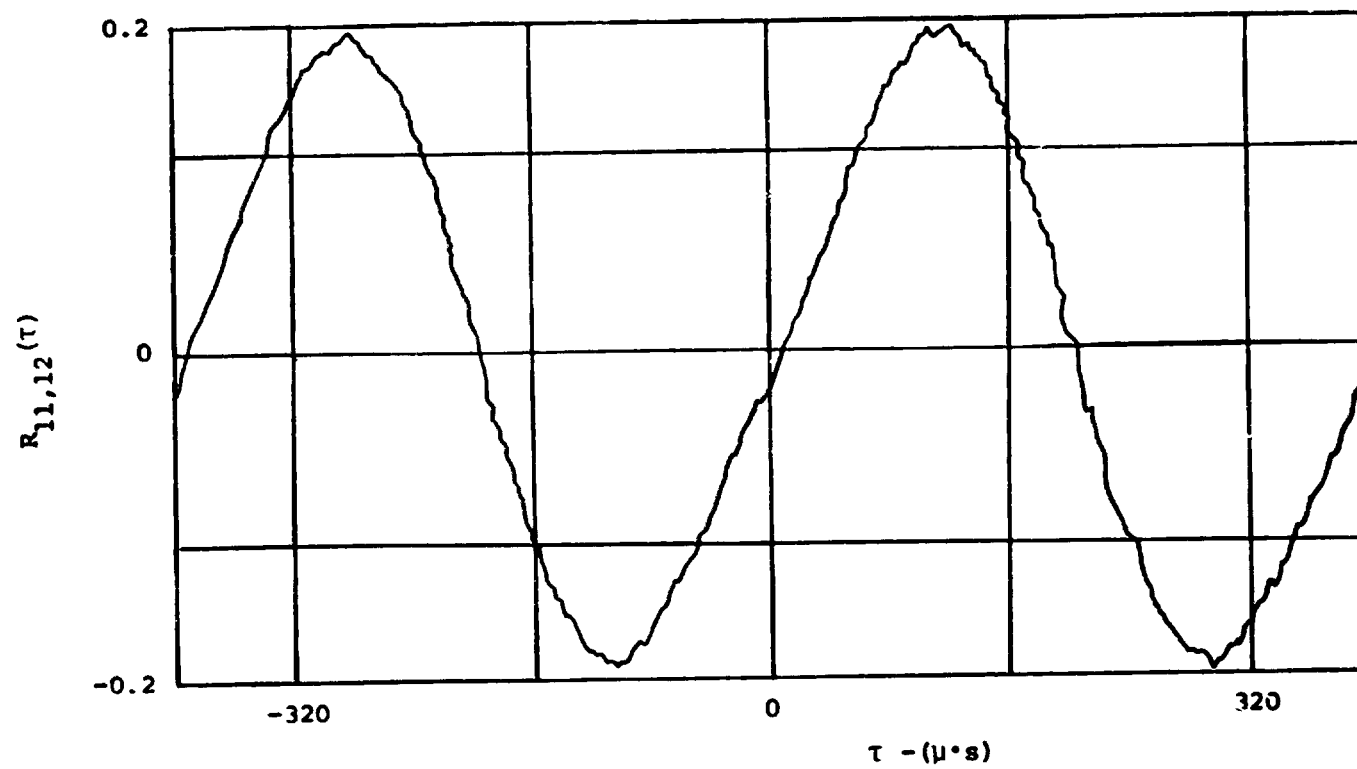


Figure III.16 Cross- Correlation of the Filtered Pressure Signal from Transducers #11 and #12, in the Blunt Trailing Edge

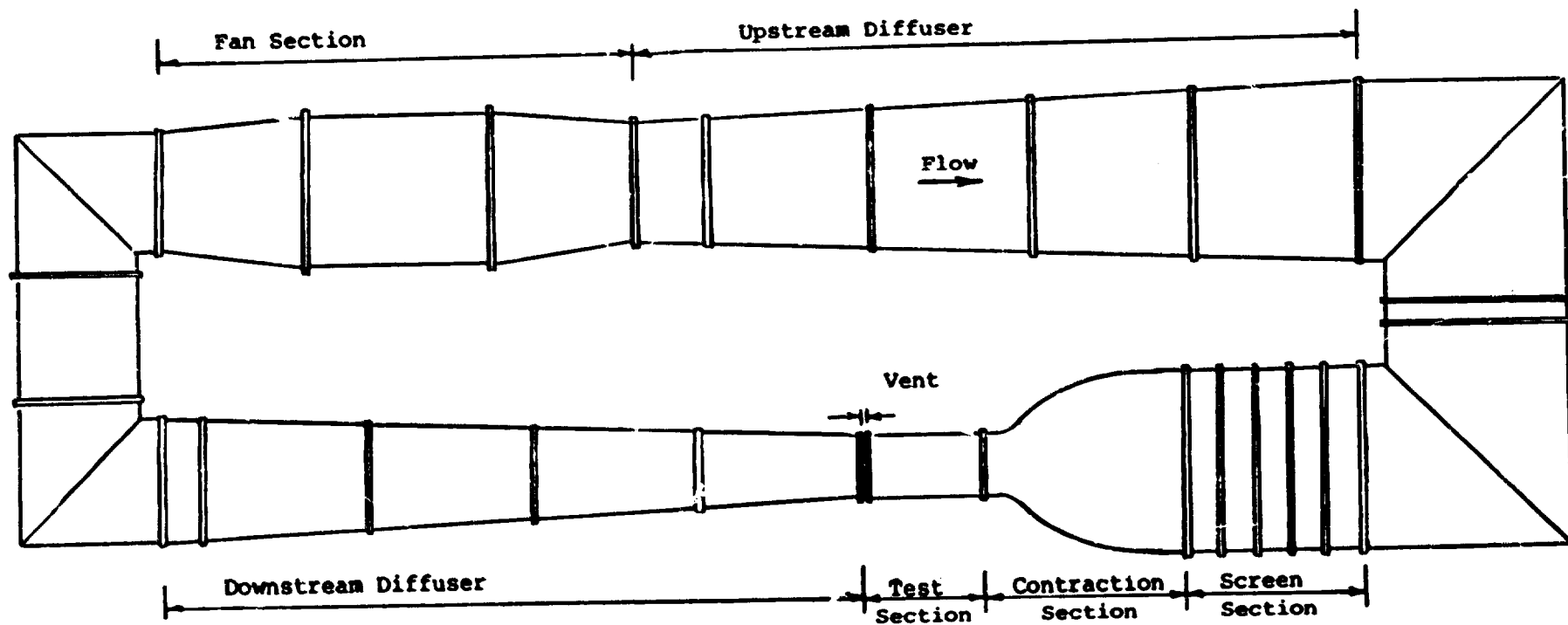
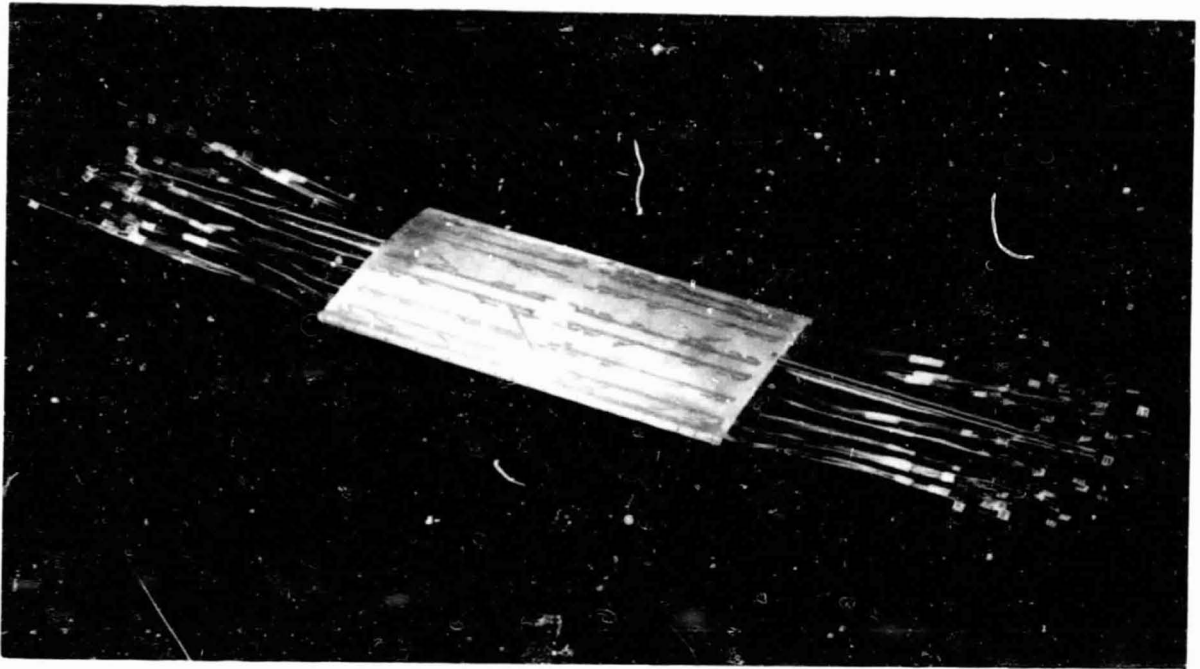
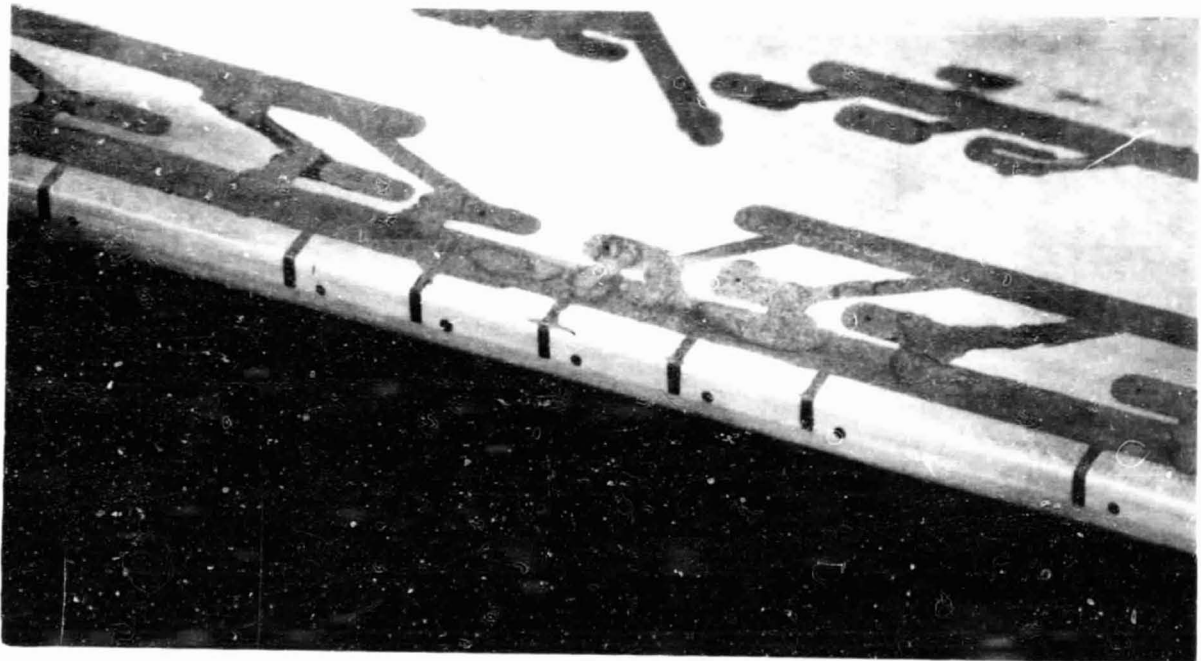


Figure IV.1 Plan View of the 45.7 x 45.7cm Subsonic Wind Tunnel

ORIGINAL PAGE
BLACK AND WHITE PHOTOGRAPH



a) Airfoil II with Pressure Tubes



b) Close View of the Trailing Edge

Figure IV.3 Blunt Trailing Edge Airfoil with Static Pressure taps
(Airfoil II)

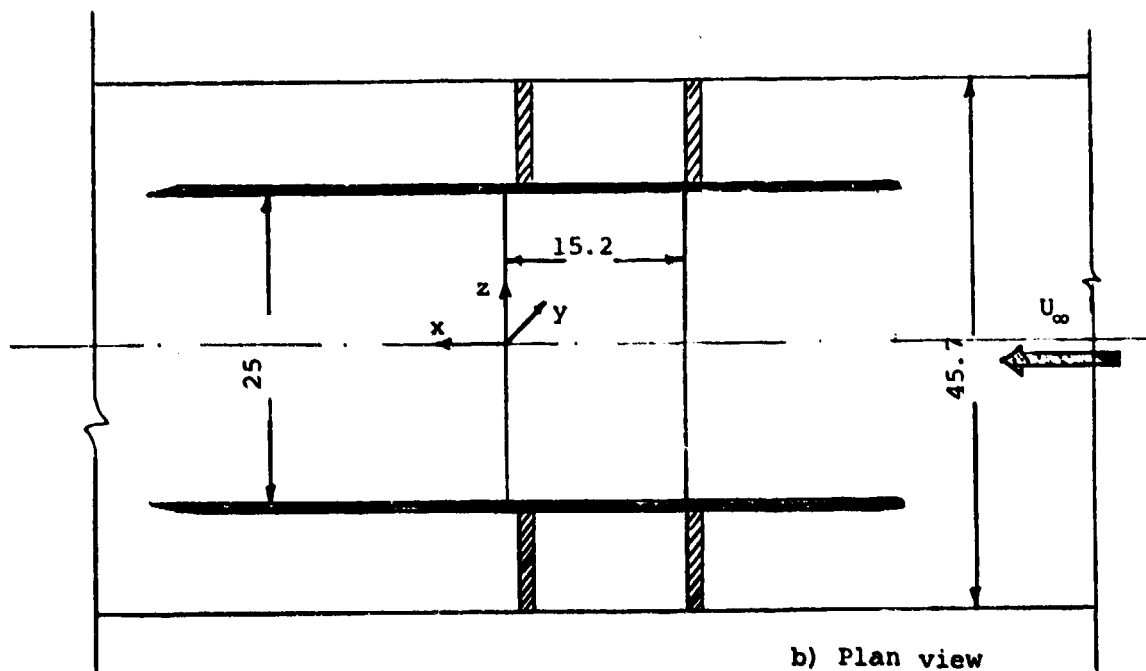
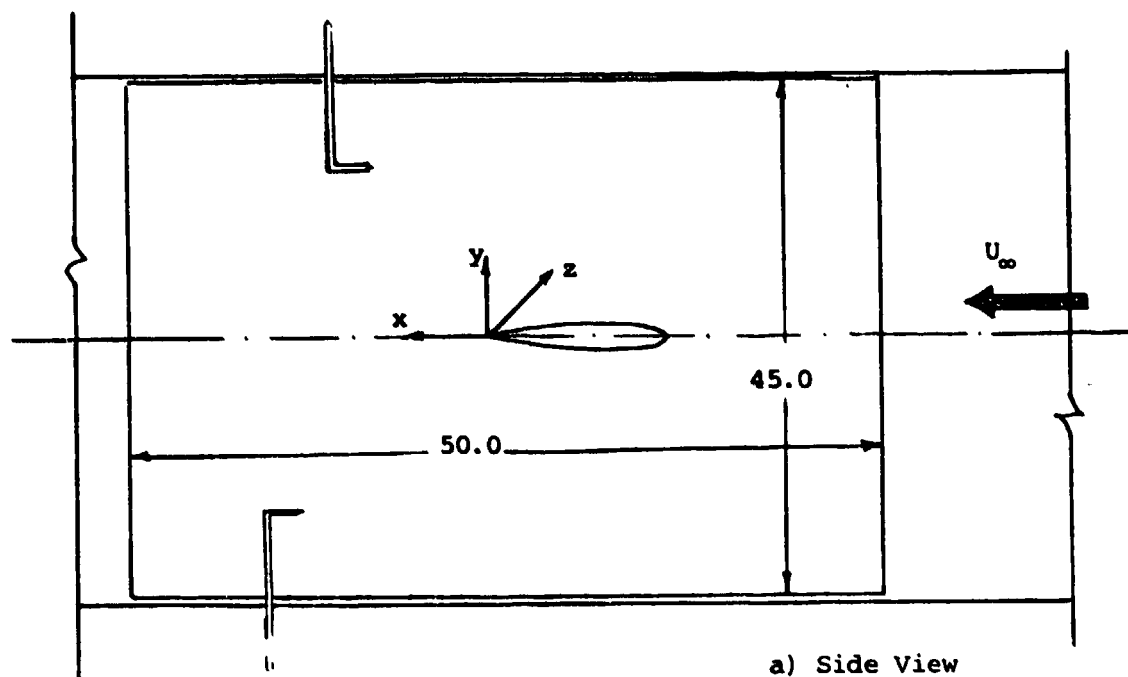
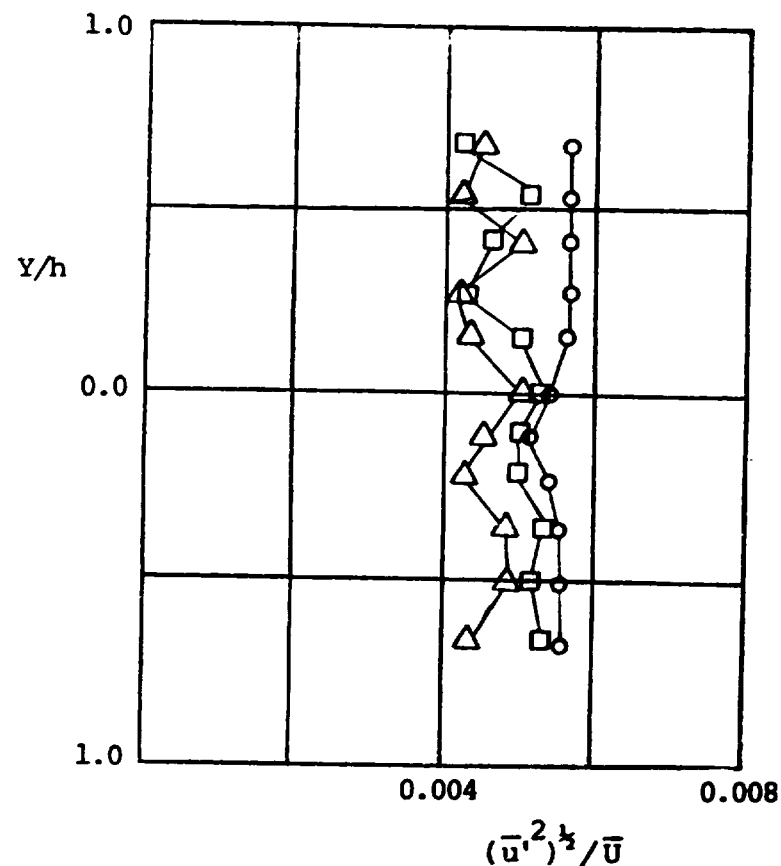
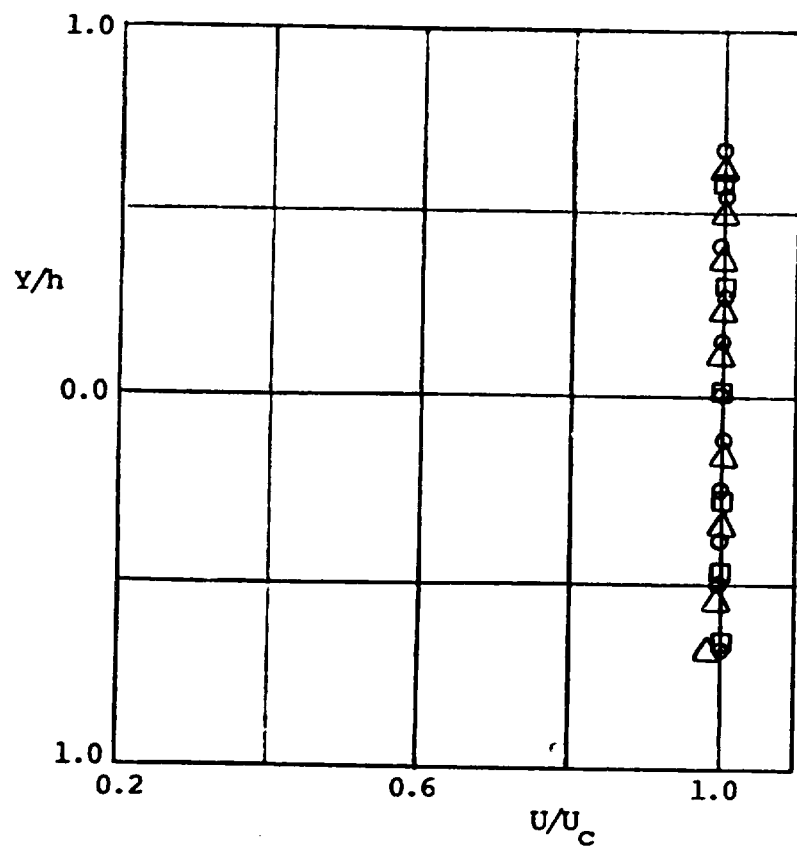
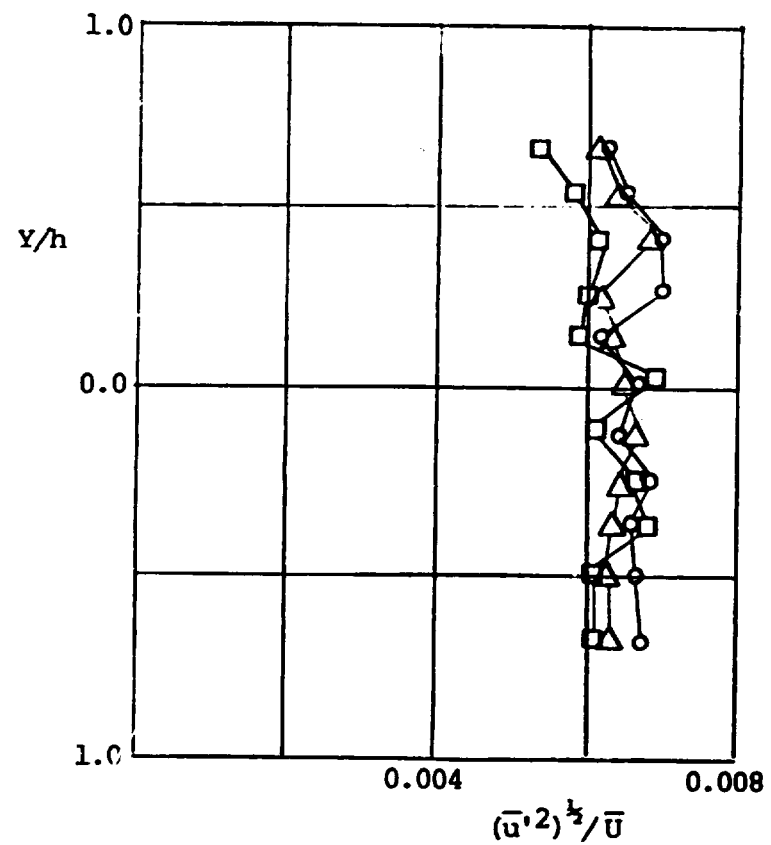
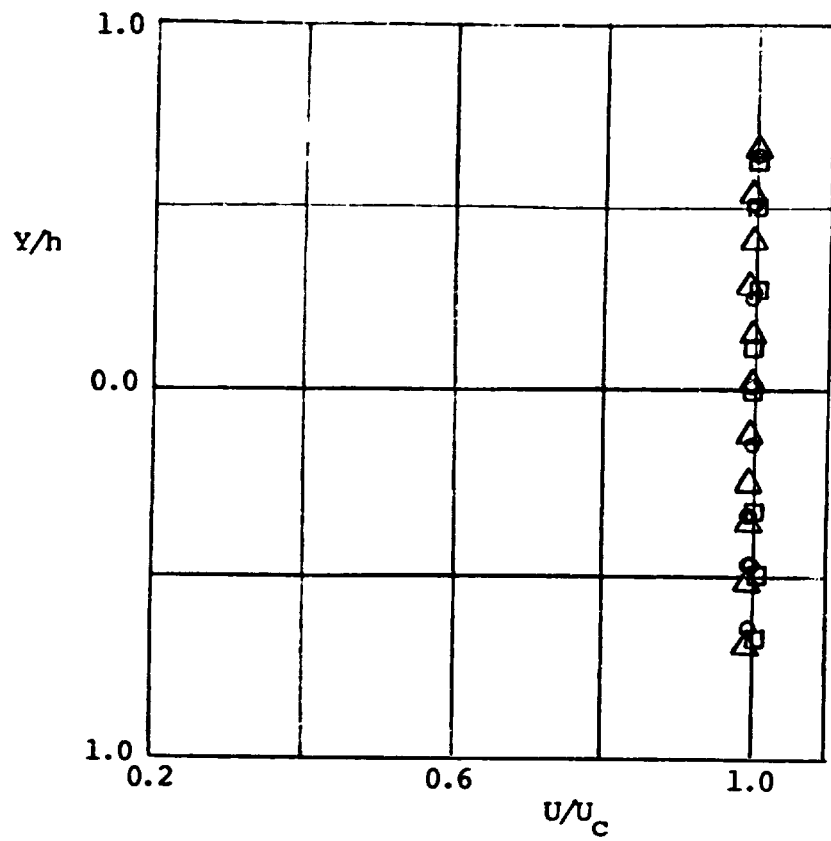


Figure IV.4 Airfoil Model Held Between the End Plates and in the Tunnel (all dimensions are in cm.)



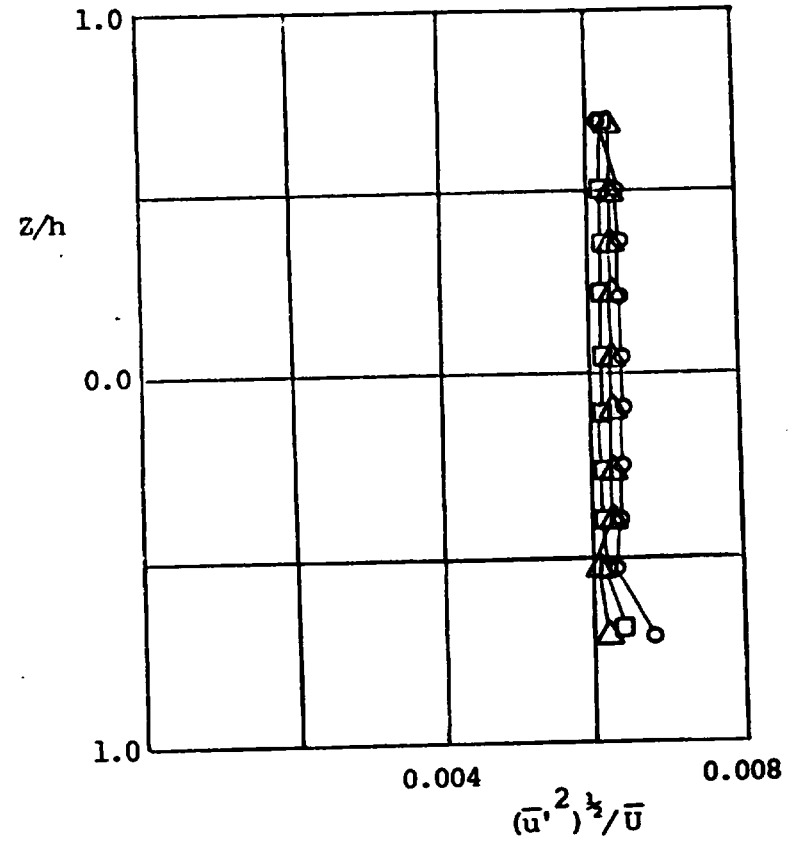
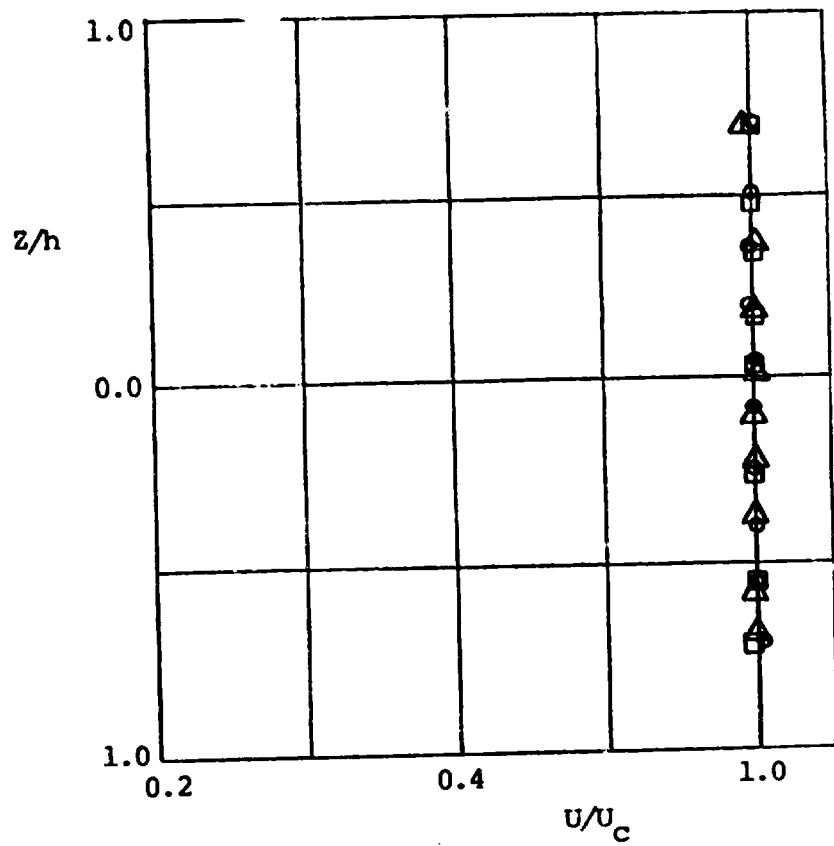
a) $U_\infty = 32\text{m/s}$

Figure IV.5 Profiles of the Mean Velocity and RMS Fluctuating Velocity in the mid vertical plane for empty test section.
(distance from the upstream edge of the test section: 16.7cm , \circ ; 36.2cm , Δ ; 46.2cm , \square)



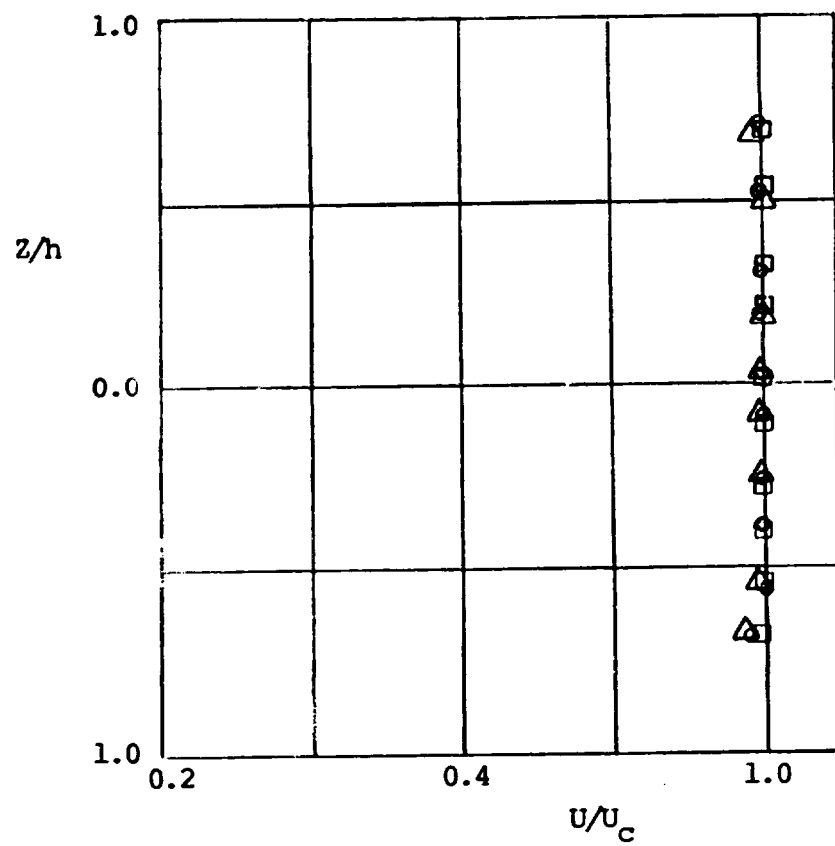
b) $U_\infty = 48 \text{ m/s}$

Figure IV.5 (continued)



a) $U_\infty = 32\text{m/s}$

Figure IV.6 Mean Velocity and RMS Fluctuating Velocity in the Mid Horizontal Plane with empty test section
(distance from the upstream edge of the test section : 16.7cm , \circ ; 36.2cm , Δ ; 48.0cm , \square)



b) $U_\infty = 48\text{m/s}$

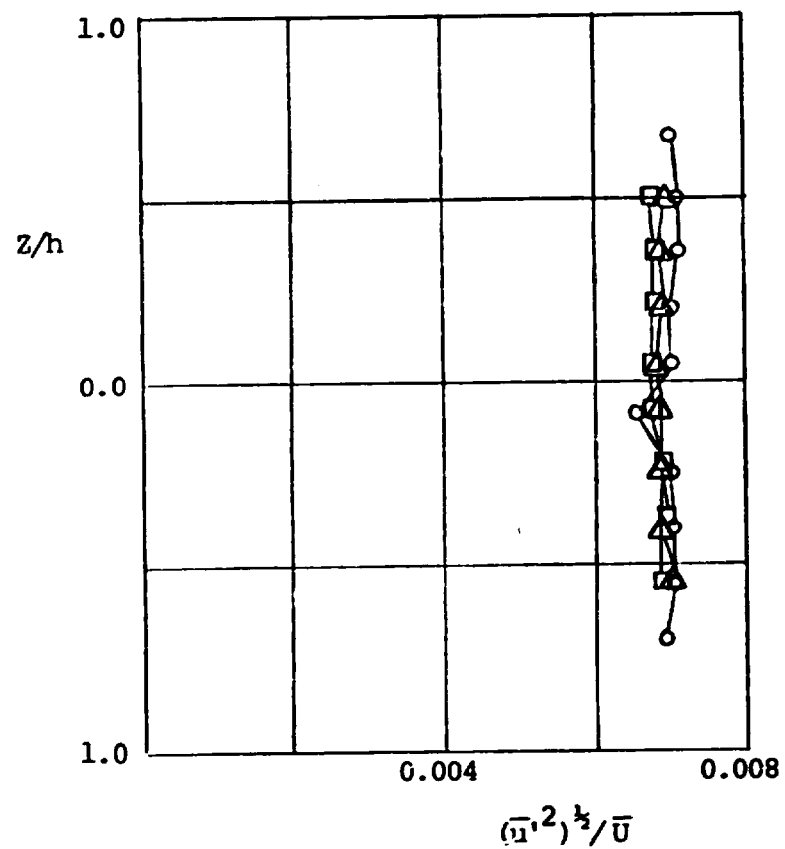
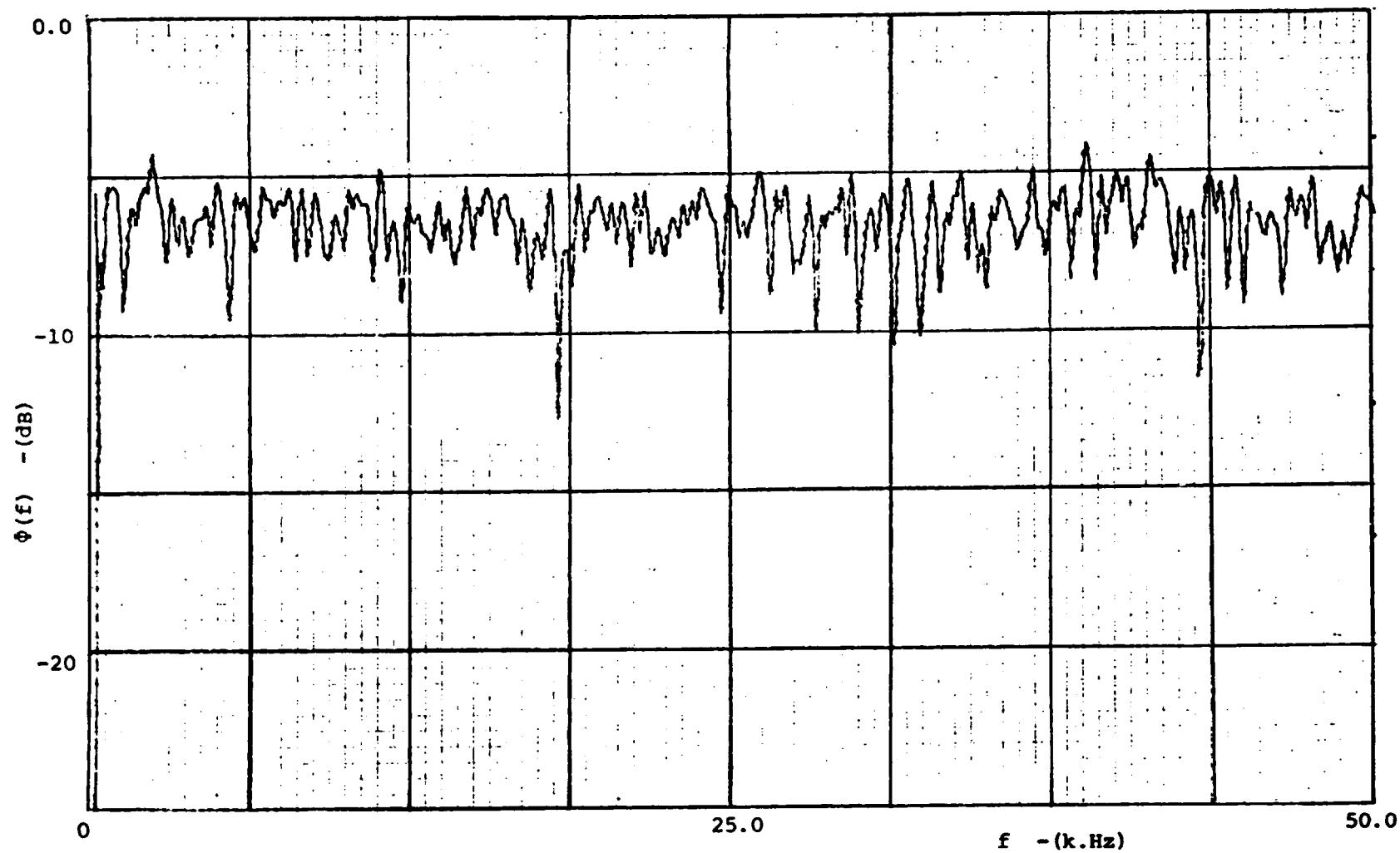
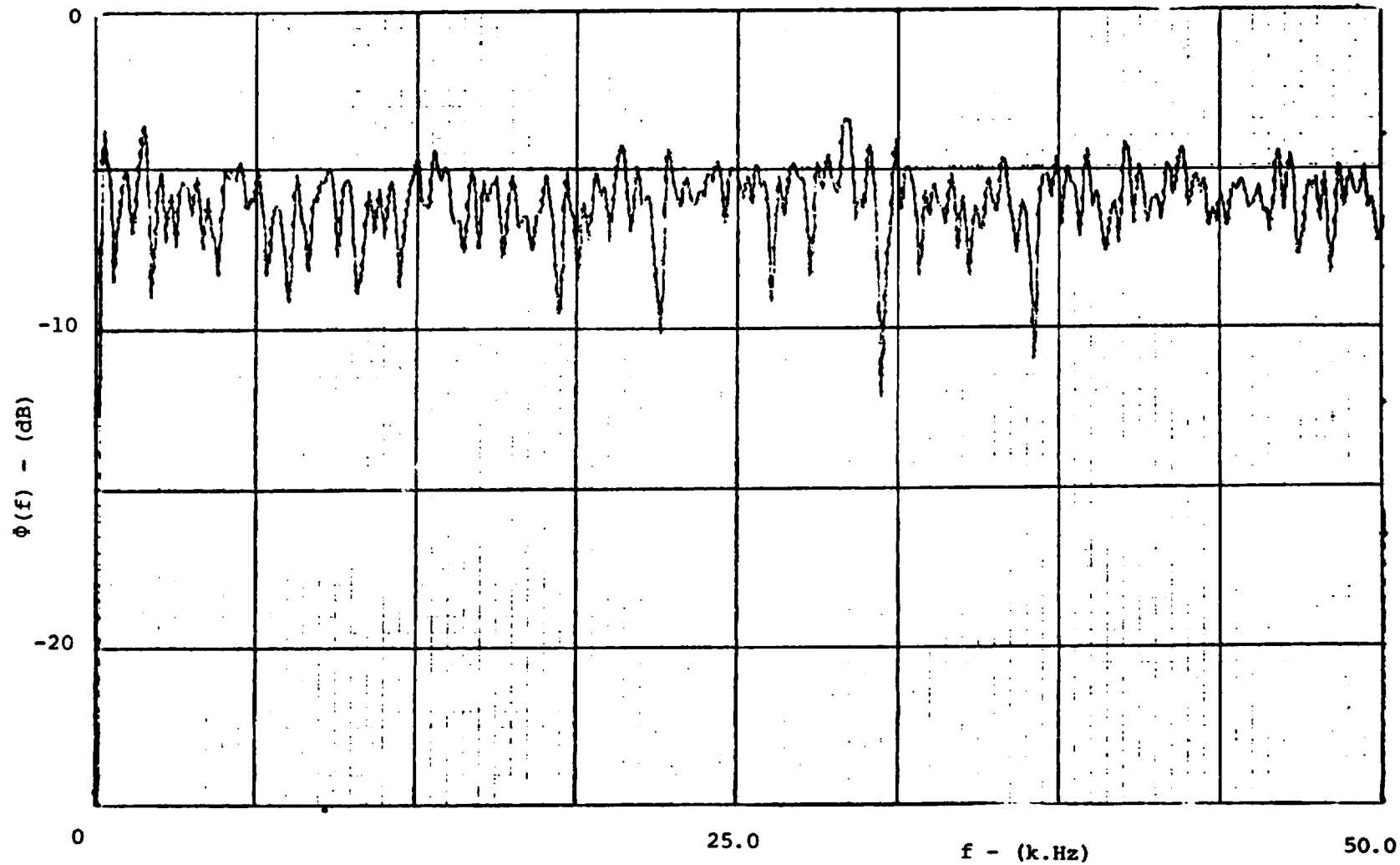


Figure IV.6 (continued)



a) $U_{\infty} = 32m/s$

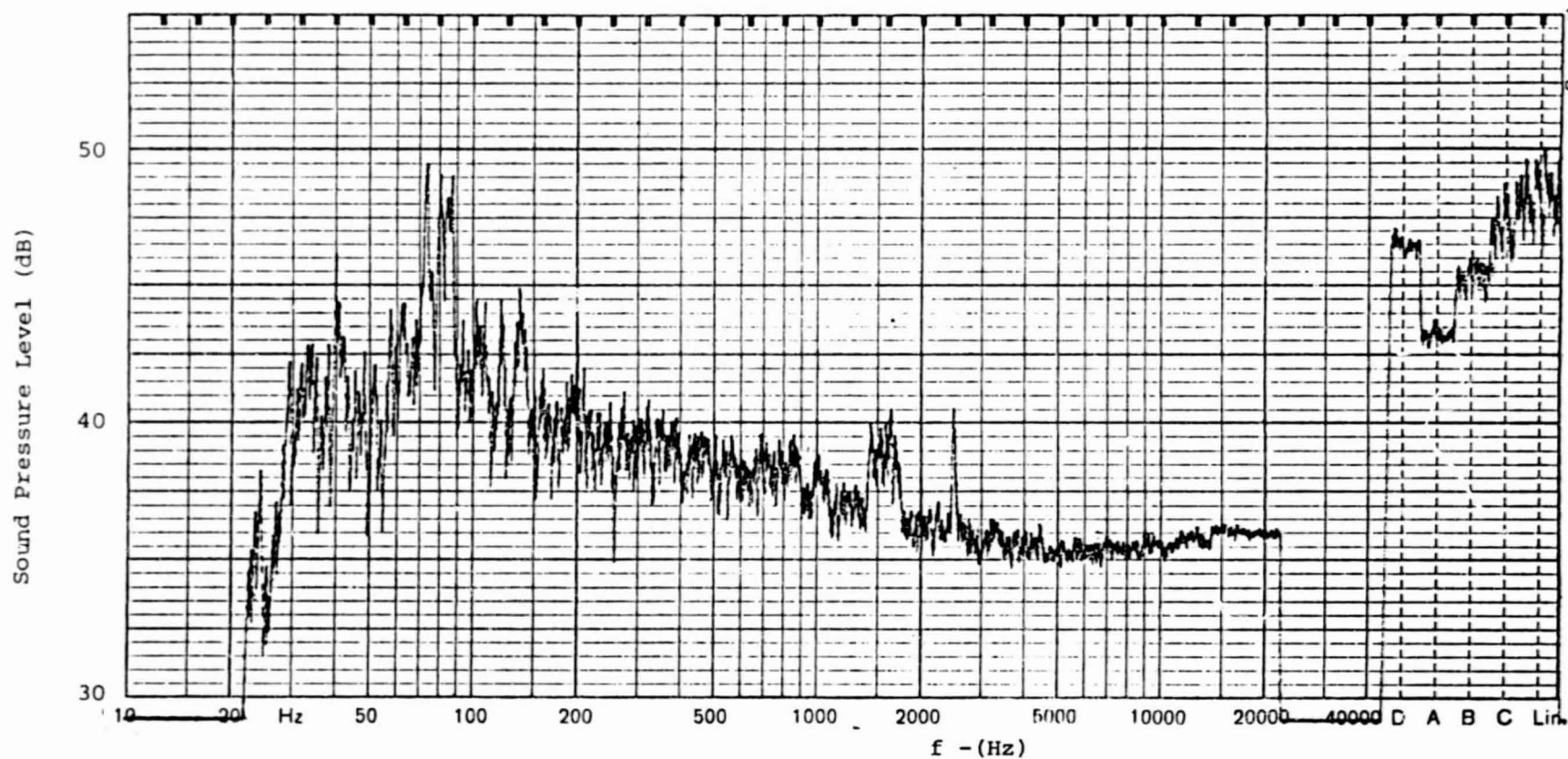
Figure IV.7 Power Spectral Density of Fluctuating Velocity Component



b) $U_{\infty} = 48\text{m/s}$

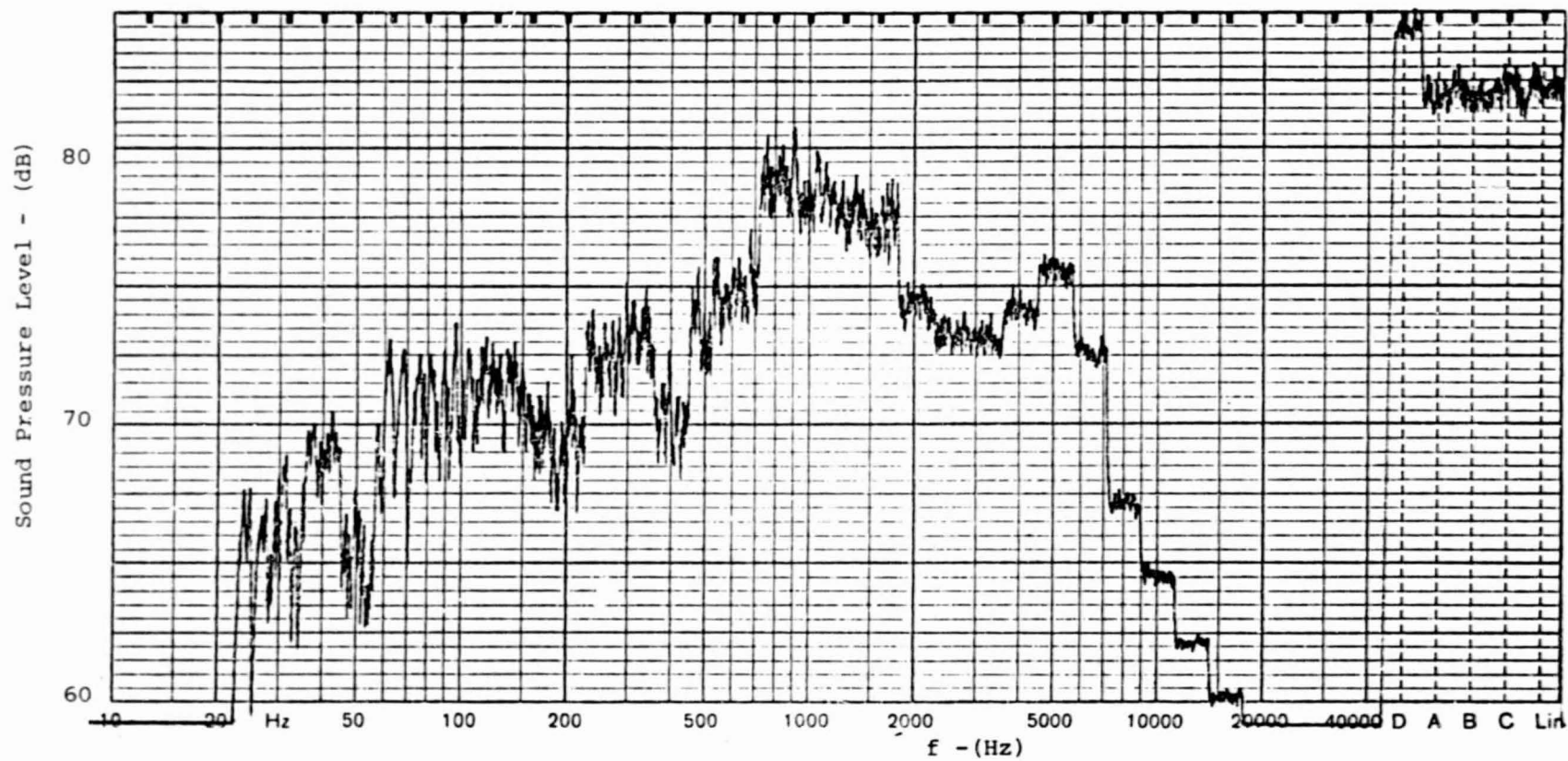
Figure IV.7 (continued)

ORIGINAL FROM IT
OF POOR QUALITY



a) No Flow

Figure IV.8 Measured 1/3 Octave Band Acoustic Spectrum at the Center of the Empty Test Section



b) $U_{\infty} = 24\text{m/s}$

Figure IV.8 (continued)

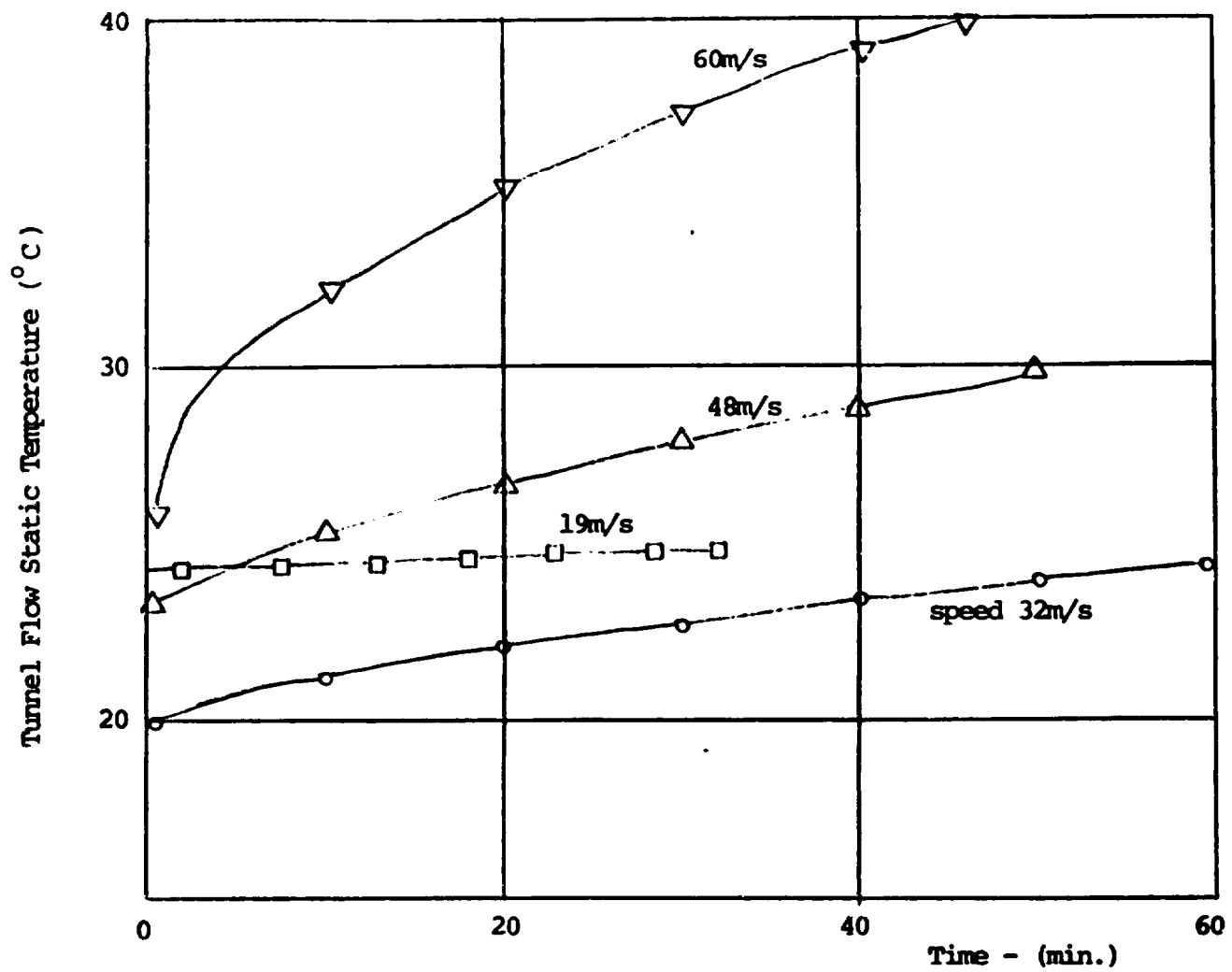


Figure IV.9 Time Variation of Static Temperature in Test Section Flow

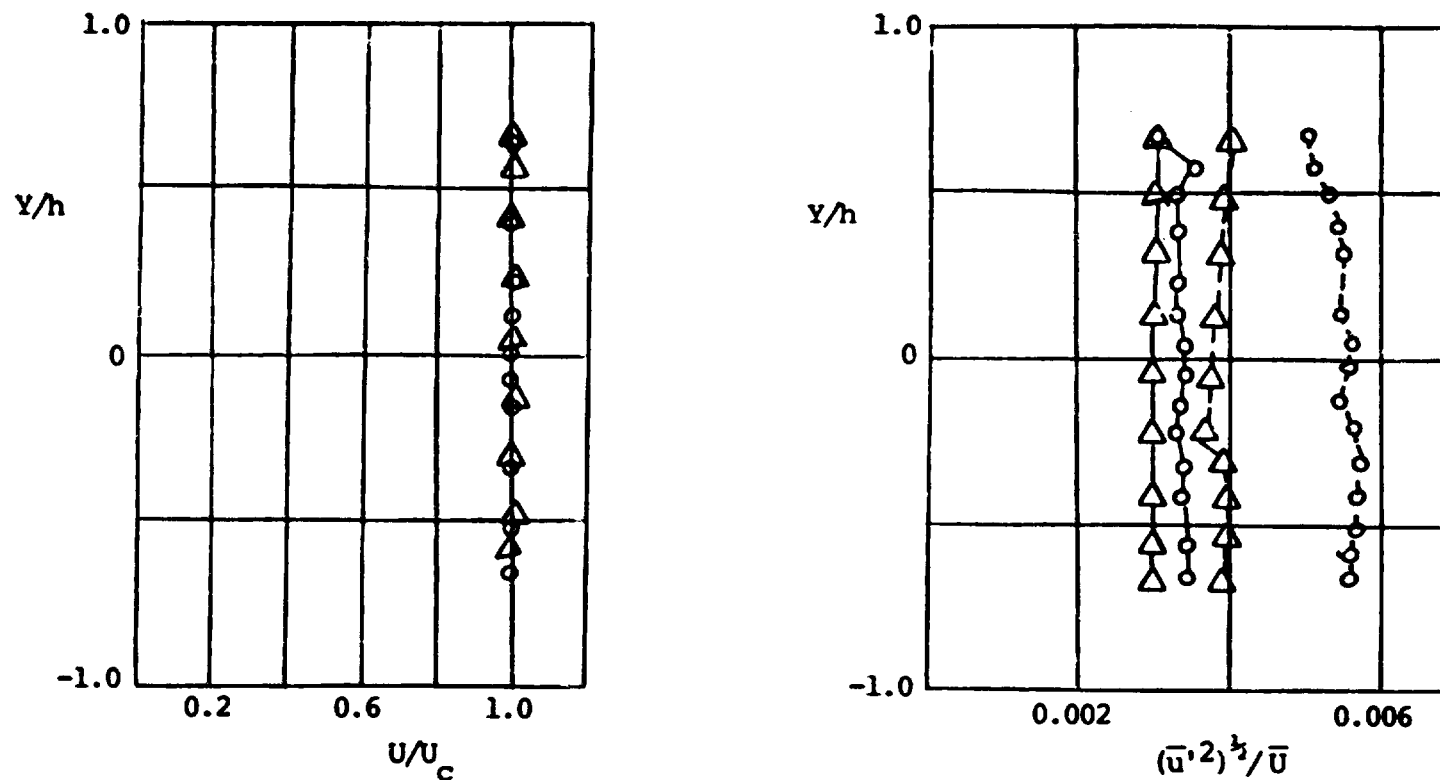


Figure IV.10 Profiles of Mean Velocity and RMS of Fluctuating Velocity in the Vertical Plane, With End Plates in the Test Section (distance from Upstream edge of test section ;
 at 31.0cm : —○—, 24m/s; —△—, 48m/s ;
 at 42.0cm : --○--, 24m/s; --△--, 48m/s)

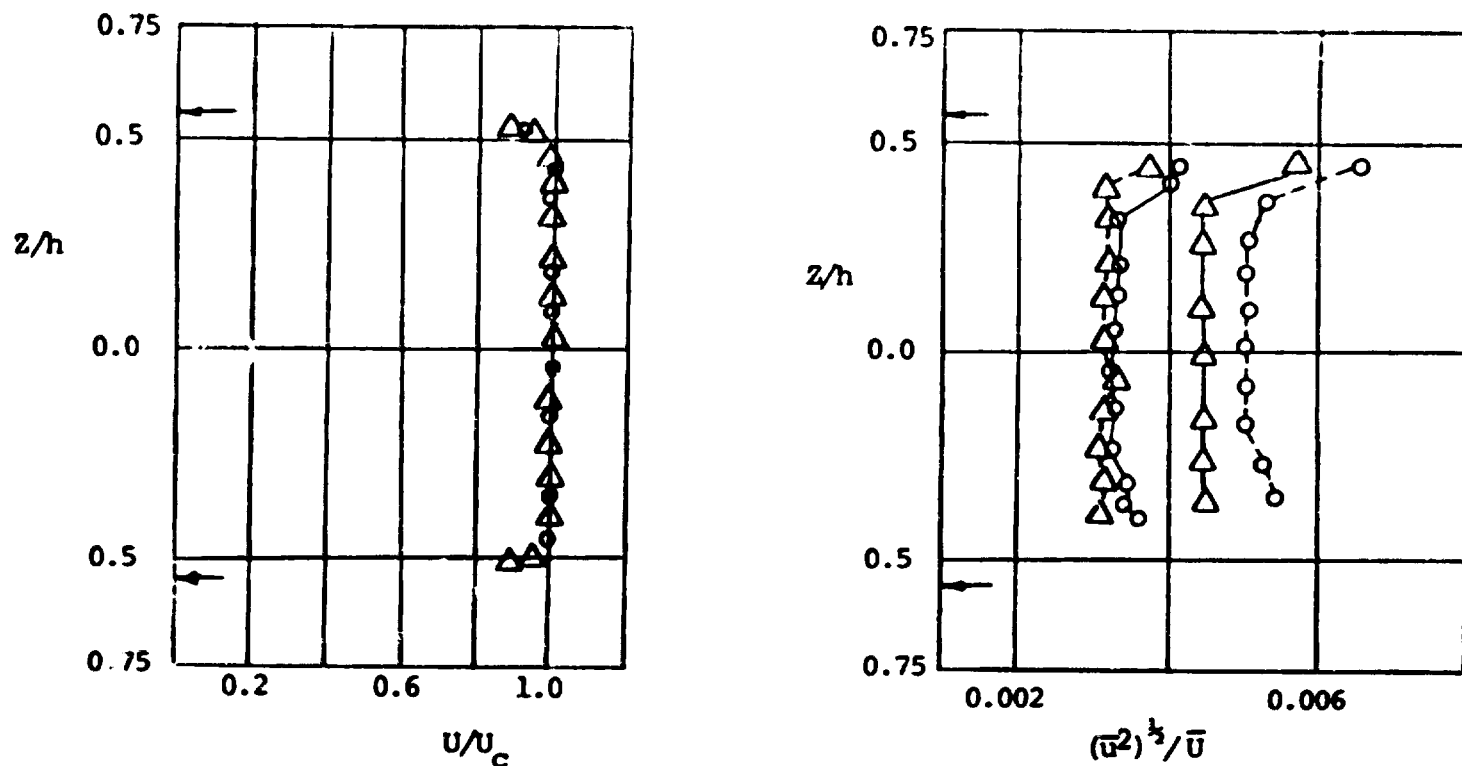


Figure IV.11 Profiles of Mean Velocity and RMS of Fluctuating Velocity in a Horizontal Plane, with End Plates in Test Section (arrows mark the position of the end plates in the test section; distance from upstream edge of the test section; at 31.0cm : $\text{---}\bigcirc\text{---}$, 24m/s ; $\text{---}\triangle\text{---}$, 48m/s ; at 41.5cm : $\text{---}\bigcirc\text{---}$, 24m/s ; $\text{---}\triangle\text{---}$, 48m/s)

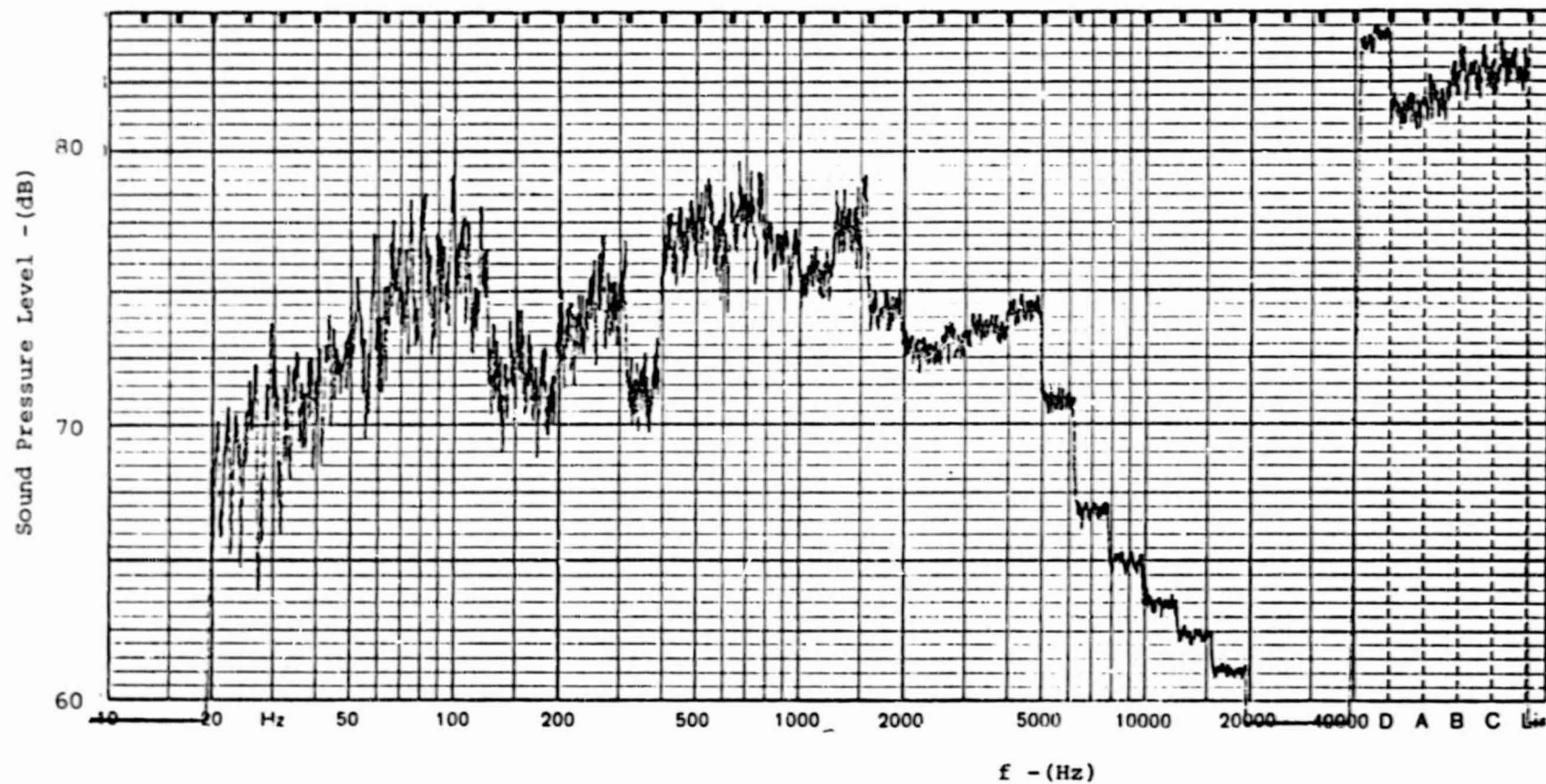
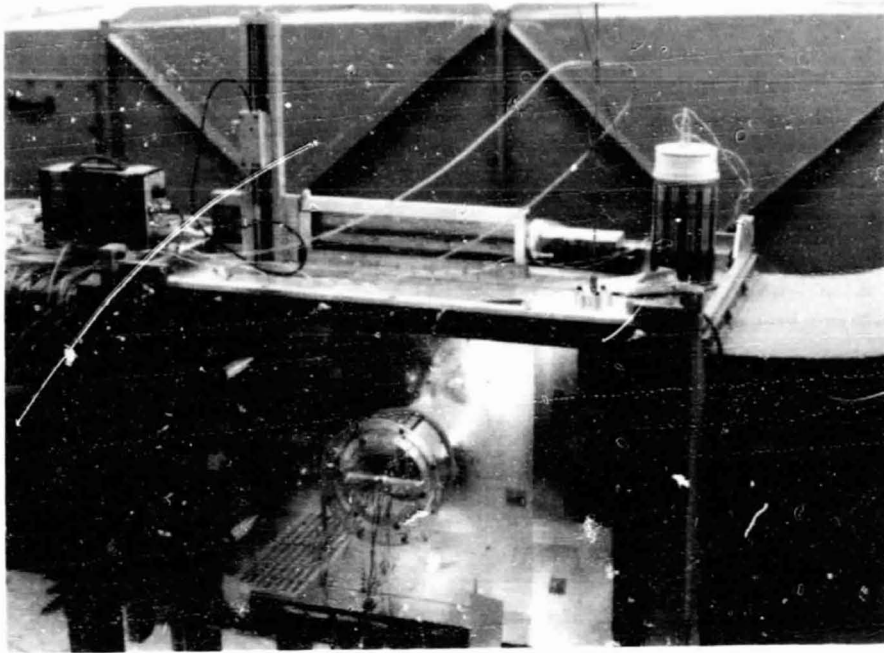
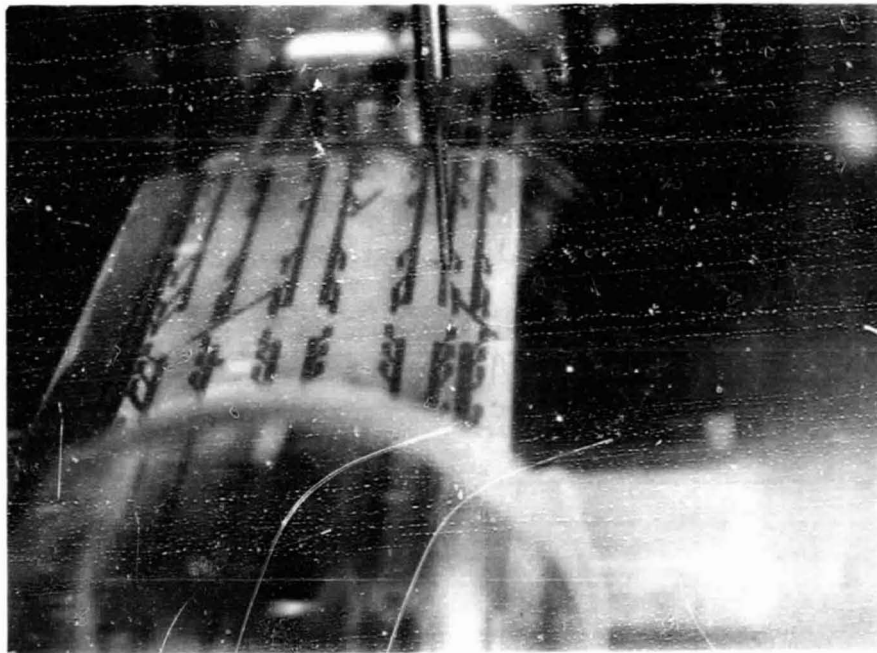


Figure IV.12 Measured 1/3 Octave Band Acoustic Spectrum at the Center of the Test Section, with End Plates and at a Velocity of 24m/s

ORIGINAL PAGE
BLACK AND WHITE PHOTOGRAPH



a) View of the model in tunnel



b) Close up view of the airfoil model

Figure V.1 Airfoil Model in the 45.7 x 45.7cm Tunnel

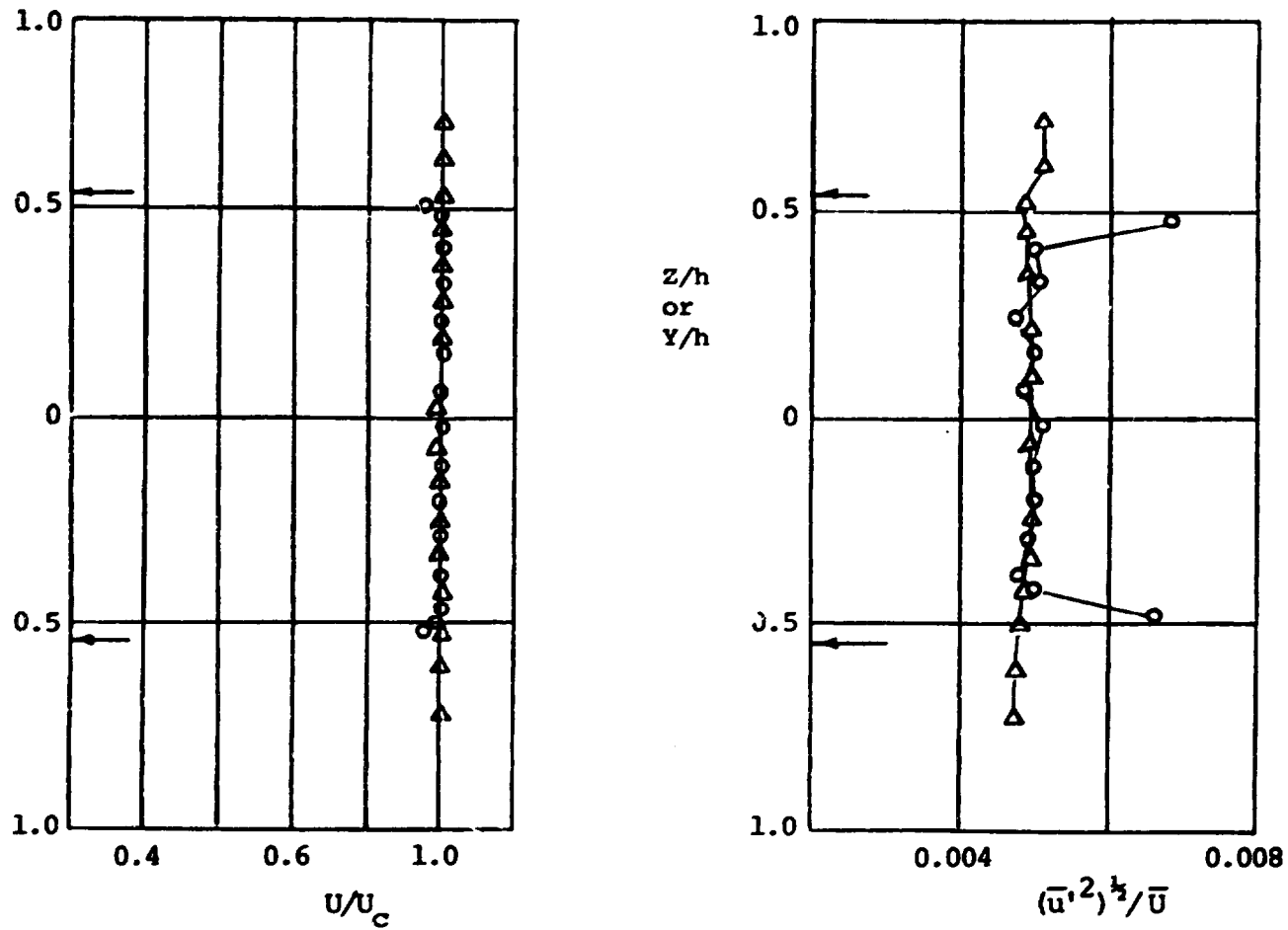
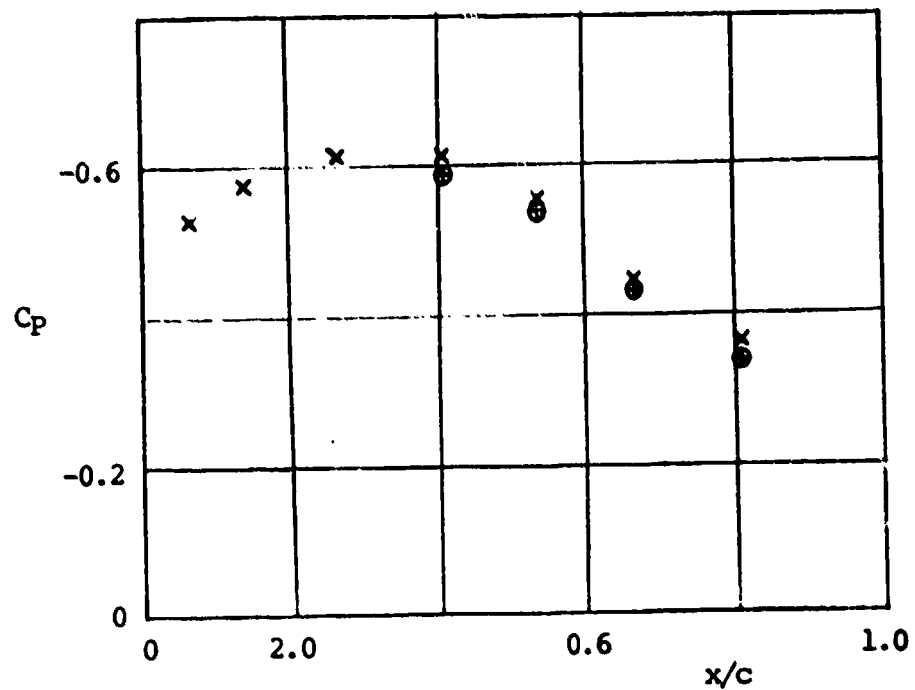
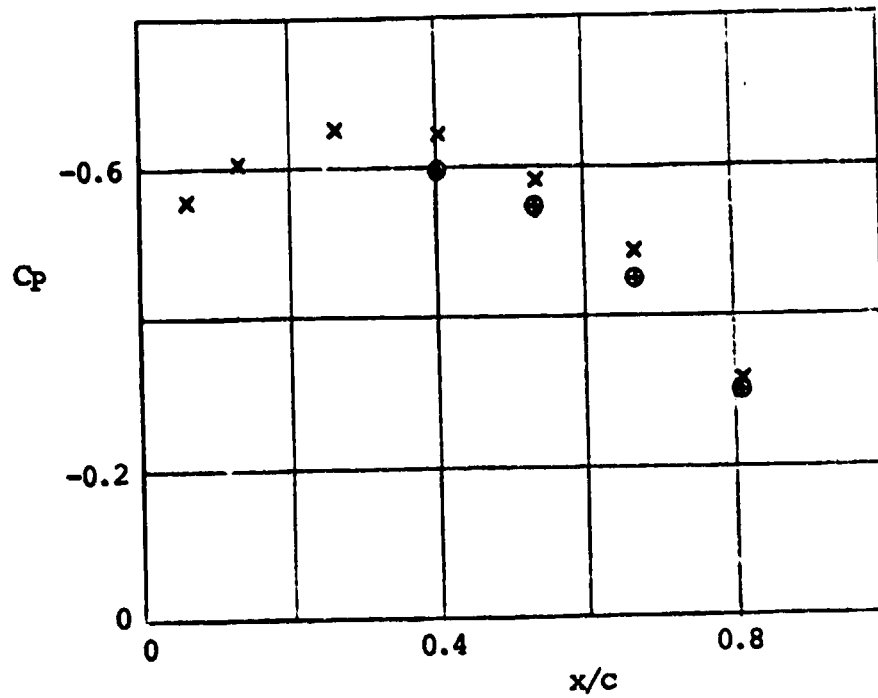


Figure V.2 Velocity Profiles Measured at 6cm Upstream of the Leading Edge of the Airfoil Model at a Velocity of 26m/s (measuring position corresponds to 32.6cm from the upstream edge of the test section; arrows mark the position of the end plates ; in the vertical plane, —○—; in the horizontal plane, —△—)



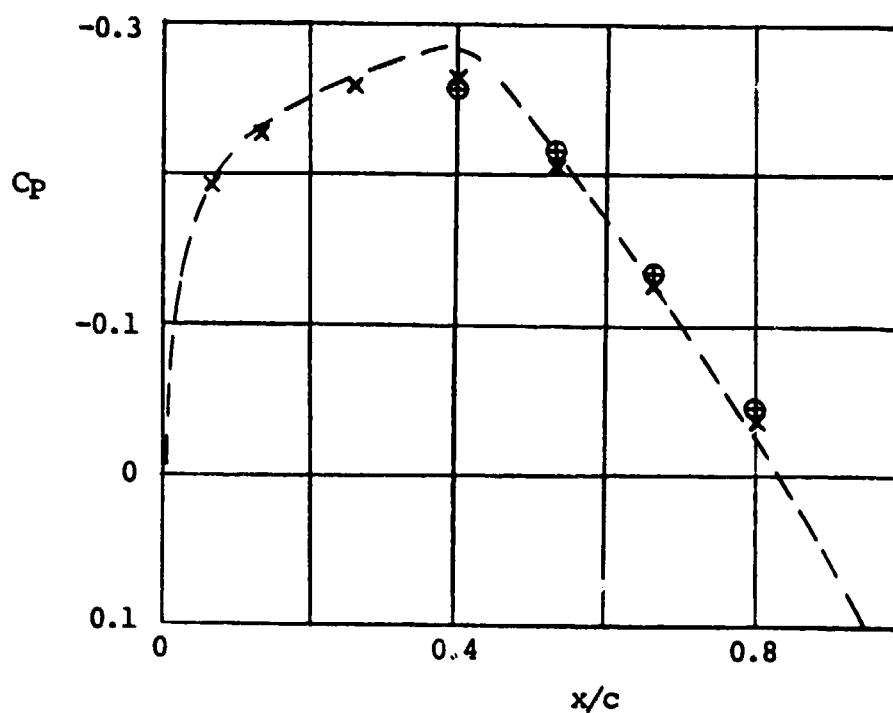
a) $U_{\infty} = 24\text{m/s}$

Figure V.3 Chordwise Distribution of Static Pressure of Smooth Trailing Edge Airfoil (Airfoil III) along the Mid Span
(without the boundary layer trip, x ;
with the boundary layer trip , ⊙)



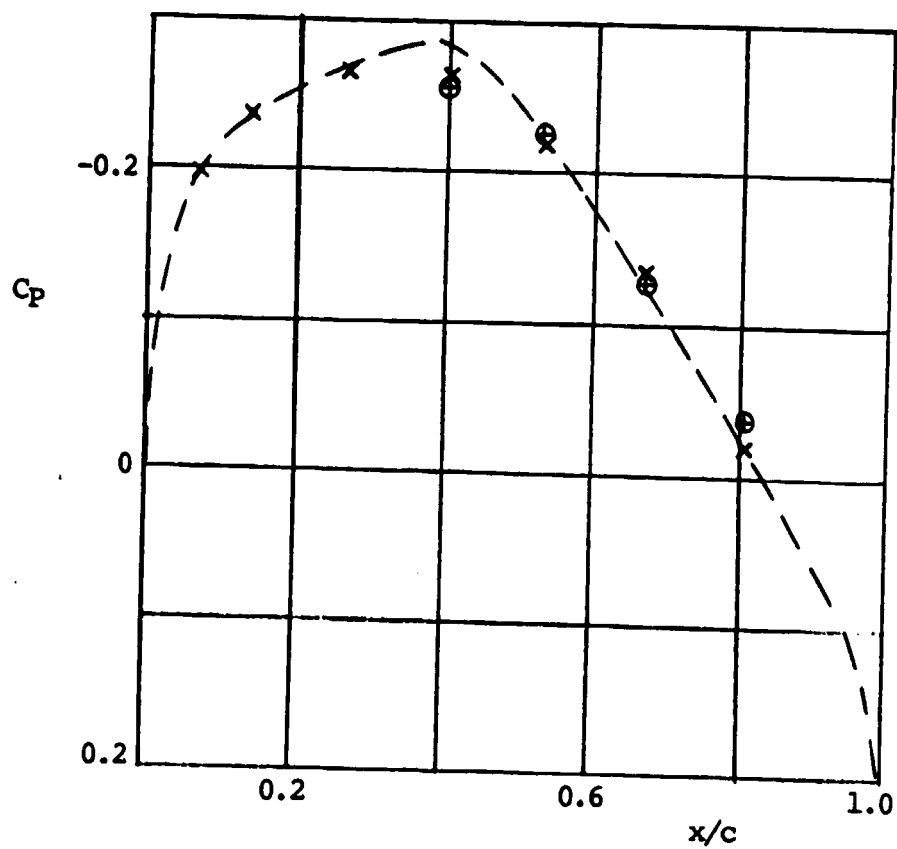
b) $U_{\infty} = 45\text{m/s}$

Figure V.3 (continued)



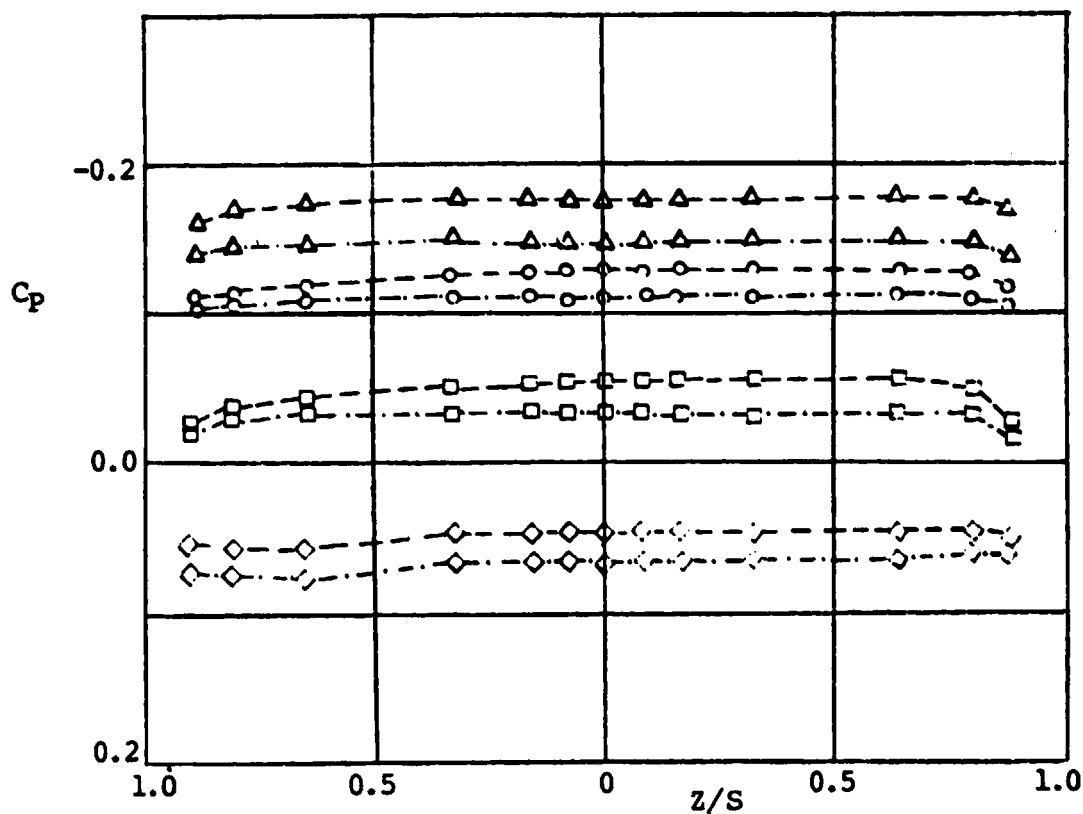
a) $U_\infty = 24 \text{ m/s}$

Figure V.4 Comparison of Corrected Static Pressure Distribution of the Smooth Trailing Edge Airfoil along the Mid Span with the Theoretical Distribution
 (without the boundary layer trip, x ;
 with the boundary layer trip , \oplus ;
 theoretical curve (Abbott, 1959), ---)



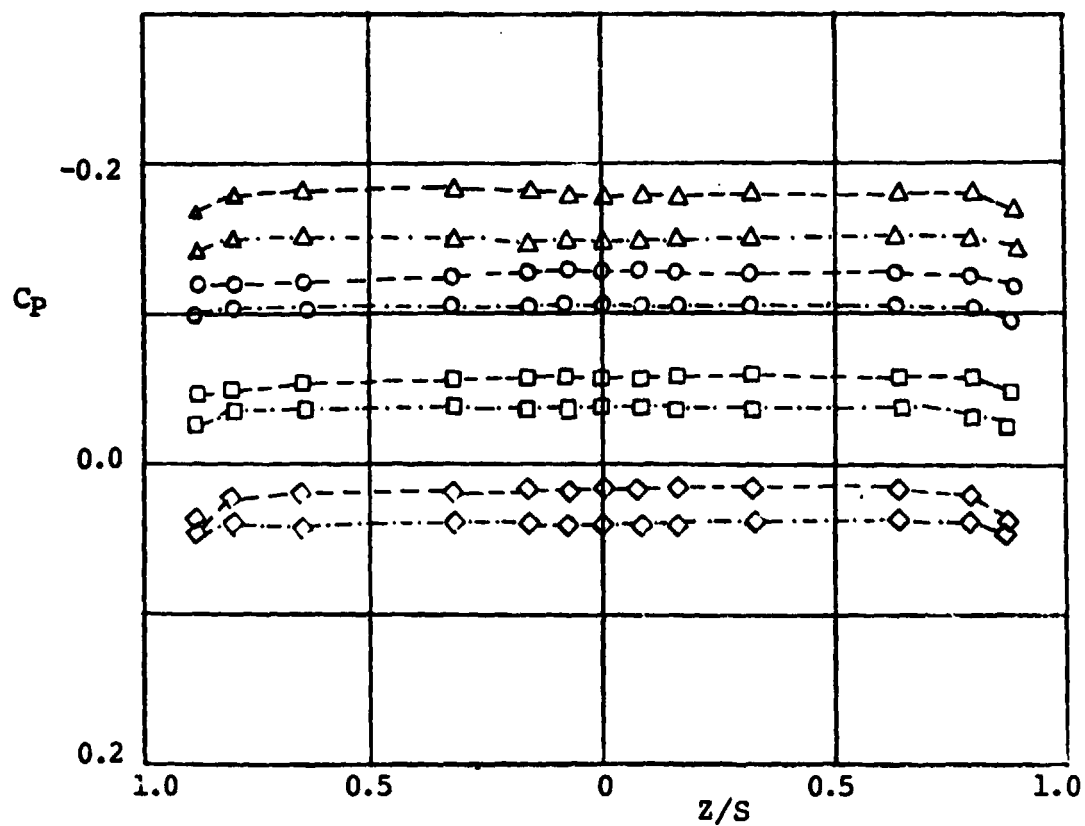
b) $U_\infty = 45 \text{ m/s}$

Figure V.4 (continued)



a) $U_{\infty} = 24\text{m/s}$

Figure V.5 Spanwise Distribution of the Static Pressure of the Smooth Trailing Edge Airfoil
 (without the boundary layer trip , — — — ;
 with the boundary layer trip , - - - - - ;
 at $x/c = 0.42$, Δ ; at $x/c = 0.55$, \circ ;
 at $x/c = 0.68$, \square ; at $x/c = 0.82$, \diamond)



b) $U_\infty = 45 \text{ m/s}$

Figure V.5 (continued)

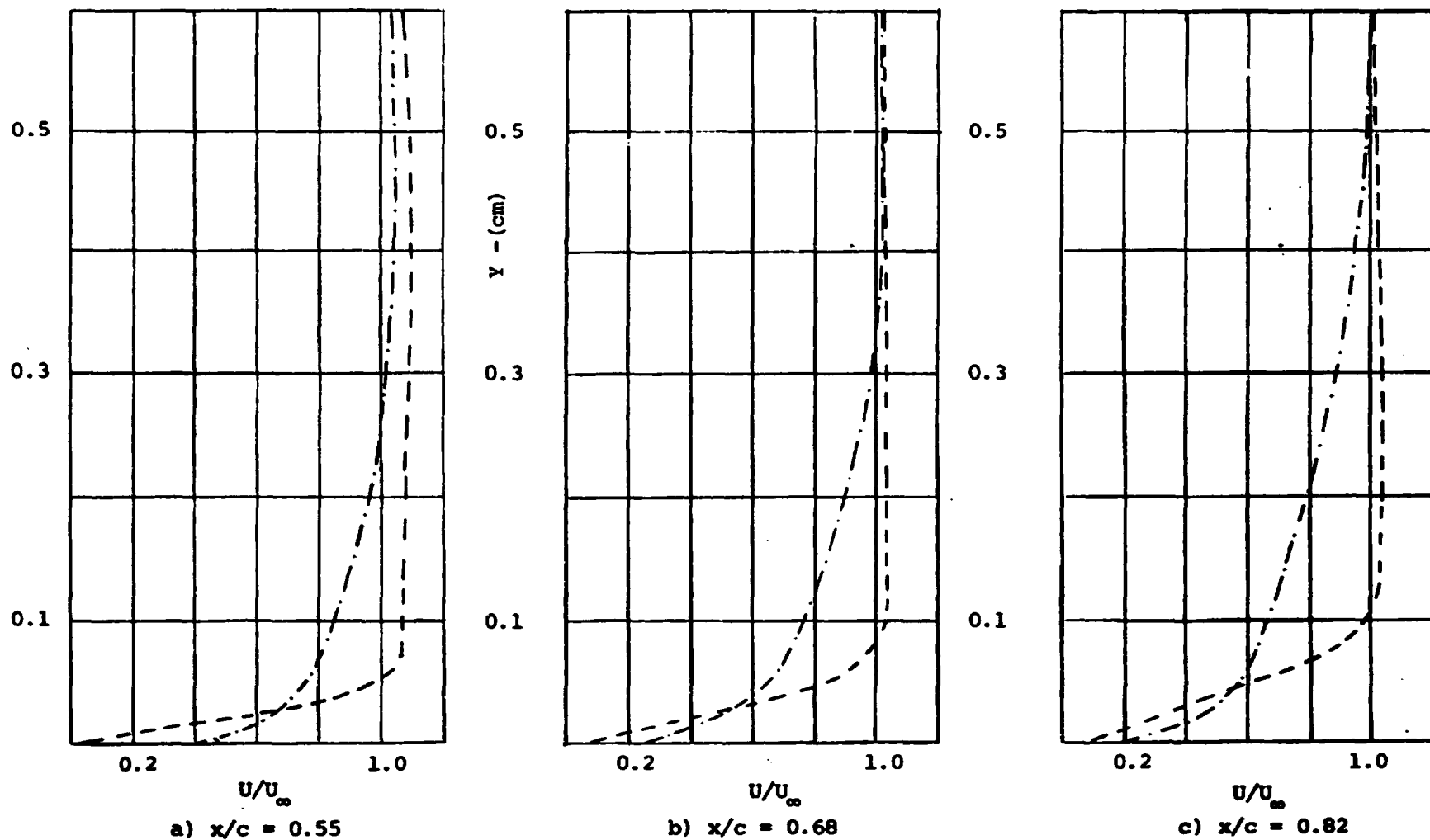
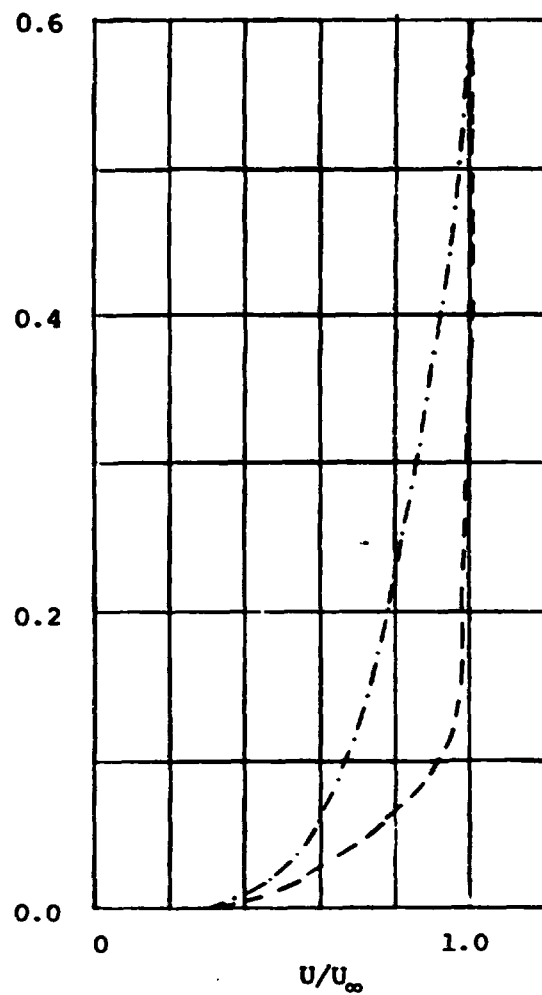
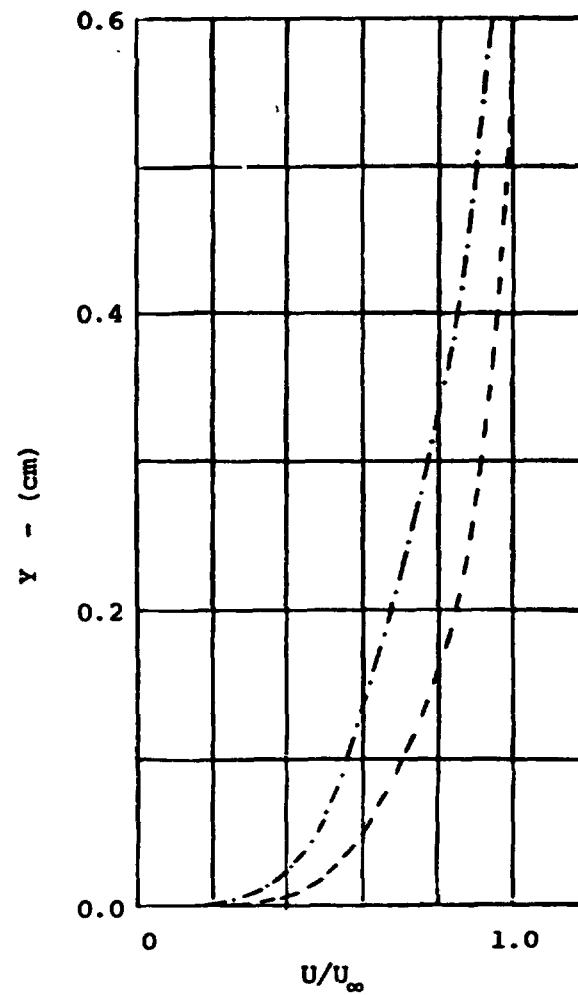


Figure V.6 Boundary Layer Profiles on the Smooth Trailing Edge Airfoil along the MidSpan at Velocity of 45m/s
(Without the boundary layer trip ,---; with the boundary layer trip ,---.---)



d) $x/c = 0.85$



e) $x/c = 0.99$

Figure V.6 (continued)

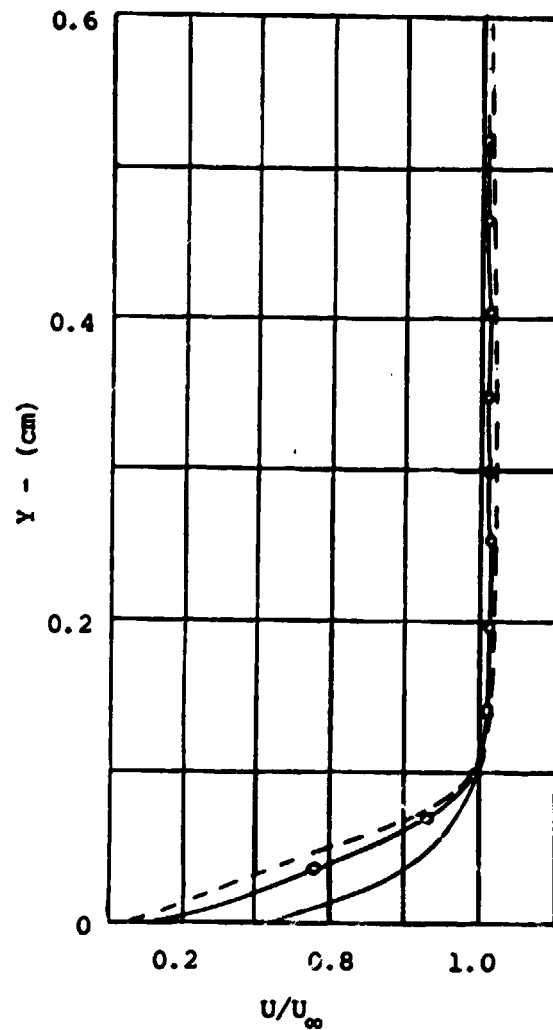
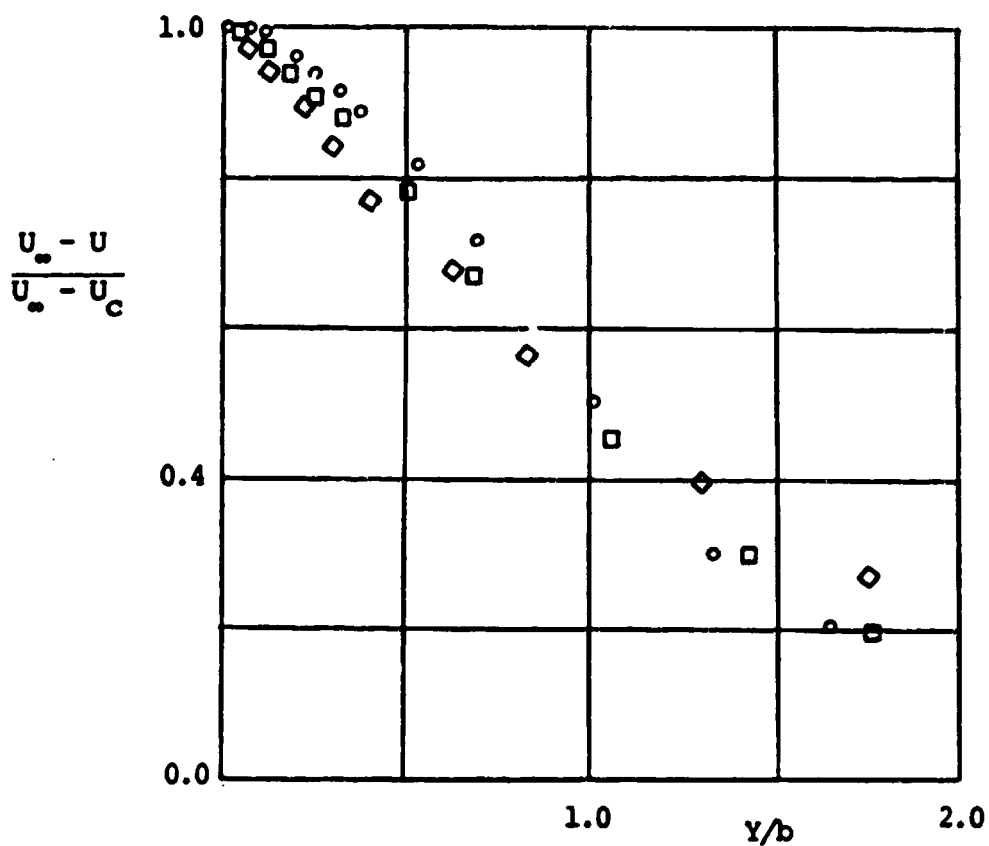
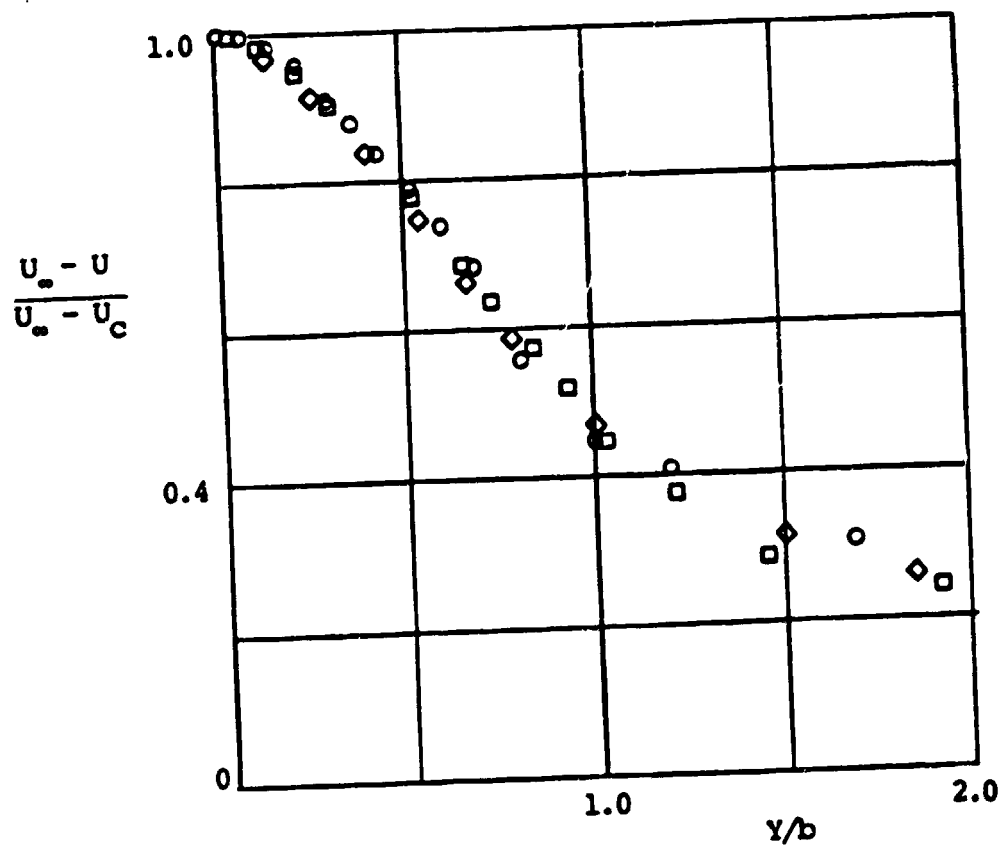


Figure V.7 Comparison of the Boundary Layer Profiles at $x/c = 0.82$
 (without the boundary layer trip configuration :
 $Re_c = 4.8 \times 10^5$, - - - -
 $Re_c = 2.5 \times 10^5$, —○—
 from NACA TN-2235 for a NACA64a010 profile
 at $Re_c = 4.1 \times 10^6$, at $0.8C$, ———)



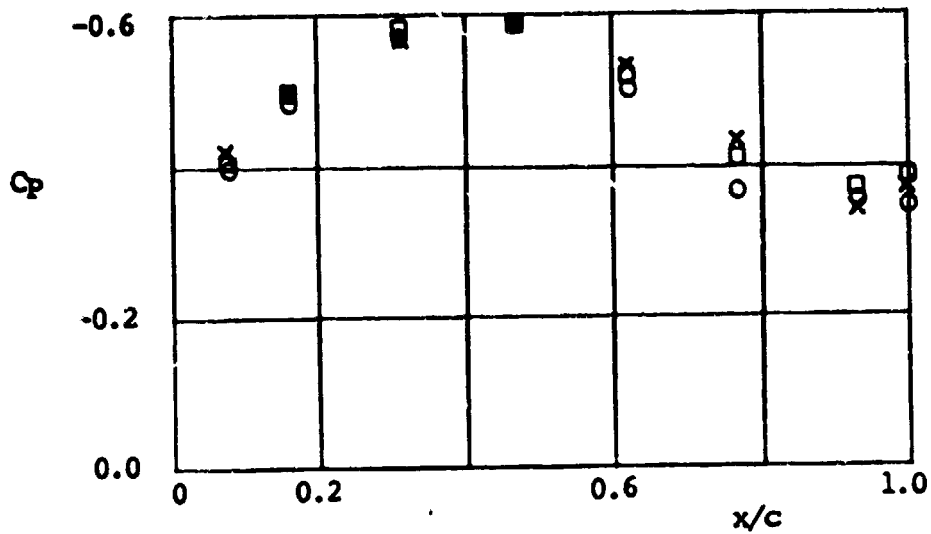
a) Without the Boundary Layer Trip

Figure V.8 Measured Wake Profiles Behind the Airfoil with Smooth Trailing Edge along the Mid Span at Velocity of 45m/s
 (at $x/c = 0.033$, \circ ; at $x/c = 0.133$, \square ;
 at $x/c = 0.266$, \diamond)

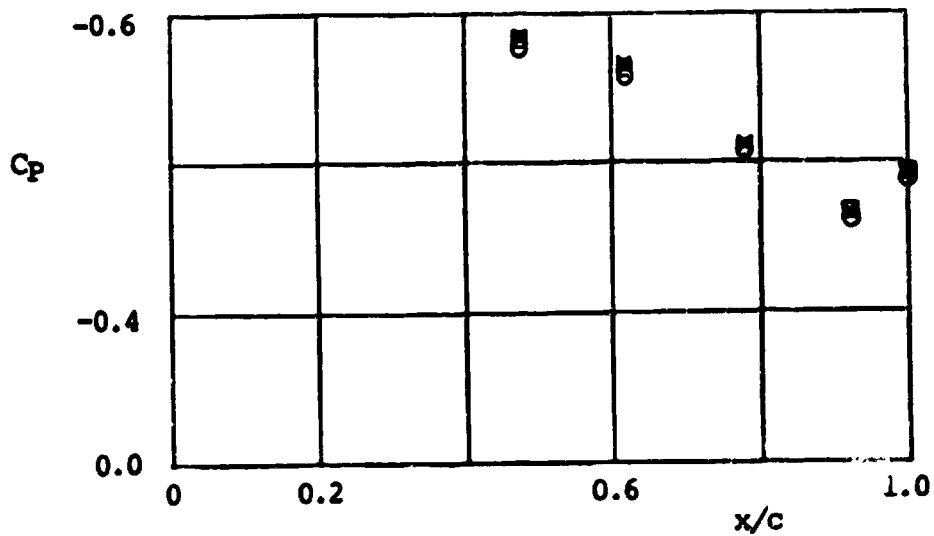


b) With Boundary Layer Trip

Figure V.8 (continued)

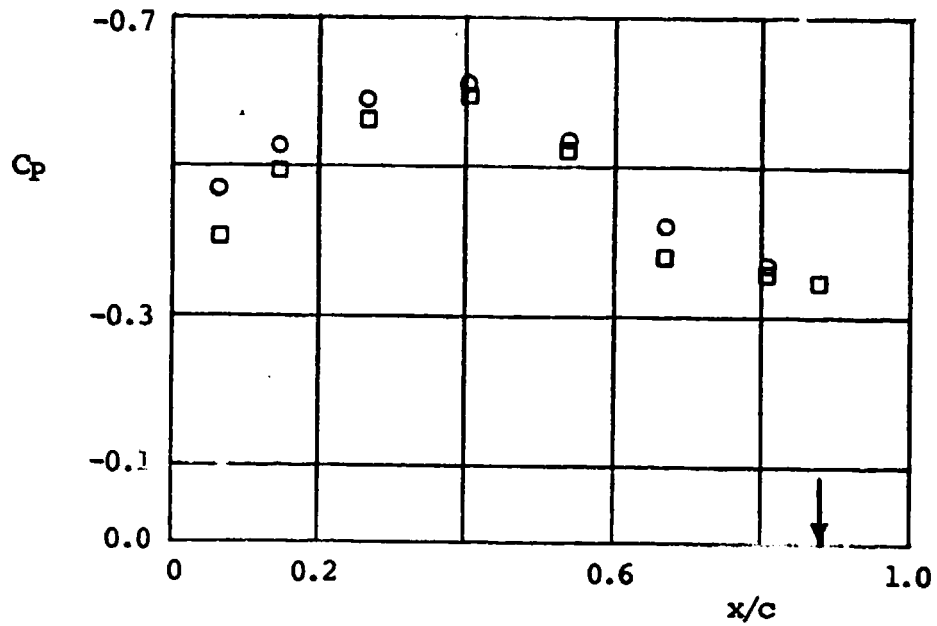


a) without boundary layer trip

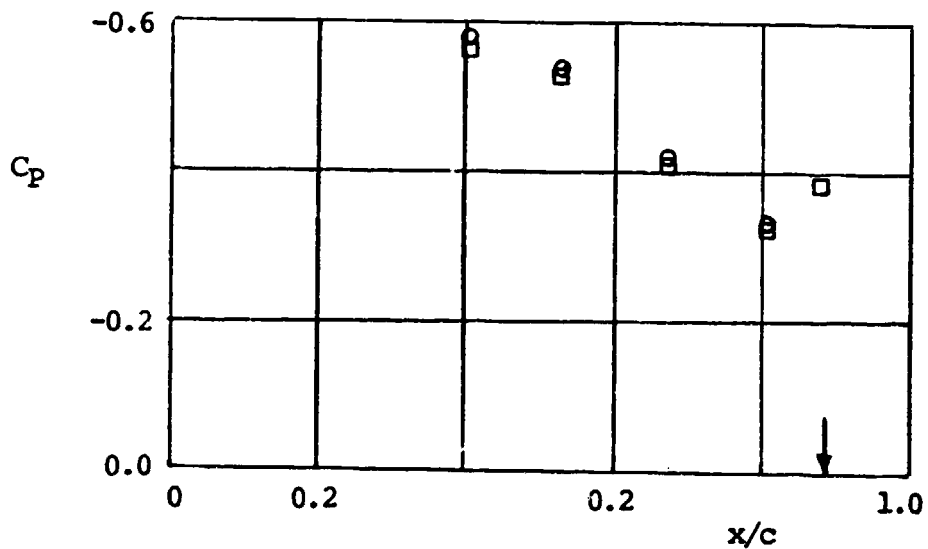


b) with the boundary layer trip

Figure V.9 Chordwise Static Pressure Distribution for Blunt Trailing Edge Airfoil with Pressure Taps in the Mid Span
(at velocity of 24m/s , O ; 33m/s , □ ; and at 44m/s , x)

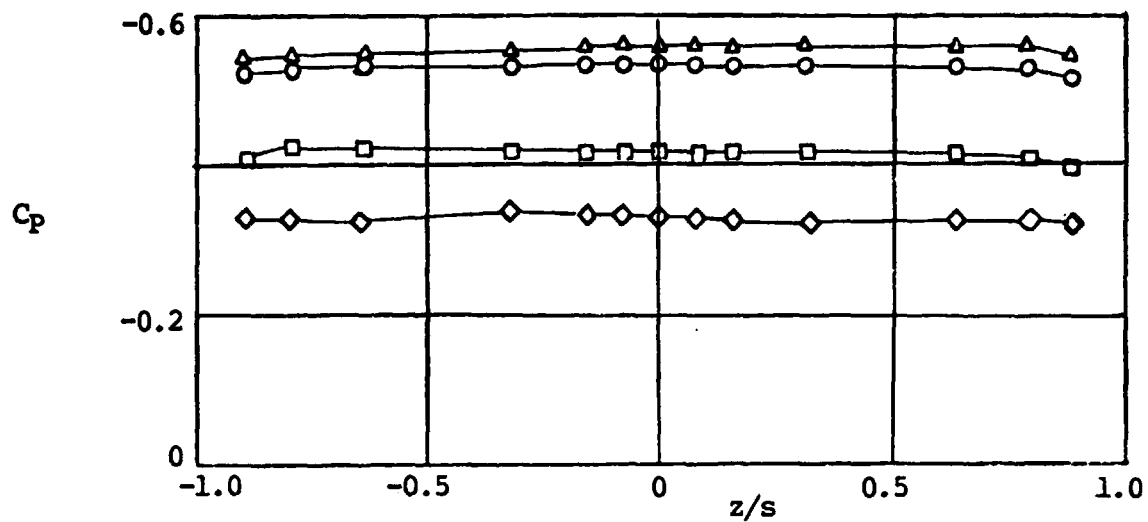


a) without the boundary layer trip

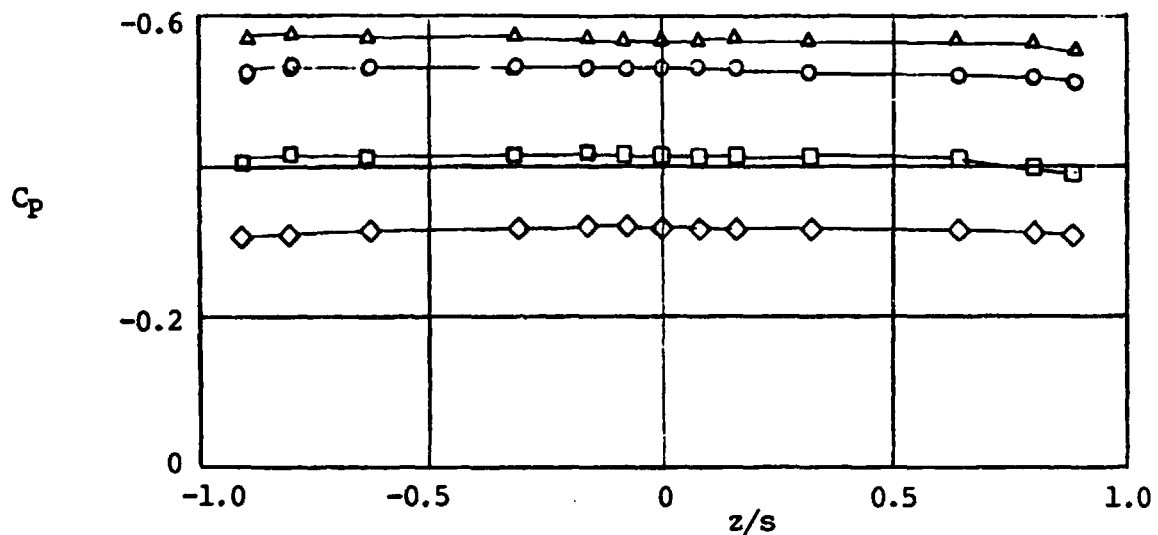


b) with the boundary layer trip

Figure V.10 Comparison of the Chordwise Distribution of Static Pressure in the Midspan and at Velocity of 24m/s
(arrow marks the position of the blunt trailing edge; C : chord of untruncated airfoil, ;
for smooth trailing edge airfoil , O ;
for blunt trailing edge airfoil , □)



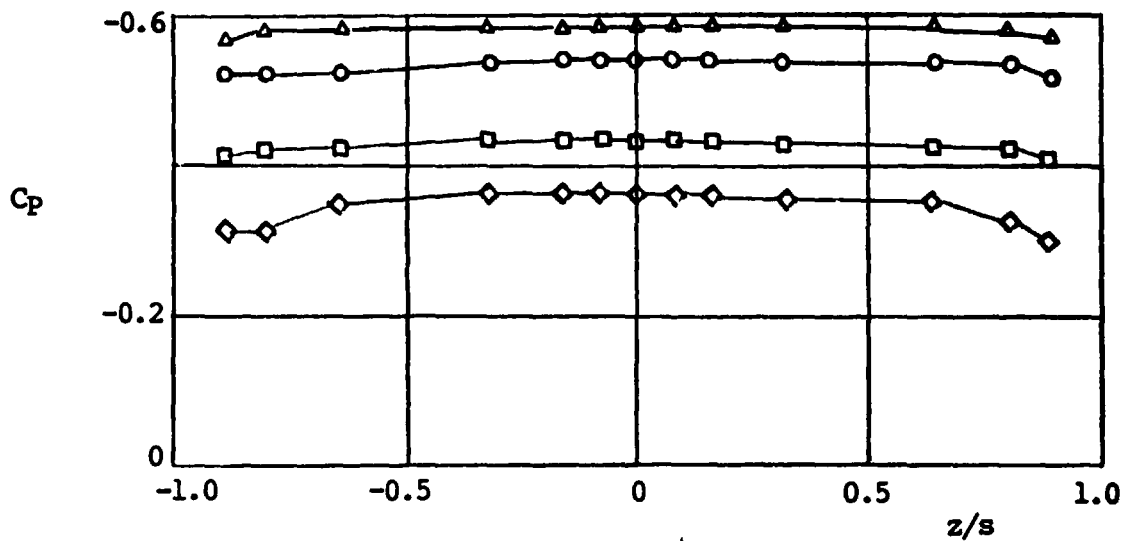
a) at 33m/s



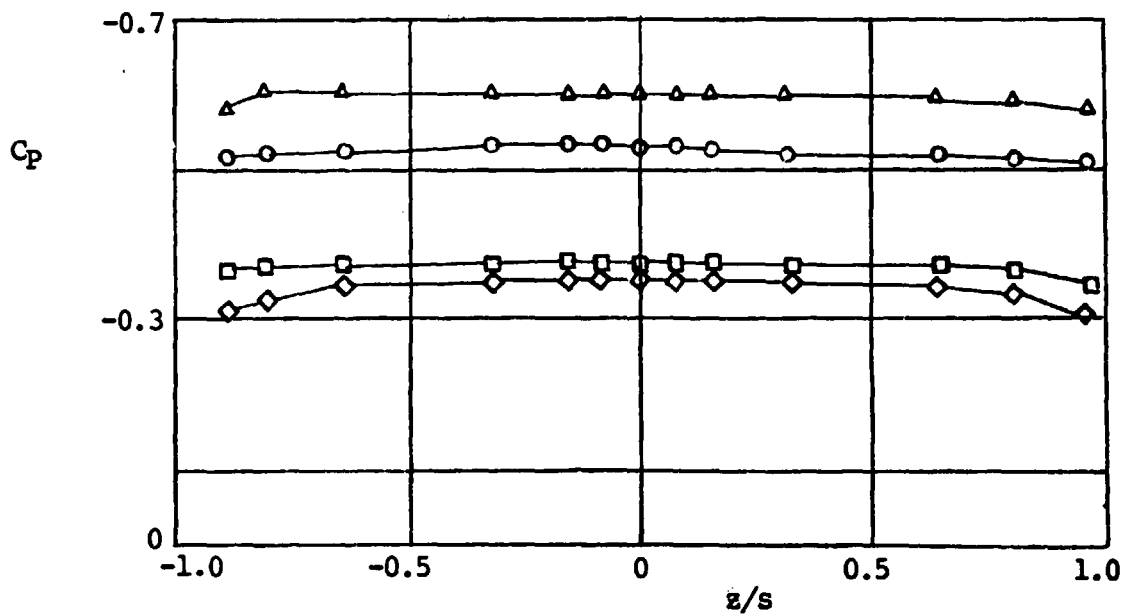
b) at 24m/s

Figure V.11 Spanwise Static Pressure Distribution for the Blunt Trailing Edge Airfoil with Boundary Layer Trip

(at $x/c = 0.46$, Δ ; at $x/c = 0.65$, \circ ; at $x/c = 0.77$, \square
; and at $x/c = 0.92$, \diamond)

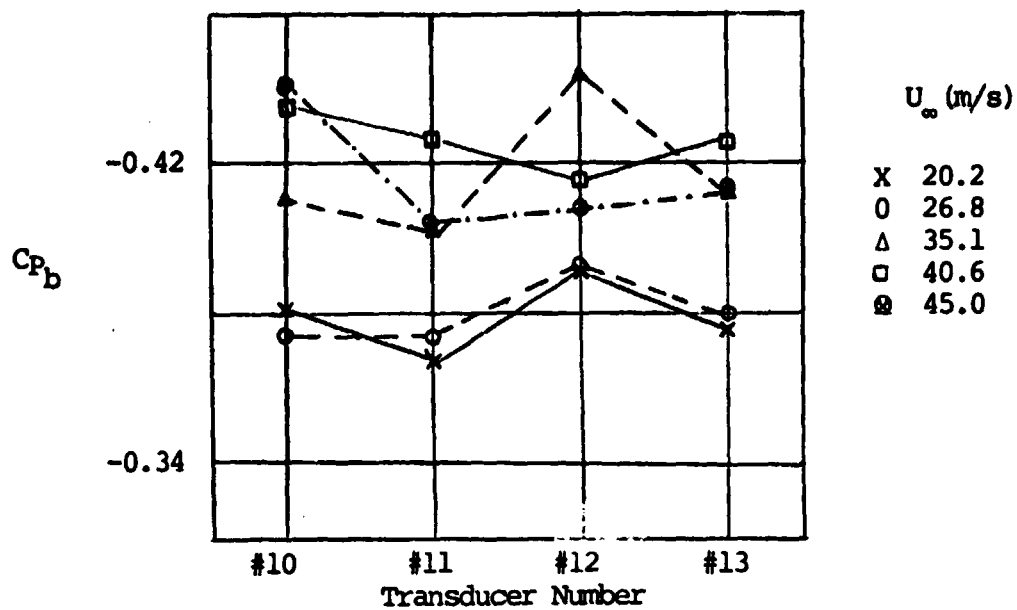


a) at 33m/s

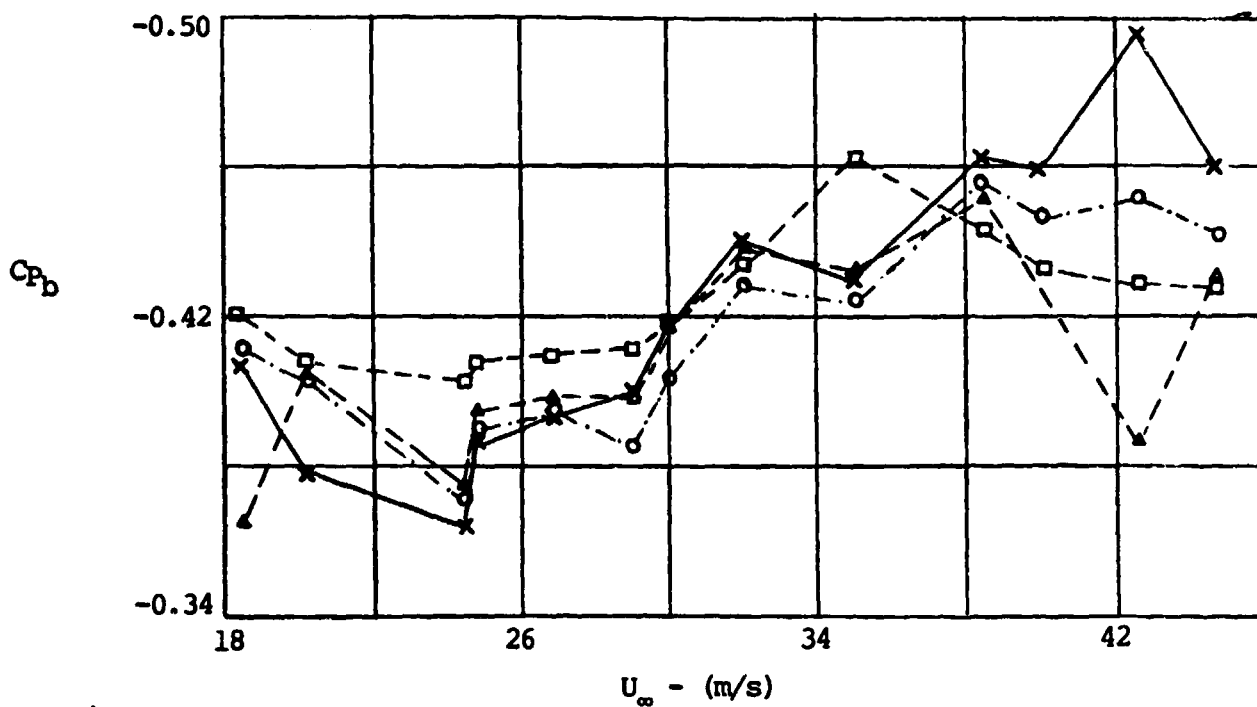


b) at 24m/s

Figure V.12 Spanwise Static Pressure Distribution Over the Blunt Trailing Edge Airfoil, Without the Boundary Layer Trip
(at $x/c = 0.46$, Δ ; at $x/c = 0.65$, \circ ; at $x/c = 0.77$, \square ; and at $x/c = 0.92$, \diamond)



b) Spanwise Distribution



a) variation with velocity
(X, #10; O, #11; \square , #12; Δ , #13)

Figure V.13 Base Pressure Distribution for the Airfoil with Pressure Transducers

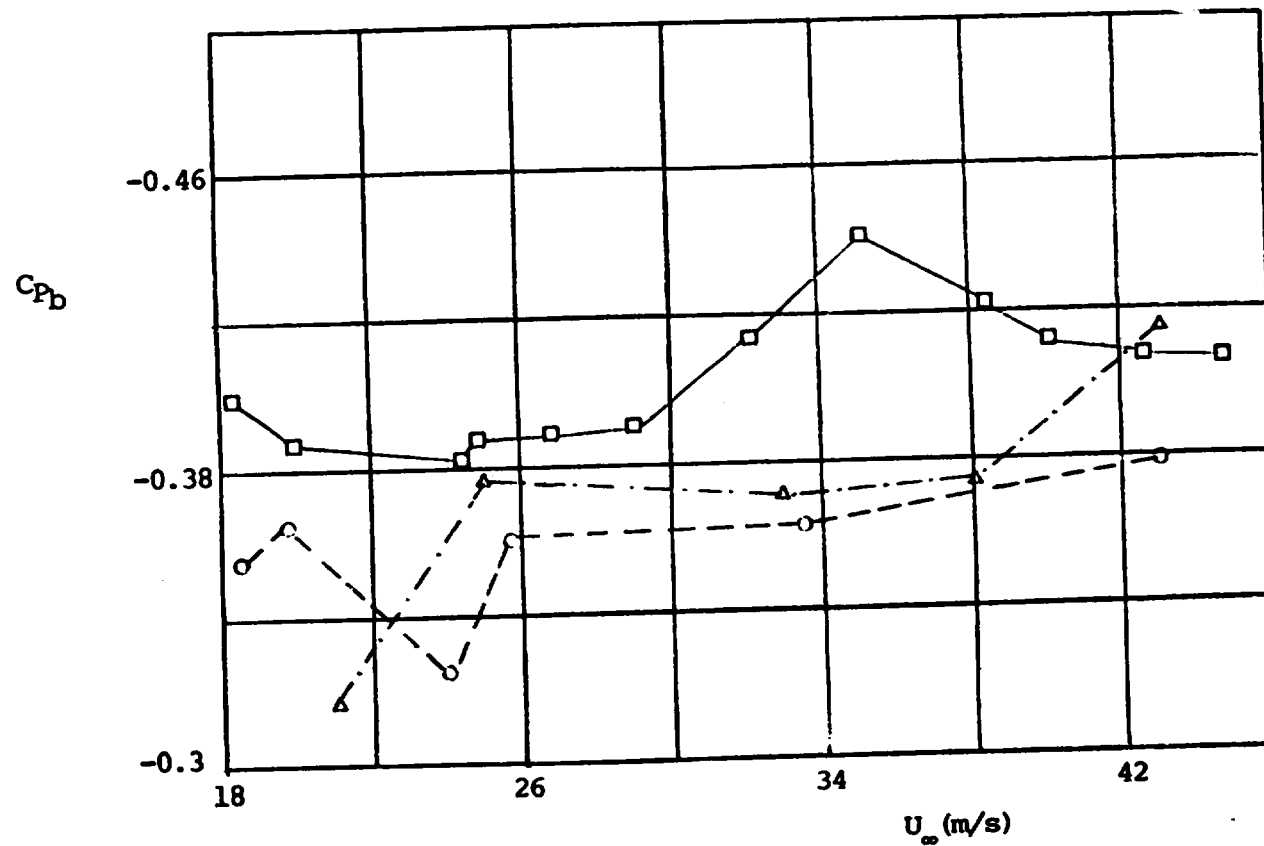


Figure V.14 Comparison of the Base Pressure with the Velocity
 (blunt trailing edge airfoil with transducers , \square ;
 blunt trailing edge airfoil with pressure taps :
 without the boundary layer trip configuration, \circ ;
 with the boundary layer trip configuration , Δ)

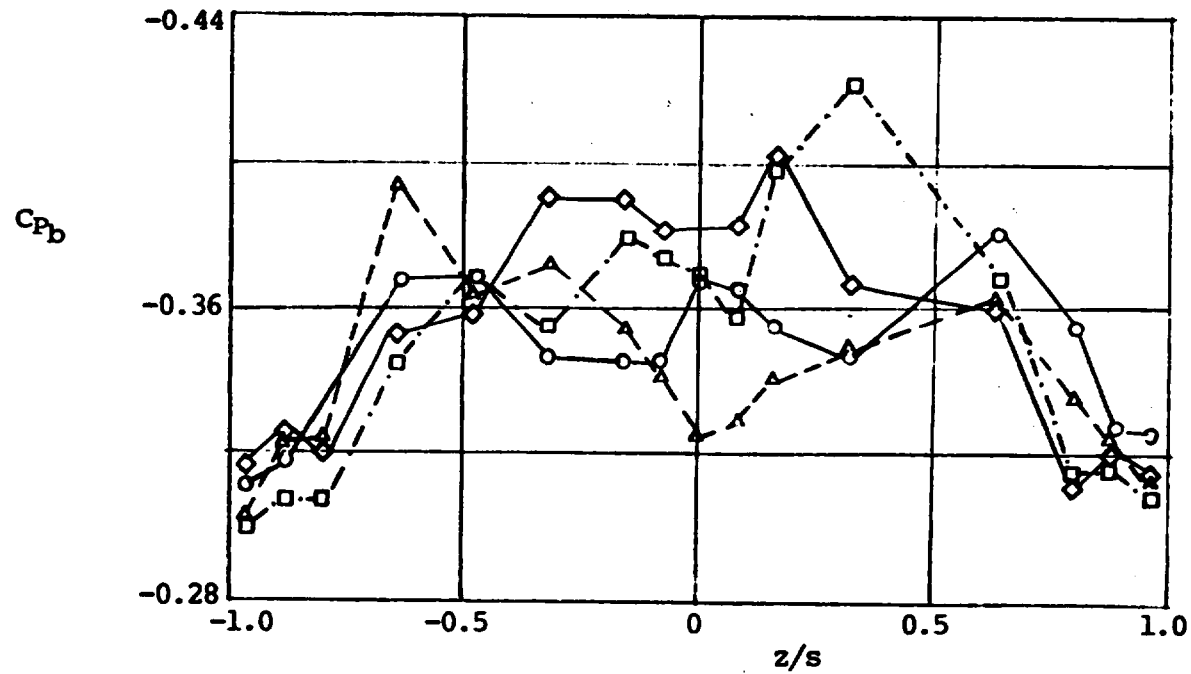


Figure V.15 Variation of Base Pressure in the Spanwise Direction for the Blunt Trailing Edge Airfoil with Pressure taps, Without the Boundary Layer Trip
 (at velocity of 19.7m/s, O ; at velocity of 24m/s, Δ ;
 at velocity of 34m/s , □ ; and at velocity of 43 m/s, ◇)

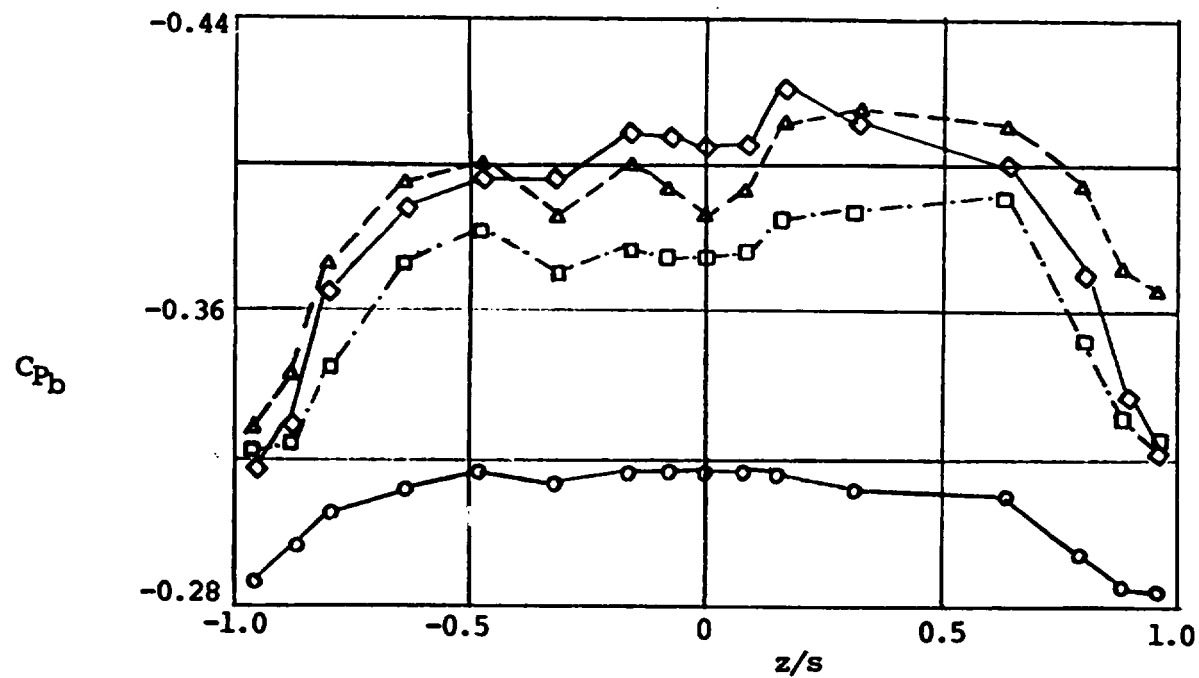
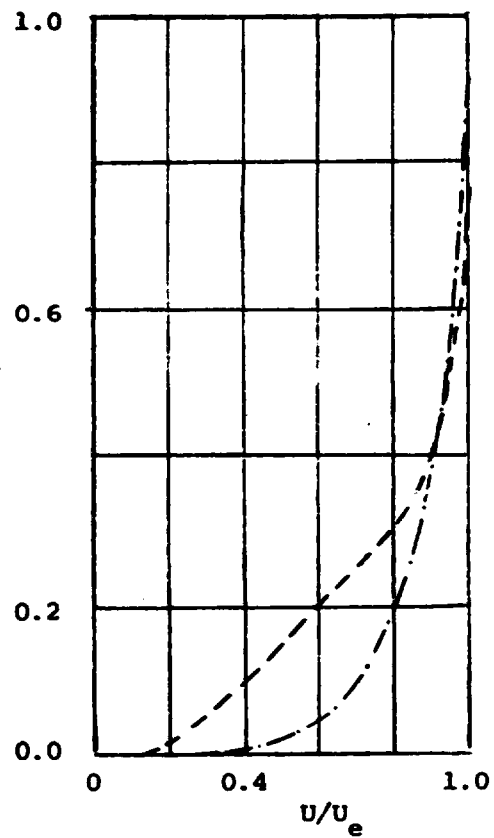
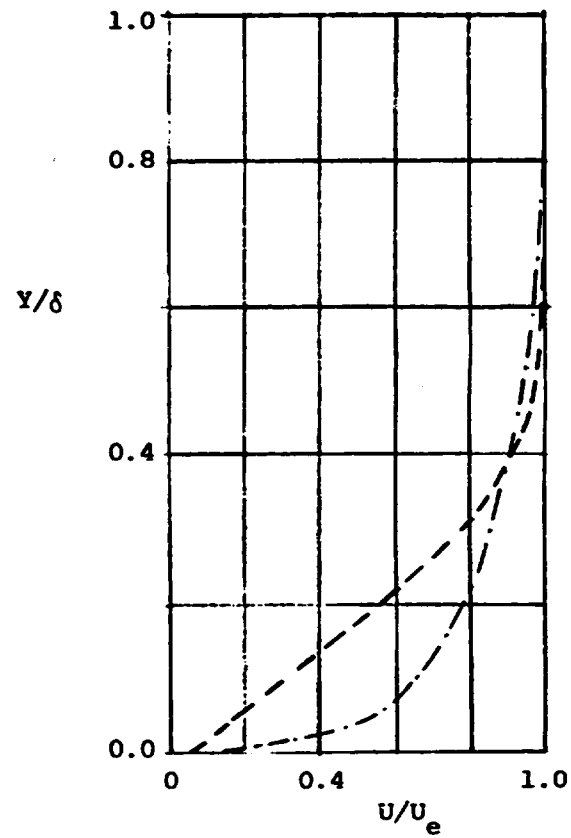


Figure V.16 Variation of Base Pressure in the Spanwise Direction for the Blunt Trailing Edge Airfoil with Pressure Taps, With the Boundary Layer Trip
 (at velocity of 21m/s , O ; at velocity of 25m/s , Δ ;
 at velocity of 34m/s , □ ; and at velocity of 43m/s , ◇)

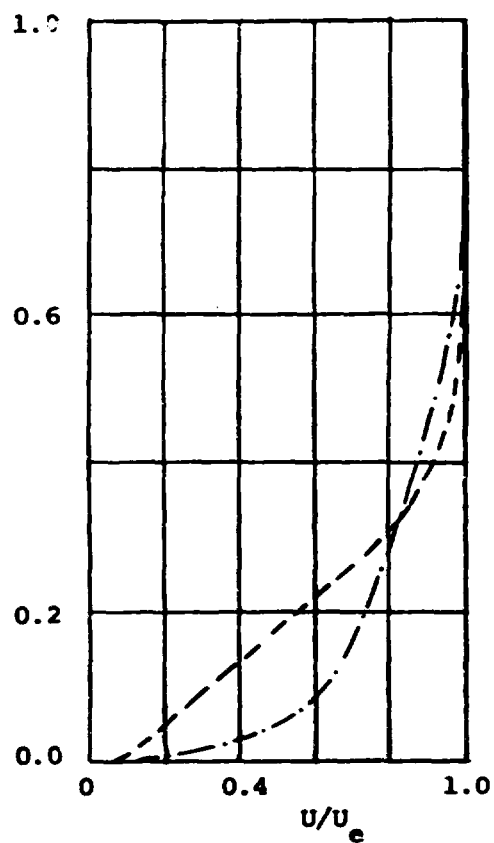


$x/c = 0.62$

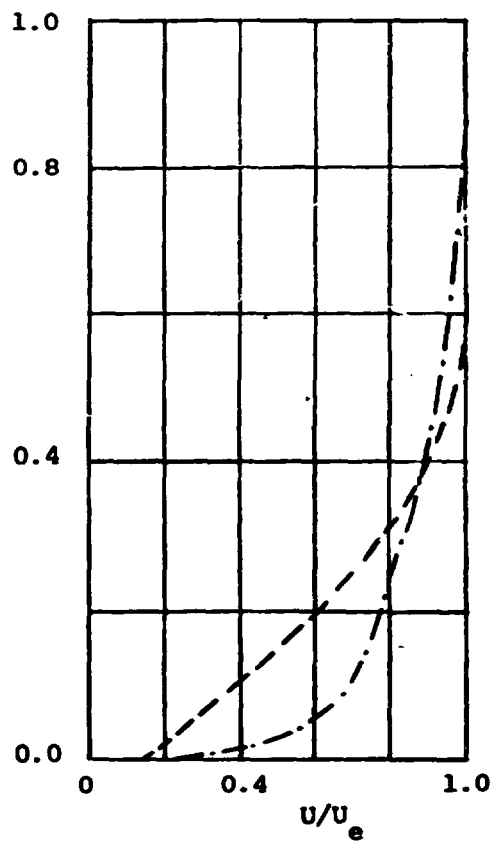


$x/c = 0.77$

Figure V.17 Boundary Layer Profiles for the Truncated Airfoil with Pressure Taps at a velocity of 24m/s
(without boundary layer trip, - - - -;
with boundary layer trip, - · - · - ·)

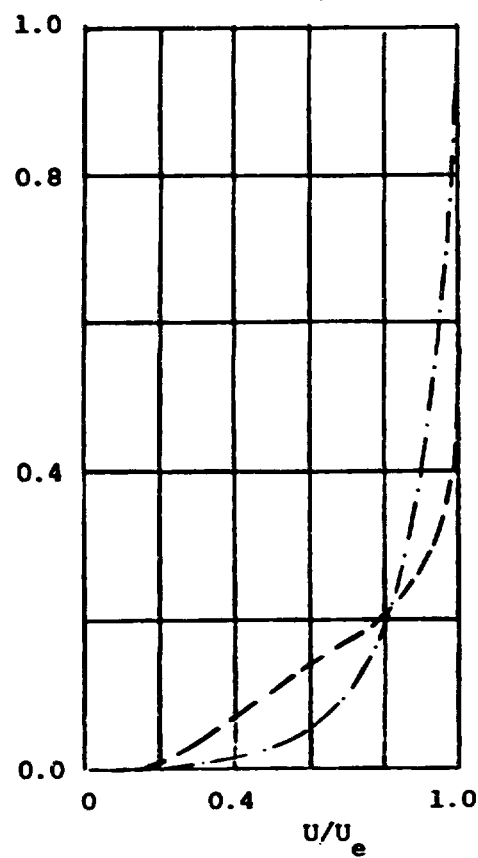


$x/c = 0.92$

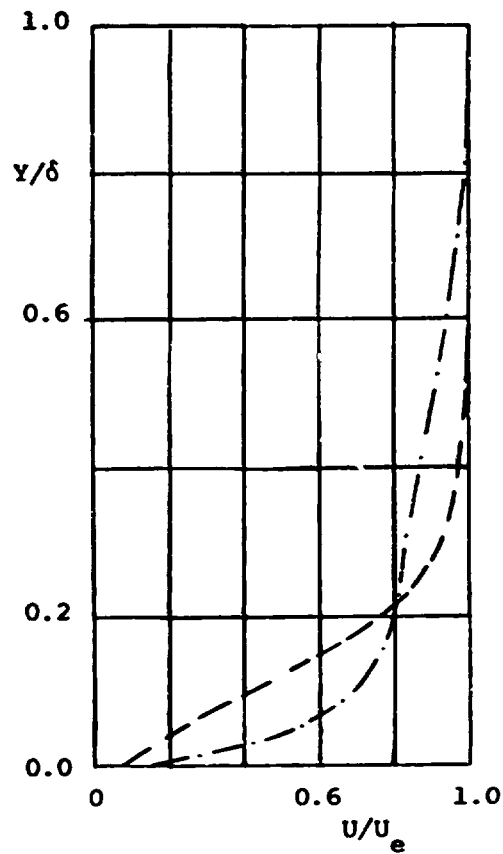


$x/c = 0.99$

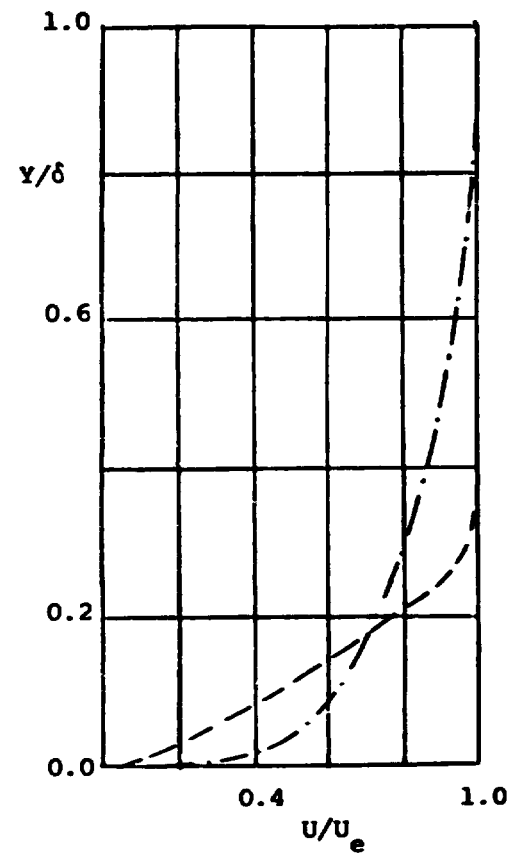
Figure V.17 (continued)



$x/c = 0.62$



$x/c = 0.77$



$x/c = 0.92$

Figure V.18 Boundary Layer Profiles for the Truncated Airfoil with Pressure Taps at a Velocity of 34m/s

(without boundary layer trip, - - - - ;
with boundary layer trip, - . . . -)

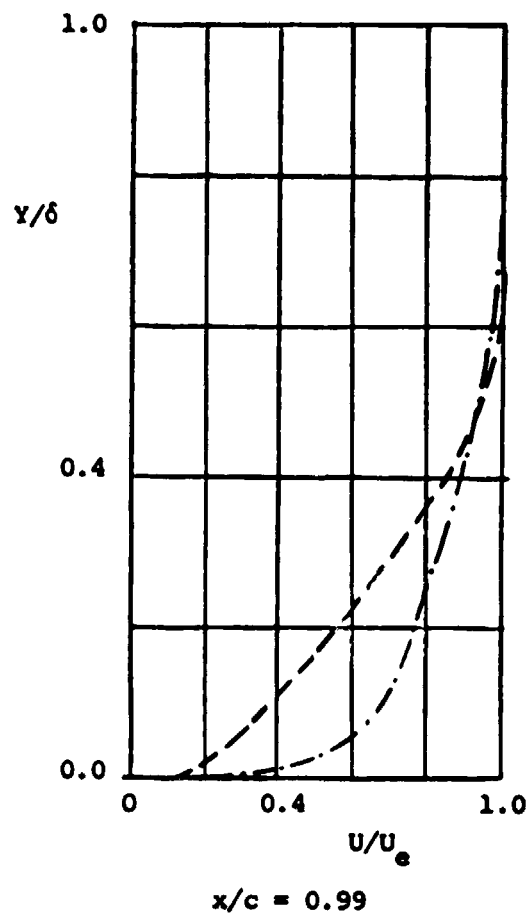
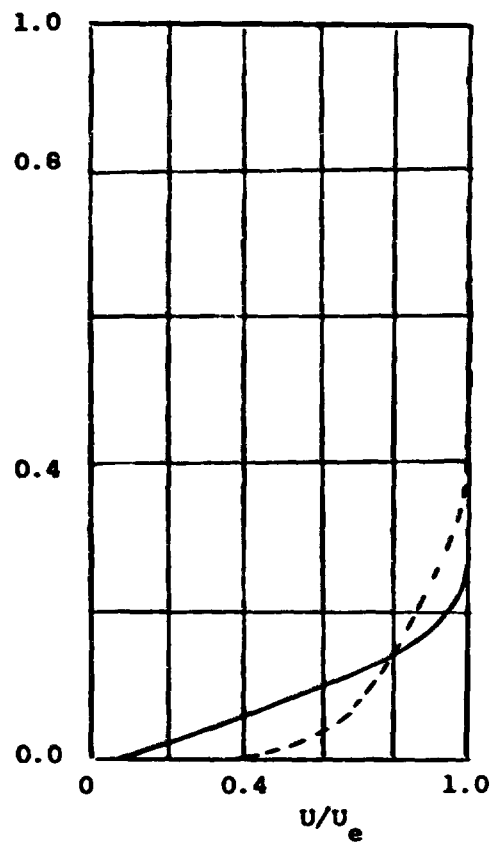
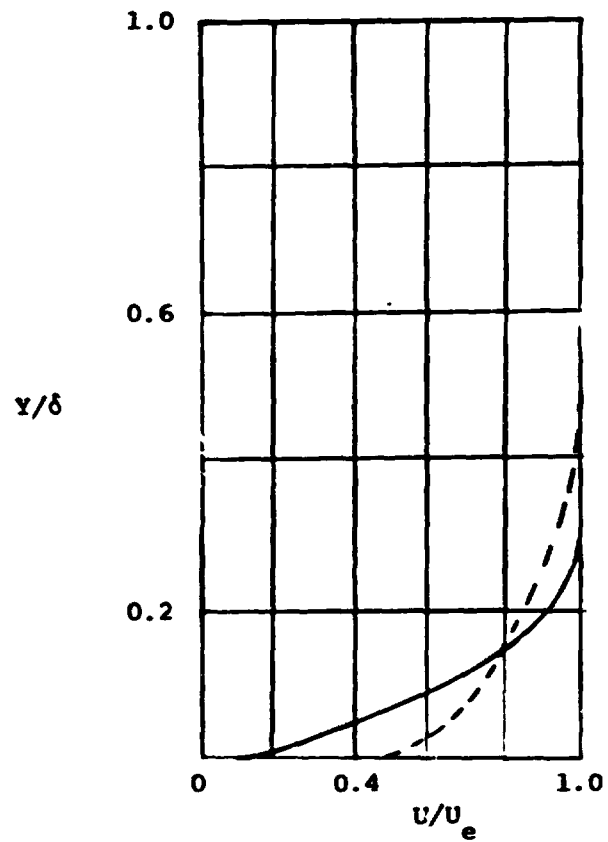


Figure V.13 (continued)



$x/c = 0.89$



$x/c = 0.99$

Figure V.19 Boundary layer Profiles, along the Midspan on the Truncated Airfoil with Transducers
(at a velocity of 24m/s, —; at a velocity of 45m/s, ---)

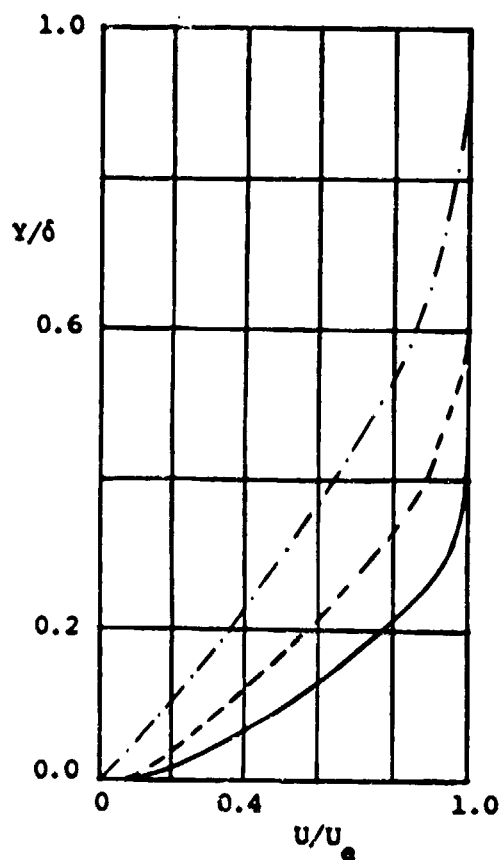


Figure V.20 Comparison of Boundary Layer Profiles of Blunt Trailing Edge Airfoils With Un-tripped Boundary Layer at x/c of 0.99 and velocity of 24m/s
 (airfoil with transducers, —; airfoil with pressure taps, - -; Blausius boundary layer profile, - · - ·)

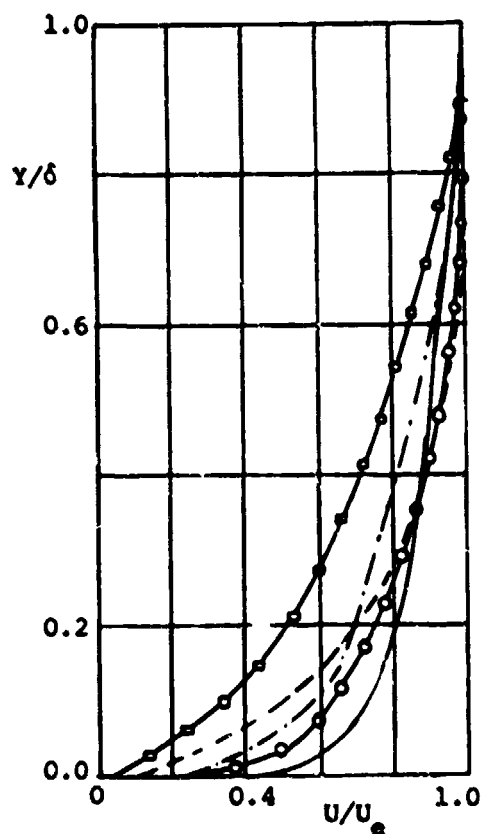


Figure V.21 Comparison of the Boundary Layer Profiles for the Airfoils with Pressure Taps, at a Velocity of 45m/s

blunt trailing edge airfoil at $x/c = 0.98$:
 without the boundary layer trip , \circ — \circ ;
 with the boundary layer trip , \circ — \circ ;
 smooth trailing edge airfoil at $x/c = 0.85$:
 without the boundary layer trip , --- ;
 with the boundary layer trip , - · - · - ;
 turbulent boundary layer profile, ———
 (with 1/7 power law)

The chord wise distance was normalized with
 respective airfoil chords.

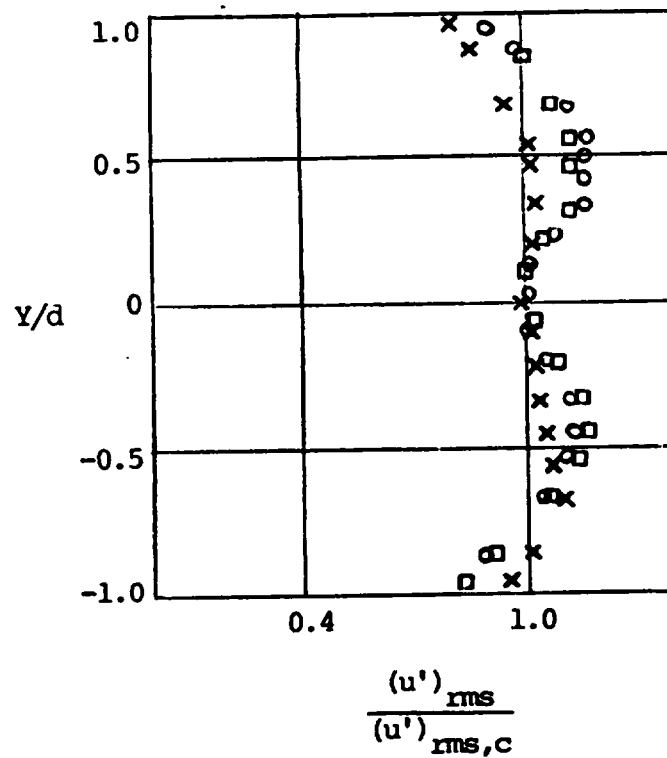
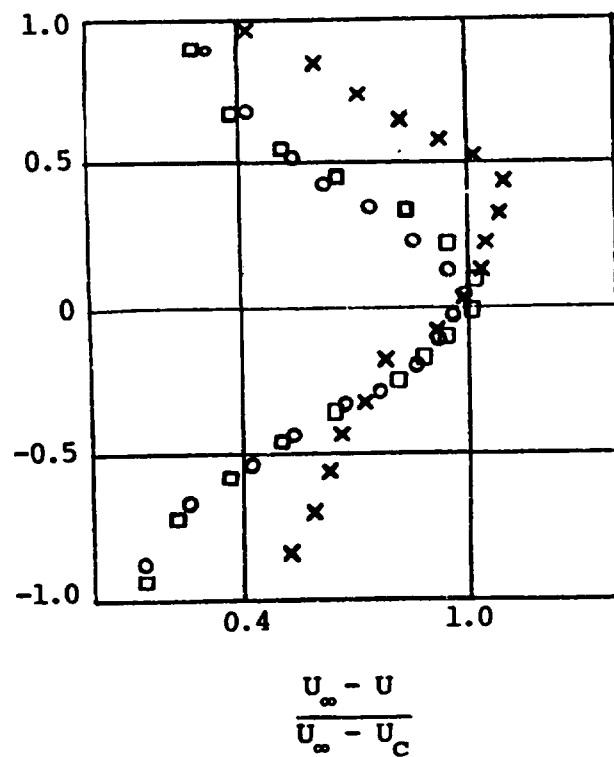
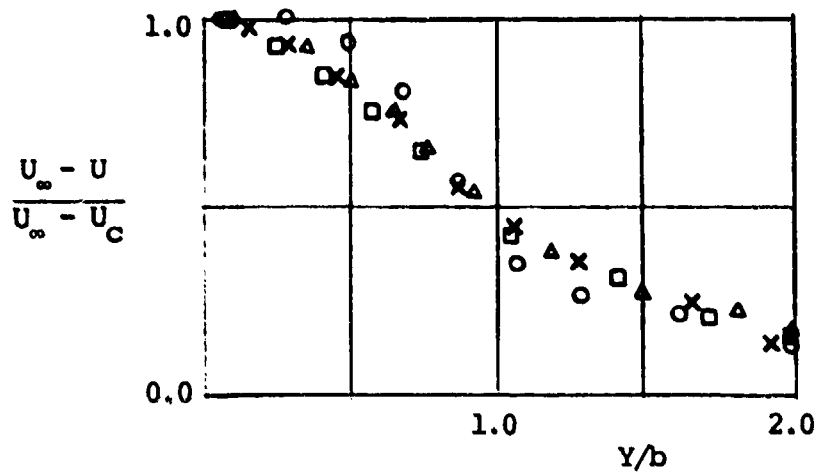
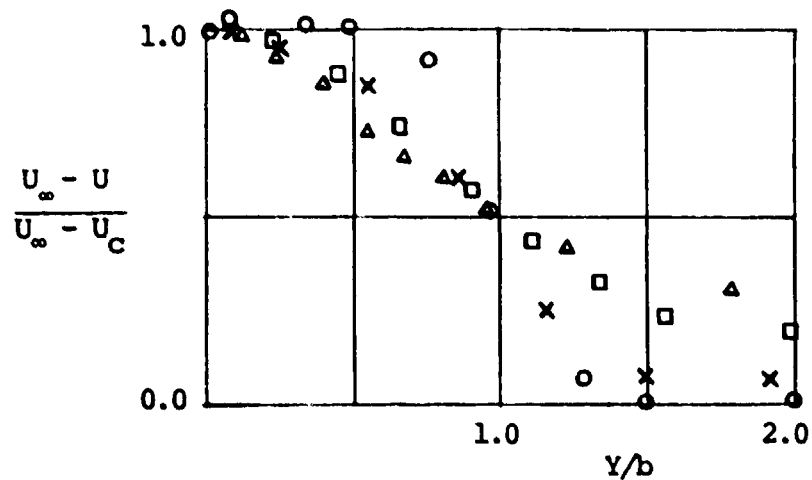


Figure V.22 Wake Profiles Behind the Truncated Airfoil with Transducers at a Velocity of 26m/s and at x/d of 3.3
 (at spanwise position of $z/s = 0.0$, x ; at $z/s = 0.5$, o ; at $z/s = -0.5$, \square)

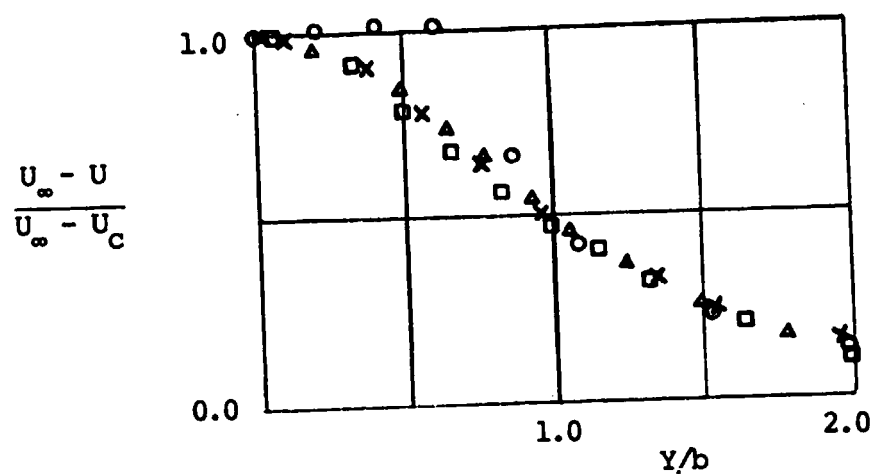


a) with the boundary layer trip

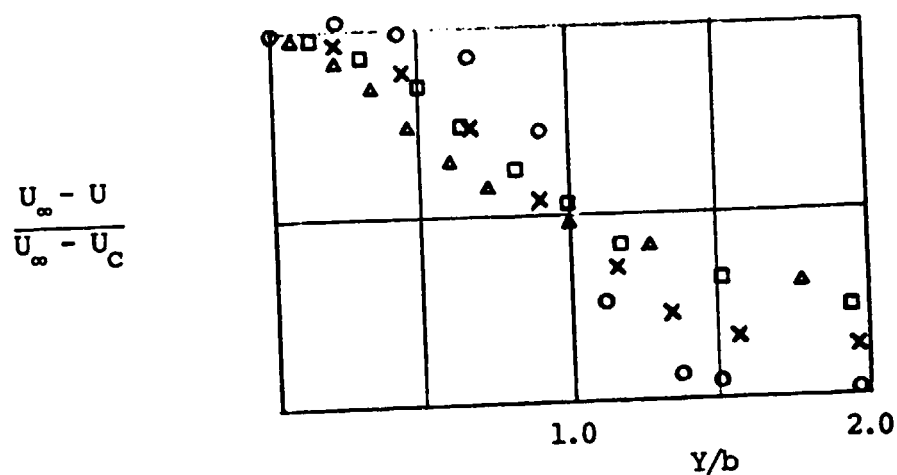


b) without the boundary layer trip

Figure V.23 Wake Profiles of the Truncated Airfoil with Pressure Taps along the Midspan at Velocity of 24m/s
(at a position of $x/d = 0.5$, \circ ; at $x/d = 1.0$, \times ;
at $x/d = 2.0$, \square ; at $x/d = 4.0$, \triangle)

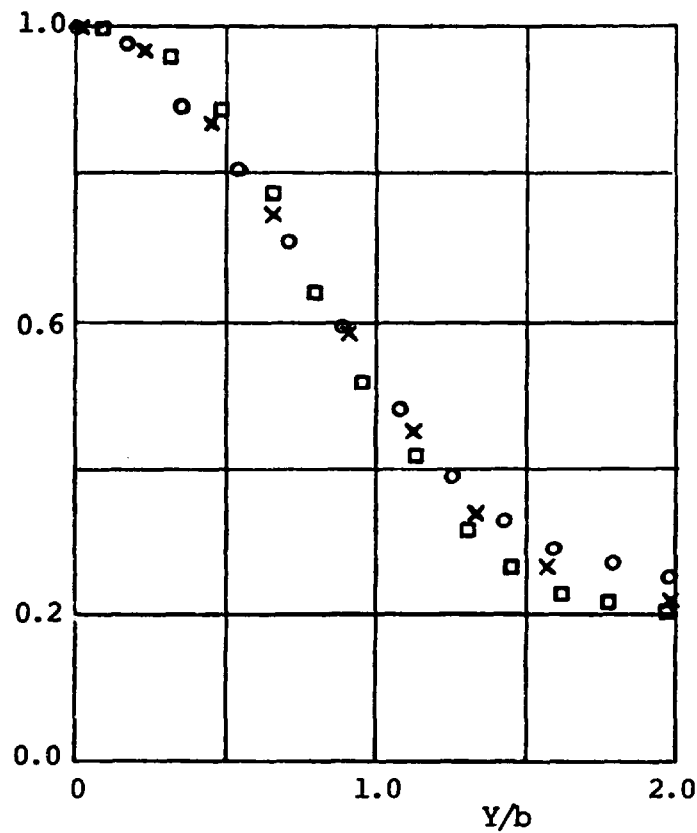


a) with the boundary layer trip

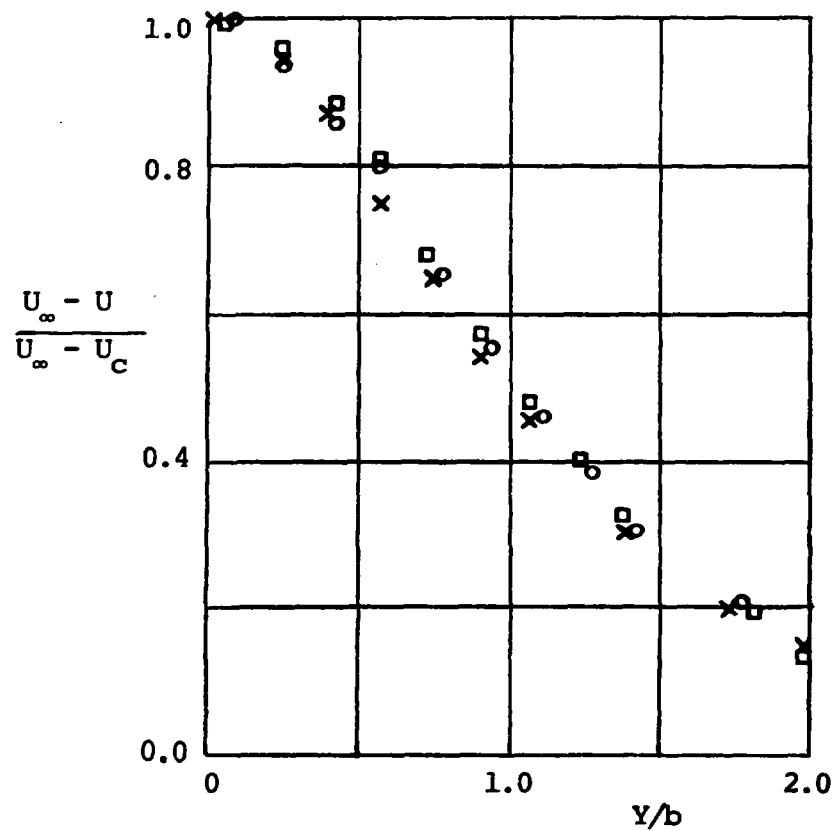


b) without the boundary layer trip

Figure V.24 Wake Profiles of the Truncated Airfoil with Pressure Taps along the Midspan at Velocity of 34 m/s
(at a position of $x/d = 0.5$, O ; at $x/d = 1.0$, x ;
at $x/d = 2.0$, □ ; at $x/d = 4.0$, Δ)

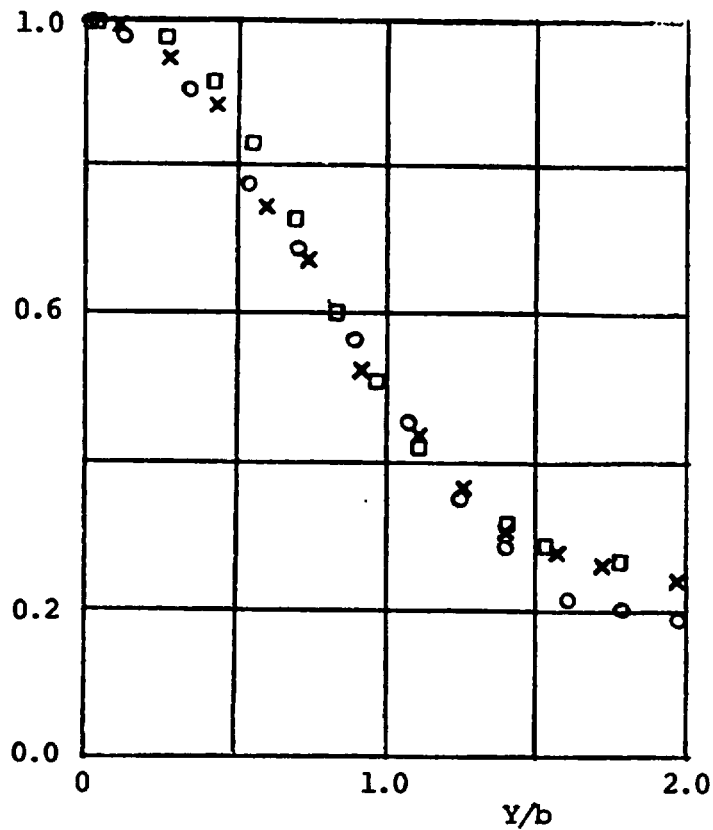


a) without the boundary layer trip

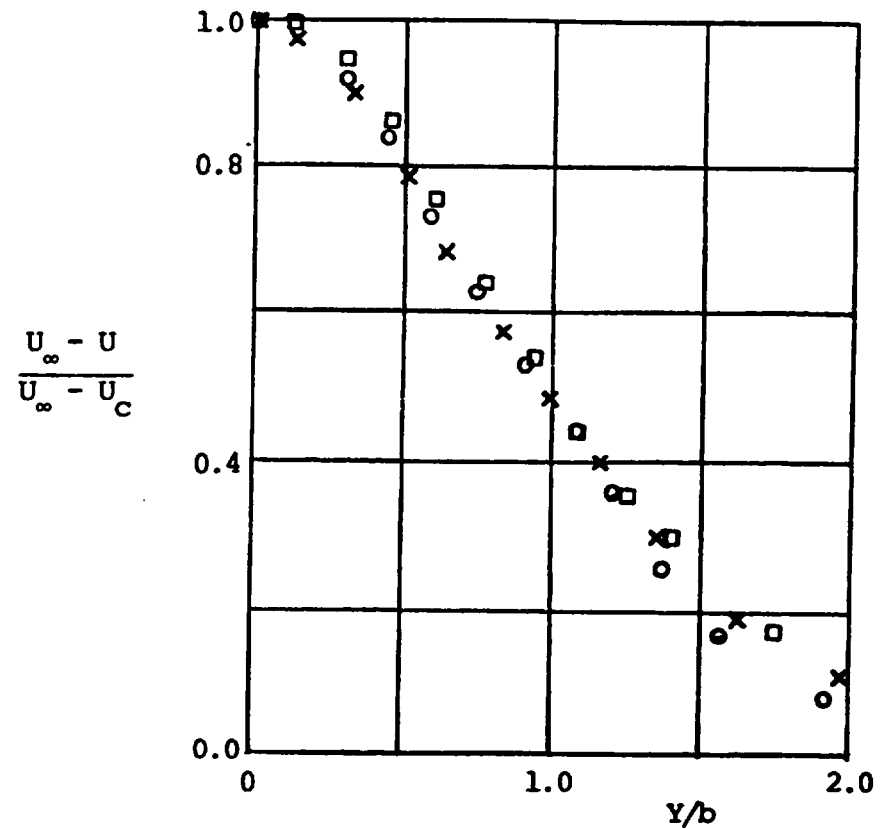


b) with the boundary layer trip

Figure V.25 Wake Profiles of the Airfoil with Pressure Taps at Different Spanwise Positions at x/d of 2.0 and at Velocity of 24m/s
(at spanwise position of $z/s = 0.0$, \times ; at $z/s = 0.33$, \square ; at $z/s = -0.33$, \circ)



a) without the boundary layer trip



b) with the boundary layer trip

Figure V.26 Wake Profiles of the Airfoil with Pressure Taps at Different Spanwise Positions at x/d of 2.0 and at Velocity of 34m/s
(at spanwise position of $z/s = 0.0$, \times ; at $z/s = 0.33$, \square ; at $z/s = -0.33$, \circ)

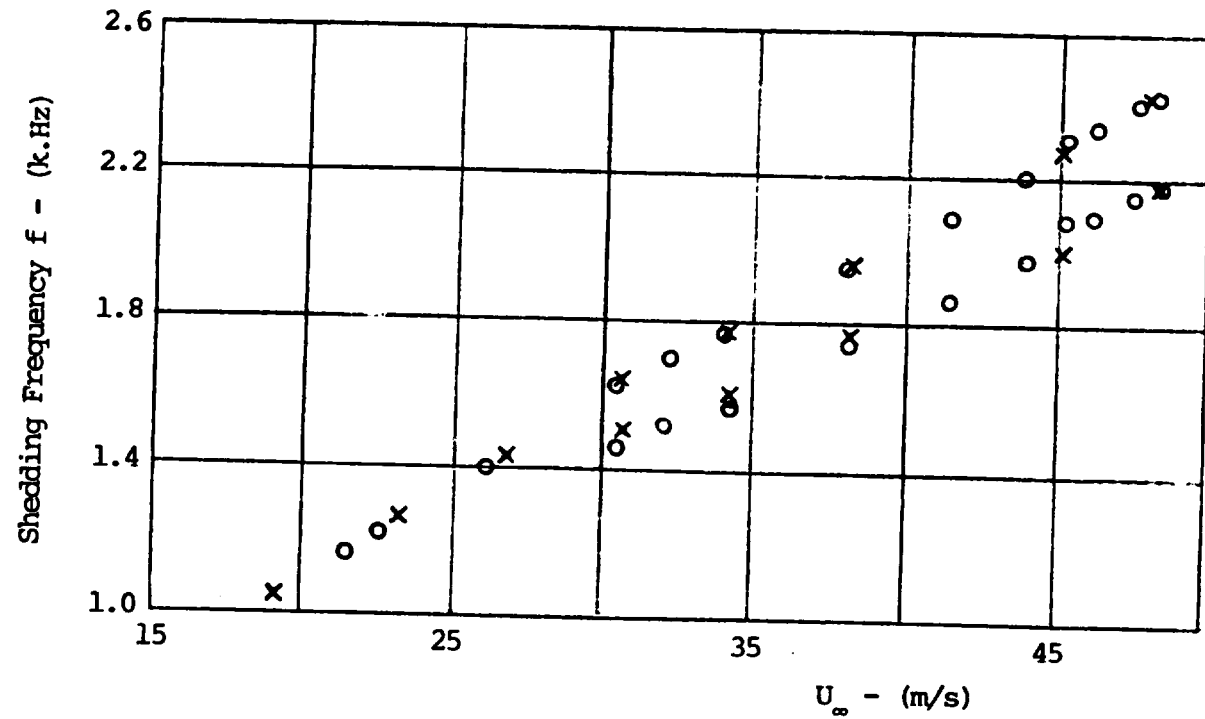


Figure V.27 Characteristic Vortex Shedding Frequency of the Truncated Airfoil with Transducers at different Velocities
(at streamwise position of $x/d = 2.2$, O ; at $x/d = 4.4$, x)

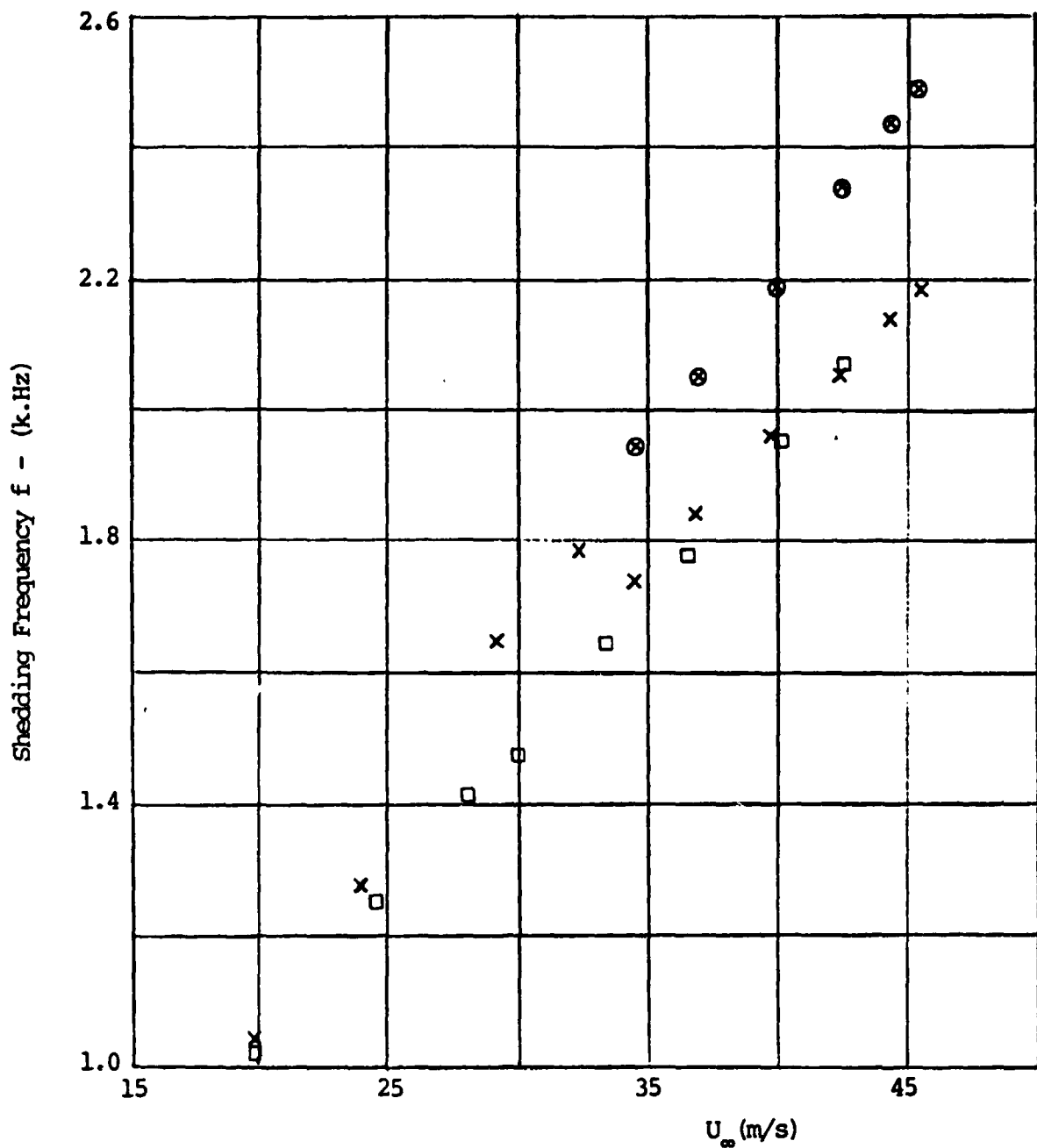


Figure V.28 Comparison of the Shedding Frequency between the Truncated Airfoil with Transducers and a Circular Cylinder
 (blunt trailing edge airfoil with transducers :
 primary frequency, x ; secondary frequency, ⊗ ;
 circular cylinder measurements, □)

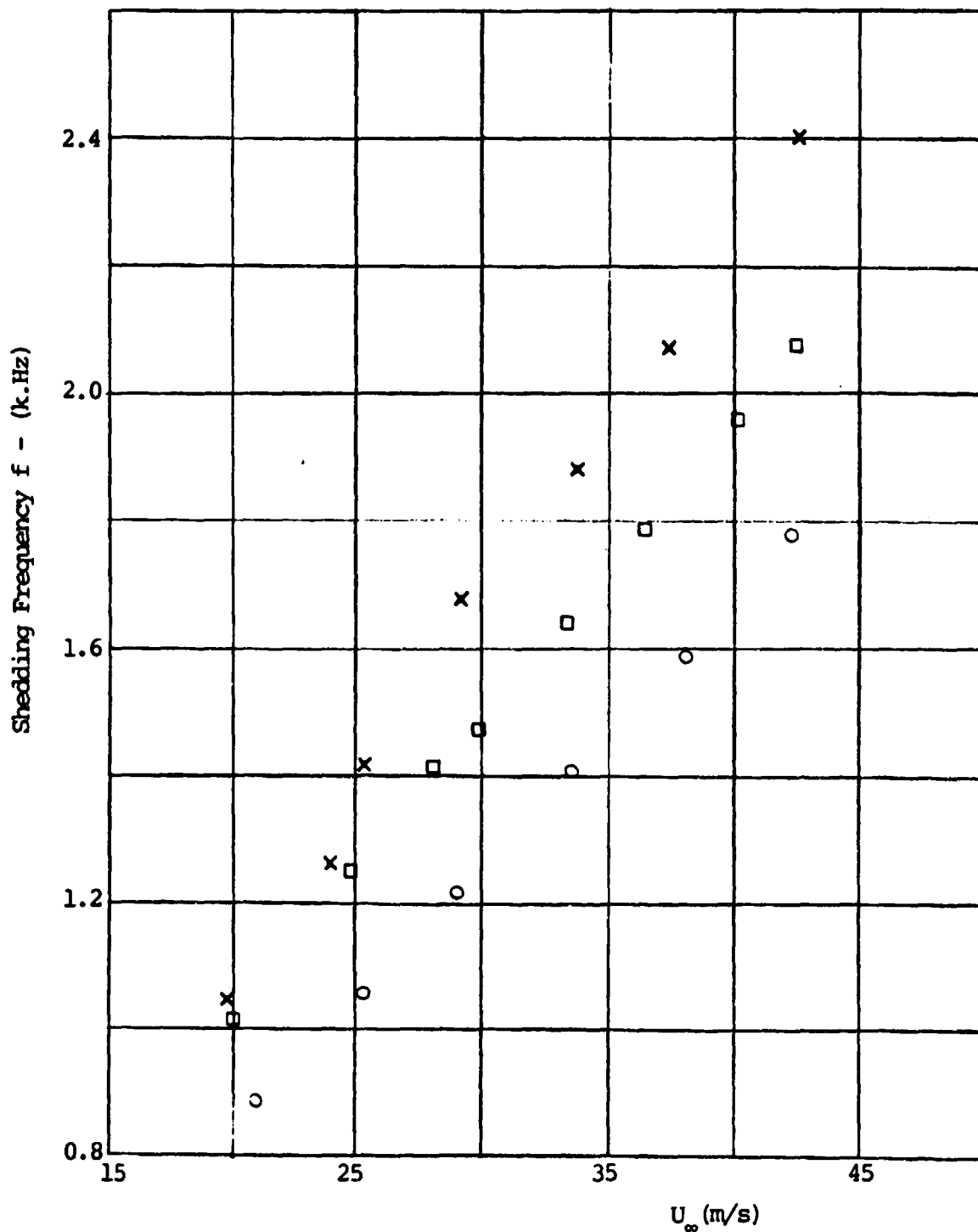


Figure V.29 Variation of the Vortex Shedding Frequency with Velocity
 (truncated airfoil with pressure taps ;
 without the boundary layer trip configuration , x ;
 with the boundary layer trip configuration , o ;
 circular cylinder measurements , □)

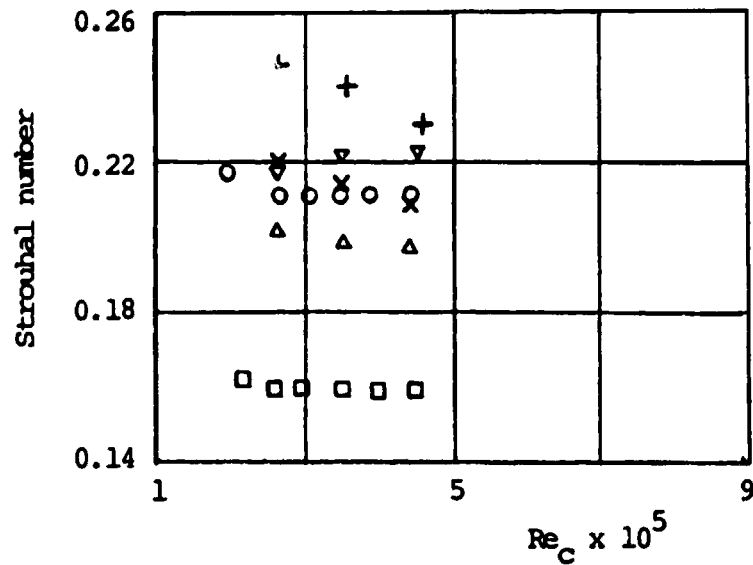


Figure V.30 Comparison of the Strouhal Number

(St = $\frac{fd}{U}$) -- with the boundary layer trip, \square
 ; without boundary layer trip, \circ

St = $\frac{f(d+2\delta)}{U}$ with the boundary layer trip, +
 ; without boundary layer trip, x

St = $\frac{f(d+2\theta)}{U}$ with the boundary layer trip, \triangle
 ; without boundary layer trip, ∇

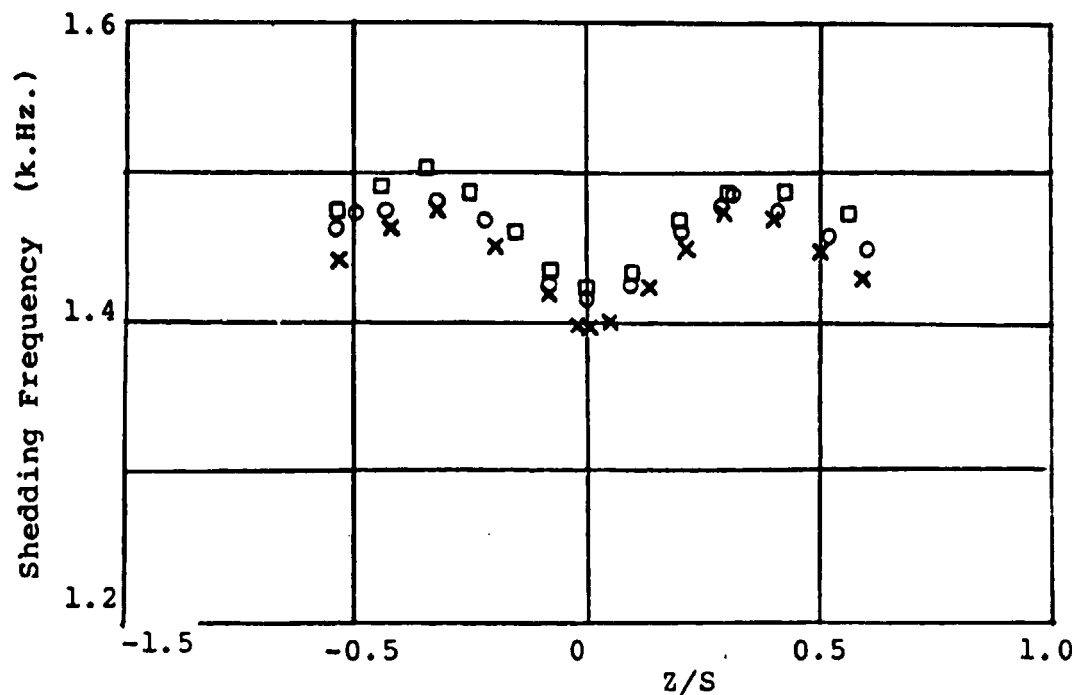


Figure V.31.a Variation of Shedding Frequency in the Spanwise Direction of the Truncated Airfoil with Transducers, at a velocity of 26m/s
 (at streamwise position of $x/d = 0.35$, \times ;
 at $x/d = 3.3$, O ; at $x/d = 4.6$, \square)

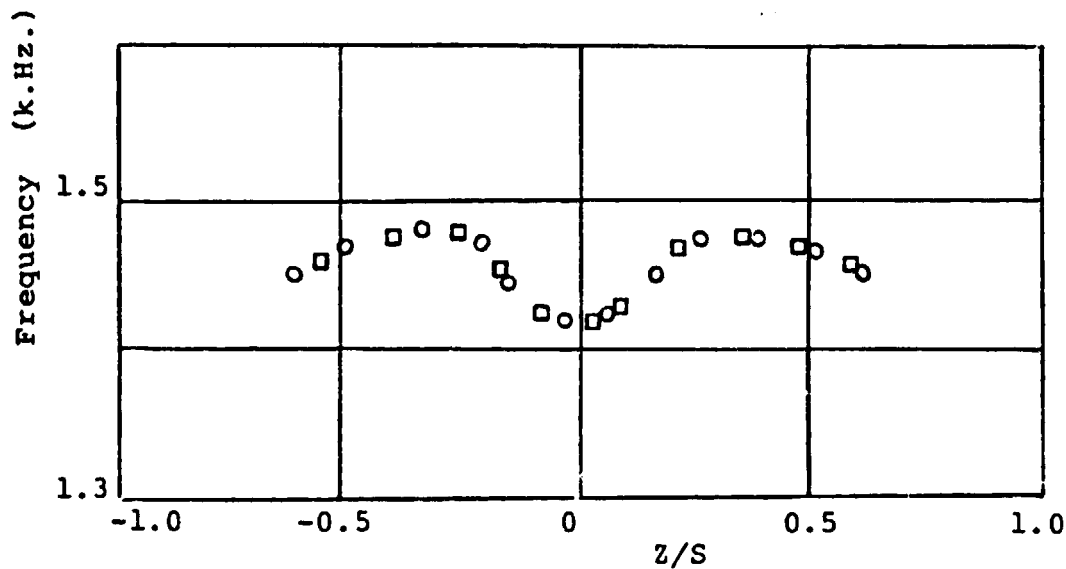


Figure V.31.b Variation of Shedding Frequency of Truncated Airfoil with Transducers at x/d of 3.33 and at a velocity of 26m/s
 (behind upper separation point , O ;
 behind lower separation point , \square)

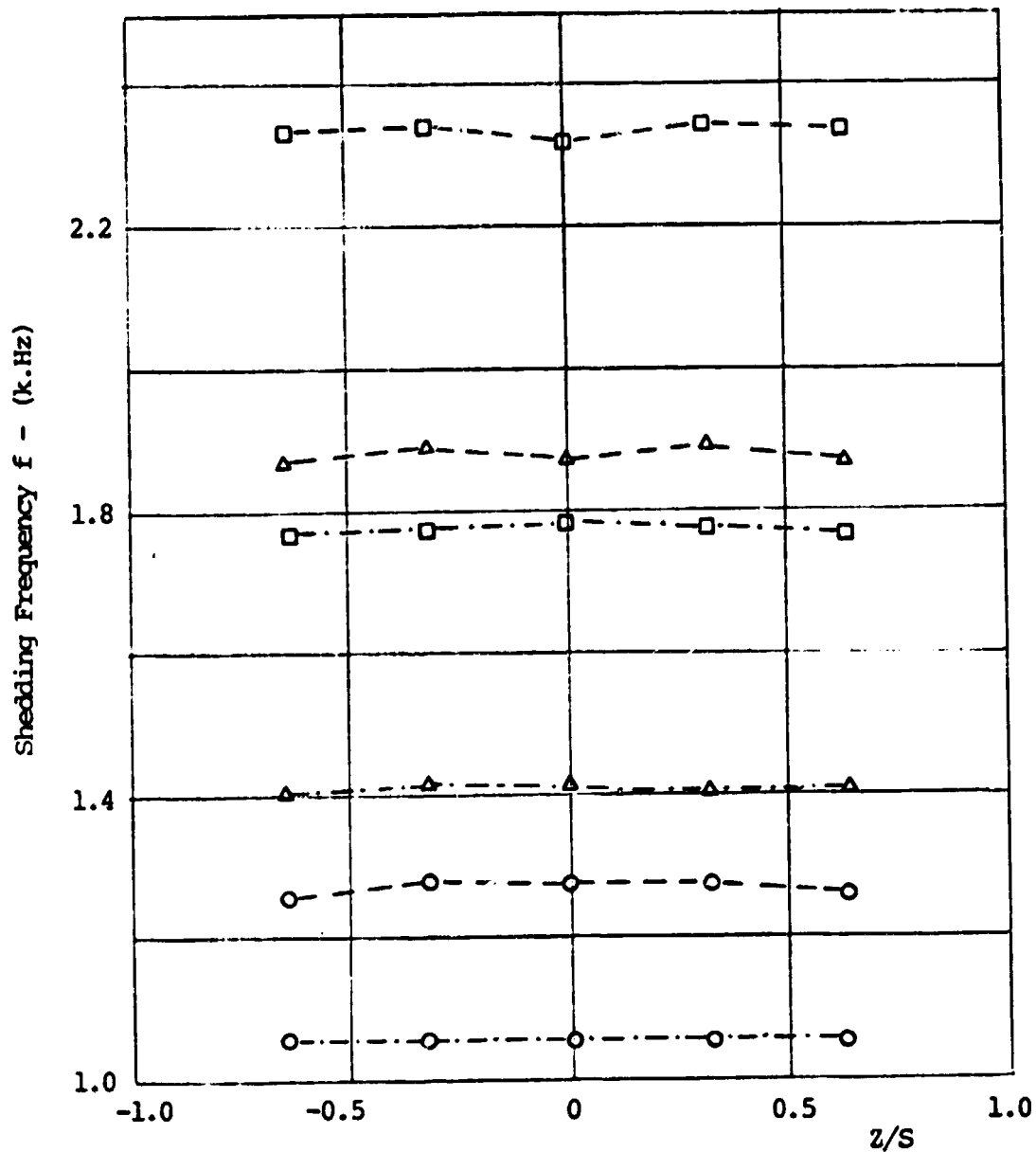


Figure V.32 Variation of Shedding Frequency in the Spanwise Direction of the Truncated Airfoil with Pressure Taps, at $x/d = 2.0$ for various Velocities
 (without the boundary layer trip configuration, ---; with the boundary layer trip configuration, -.-.-; at a tunnel flow velocity of 26m/s, ○ ; at 34m/s, Δ ; and at 44m/s, □)

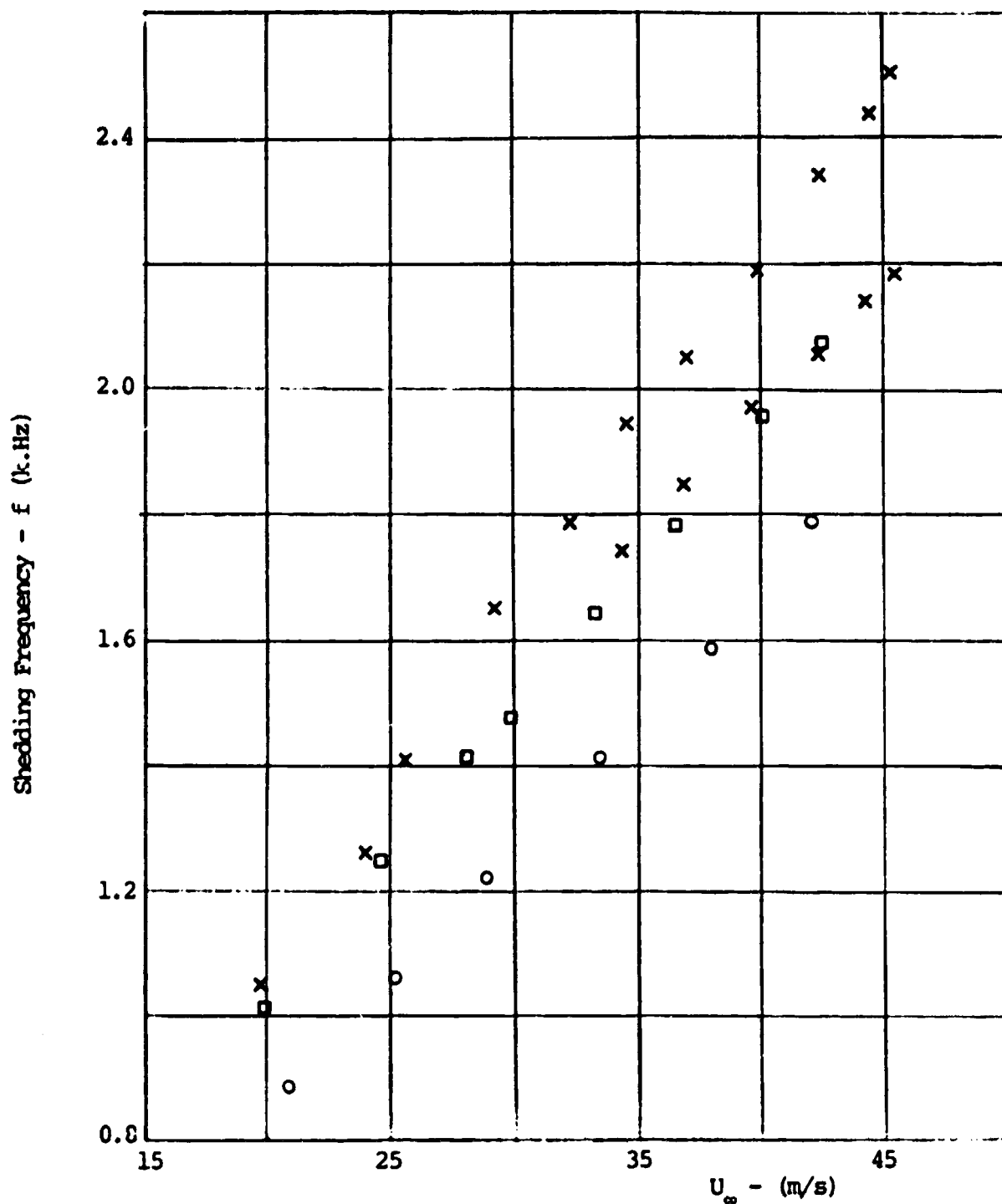


Figure V.33 Characteristic Vortex Shedding Frequency of a Circular Cylinder at different Velocities
 (measurements behind a circular cylinder, diameter equal to the thickness of the blunt trailing edge, \square ; truncated airfoil with transducers, \times ; truncated airfoil with pressure taps and tripped boundary layer configuration \circ .)

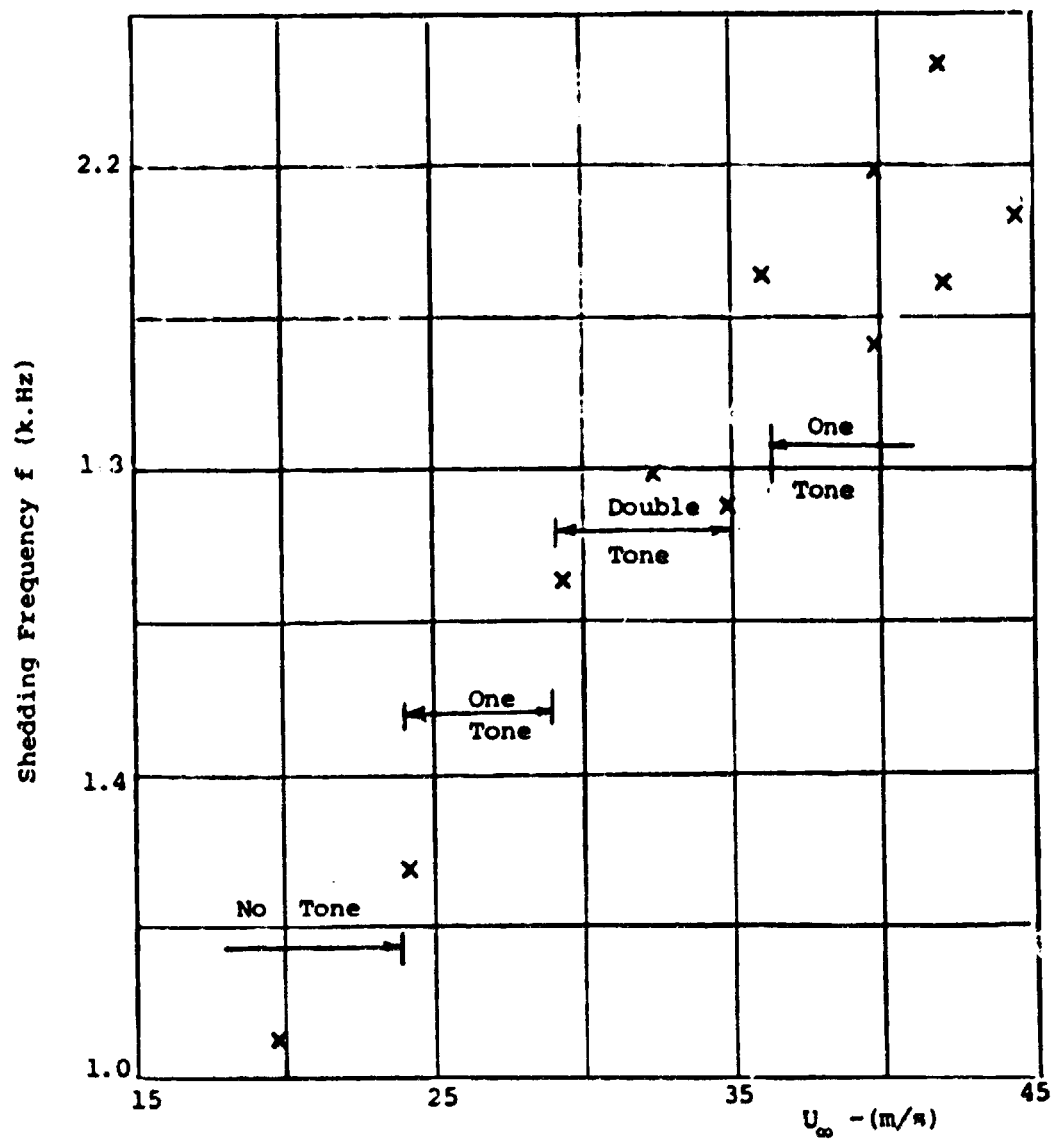


Figure V.34 Resonance characteristic of the tunnel measured with the truncated airfoil

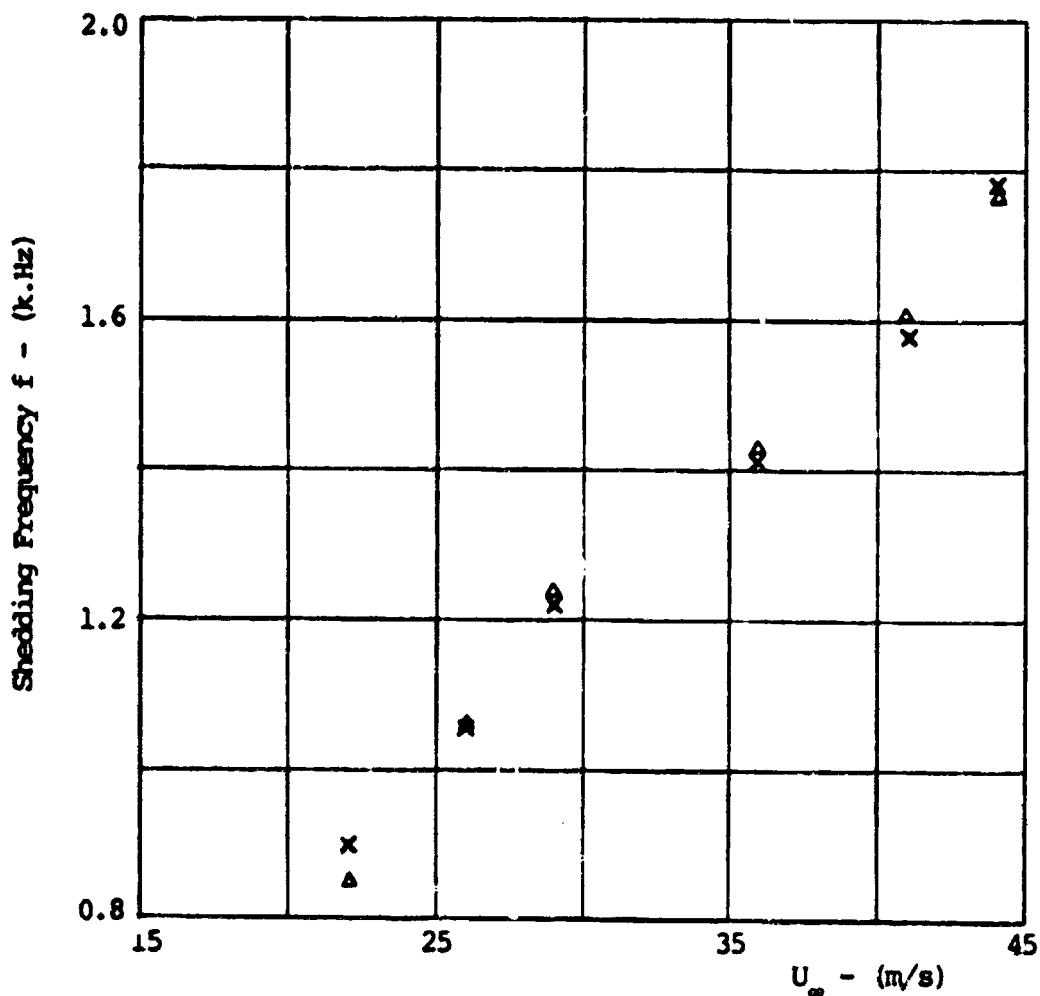
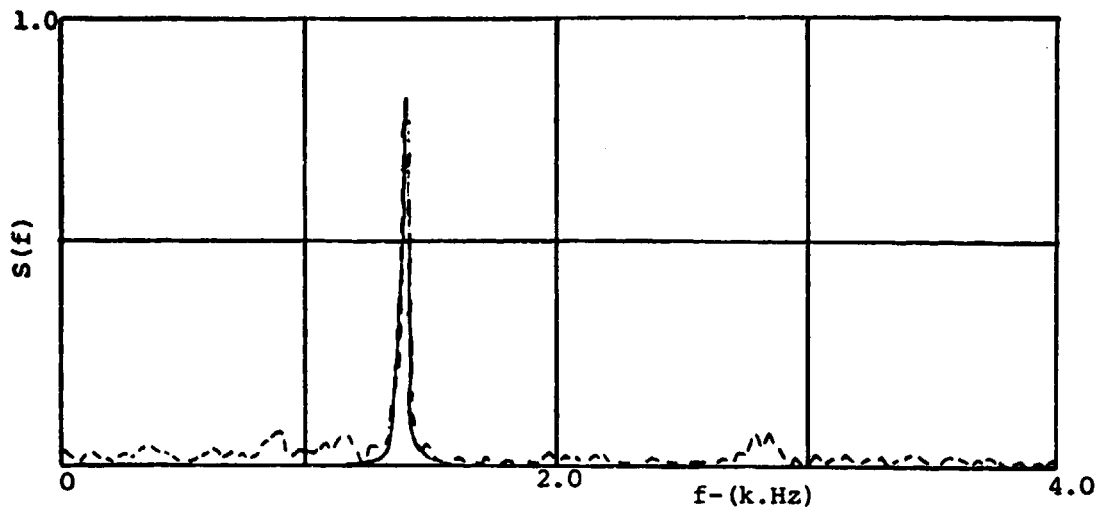
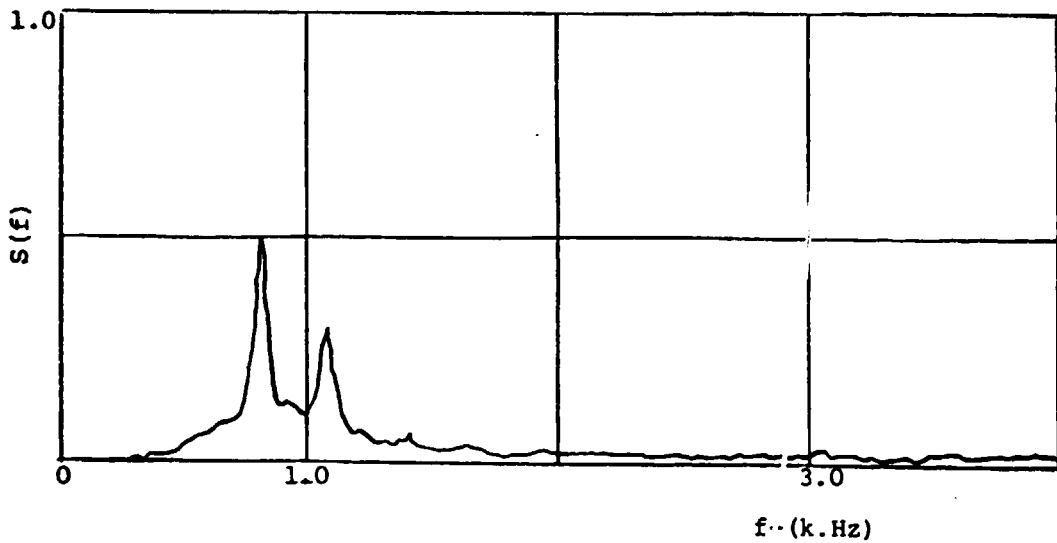


Figure V.35 Frequency Measurements of the Truncated Airfoil with Pressure Taps for Tripped Boundary Layer Configuration
 (measurement at streamwise station of $x/d = 2.0$ and hotwire probe , x ; measurement by microphone placed outside the test section , Δ)

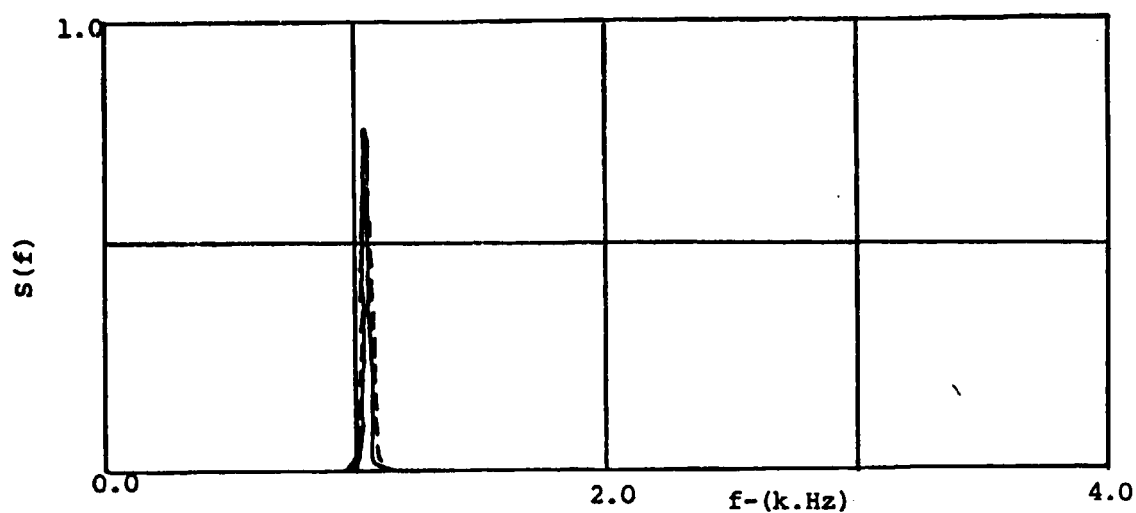


a) Auto spectral density of Hotwire signal, —
Cross spectral density of Hotwire and microphone signals, ---

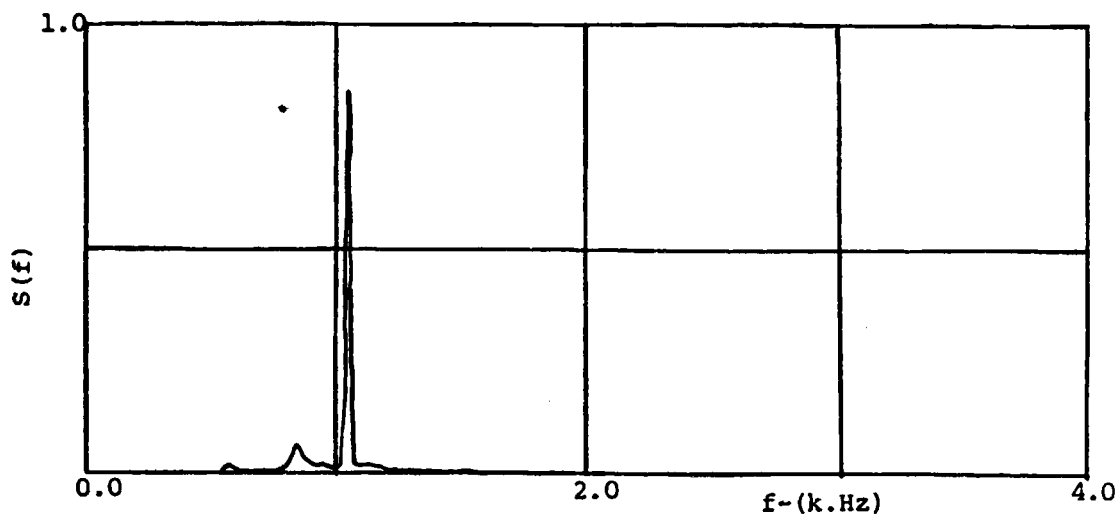


b) Auto spectral density of microphone signal, —

Figure V. 36 Measured Power Spectral Density for Tripped Boundary Layer Configuration of the Blunt Trailing Edge Airfoil with Pressure Taps at a Velocity of 34m/s



a) Auto spectral density of Hotwire signal, —,
 Cross spectral density of Hotwire and microphone signal, ---



b) Auto spectral density of microphone signal, ———

Figure V.37 Measured Power Spectral Density Tripped Boundary Layer
Configuration of for the Truncated Airfoil with Pressure Taps
at a Velocity of 24m/s

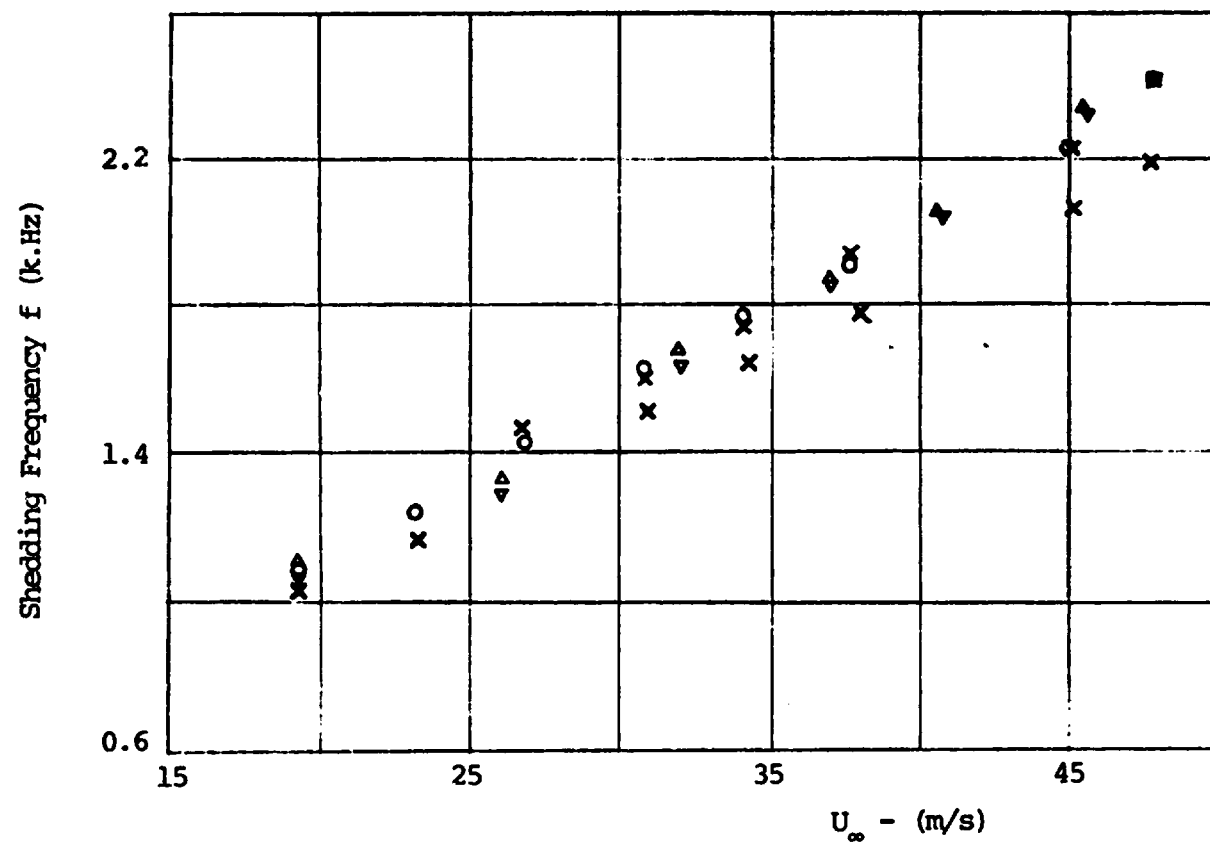
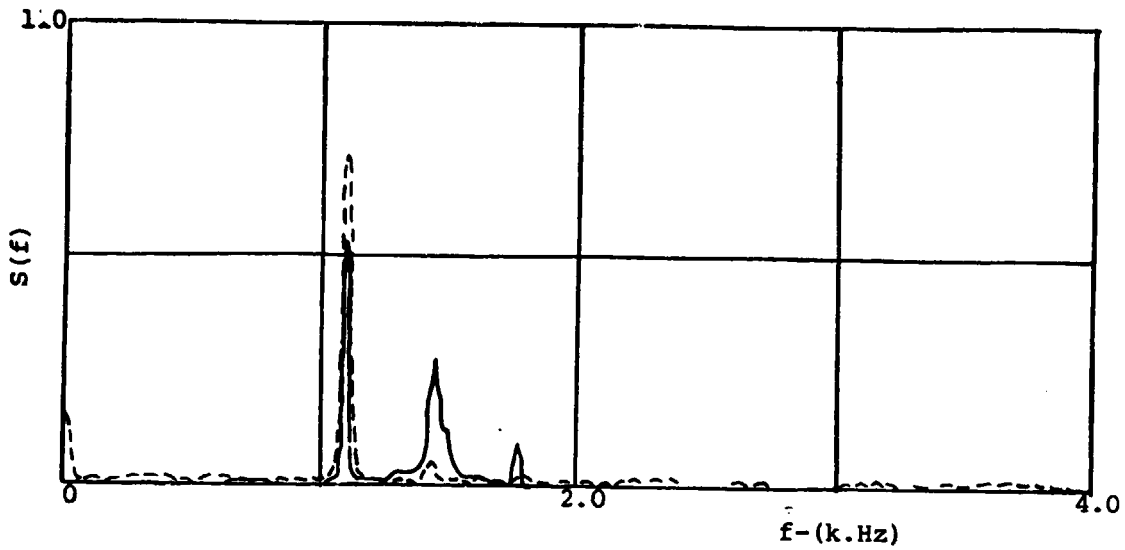
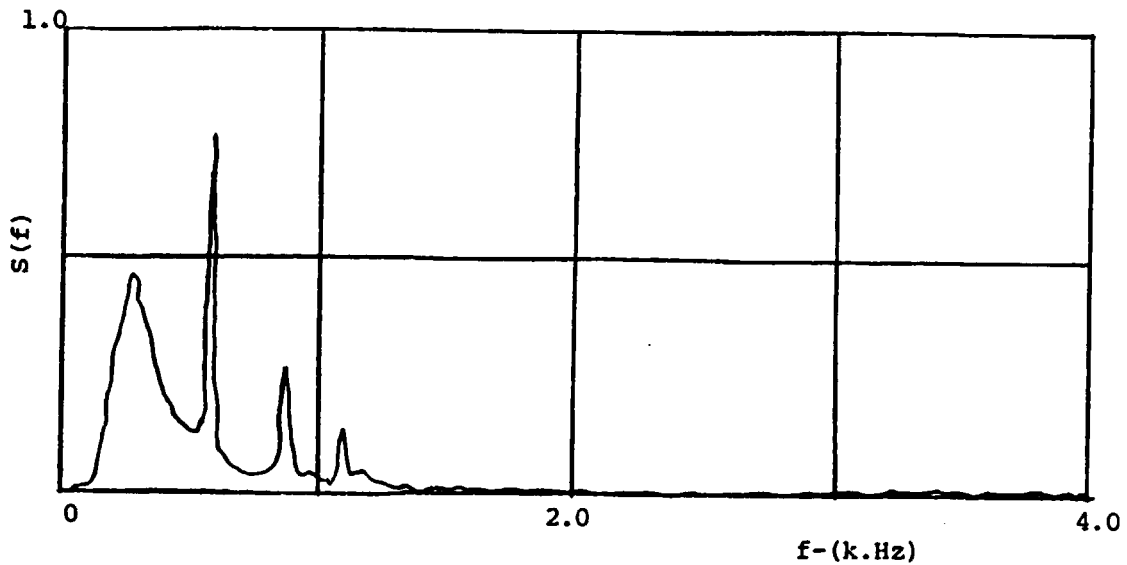


Figure V.38 Characteristic Vortex Shedding Frequency Measurements of the Truncated Airfoil with Untripped Boundary Layer
 (truncated airfoil with transducers :
 from hotwire measurements , x ; from microphone measurements , O ;
 truncated airfoil with pressure taps :
 from hotwire measurements , Δ ; from microphone measurements , ∇)



a) Auto spectral density of hotwire signal
Cross spectral density of hotwire and microphone signal, ---



b) Auto spectral density of microphone signal, —

Figure V.39 Measured Power Spectral Density of the Untripped Boundary Layer for the Truncated Airfoil with Pressure Taps at Velocity of 24m/s

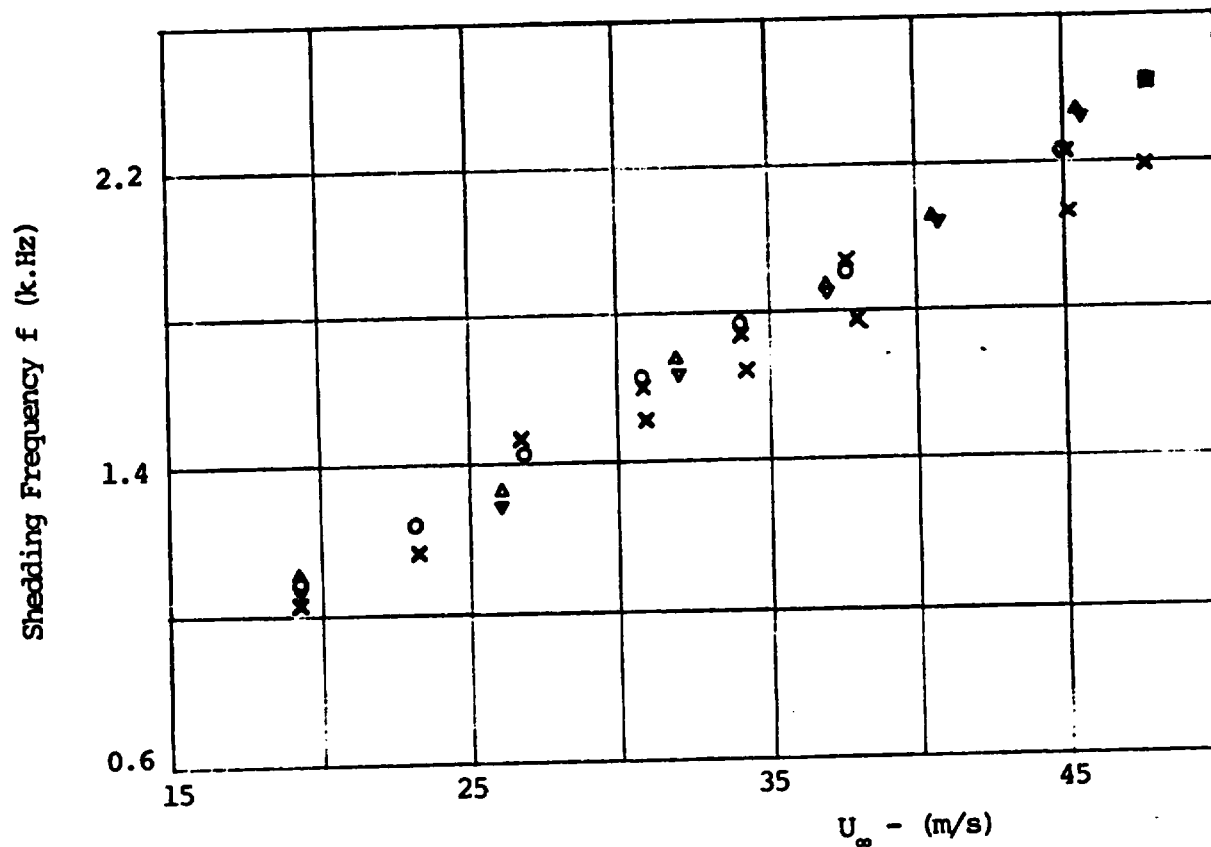
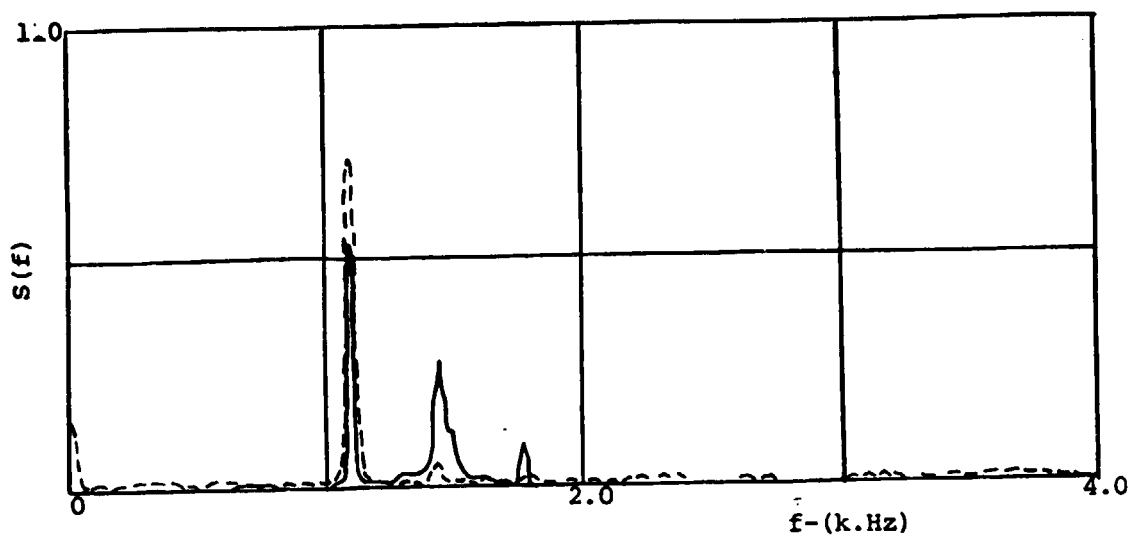
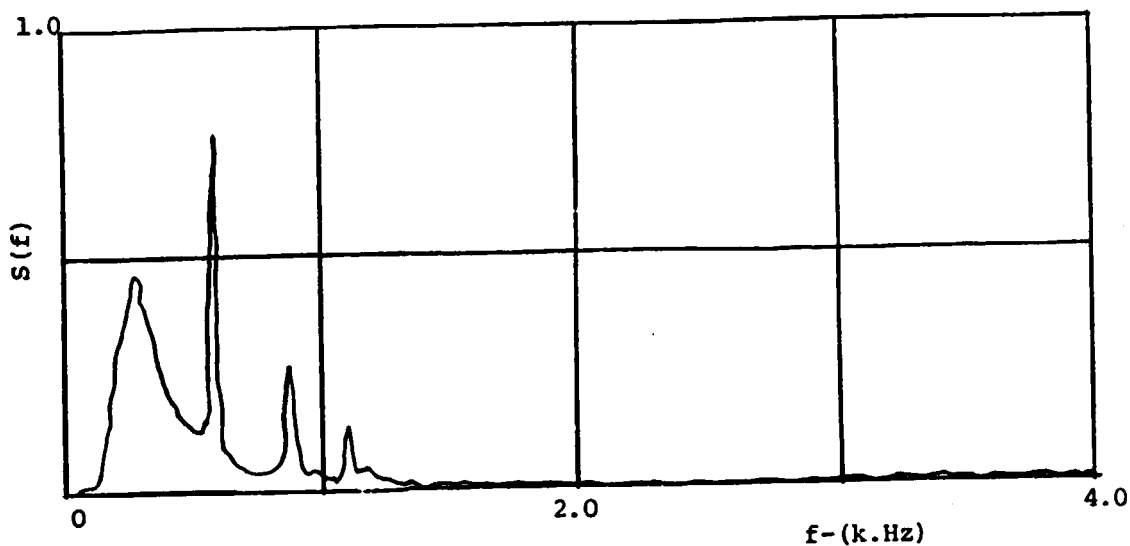


Figure V.38 Characteristic Vortex Shedding Frequency Measurements of the Truncated Airfoil with Untripped Boundary Layer
 (truncated airfoil with transducers :
 from hotwire measurements , X ; from microphone measurements , O ;
 truncated airfoil with pressure taps :
 from hotwire measurements , Δ ; from microphone measurements , ▽)

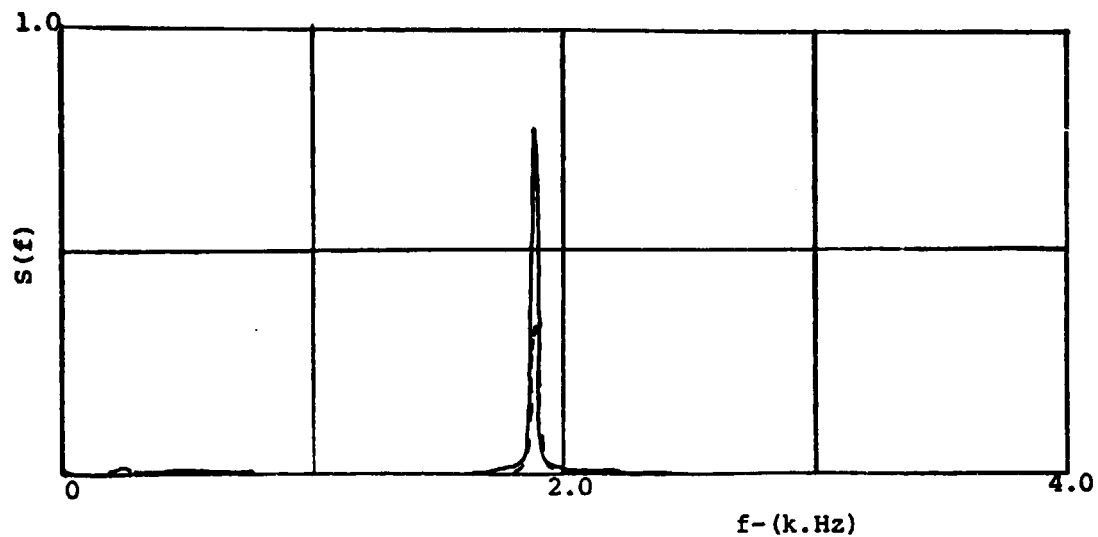


a) Auto spectral density of hotwire signal
Cross spectral density of hotwire and microphone signal, ---

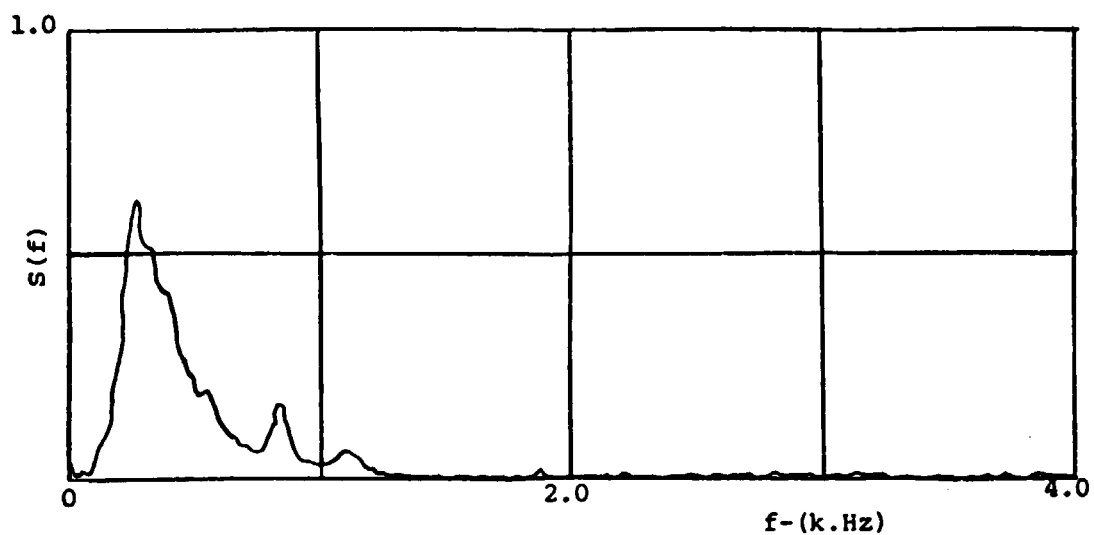


b) Auto spectral density of microphone signal, —

Figure V.39 Measured Power Spectral Density of the Untripped Boundary Layer for the Truncated Airfoil with Pressure Taps at Velocity of 24m/s



a) Auto spectral density of Hotwire signal, —
 Cross spectral density of Hotwire and microphone signals, ---



b) Auto Spectral density of microphone signal, —

Figure V.40 Measured Power Spectral Density of the Untripped boundary layer for the Truncated Airfoil with Pressure Taps at Velocity of 34m/s



ORIGINAL PAGE IS
OF POOR QUALITY

a) without the boundary layer trip

Figure V.41 1/3 Octave Band Spectrum from Microphone outside the Tunnel for the Truncated Airfoil with Pressure Taps at Velocity of 33m/s



b) with the boundary layer trip

Figure V.41 (continued)

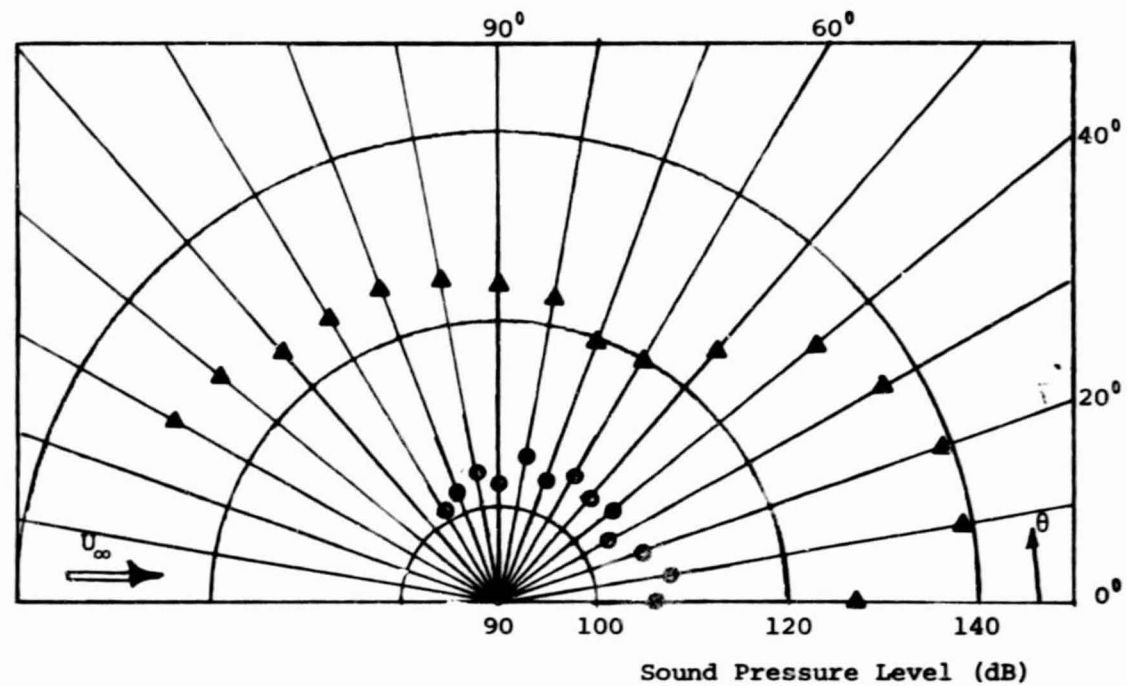


Figure V.42 Near Field Pressure Directivity Pattern for the Blunt Trailing Edge Airfoil with Pressure Taps at a Velocity of 26m/s and at a distance of $R = 2.0\text{cm}$

(without boundary layer trip - \circ , $f = 1420$;
 with boundary layer trip - \blacktriangle , $f = 1060$)

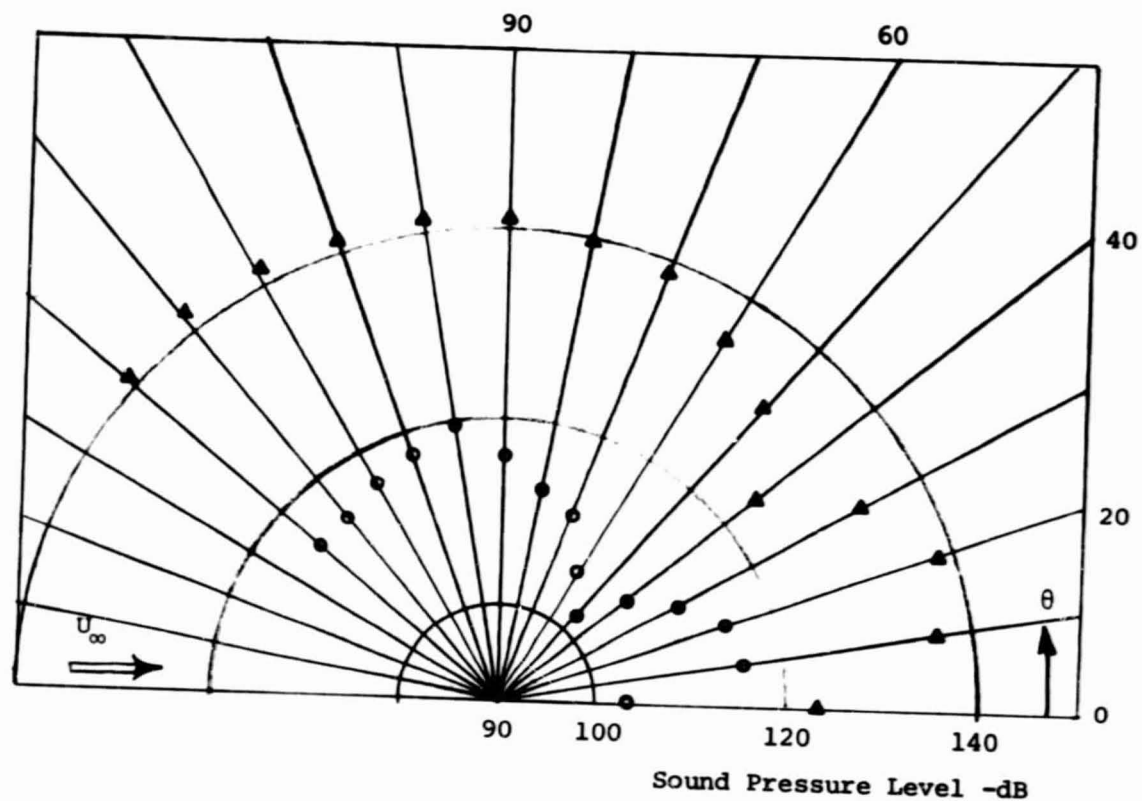


Figure V.43 Near Field Pressure Directivity Pattern for the Blunt Trailing Edge Airfoil with Pressure Taps at a Velocity of 34m/s and at a distance of $R = 2.0\text{cm}$
 (without boundary layer trip - \circ , $f = 1880$;
 with boundary layer trip - \blacktriangle , $f = 1410$)

Table III.1

Intensities of the Fluctuating Pressure Signal
as Measured by the Transducers

Upstream Distance from the B.T.E., cm.	Transducer No.	The RMS Value of the Fluctuating Pressure	
		N/sq. m.	db
0.0	11	0.0284	59.83
0.0	12	0.0275	59.58
0.25	8	0.0313	60.66
0.508	7	0.0175	56.55
0.758	5	0.0134	53.38
1.0	4	0.0095	50.33
10.24	3	0.0275	59.58
10.63	2	0.0129	52.97
11.033	1	0.0044	43.79

Table III.2

Phase Speeds and Angles from the
Oblique Wave Model

Transducer No.	Angle (θ)	Phase Speed a
4, 5, 8	10.42 deg	-257 m/s
4, 5, 7	-65.93 deg	-11.7 m/s
5, 7, 8	89.98 deg	-6.74 m/s

Table IV.1
Blade Passing Frequencies of the
Tunnel Drive Fan

Harmonic number	Frequency (Hz.)
1	306.7
2	613.3
3	920.0
4	1226.7
5	1533.3
6	1840.0
7	2146.7
8	2453.3
9	2760.0
10	3066.7

Table IV.2
Duct Mode Frequencies for the
45.7 x 45.7cm Tunnel

m/n	0	1	2	3	4	5
0	0	376.3	752.7	1129.1	1505.5	1881.8
1	376.3	532.2	841.5	1190.1	1551.8	1919.1
2	752.7	841.5	1064.5	1357	1683	2026.8
3	1129.1	1190.1	1357	1596.0	1881.8	2194.6
4	1505	1551.8	1683.1	1881.8	2139.	2409.9
5	1881.8	1919.1	2026.8	2194.6	2409.9	2661.3
6	2258.2	2289.3	2380.3	2524.7	2714.	2939.5
7	2634.2	2661.3	2739.9	2866.3	3034.4	3237.6
8	3010.9	3034.4	3103.6	3215.7	3366.3	3550.6
9	3387.3	3408.1	3469.9	3570.5	3706.8	3874.9

Table IV.3

Static Temperature Rise in the Tunnel Flow

Speed m/s	T (start) °C	T (end) °C	Period of Run minutes
18.7	19.7	22.4	45
32	20.3	24.1	60
47.6	20.3	29.7	50
56	28.2	33.0	45

Table IV.4

Duct Mode Frequencies for the
25.0 x 45.7cm Tunnel

m/n	0	1	2	3	4	5
0	0	688	1376	2064	2752	3440
1	376.4	784.2	1426.5	2098	2777.6	3460.5
2	752.7	1019.7	1568.4	2196.9	2853	3521
3	1129	1322	1779.9	2352.7	2974.6	3620.5
4	1505	1655.2	2039.6	2554.7	3136.8	3755
5	1881.1	2003	2331	2793	3333.9	3921
6	2258	2360.7	2644.4	3059.4	3559.9	4114.9
7	2634.6	2722.9	2972.3	3346.8	3809.8	4332.9
8	3010.9	2088.5	3310.5	2605.5	4079.1	4571.6
9	3387	3456.5	3656.1	3966.6	4364.3	4827.7

Table V.1

Shedding Frequencies of the Hotwire Support Rods

Velocity (m/s)	Top Support Rod (d = 0.9525cm)		Bottom Support Rod (d = 0.635cm)	
	measured (Hz)	calculated (Hz)	measured (Hz)	calculated (Hz)
21.0	740	670	458	440
27.5	873	771	530	514
31.0	1075	976	663	651
35.0	1215	1103	752	735
40.0	1385	1260	853	840
43.0	1485	1345	903	903

Table V.2

Shedding Frequency Variation Behind the Airfoil
With Transducers in the Spanwise Direction

Velocity (m/s)	Measured Frequency (Hz)		
	z/s = -0.5	z/s = 0.0	z/s = +0.5
19.0	1050	1050	1050
23.2	1265	1255	1285
26.5	1470	1430	1475
30.5	1625	1525	1620
34.0	1775	1775	1800
45.0	2220	2230	2225
48.0	2450	2420	2420

Table V.3

Measured Shedding Frequencies Behind A
Circular Cylinder

Velocity (m/s)	at spanwise location of z/s				
	-0.66	-0.33	0.0	+0.33	+0.66
a) configuration without small end plates					
24.0	1300	1275	1265	1275	1300
33.0	1695	1650	1645	1670	1710
43.0	2100	2050	2040	2050	2100
b) configuration with small end plates					
24.0	1260	1275	1275	1270	1255
33.0	1670	1645	1635	1645	1670
43.0	2080	2050	2040	2045	2080

BIBLIOGRAPHY

- Abbott, I.H., Van Doenhoff, A.E. (1959) "Theory of Wing Sections," Dover Publications.
- Bauer, A.B. (1961) "Vortex Shedding from Thin Flat Plates Parallel to the Free Stream," Journal Aerospace Sciences, Vol. 28(4), pp. 340-341.
- Bearman, P.W. (1965) "Investigation of the Flow Behind a Two-Dimensional Model with Blunt Trailing Edge and Fitted with Splitter Plate," Journal of Fluid Mechanics, Vol. 21(2), pp. 241-255.
- Bearman, P.W. (1966) "Investigation into the Effect of Basebleed on the Flow Behind a Two-Dimensional Model with Blunt Trailing Edge," AGARD - Cp-4.
- Bearman, P.W. (1969) "Correction for the Effect of Ambient Temperature Drift on Hotwire Measurements in Incompressible Flow," NPL Report 1382.
- Cowdrey, C.F. (1962) "A Note on the Use of End Plates to Present Three-Dimensional Flow at the Ends of Bluff Bodies," ARC-CP 683.
- Davis, S.S. (1975) "Theory of Discrete Vortex Noise," AIAA, Journal Vol. 13(3), pp 375-380. (AIAA paper 74-90).
- Davis, S.S. (1975) "Measurements of Discrete Vortex Noise in a Closed-throat Wind Tunnel," AIAA, paper 75-488.
- Garner, H.C., Rogers, E.W.E., Acum, W.E.A. and Maskell, E.C. (1966) "Subsonic Wind Tunnel Wall Corrections," AGARDograph 109.
- Graham, J.M.R. (1970) "Similarity Rules for Thin Aerofoils in Non-Stationary Flows," Journal of Fluid Mechanics, Vol. 43, pp. 743-756.
- Ghram, J.M.R. (1969) "The Effect of End Plates on the Two Dimensionality of a Vortex Wake," The Aeronautical Quarterly, Vol. 20(3), pp. 237-247.
- Greenway, M.E., Wood, C.J. (1973) "The Effect of a Bevelled Trailing Edge on Vortex Shedding and Vibration," Journal of Fluid Mechanics, Vol. 61(2), pp. 323-335.
- Howe, M.S. (1978) "A Review of the Theory of Trailing Edge Noise," Journal of Sound and Vibration, Vol. 61(3), pp. 437-465.

- Keefe, R.T. (1961) "An Investigation of the Fluctuating Forces Acting on a Stationary Circular Cylinder in a Subsonic Stream and of the Associated Soundfield," UTIA-Report, No. 76, September.
- Kristensen, H.S. (1974) "Hotwire Measurements in Turbulent Flows," DISA-Information.
- Lawrence, I., Lindley, D. (1974) "Effect of Trailing Edge Thickness on the Aerodynamic Performance of Airfoil," presented at the 5th Australian Conference on Hydraulics and Fluid Mechanics, University of Centerbury, December.
- Maul, D.H., Hoole, B.H. (1967) "The Effect of Boat-tailing on the Flow Round the Two Dimensional Blunt Based Airfoil at Zero Incidence," Journal of Aerospace Sciences, Vol. 71(12), pp. 854-858.
- Maul, D.J. (1966) "The Pressure Distribution at Low Speeds on Two Dimensional Aerofoils with Blunt Trailing Edges at Zero Incidence," Journal of the Royal Aeronautical Society, Vol. 70, pp. 727-729.
- Morsse, P.M., Ingard, U. (1968) "Theoretical Acoustics," McGraw-Hill, pp. 497.
- Nash, J.F. (1962) "An Analysis of Two Dimensional Turbulent Base Flow, Including the Effect of the Approaching Boundary Layer," ARC R & M 3344.
- Nash, J.F. (1964) "An Analysis of the Subsonic Flow Past Symmetrical Blunt Trailing Edge Airfoil Sections at Zero Incidence in the Absence of a Vortex Street," ARC R & M 3436.
- Nash, J.F., Quencey, V.G., Callinan, J. (1963) "Experiments on Two Dimensional Baseflow at Subsonic and Transonic Speeds," ARC R & M 3427.
- Nash, J.F. (1962) "A Review of Research on Two Dimensional Base Flow," ARC R & M 3323.
- National Aeronautical Laboratory "Baseflow: A Bibliography (1950-1972)" October 1973, (N74-257ab).
- Pankhurst, R.C., Holder, D.W. (1952) "Wind Tunnel Technique," Pitman, London.
- Parker, R. (1956) "Resonance Effects in Wake Shedding from Parallel Plates: Some Experimental Observations," Journal of Sound and Vibration, Vol. 4(1), pp. 67-72
- Peterson, R.F., "The Boundary Layer and Stalling Characteristics of the NACA64A010 Airfoil Section," NACA TN-2235(1950).
- Pope, A., Harper, J.J. (1965) "Low-speed Wind Tunnel Testing," Wiley & Son, Inc.

Roshko, A. (1955) "On the Wake and Drag of Bluff Bodies," Journal of Aerospace Sciences, Vol. 20, pp. 124-132, and also as NACA TN-3169.

Simmons, J.E.L. (1975) "Effect of Separation Angle on Vortex Streets," Journal of Engineering, Mechanics Divisions, A.S.C.E., Vol. 101, EM5, pp. 649-661.

Smith, C.A., Karamcheti, K. (1978) "Some Features of Wake Tone Flow Field," AIAA Paper, 78-238, and also JIAA-TR-9 (1978).

Smith, C., Varzaly, A., Baganoff, D., "Characteristics of the Subsonic Windtunnel" (unpublished report).

Varzaly, A., Karamcheti, K. (1978) "Some Features of Low Speed Flow Over a Rectangular Cavity," JIAA TR-10, July 1978.

Wood, C.J. (1964) "The Effect of Base Bleed on a Periodic Wake," Journal of the Royal Aeronautical Society, Vol. 68(7), pp. 477-482.

Additional reference:

On Aerocoustics

Amiet, R.K. (1974) "Compressibility Effect in Unsteady Thin Airfoil Theory," AIAA Journal, Vol. 12, pp. 252-255.

Chase, D.M. (1972) "Sound Radiated by Turbulent Flow off a Rigid Halfplane as Obtained from a Wave Number Spectrum of Hydrodynamic Pressure," Journal of the Acoustical Society of America, Vol. 52, pp. 1011-1023.

Clark, L.T. (1971) "The Radiation of Sound From an Airfoil Immersed in a Laminar Flow," Journal of Engineering for Power, October, pp. 366-376.

Crighton, D.G. (1972) Radiation from Vortex Filament Motion Near a Halfplane," Journal of Fluid Mechanics, Vol. 51(2), pp. 357-362.

Crighton, D.G., Lippington, F.G. (1970) "Scattering of Aerodynamic Noise," Journal of Fluid Mechanics, Vol. 43(1), pp. 721-736.

Curle, S.N. (1955) "The Influence of Solid Boundaries upon Aerodynamic Sound," Proceedings of the Royal Society Series A, Vol. 231, pp. 505-514.

Dean, L.W. (1971) "Broad Band Noise Generated by Airfoil in Turbulent Flow," AIAA, paper 71-587.

- Fathy, A., Rashed, M.I., Lunsdaine, E. (1977) "A Theoretical Investigation of Laminar Wakes Behind Airfoils and the Resulting Noise Pattern," Journal of Sound and Vibration, Vol. 50(1), pp. 133-144.
- Filotas, L.T. (1969) "Theory of Airfoil Response in a Gusty Atmosphere - Part I, II," University of Toronto Institute Aerospace Studies, Report 139, 141.
- Fink, M.R. (1975) "Prediction of Airfoil Ton Frequencies," Journal of Aircraft, Vol. 12(2), pp. 188-119.
- Hayden, R.E. (1972) "Noise from Interaction of Flow with Rigid Surfaces: A Review of Current Status of Prediction Techniques," NASA CR-2126.
- Jackson, R., Graham, K.M.R., Maull, D.J. (1973) "The Lift on a Wing in a Turbulent Flow," The Aeronautical Quarterly, pp. 155-166.
- Jones, D.S. (1972) "Aerodynamic Sound Due to a Source Near a Half-Plane," Journal
- Joshi, M. C., Yu, J.C. (1979) "An Experimental Study of USB Flap Noise Reduction Through Mean Flow Modification," AIAA Paper, 79-0607.
- Kaji, S. (1975) "Non-compact Source Effect on the Prediction of Tone Noise From a Fan Motor," AIAA paper. 75-446.
- Kuethé, A.M. (1972) "Effect of Streamwise Vortices on Wake Properties Associated with Sound Generation," AIAA, Vol. 9(10), pp. 715-719.
- Liepman, H.W. (1955) "Extension of the Statistical Approach to Buffeting and Gust Response of Wings of Finite Span," Journal of Aerospace Sciences, Vol. 22, pp. 197-200.
- Mugridge, B.D. (1971) "Acoustic Radiation from Aerofoils with Turbulent Boundary Layers," Journal of Sound and Vibration, Vol. 16(4), pp. 593-614.
- Mugridge, B.D. (1971) "Turbulent Boundary Layers and Surface Pressure Fluctuations on Two-Dimensional Aerofoils," Journal of Sound and Vibration, Vol. 18(4), pp. 475-486.
- Osborne, C. (1973) "Unsteady Thin Airfoil Theory for Subsonic Flow," AIAA, Vol. 11, pp. 205-209.
- Parker, R. (1957) "Resonance Effect in Wake Shedding from Parallel Plates: Calculations of Natural Frequency," Journal of Sound and Vibration, Vol. 5(2), pp. 330-343.
- Paterson, R. W., Amiet, R.K. (1976) "Acoustic Radiations and Surface Pressure Characteristics of an Airfoil due to Incident Turbulence," AIAA Paper 76-571.

- Paterson, R.W., Vogt, P.G., Fink, M.R., Munch, C.L. (1973) "Vortex Noise of Isolated Airfoils." Journal of Aircraft, Vol. 10(5).
- Powell, A.O. (1959) "On the Aerodynamic Noise of a Rigid Flat Plate Moving at Zero Incidence," Journal of the Acoustical Society of America, Vol. 31(12), pp. 1649-1653.
- Ribner, H.S. (1956) "Spectral Theory of Buffeting and Gust Response: Unification and Extension," Journal of Aerospace Sciences, pp. 1075-1077.
- Schinkler, R.H. (1977) "Airfoil Trailing Edge Noise Measurements with a Directional Microphone," AIAA Paper, 77-1269.
- Schinkler, R.H., Fink, M.R., Amiet, R.K. (1976) "Vortex Noise from Non-rotating Cylinders and Airfoils," AIAA Paper, 76-81.
- Sears, W.R. (1941) "Some Aspects of Non-stationary Airfoil Theory and its Practical Application," Journal of Aerospace Sciences, Vol. 8(1), pp. 104-108.
- Sharland, I.J. (1964) "Source of Noise in Axial Flow Fans," Journal of Sound and Vibration, Vol. 1(3), pp. 302-322.
- Siddon, T.E. (1973) "Noise Source Diagnostics Using Causality Correlations," AGARD Cp-131(7).
- Sunyach, M., Arbey, H., Robert, D., Bataille, J., Comte-Bellot, G. (1973) "Correlations Between Far Field Acoustic Pressure and Flow Characteristics for a Single Airfoil," AGARD, Cp-131.
- Tam, C.K.W. (1974) "Discrete Tones of Isolate Airfoils," Journal of the Acoustical Society of America, Vol. 55(6), pp. 1173-1177.
- Tam, C.K.W., Yu, Y.C. (1975) "Trailing Edge Noise," AIAA Paper, 75-489.
- Von Karman, T., Sears, W.R. (1938) "Airfoil Theory for Non-uniform Motion," Journal of Aerospace Sciences, Vol. 5, pp. 379-390.
- Yu, J.C., Tam, C.K.W. (1977) "An Experimental Investigation of the Trailing Edge Noise Mechanism," AIAA Paper, 77-1291.
- Yu, J.C., Joshi, M.C. (1979) "On Sound Radiation from the Trailing Edge of an Isolated Airfoil in Uniform Flow," AIAA Paper, 79-0603.

On Blunt Based Body

- Archibald, F.S. (1975) "Self-Excitation of an Acoustic Resonance by Vortex Shedding," Journal of Sound and Vibration, Vol. 38(1), pp. 81-103).
- Archibald, F.S. (1975) "The Laminar Boundary Layer Instability Excitation of an Acoustic Resonance," Journal of Sound and Vibration, Vol. 38(3), pp. 387-402.
- Bellhouse, B.J., Wood, C.J. (1965) "The Upstream Influence of Basebleed on Surface Pressure and Skin Friction," Journal of the Royal Aeronautical Society, Vol. 69, pp. 789-791.
- Belvins, R. D., Burton, T.E. (1976) "Fluid Forces Induced by Vortex Shedding," Journal of Fluid Engineering, March, pp. 14-26.
- Brogna, S.J., Hawks, R.J. (1978) "Effect of Base Suction on Subsonic Drag of Bluff Bodies," Journal of Aircraft, Vol. 15(7).
- Eagleson, P.S., et. al. (1961) "Turbulence in the Early Wake of a Fixed Flat Plate," MIT Hydrodynamics Lab Report, No. 46.
- Etheridge, D.W., Kemp, P.H. (1978) "Measurements of Turbulent Flow Downstream of a Rearward Facing Step," Journal of Fluid Mechanics, Vol. 86(3), pp. 545-566.
- Hanson, C.E. (1970) "An Investigation of the Near Wake Properties Associated with Periodic Vortex Shedding from Airfoils," Acoustics and Vibrations Lab, MIT, Report # 76234-5.
- Herketed, G., Colberts, D.R. (1960) "Influence of Trailing Edge Geometry on Hydraulic-Turbine-Blade Vibration Resulting from Vortex Excitation," Journal of Engineering for Power, Vol. 82, pp. 103-110.
- Hoerner, S.F. (1950) "Base Drag and Thick Trailing Edges," Journal Aerospace Sciences, Vol. 17, pp. 22-628.
- Holder, D.W., Pearcey, H.H., and Nash, J.F. (1962) "Some Aerodynamic Advantages of Thick Trailing Edges in High Speed Flight," paper presented to the Royal Aeronautical Society, February, (referred to by Nash, Ref. 2).
- Majola, O.O., Young, A.D. (1972) "An Experimental Investigation of the Turbulent Boundary Layer Along a Streamwise Corner," AGARD, Cp-93.
- Marris, A.W. (1964) "A Review on Vortex Street, Periodic Wakes and Induced Vibrations Phenomena," Journal of Basic Engineering, June, pp. 185-196.

- Prasad, J.K., Grupta, A.K. (1977) "Velocity Correlations in the Turbulent Near Wake of Bluff Bodies," Journal AIAA, Vol. 15(11), pp. 1569-1574.
- Roshko, A. (1953) "On the Development of Turbulent Wakes from Vortex Streets," NACA Report, 1911, also NACA TN-2913.
- Sato, H., Kurki, K. (1961) "The Mechanism of Transition in the Wake of a Thick Plate Placed Parallel to a Uniform Flow," Journal of Fluid Mechanics, Vol. 11, pp. 321-352.
- Sato, H. (1970) "An Experimental Study of Non-linear Interactions of Velocity Fluctuations in the Transition Region of a Two Dimensional Wake," Journal of Fluid Mechanics, Vol. 44, pp. 741.
- Sulery, R.K., Grupta, A.K., Moorthy, C.S. (1975) "Similarity in the Turbulent Near Wake of Bluff Bodies," Journal AIAA, Vol. 13(11), pp. 1425-1429.
- Tanner, M. (1966) "The Wake Pressure Behind Wedges as Influenced by Splitter Plates and Suction," AGARD, p. 4, pt.2.
- Tanner, M. (1974) "New Investigations for Reducing the Base Drag of Wings with a Blunt Trailing Edge," AGARD cp-124.
- Toeber, G.H., Eagelson, D.S. (1961) "Hydro Elastic Vibrations of Flat Plates Related to Trailing Edge Geometry," Journal of Basic Engineering, December, pp. 671-678.

On Bluff Body Cylinder

- Ayoub, A., Karamcheti, K. (1976) "Pressure Fluctuations on the Surface of a Cylinder in Uniform Flow," JIAA TR-3.
- Berger, E., Wille, R. (1972) "Periodic Flow Phenomena," Annual Review of Fluid Mechanics, Vol. 4, pp. 313-340.
- Clement, R. (1973) "An Inviscid Model of Two-Dimensional Vortex Shedding," Journal of Fluid Mechanics, Vol. 57(3), pp. 321-336.
- El-Baroudi, M.Y. (1960) "Measureent of Two Point Correlations of Velocity Near a Circular Cylinder Shedding a Karman Vortex Street," UTIA-TN-31.
- Gerrad, J.H. (1966) "The Mechanism of the Formation Region of Vortices Behind Bluff Bodies," Journal of Fluid Mechanics, Vol. 25(1), pp. 401-413.

- Gerrad, J. H. (1965) "A Disturbance-Sensitive Reynolds Number Range of the Flow Past a Circular Cylinder," Journal of Fluid Mechanics, Vol. 22(1), pp. 187-196.
- Gerrad, J.H. (1961) "An Experimental Investigation of the Oscillating Lift and Drag of a Circular Cylinder Shedding Turbulent Vortices," Journal of Fluid Mechanics, Vol. 11(2), pp. 244-256.
- Hema, F.R. (1957) "Three Dimensional Vortex Pattern Behind a Circular Cylinder," Journal of Aerospace Sciences, pp. 156-158.
- Humphrays, J.S. (1960) "Note on a Circular Cylinder in a Steady Wind at Transition Reynolds Number," Journal of Fluid Mechanics, Vol. 9(4), pp. 603-612.
- Koopman, G.H. (1967) "The Vortex Wakes of Vibrating Cylinders at Low Reynolds Numbers," Journal of Fluid Mechanics, Vol. 28, pp. 501-512.
- Kovaznay, L.S.G. (1949) "Hotwire Investigation of the Wake Behind Cylinders at Low Reynolds Number,s" Proceedings of the Royal Society Series A, Vol. 198, pp. 174.
- McGregor, D.M. (1957) "An Experimental Investigation of the Oscillating Pressures on a Circular Cylinder in a Fluid Strea," UTIA-IN-14.
- Morkavin, M.V. (1964) "Flow Around Circular Cylinder - A Kaleidoscope of Challenging Fluid Phenomena," paper presented as A.S.M.E. Symposium on Fully Separated Flows, Philadelphia, Pa., pp. 102-118.
- Nakaya, C. (1976) "Instability of the Near Wake Behind a Circular Clydinger," Journal of Physical Society of Japan, Vol. 41, pp. 1087-1088.
- Ogawa, A., Nakagawa, K. (1978) "Stability of the Vortex Street in the Wake of Stationary and Vibrating Cylinder," Transactions of the Japan Society of Aerospace Sciences, Vol. 20(5) , pp. 176-186.
- Pendergast, V. (1958) "Measurement of Two Point Correlations of the Surface Pressure on a Circular Cylinder," UTIA-TN-23.
- Phillips, O.M. (1956) "The Intensity of Aeolian Tones," Journal of Fluid Mechanics, Vol. 1(6).
- Rosenhead, L. (1953) "Vortex Systems in Wakes," Advances in Applied Mechanics, Vol. 3, pp. 185-195.
- Roshko, A. (1954) "A New Hodograph for Freestream Line Theory," NACA TN-3168.
- Sallet, D.W. (1973) "The Lift Force Due to Von Karman's Vortex Wake," Journal of Hydronautics, Vol. 7(4), pp. 161-165.

- Tritten, D.J. (1959) "Experiments on the Flow Past a Circular Cylinder at Low Reynolds Numbers," Journal of Fluid Mechanics, Vol. 6.
- Van Nunen, J.W.G. (1972) "Pressures and Forces on a Circular Cylinder in a Cross Flow at High Reynolds Numbers," in Flow Induced Structural Vibrations, ed., E. Naudascher, pp. 748-754.
- Wille, R. (1950) "Karman's Vortex," Advances in Applied Mechanics, Vol. 6, pp. 273-287.
- Wille, R. (1966) "On Unsteady Flows and Transient Motions," Progress in Aeronautical Science, Vol. 7, pp. 195-207.

on Wind Tunnel Interference

- Allen, H.J., Vincenti, W.G. (1946) "Wall Interference in a Two-Dimensional-Flow Wind Tunnel with Consideration of the Effect of Compressibility," NACA Report 782.
- Batchelor, G.K. (1944) "Interference on Wings, Bodies and Airscrews in a Closed Tunnel of Octogonal Section," Report ACA-5 (Australia)
- Calvert, J.R. (1966) "Blockage Corrections for Blunt Based Bodies of Revolution," Journal of the Royal Aeronautical Society, Vol. 70, PP. 532-533.
- Glaurent, H. (1933) "Wing Tunnel Interference on Wings, Bodies and Airscrews," ARC R & M 1566.
- Goldstein, S. (1942) "Two-Dimensional Wind Tunnel Interference," ARC R & M 1902.
- Hensel, R.W. (1951) "Rectangular-Wind-Tunnel Blocking Corrections using the Velocity-Ratio Method," NACA TN-2372.
- Maskel, E.C. (1963) "A Theory of the Blockage Effects on Bluff Bodies and Stalled Wings in a Closed Wind Tunnel," ARC R & M 3400.
- Thom, A. (1943) "Blockage Corrections in a Closed high-speed Tunnel," ARC R & M 2033.
- Thompson, J.S. (1945) "Present Methods of Applying Blockage Corrections in a Closed Rectangular High Speed Wind Tunnel," ARC Report 11385. (reported in Reference AGARDograph 109).
- Young, A.D. Squire, H.B. (1945) "Blockage Corrections in a Closed Rectangular Tunnel," ARC R & M 1984.